Surface Enhanced Spatially Offset Raman Spectroscopy for the Detection of Breast Cancer Using Turbid Optical Phantoms

Submitted by

Louise Margaret Joan Clark

to the University of Exeter
as a thesis for the degree of

Doctor of Philosophy in **Physics**

December 2017

I certify that all material in this thesis which is not my own work has been identified and that no material has previously been submitted and approved for the award of a degree by this or any other University.

……………………………………………………

Louise Clark

Abstract

Breast cancer is a prevalent disease within today's modern society, affecting 1 in 8 women and 1 in 870 men within a lifetime. With the introduction of mammographic breast screening in 1987 and marked improvements to targeted therapies, mortality rates declined, highlighting the need for early diagnosis and tailored treatment to halt disease progression in its foremost stages. Histology assessed biopsies, alongside initial two-view mammographic imaging, are paired as the current diagnostic "gold standard". The need to incorporate several techniques, applying an "all-angles" approach to diagnostics, provides an effective, streamlined diagnostic pathway, reducing patient wait times between testing and results – crucial in preventing disease progression.

Optical spectroscopic techniques for the characterisation of biomolecular compounds and structures present within tissue are fast becoming the biomedical analysis tools of choice, coming to the forefront of clinical applications. Raman spectroscopy is one such technique providing highly chemically specific results, in a non-ionising and non-invasive way. When used in conjunction with metal nanoparticle probes, the inherently weak Raman signals of the biomolecules surrounding the nanoparticle surface undergo extensive levels of enhancement – an eponymous technique, Surface Enhanced Raman Scattering (SERS).

This thesis is split into two principal areas of study. The first explores extrinsic SERS nanoparticles at depth within optical phantoms, "imaged" in a Transmission orientation, mimicking the composition of the breast within a cranio-caudal mammographic imaging position. The second concerns the micro-Raman quantification of gold nanoparticles, functionalised to a biocompatible level for the active targeting of hydroxyapatite – a calcium apatite form which, when dominant within breast microcalcifications, act as a biomarker for malignancy.

Key aspects drawn from the results include a greater understanding of Raman reporter gold nanoparticles at depth, and how the absorption profile of the sample material affects the garnered intensity profile. The synthesis of a novel nanoparticle probe was also founded, with promising future applications in terms of targeting and theranostic capabilities. Furthermore, a protocol into the implementation of an automated mapping system within an open optical set-up is given, detailing the software, hardware and electrical installation requirements.

The advantages of Raman spectroscopy integration within current diagnostic practices are highlighted, with limitations such as nanoparticle biocompatibility issues, the inherent optical properties of biological tissues, and system conditions touched upon.

Acknowledgments

This thesis was made possible through the generous funding given by Cobalt Health, a Registered Charity (No. 1090790).

It was also made possible through the ceaseless encouragement and inspiring teachings of my supervisors, Prof Nick Stone and Dr Francesca Palombo, and my mentor Dr Sharon Strawbridge. Nick, thank you for always believing in me, and helping me through the past four years. There were countless times that I was unsure on my feet, so it is truly a testament to both your kind nature and passion for research that I am writing this today. Francesca, you are an undeniably dedicated force to be reckoned with! Thank you for showing me that hard-work and dedication truly pays off, and for always being a warm and comforting presence. Sharon, the generous offerings of books and insightful anecdotes will be truly missed. I often think of your stories and the achievements you have made and am always inspired to pursue and accomplish anything I set my sights to. I feel very grateful to have worked alongside such talented, enthusiastic and understanding scientists, nay people; you have my deepest respect and appreciation.

I would also like to thank several people who were instrumental in the experimental completion of this body of work. Nick Cole and the workshop – you were always kind and resourceful, no matter how odd the request! Ellen – thank you for patience and experienced help, and for managing the wet lab so impeccably despite all the chaos! Dave – there would be no Biophysics without your lab as the lunchtime hub, and breast making would have been far less practical or fun. Thanks for looking out for us and being a stand-up friend. Inge – you were there helping me get to grips with everything right from the go, thank you for the solid foundation to help build my nanoparticle work from. Ben – thank you for all your constant support and help with the deep Raman, and for not losing all hope when I would come with all variety of questions! Alexis – I am so grateful to have received your knowledgeable biochemistry help for nanoparticle functionalisation. Without this, my designs would have struggled to come to fruition at all, thank you. Claudio – thank you for your amazing MATLAB wizardry and the organisation of excellent walks. Hong – your help with the TEM analysis and accompanying warm chats were always fantastic, thank you. John Gleeson – thank you for allowing me to experiment with the Hydroxycoll, and for all your wisdom applying to collagen scaffolds.

Of course, without the undying support, endless cups of tea and shared laughs from the Biophysics team, completing this journey would have been far gloomier. Martha and Kelly – you are like my older sisters, constantly steering me in the right direction and never afraid of giving me your honest opinion! Sahand – you will always be my brother… and my son. Thanks for all the much-needed laughs and tears we share, there will always be home for you here. Leanne – for getting through this PhD thing together and being such a truly wonderful person, I'm lucky to call you my friend. Ryan and Alex Clowsley – thank you for being the best work husbands and friends. Ryan, you are the tea saint that we desperately need, but no one truly deserves. And the countless other people, Jen, Krups, Lauren, Natalie, Laureline, Sam, Adrian, Alex D, Sarah, Carl, Rikke, Pascaline and Toby, to name but a few! And thanks go to all my good friends in and out of Exeter, but especially to Karl – you've stuck by me for years, thank you for always being there, you always inspire me to work hard & enjoy life; Penny, Natalie, Frances and Krystyna – you girls are one of a kind.

To my wonderful family, thank you for your unconditional love and support, both emotionally and financially! Mum and Dad, you are my inspiration – our weekly phone calls kept me sane and on track to success. Thanks to you both for cheerleading me to the finish line, I am always striving to do better to make you both proud. Jen, I am lucky to have a sister as wonderful as you, I'm strong and confident knowing we have each other's back. Nan and Grandad, and

Granny, thank you for being the doting grandparents that you are, I feel very lucky and grateful to be able to share life experiences and to grow and learn from you. And Felix, I could not have done this without you – we have supported and looked after each other throughout the hardships of the past few years, and come out stronger. Thank you for taking care of me, keeping me focussed on the end goal, and making me the better person that I am today.

Table of Contents

List of Figures

Abbreviations

2-NT	2-Napthelthiol
2-NT-PEG	2-Napthelthiol and PEG functionalisation
2-NT-PEG-BP functionalisation	2-Napthelthiol, PEG and Bisphosphonate
4-ATP	4-Acetaminothiol
4-MBA	4-Mercaptobenzoic Acid
AuNP	Gold Nanoparticle
BP	Bisphosphonate
CC	Craniocaudal
CT	Computer Tomography
CCD	Charged Coupled Device
DI Water	De-Ionised Water
DCC	N',N'-dicyclohexyl carbodiimide
DCIS	Ductal Carcinoma In-Situ
EDC	1-ethyl-3-(-3-dimethylaminopropyl) carbodiimide
EPR	Enhanced Permeability and Retention
ER	Estrogen Receptor
GUI	Graphical User Interface
HAP	Hydroxyapatite
EPR	Enhanced Permeability and Retention
GUI	Graphical User Interface
HAP	Hydroxyapatite
HED	Human Equivalent Dose
IFP	Interstitial Fluid Pressure
keV	Kiloelectronvolt
LCIS	Lobular Carcinoma In-Situ
LSPR	Localised Surface Plasmon Resonance
MLO	Mediolateral-oblique
MPS	Mononuclear Phagocyte System
NHS (Chemistry)	*N*-hydroxysuccinimide
NHS	National Health Service
NHSBP	NHS Breast Screening Programme
NICE	National Institute for Health and Care Excellence
NP	Nanoparticle
PD	Photon diode
PBS	Phosphate Buffered Saline

PCA	Principal Component Analysis
PEG	Polyethylene Glycol
PDMS	Polydimethylsiloxane
RR	Raman Reporter
RES	Reticuloendothelial System
RR-AuNPs	Raman Reporter gold nanoparticles
SERS	Surface Enhanced Raman Spectroscopy
SNR	Signal to Noise Ratio
SORS	Spatially Offset Raman Spectroscopy
SESORS	Surface Enhance Spatially Offset Raman Spectroscopy
TEM	Transmission Electron Microscopy
TiO_2	Titanium Dioxide
TRS	Transmission Raman Spectroscopy
UV/Vis	Ultra Violet/Visible Spectrophotometry
Z	Atomic number
λ	Wavelength
μ_a	Absorption Coefficient
μ_s	Scattering Coefficient
$\mu_s{}'$	Reduced Scattering Coefficient

1. Introduction

A rapidly developing area in the field of biomedical research, optical techniques such as Raman and Infra-Red (IR) spectroscopy are fast becoming invaluable tools in cancer diagnostics. Specifically, Raman microspectroscopy and surface enhanced Raman spectroscopy (SERS) have gained widespread acceptance for their ability in characterizing biological samples. The on-going development of these techniques and constituent areas, such as the physio-chemical advancement of nanoparticles as photonic probes, has broadened the scope of samples able to undergo analysis from in vitro to minimally invasive in vivo, providing much motivation for the work presented in this thesis.

This introductory chapter presents the outline of the thesis together with some historical context of the spectroscopic techniques employed towards biomedical diagnostics.

1.1 The History of Raman Spectroscopy

The classical theory of light scattering without frequency change was postulated by Lord Rayleigh in 1871, through explanation of the age-old-question: "why is the sky blue?".[1] Theorised by Austrian theoretical theorist Smekal in 1923,[2] the phenomenon of inelastic light scattering, producing light of a higher and lower wavelength, was experimentally discovered by C.V. Raman and K.S. Krishnan in 1928, by focussing sunlight through a telescope onto a sample.[3] A narrow band filter creates a monochromatic light source used to excite molecules producing scatter: elastically as Rayleigh scattering, and inelastically as the Raman effect – an extremely rare event where the frequency of ~1 in 10^6 photons exhibits a change in wavelength.

High-powered water-cooled mercury arcs were traditionally used as light sources – cumbersome and impractical, Raman was strictly a scientists' gadget.[1] Invented by Theodore

Maiman in 1960,[4] the advent of coherent "light amplification by stimulated emission of radiation", or the laser, allowed Raman spectroscopy to become more instrumental. Subsequent technological advancement created accessible instrumentation at an affordable price and convenient size. This further increased applicability, however the inherently insensitive nature of the technique limited its growth.

In 1973, a British group of scientists consisting of electrochemist Martin Fleishmann, Raman spectroscopist Patrick J. Hendra and postdoctoral fellow James McQuillan endeavoured to study in-situ electrochemical processes of species adsorbed on the surface of electrodes.[5] Initial studies involving mercury chloride on platinum electrodes was limited in ability of signal detection.[6] In an effort to enhance the Raman signal, a strong Raman scatterer, pyridine, was selected as the adsorbate, and silver as an electrode material suitable for electrochemical surface roughening to create a large surface area.[7] In a landmark discovery, the Raman signal had been enhanced by a factor of $\sim 10^6$ comparative to pyridine in solution, with adsorption in two distinct configurations.[8] The finding was further confirmed in 1977 by David Jeanmarie and Richard Van Duyne with their prediction of an electromagnetic effect acting as the mechanism;[9] and, Albrecht and Creighton in their proposal of a chemical, charge-transfer effect taking place.[10] Both groups independently verified the enhanced signal could not be solely attributed to an increased concentration of the pyridine molecule.

This localised enhancement phenomenon, known as Surface Enhanced Raman spectroscopy (SERS), allowed Raman to become a fully realised analytical technique for real-life applications, from bulk samples down to single molecules.

More recently, the characterisation of the layers within bulk, turbid samples came with the development of Spatially Offset Raman spectroscopy, or SORS, in 2005 by Pavel Matousek et al. at the Rutherford Appleton Laboratory in the UK.[11] The technique, involving the collection of scattered photons lateral to the illumination source, has been used in combination with SERS to great effect, developed into the new expertise of SESORS.[12]

The development of Raman spectroscopic techniques to real-world applications has expanded dramatically over the past three decades. Delving into a variety of fields including: art and archaeology including the determination of age and legitimacy of paintings;[13–15] the detection of small quantities of illegal drugs or explosives adsorbed upon surfaces;[16–19] and tamper-reducing drug characterisation from within pharmaceutical blister packaging.[20–22] One of the largest growing areas, however, is the field of biomedical diagnostics, explored further within this thesis.

1.2 Overview of Thesis

This thesis is split into two major sections: theory and experimental.

The theory chapters allow the reader to gain greater understanding of the context of the work in terms of the pathophysiology and current diagnostic and therapeutic landscape surrounding breast cancer in Chapter 2; the Raman spectroscopic theory with particular emphasis on SERS and SORS in Chapter 3; and how nanoparticle biocompatibility plays a vital role in the success of an *in vivo* agent in Chapter 4.

The preliminary experimental chapters, Chapters 5 and 6, outline the gold nanoparticle chemistry undertaken, of both synthesis and functionalisation, and the manufacturing of post-menopausal breast, optically representative turbid phantoms, respectively. Following is the detailed experimental set-up within Chapter 7, which explores the engineering of optomechanical automation; the application of instrumental signal enhancement; and the tempering of nanoparticle dose in terms of biocompatibility. These three chapters preface the main experimental results and analysis.

Multiplexed gold nanoparticles present at varying depths is explored in Chapter 8, determining the possibility of *in vivo* depth measurements at a biologically sound dose. The signal recovery of the labelled nanoparticles at depth within a representative, 3D breast model under mammographic conditions is also considered, applying the technique in a complimentary way to the current mammographic imaging methods.

Chapter 9 delves into active targeting nanoparticle functionalisation, with a combination of Raman reporter, polyethylene glycol and alendronate, a bisphosphonate. Type II microcalcifications have been presented as a major biomarker for breast carcinomas, especially within acidic environments with possible malignancy. The results obtained show that not only do these functionalised nanoparticles give the desired SERS signal, but that they do selectively target calcium phosphate present within malignant microcalcifications.

Chapter 10 is the culmination of the thesis results, discussing and concluding on the findings, with potential future works also considered.

Background and Theory

Breast Cancer

Raman Spectroscopy

Nanoparticle Biocompatibility

2. Breast Cancer

Cancer is the cause of 42% of premature deaths in England with a total of 477,667 new cases registered in 2014, totalling 234,664 men and 243,003 women. Of these new cases, breast carcinomas were most prevalent, accounting for 9.7% of all cancers. Incidence rates for men have remained stable since the late 1970s, however incidence has increased in women by 11% from 2000 to 2013.[23] Through the advent of mammography screening in 1987, and an increase of breast cancer awareness through major campaigns, crucial early diagnosis of the disease has risen, with 10-year survival rates climbing from just 40% in the early 1970s, to 78% of women in 2015.[24]

In this chapter, an examination of the population in England affected by breast cancer is detailed in Section 2.1. Anatomical pathways of the breast and the biological mechanisms leading to carcinoma is presented in Sections 2.2 and 2.3. Sections 2.4 and 2.5 consider the necessity of early diagnosis and the current diagnostic imaging methods practiced in the clinical setting, respectively. Therapeutic pathways leading from diagnosis are discussed in Section 2.6. Base knowledge of the current diagnostic and therapeutic practices, and where improvements to these methods could be made, shapes the experimental design of this thesis. Section 2.7 highlights the importance of working within the remits of current practice, to enhance the current diagnostic capabilities available through the incorporation of complimentary techniques.

2.1 Epidemiology and Aetiology

Breast cancer mainly affects women, one in eight of the UK population, with a small percentage of the male population also under threat of the disease – 46,085 women and 332 men of new diagnosis in England, 2014.[23] Women aged 45 – 69 comprised the largest proportion of disease incidence of left and right breasts combined, with an overall increase in registrations of all ages, from 2004 to 2014, of 14.3%.[25]

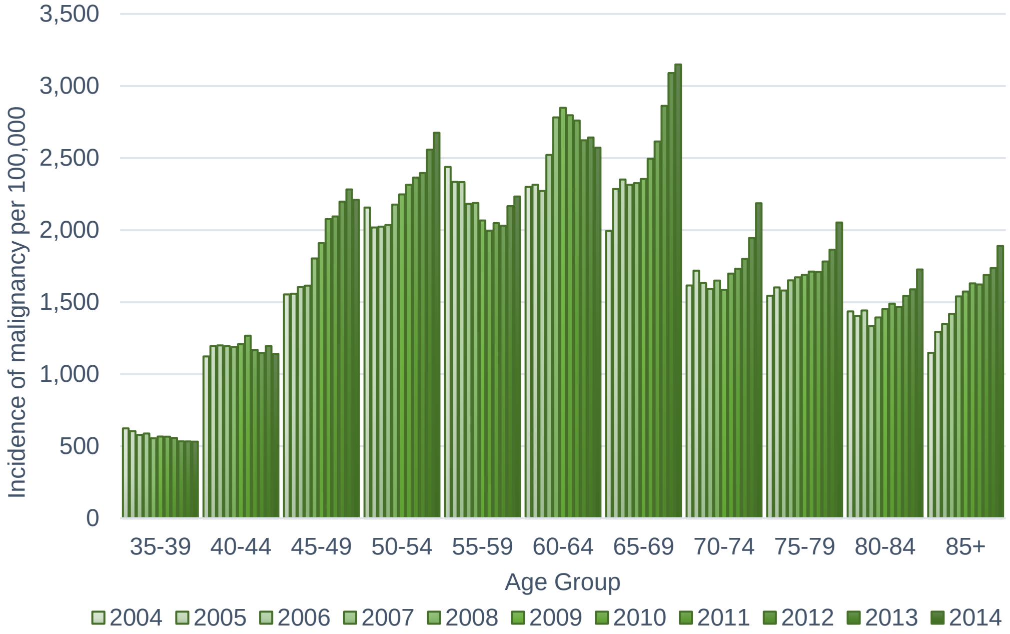

Figure 2.1: Newly diagnosed incidence rate of breast cancer (left and right breasts) in women in England from 2004 to 2014.[26]

In North America and Western Europe the age-standardized incidence rate is four-fold of that in developing countries, contributed mainly by a "Western" diet and lack of physical activity, resulting in obesity.[27] Other avoidable risk factors including smoking, consumption of alcohol, and hormonal differences, such as the oral contraceptive pill and pregnancy at a later stage in life. A combination of these elements are estimated to contribute to around 27% of female breast cancer cases in the UK.[28]

An unavoidable risk factor is familial history. The likelihood of incidence increases with the number of relatives known to have developed breast cancer – zero affected members has a base risk of 7.8%; whilst one member holds a 13.3% increase, two members rises to 21.1%.[29] Early diagnosis is crucial for the survival rates of women who fall in this category, with sufficiently high risk patients often opting for a bilateral mastectomy to eliminate the possibility of occurrence.

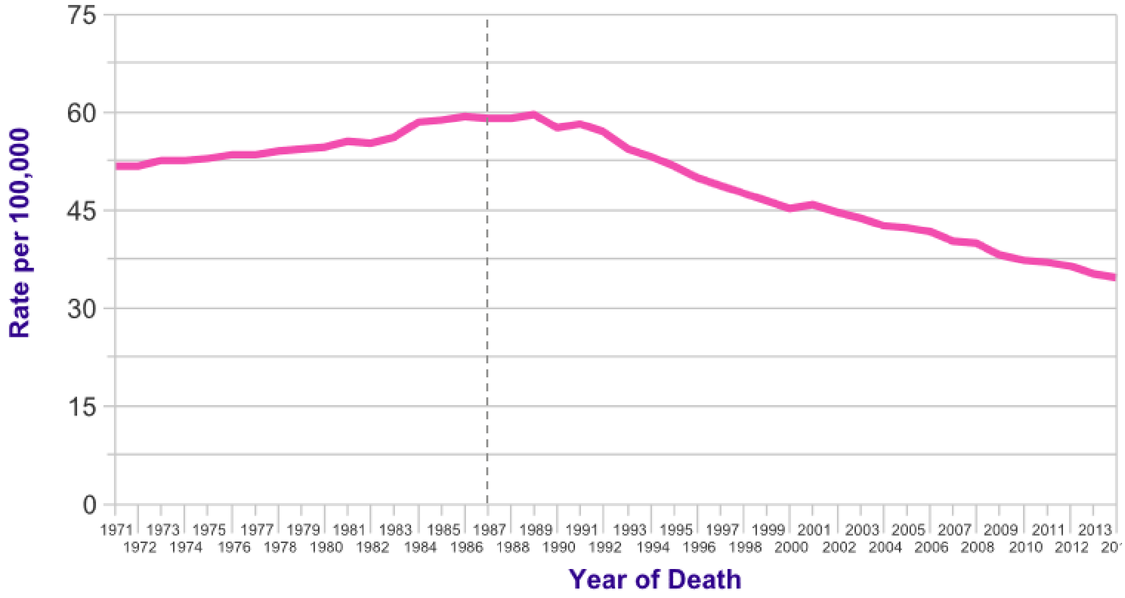

Figure 2.2: Mortality rate per 100,000 women in the UK from 1971 to 2014; the grey dotted line at the year 1987 marks the introduction of the Breast Cancer Screening Programme. Adapted from Cancer Research UK.

From 2004 to 2014, the mortality rate across all age groups in England decreased by 7.7%, most significantly in the 50 – 64 age group by 18.7%.[25] A reduction in breast cancer mortality rates of women in the UK is recognised by the implementation of the mammography screening program in 1987, as visualised in Figure 2.2.

An in-depth consideration into breast physiology gives a greater understanding into the significant role mammography plays in the diagnosis of intramammary carcinomas.

2.2 Breast Anatomy

Situated on the upper chest wall, the breast overlies the pectoral muscle in both men and women. Breast buds are formed during embryonic development. Until adolescence, the male and female breasts consist of an inactive network of lobes (glandular tissue) leading to the nipple, fatty (adipose) and connective (stromal) tissues.[30] Puberty initiates the development of the female breast into the mammary gland (Figure 2.3). Mammogenesis is regulated through growth hormones, oestrogen and progesterone, developing the ability to lactate and feed young – prolactin begins and maintains the production of milk in pregnant and nursing women.

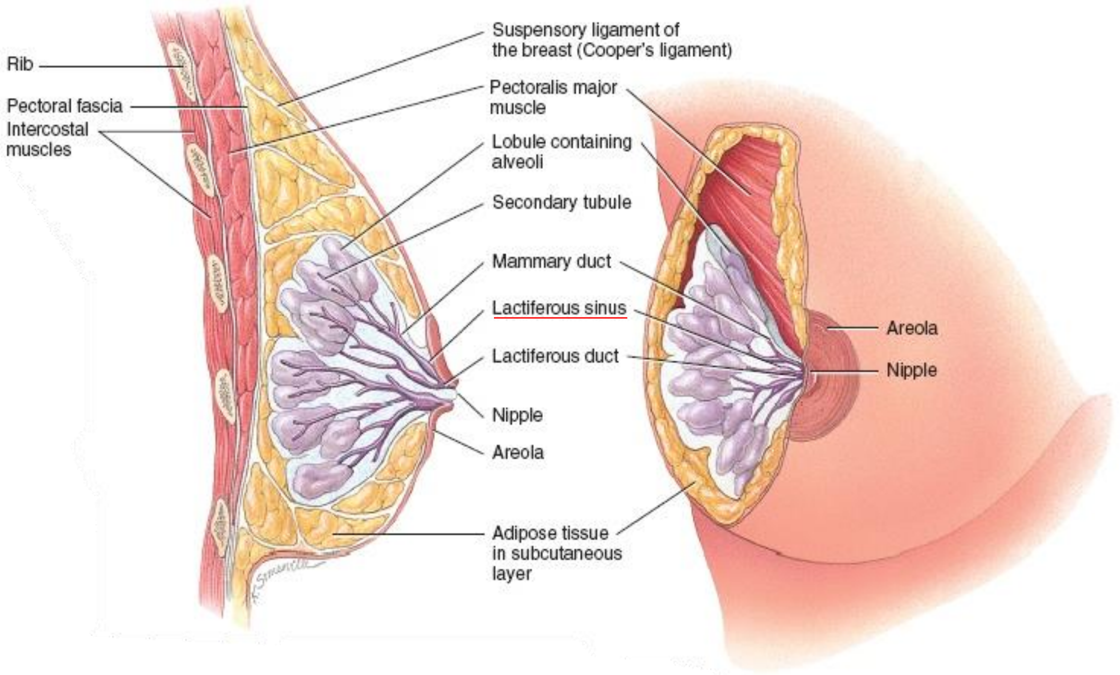

Figure 2.3: Anatomy of the mammary gland. NOTE: Lactiferous sinuses (underlined in red) were proved to not existent through ultrasonography.[31,32]

The anatomy of the breast is largely unchanged from the dissections of lactating breast cadavers conducted by Sir Astley Cooper in 1840.[33] The functioning, glandular anatomy of the breast contains alveoli consisting of dense clusters of secretory epithelial cells, which cluster together to form lobules. These lobules are connected to lactiferous ducts which have an inner layer of epithelial cells encased in myoepithelial cells.[34] Investigation with ultrasound has determined an average of 5 – 9 ducts open at the nipple, fewer than the 15 – 20 previously understood.[32,35] Adipose layers are meshed throughout the glandular tissue at a ratio of 1:1 in non-lactating breasts[31] increasing to 1:2 in lactating women.[32] Large breasts consist of a greater amount of adipose tissue. A network of stromal tissues – the extracellular matrix, blood vessels and Copper's ligaments, eponymously named – support the layers of glandular and adipose tissue.[34]

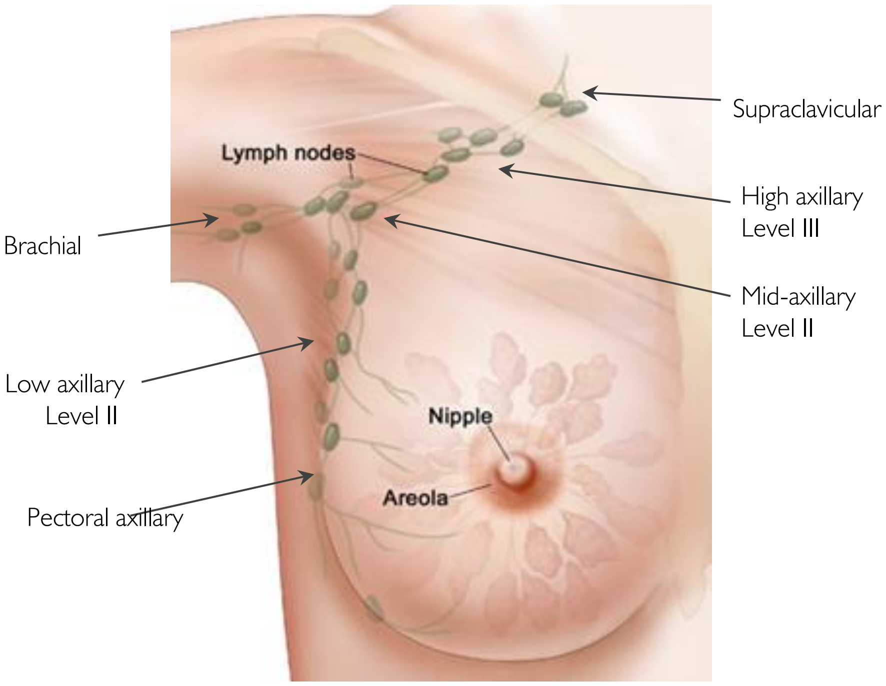

Figure 2.4: Lymphatic drainage system and lymph node regions surrounding the breast.[34]

The breast also consists of a lymphatic system dealing with immune responses to pathogens. Inflamed or enlarged lymph nodes, including all detailed in Figure 2.4, are a clinical marker for breast cancer. Neoplastic cells are able to spread through lymphatic and blood vessels forming metastases', most commonly in the bone, lung and liver.[36]

2.3 Pathology

2.3.1 Physiology

In a single breast, 25% of neoplasms occur in the upper outer quadrant, between 4 – 8% occur in the other three quadrants and only 1% in the nipple/areola and axillary areas.[23] The earliest stage of breast cancer is confined to the epithelial cells within the lining of either the ducts or lobes, known as ductal/lobular carcinoma in-situ (DCIS/LCIS). Further growth leads to infiltrating or invasive carcinoma. LCIS is less likely to turn into an invasive carcinoma, often considered as neoplasia. Necrotic and pleomorphic cells are indicative of more aggressive cancers, more likely to be associated with DCIS. Figure 2.5 shows how DCIS develops into an invasive carcinoma, requiring a network of blood vessels, enabling a rapid growth rate.

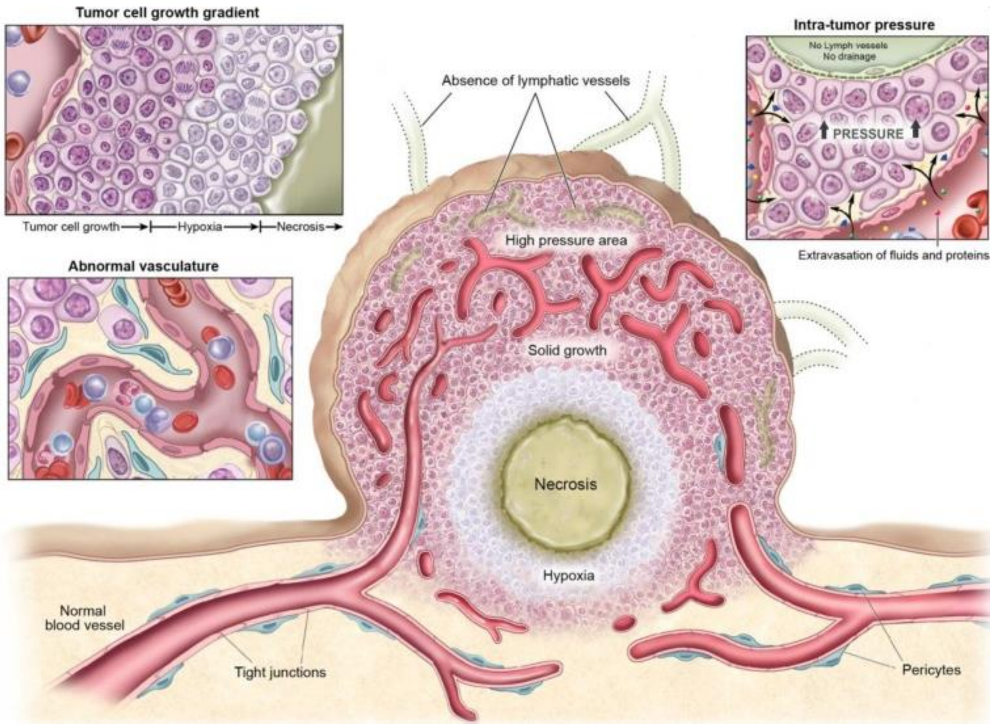

Figure 2.5: Physiological characteristics of an aggressive cancer type tumour.[37]

Malignant tumours, as small as 3 mm, rely on this rapid angiogenesis to curb hypoxic and necrotic regions from inevitably developing.[38] Poor lymphatic clearance and dilated, leaky vasculature creates a high level of interstitial fluid pressure (IFP) within the tumour. This leads to an enhanced permeability and retention effect (EPR): drawing oxygen and nutrients in and a large percentage retained, keeping a high level of growth.[39] The recently updated TNM (Tumour – Lymph Nodes – Metastasis) staging system for breast cancer is as follows:

TNM	Staging	Classification
T – Primary Tumour (Clinical and Pathological)	TX	Primary tumour not assessable
	T0	No primary tumour
	Tis	DCIS
	T1	≤20 mm in greatest dimension
	T1a	≤1 mm
	T1b	>1 but ≤5 mm
	T1c	>5 but ≤10 mm
	T1d	>10 but ≤20 mm
	T2	>20 but ≤50 mm
	T3	>50 mm in greatest dimension
	T4	Tumour with direct extension to the chest wall and/or skin
	T4a	Extension to chest wall
	T4b	Ulceration and/or satellite nodules and/or oedema
	T4c	Both T4a and T4b
	T4d	Inflammatory Carcinoma

N – Regional Lymph Nodes (RLNs) Involvement		Clinical (cN)
	cNX	RLNs cannot be assessed (e.g. previously removed)
	cN0	No RNL metastases
	cN1	Movable metastases in ipsilateral Level I, II axillary lymph node(s)
	cN1mi	Micro-metastases >0.2 mm but ≤2 mm
	cN2	Clinically fixed or matted metastases
	cN2a	Metastases in axillary lymph nodes fixed to one another or other structures
	cN2b	Metastases in ipsilateral internal mammary nodes, fixed
	cN3	Multiple Node involvement
	cN3a	Metastases in ipsilateral infraclavicular lymph node(s)
	cN3b	Metastases in ipsilateral internal mammary and axillary lymph node(s)
	cN3c	Metastases in ipsilateral supraclavicular lymph nodes(s)
		Pathological (pN)
	pNX	RLNs cannot be assessed
	pN0	No RNL metastasis identified, or Isolated Tumour Cell (ITCs)
	pN0(i+)	ITCs only (malignant cell clusters ≤0.2 mm in RNLs)
	pN0(mol+)	Positive molecular findings; no ITCs detected
	pN1	Micro-metastases
	pN1mi	Micro-metastases >0.2 mm but ≤2 mm
	pN1a	Metastases in 1–3 axillary lymph nodes, at least one metastasis ≤2 mm
	pN1b	Metastases in ipsilateral internal mammary sentinel nodes, excluding ITCs
	pN1c	pN1a and pN1b combined
	pN2	RLN Metastases present
	pN2a	Metastases in 4–9 axillary lymph nodes (at least one tumor ≤2 mm)
	pN2b	Metastases in clinically detected internal mammary lymph nodes
	pN3	Extensive RLN metastases present
	pN3a	Metastases in 10+ axillary lymph nodes (at least one tumor ≤2 mm); or metastases to the infraclavicular (Level III axillary lymph) nodes
	pN3b	pN1a or pN2a in the presence of cN2b, internal mammary nodes by imaging; or pN2a in the presence of pN1b
	pN3c	Metastases in ipsilateral supraclavicular lymph nodes
M – Metastasis	M0	No clinical or radiographic evidence of distance metastases
	cM0(i+)	No clinical or radiographic evidence of distant metastases in the presence of tumor cells or deposits ≤0.2 mm detected by molecular techniques in circulating blood, bone marrow, or other nonregional nodal tissue in a patient without symptoms or signs of metastases
	cM1d	Distant metastases detected by clinical and radiographic means
	cM1	Any histologically proven metastases in distant organs; or if in

Table 2.1: Tumour – Lymph Nodes – Metastasis (TNM) Staging Chart.[40]

This is the most common tumour staging system. To further differentiate tumours, the biomolecular characteristics are a crucial sub-classification in determining the patient specific treatment pathway.

2.3.2 Molecular Subtypes

Overexpression of three distinct types of molecular receptors define four main subtypes of breast cancer arising within cells. Oestrogen (ER), progesterone (PR) and human epidermal growth factor (HER2) receptors are overexpressed independently, resulting in either Luminal A, Luminal B, HER2 or Basal-like carcinomas, as described in the table:

Subtype	Receptor Expression
Luminal A and B	ER and/or PR +ve | HER2 -ve
HER2	ER and/or PR -ve | HER2 +ve
Triple Negative or Basal-like	ER and/or PR -ve | HER2 -ve

Table 2.2: Breast cancer subtype chart describing the presence of oestrogen, progesterone and human epidermal growth factor receptors.

The four subtypes are largely associated with invasive ductal carcinoma (50-80%) and invasive lobular carcinoma (5-15%).[40] Luminal subtypes account for around 70% (type A representing 50-60% whilst type B represents 10-20%) of all invasive breast cancers, with HER2 and Basal-like, or triple negative, types completing the last percentage with around 15% each.[41] The subtype HER2 has the best prognosis whilst Basal-like is most critical due to the aggressive nature and tendency to relapse post-treatment.[42] Luminal and HER2 subtypes are identified by ER, PR and HER2; Basal-like cancers have few or no hormone receptors, aptly described as “triple negative”, meaning non-responsiveness to targeted therapies.[43] However, the subtype has a strong association with hypoxia inducible factor 1 protein (HIF-1α) and carbonic anhydrase XI mRNA, which is overexpressed in hereditary breast cancer (BRCA1 and 2 mutation).[44] Patients with this familial history of breast cancer are annually monitored using magnetic resonance imaging (MRI).[45]

2.3.3 Microcalcifications

Breast microcalcifications are an important disease identifier presenting in around 93% of DCIS cases and having a strong association with lymph node invasion.[46] The significance of clustering and size is a reliable indicator as to whether the occlusion is benign or malignant.[47] Occurring within the lobes and ducts of the breast, the calcifications occurring within each have different appearances upon x-ray, as seen in Figure 2.6.

Large, smooth, "tea cup" shaped calcifications which appear less clustered are associated with lobular areas, and tend to be classed as benign; smaller, pleomorphic and highly clustered calcifications are associated with ducts, and treated as suspicious or malignant. As Figure 2.6 shows, both types of calcifications can be present at the same time.

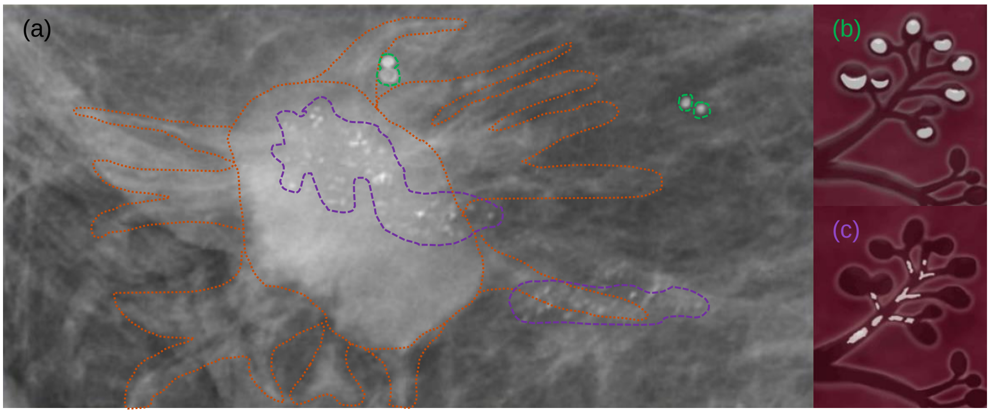

Figure 2.6: (a) Mammogram of a spiculated mass of invasive DCIS with both lobular and ductal microcalcifications present; graphics representing (b) benign lobular calcifications and (c) malignant ductal calcifications.

A study by Frappart et al. looked at microcalcifications within benign and malignant breast tissue specimens using a microprobe and electron microscopy. Analysis found two distinct types: weddellite crystals, or calcium oxalate dihydrate, or Type I calcifications, and calcium phosphates characteristic of hydroxyapatite (HAP) make up Type II. Type I appears almost entirely in benign tissue and rarely non-invasive LCIS, whilst Type II is mainly associated with malignant tissue.[48]

More recently, investigation with Raman and Infrared spectroscopy has considered the chemical composition of the microcalcifications. HAP undergoes carbonate ($-CO_3{}^{2-}$) substitution, with hydroxy groups (-OH) known as Type A, or the phosphate groups ($-PO_4^{3-}$) Type B. HAP specifically in breast malignancies undergoes B-type substitution,[49] with a higher substitution percentage lending to an increase in tumour malignancy.[50]

2.3.3.1 Bisphosphonates

Bisphosphonates (BPs) have a high affinity and selective uptake for the bone mineral hydroxyapatite.[51] BPs are administered for the skeletal disorders osteoporosis, however high doses administered either intravenously or orally can lead to osteonecrosis of the jaw.[53-55] Fundamentally, the BPs with the highest binding affinity to HAP contain a nitrogen ending, R^2 side chain. The ability of BPs to resorb bone is dramatically affected by the slightest change to the structure of this side chain.[54]

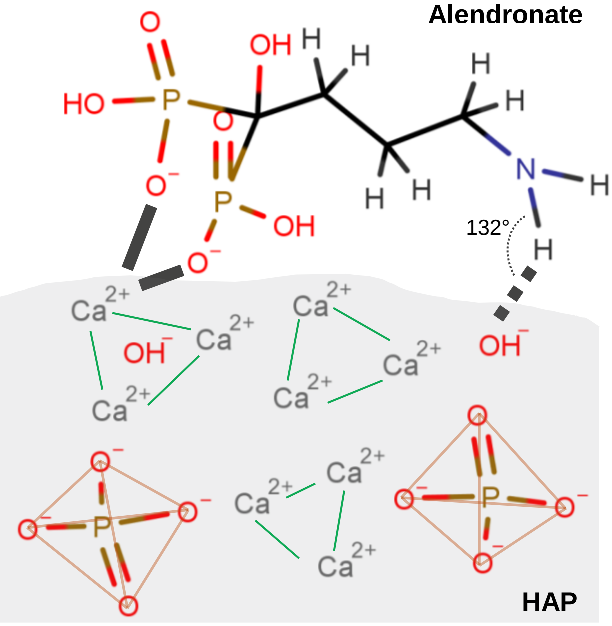

Figure 2.7: Alendronate binding sites on basic HAP structure demonstrated: $-O^-$ from the $-PO_4^{3-}$ groups bind to the $-Ca^{2+}$; strong H-bonding interaction occurs between $-NH^2$ and oxygen groups.

There are two main binding sites on BPs: the free $-O^-$ form an ionic bond with the $Ca2^+$ ions within the HAP, whilst the N-H hydrogen bonds to the free $-OH^-$ within the HAP. Alendronate binding to HAP is visualised in

Figure 2.7. The binding angle at the hydroxyl site greatly affects the binding affinity: a larger angle forms a stronger electrostatic attraction.

In recent advances, BPs have been proven to help reduce pain encountered with bone cancer, reduce tumour growth rates within breast and prostate tissue, and slow or even halt the development of bone metastases.[55–58] Recent studies have suggested the use of BP labelled AuNPs in order to provide a targeted contrast agent when using x-ray to image bone malignancies.[59]

2.4 Early Diagnosis

The early diagnosis of cancer is crucial in reducing mortality and morbidity, providing patient peace-of-mind and relief from underlying symptoms.[60] The World Health Organisation has three steps to early diagnosis: cancer awareness and access to healthcare; clinical evaluation, diagnosis and staging; and access to treatment.[61] A Walters et al. study looking at breast cancer survival over a seven-year period in six developed countries found that the UK 3-year survival rate was 87-89%, comparative to 91-94% in four other countries including Australia, Canada and Sweden.[62] The National Awareness and Early Diagnosis Initiative (NAEDI) was launched across England in 2008 to bring awareness to the need for early diagnosis – however, the British trait of a tendency to avoid seeking medical advice or aid is difficult to overcome. Healthcare and treatment within the UK is widely accessible, although delay between symptom onset to diagnosis, and diagnosis to treatment greatly affects patient mortality.

A systematic review by Richards et al. found that patients who had a 3 – 6 month delay between symptoms and diagnosis of breast cancer had a 7% worse 5-year survival rate than those with a shorter delay.[63] Aiming to reduce this delay, the latest NICE guidelines for suspected cancer has set the national target of referral within 2 weeks of initial patient assessment.[64]

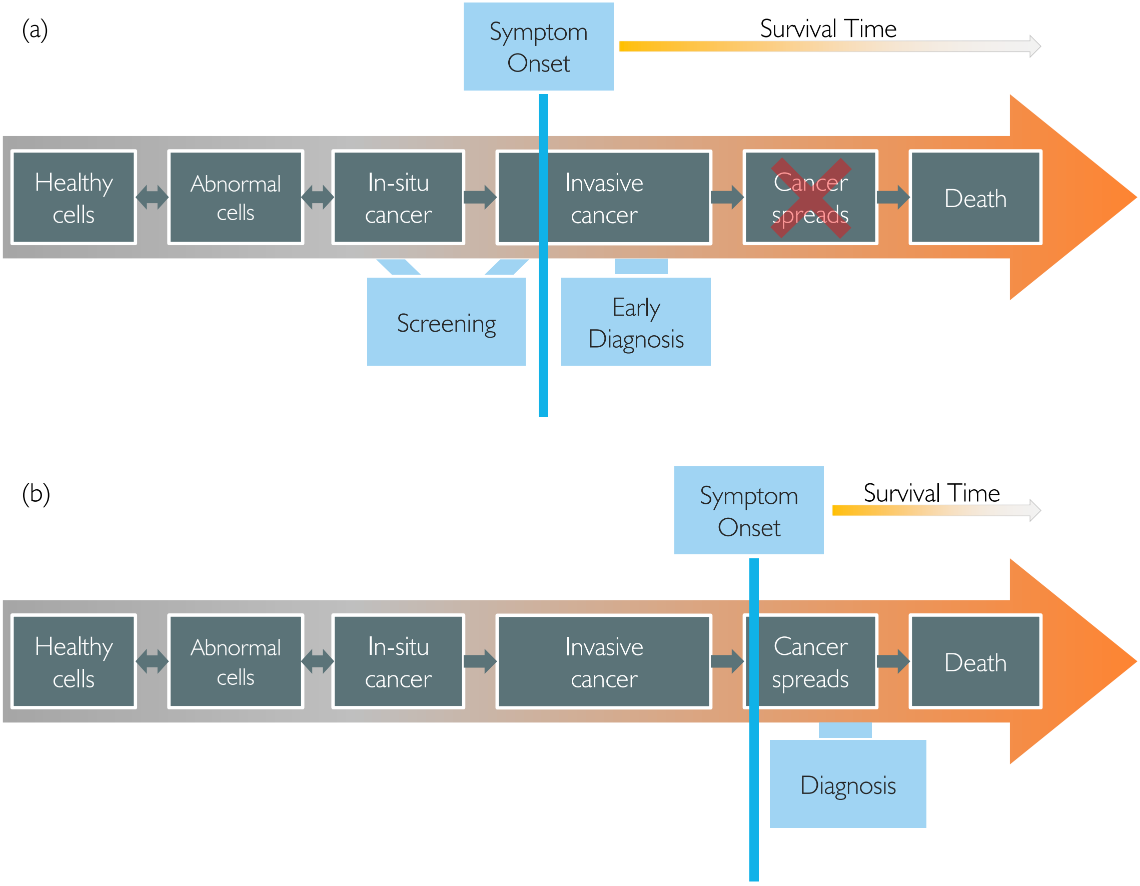

Figure 2.8: Graphic detailing whether early diagnosis is beneficial or conceivable for: (a) breast cancer, where early diagnosis is likely even before symptom onset with the use of screening, delaying or completely offsetting mortality; and (b) colorectal cancer, where symptomatic diagnosis is unable to improve mortality. Adapted from [61]

Despite increased awareness and improvements to early diagnosis, with some cancers, such as pancreatic or colorectal, the patient can remain asymptomatic until the disease has progressed to a level of poor prognosis, see Figure 2.8. In 2015, a Delphi study was undertaken to find expert consensus by ranking 21 common cancers by how beneficial early diagnosis would be for patient mortality and/or morbidity.[60] After two-rounds, the final ranking conclusively placed breast cancer at the top with the greatest potential benefit. Pancreatic, brain and oesophageal had the lowest rankings – unlike breast cancer, as seen in Figure 2.8, screening is unviable and treatment options are sparse making early diagnosis nowhere near as beneficial.[65]

From these findings, it can be said that the early diagnosis of breast cancer is clearly favourable and justified, as a major factor in increased survival rates and reduced recurrence rates.

However, when determining the effectiveness of screening for early diagnosis, it is important to analyse the age-specific mortality of the patients, rather than survival rates. This is due to lead time bias, as shown in Figure 2.9.

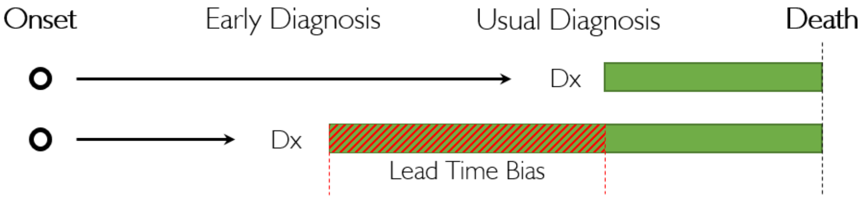

Figure 2.9: Visualisation of lead time bias affecting breast cancer survival rate statistics

In this example two patients with an identically timed onset of breast cancer succumb to the disease at the same age, however one patient was diagnosed earlier than the other due to screening. The period between the two patients for early and usual diagnosis is the lead time bias, in dashed red, hence markedly increasing the survival rate of this patient, in green, comparative to the usually diagnosed patient. Instead of this patient living for a longer time, as assumed with survival rates, the early diagnosed patient is just knowingly living with the disease. Hence, the age-specific mortality should be preferentially used to analyse screening studies.

The cost of different diagnostic and therapeutic pathways of breast cancer, per person per year, in the UK is visualised in the bar charts below, Figure 2.10.

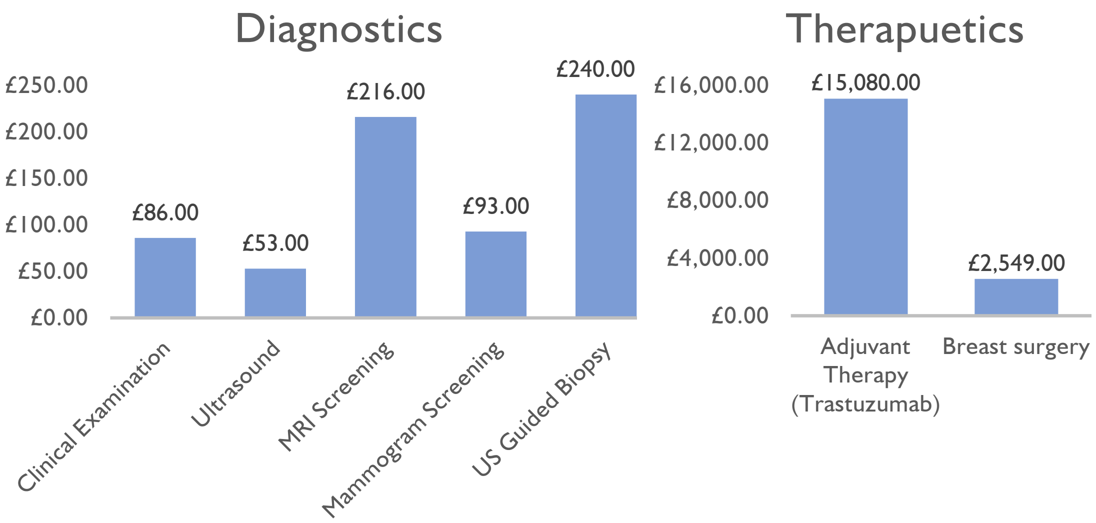

Figure 2.10: Charts outlining the annual cost of diagnostics (clinical examination, ultrasound, MRI and mammography breast cancer screening and ultrasound guided biopsy) and breast cancer therapeutics (adjuvant therapy using Trastuzumab, a HER2 chemotherapy drug, and breast surgery) of per person in the UK. Figures are extracted from reports between 2009 - 2016.[66–70]

Many breast cancer cases will involve all four cost factors outlined above, totalling £18,352.30 for a single patient in the year since diagnosis. Multiple adjuvant therapies, repeat check-up mammograms and sometimes more global surgery is required, increasing costs further. As such, it is imperative to diagnose and treat breast cancer as early as possible.

2.5 Current Diagnostic Methods

Diagnostic imaging methods of breast cancer range from mammography to ultrasound, and MRI, with histopathology as the "gold standard" in confirming diagnosis. A 2016 update to the NICE Quality Statements now requires "timely diagnosis" via a multimodality, triple diagnostic assessment, comprised of a physical examination, a mammogram or ultrasound imaging, and biopsy, in a single hospital visit.[71]

2.5.1 Clinical Examination

Regular self-breast examination (SBE) is encouraged as a low-cost, low-risk, self-performed method to catch breast cancer in the early stages to decrease morbidity and mortality.[72] Despite little evidence confirming this, it is a useful tool in breast awareness encouraging women to take responsibility in their health.[45] The low-cost of self and clinical breast examination (CBE) has hence become an invaluable screening method poorer areas of developing countries where diagnostic imaging is costly resource.[73]

In a CBE both breasts and the lymph nodes from the axillae to above the clavicles are assessed. The clinician checks for numerous “red flags”: breast symmetry; movement of any palpable lumps; dimpling of the skin; inflammation or soreness in the lymph nodes; and unusual inversion or crusting of the nipple.[74] This clinical examination is age followed up by either mammography, for post-menopausal women, or ultrasound, for pre-menopausal women or those with dense breast tissue.

2.5.2 Mammography

Mammography is the “gold standard” screening and diagnostic imaging method as it is tailored to the detection of slow-growing tumours within the general affected population of women.[27] Ionising radiation is used to produce a high contrast image of the breast tissue allowing visualisation of dense masses and microcalcifications which may be present. Mammograms are a risk factor in themselves - a single bi-lateral mammogram contributes a lifetime risk of inducing fatal breast cancer of 1.3–1.7 cases in 100,000 women aged 40 years at exposure.[75]

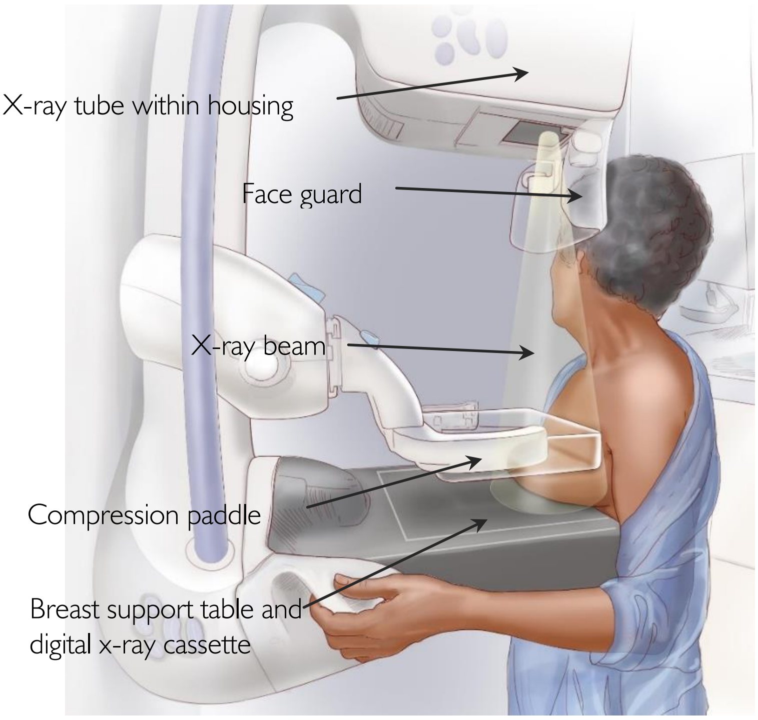

Figure 2.11: Annotated image of a mammography x-ray unit imaging patient in a cranial-caudal view.

The two views are “cranial-caudal” or CC taken from above, and an oblique view “mediolateral-oblique” or MLO. The breast is compressed by the paddle, as seen in Figure 2.11, at around 110 – 120 Newtons to gain a diagnostically “good” to “perfect” image under parameters set by the NHS Breast Screening Programme (NHSBSP) publication “Quality Assurance Guidelines for radiographers”.[76]

Breast compression plays a key role in improving the image quality in several ways. An overall reduction in breast thickness will produce a thinner, uniform mass which requires a lower radiation dose. This minimizes x-ray scatter reducing the signal to noise ratio (SNR) whilst improving contrast[77]. Compression spreads the tissue layers apart allowing easier visualisation[78]; and the reduction of patient movement will create a sharper image.[77] A further imaging technique of spot compression, as in Figure 2.12, focuses on a small area of the breast to maximise separation of the tissue allowing better contrast and visualisation of margins and microcalcifications.[78]

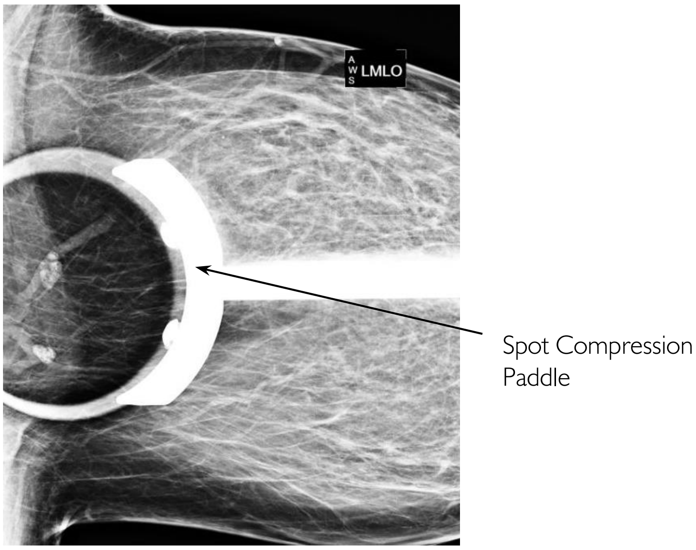

Figure 2.12: Left MLO projection using spot compression on a dense breast to highlight two large, posterior densities.[79]

In recent years, Digital Breast Tomosynthesis (DBT) has been employed as an additional mammographic technique, enabling tomographic, pseudo-3D imaging of the breast combatting the "anatomical noise" created by overlying breast tissue features.[82] This ability to easily visualise and better discriminate between tissues has been proven to markedly increase sensitivity leading to earlier detection of neoplasms in two meta-analysis studies in post pre- and post-menopausal women.[83,84]

Risk factors in using mammography include the use of ionising radiation to obtain an image, false-positives - the patient does not have the disease despite positive results from both mammography and biopsy - of which there were 3.3% in 2011-12 leading to over-diagnosis and over-treatment.[80] These risks are not only detrimental to the patient psychologically and physically, but also raises expenditure within the NHS. The specificity and sensitivity of mammography screening is vastly reduced when contending with patients who are premenopausal, present with glandular tissue, or have breast implants – ultrasound is the preferred imaging method for these patients.[81] On average, the chance of a false positive result after each mammogram is 10.7%, leading to an unnecessary biopsy; false negative diagnosis affects 20 – 26% of patients, delaying their true diagnosis.[27]

2.5.2.1 Screening

In the UK, women aged between 50 – 70 are invited every three years for breast screening. Between 2008 and 2009, 2,116,588 women were screened by the UK NHSBSP. In 17,045 cases cancer was detected (8.1 per 1,000 women screened), of which 13,532 (79%) were invasive.[82] The development of cancer from staging the invasive carcinoma at screening, to the surgically removed tumour size, shown in Figure 2.13, highlights the need for a streamlined diagnosis-to-treatment pathway. 93.1% of all breast screening patients were seen within the 62-day period between referral from an NHS screening service and first definitive treatment, between 2015 and 2016.[83]

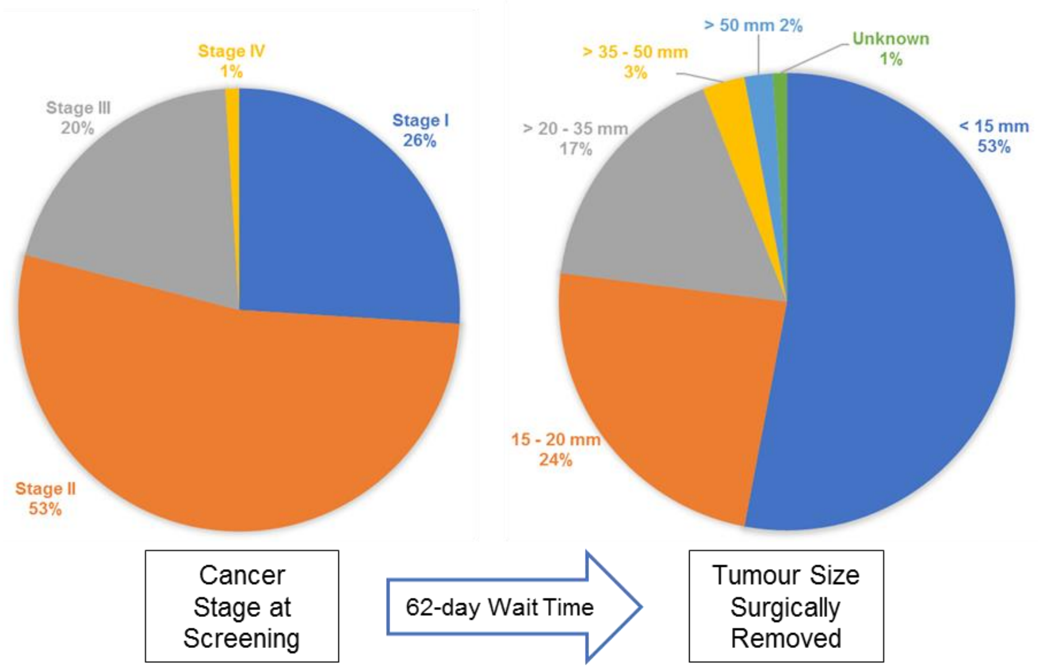

Figure 2.13: Invasive breast cancer discovered through screening, percentage categorized into: left pie chart – invasive cancer staging; right pie chart – size of the tumour surgically removed.

One of the most important factors in determining the success of a screening programme is patient uptake and re-attendance, and the diagnostic accuracy of the technique.[80] In 2013, a systematic review by Whelehan et al found that 25% – 46% cited pain due to compression as the main reason why they did not re-attend, which is comparable to approximately 47,000 to 87,000 women per year in England alone.[84] Growing rates of obesity in postmenopausal women is not only an associated risk factor but is affecting the required Newtons of compression needed to gain a diagnostic image. A positive trend has occurred in the standard CC breast thickness size. Traditionally, the average, compressed breast thickness was defined as 45 mm. After a review in 2005 this rose to 53 mm, which is now argued to be increased to ~60 mm.[85] A study in 2015 looked at variations of breast compression in three UK sites, Manchester, Chester and Burnley, where the obesity prevalence rate is 61.5%, 64.2% and 69.2% respectively.[86] The mean CC thickness across all three sites was 50.4 mm, whilst the largest recorded thickness was 62.61 mm, with increased and variable compression force applied.[87] Difficulty penetrating the breast tissue sufficiently for a diagnostic image leads to a higher rate of false positives and false negatives.

2.5.3 Ultrasound

Ultrasound (US) is an imaging technique which produces non-ionising, ultra-high-frequency soundwaves (standard clinical range 5-15 MHz) from piezoelectric crystals. A voltage is applied across the crystals causing them to oscillate, emitting ultrasonic waves from the medical transducer into the patient. The transducer detects the returning echoes from the tissue and interprets them into a monochromatic image. US is a highly sensitive technique capable of differentiating benign cysts and solid mass likely to be malignancies, usually presenting as anechoic and hyperechoic respectively.

Ultrasound has a higher sensitivity to non-palpable breast masses and premenopausal, dense breasts.[88] A large trail study found that US detected an additional 3.7 cancers per 1000 women post mammography screening, with the risk of false positives decreasing significantly.[89]

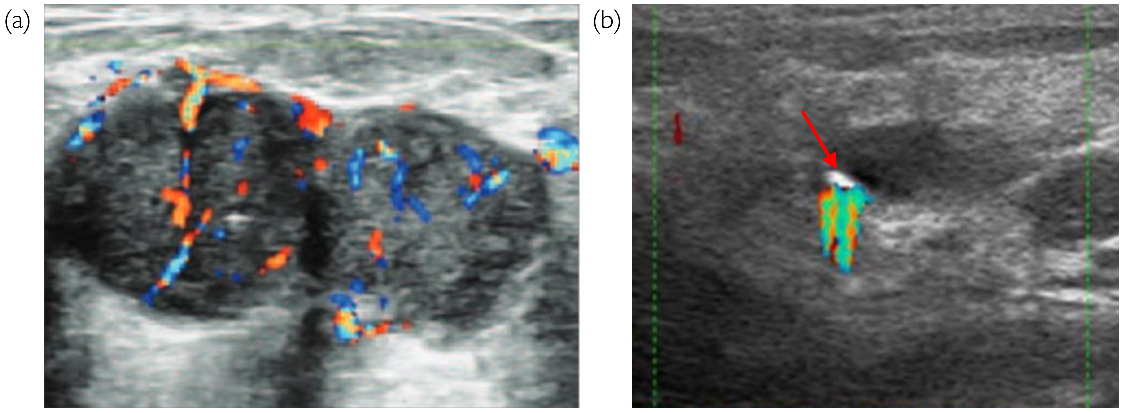

Figure 2.14: Doppler ultrasound imaging of (a) a malignant tumour with irregular vasculature and (b) a breast microcalcification, highlighted with the red arrow, creating a twinkling artifact.[90]

Doppler US is a useful tool for assessing vascular abnormalities within a mass – leaky and enlarged vasculature present in malignant masses are easily identified this way.[91] Microcalcifications are reflective to Doppler US giving the appearance of turbulent blood flow, known as a twinkling artefact as seen in Figure 2.14(b).[90]

The detection of microcalcifications with US is limited. A main attribute to this is the spatial resolution of the system – increasing the transducer to a high-frequency, 30 – 70 MHz, provides better visualisation, but this is traded with a lower level of depth penetration into the tissue.[97-99] US also requires highly trained sonographers to image breast lesions effectively and in guiding the needle used for percutaneous biopsies.

2.5.4 Biopsy and Histopathology

There are two main types of breast biopsy – fine needle aspiration (FNA) and core biopsy, as pictured in Figure 2.15. FNA, as the name suggests, uses a fine needle to aspirate a small volume of tissue from a suspicious lesion. Core biopsies, and vacuum-assisted core biopsies, use a much larger needle to extract a larger, cylindrical volume of tissue.[93] Though providing a larger sample, core biopsies require local, or sometimes general, anaesthetic which comes with a patient risk of allergic reaction to the anaesthesia.

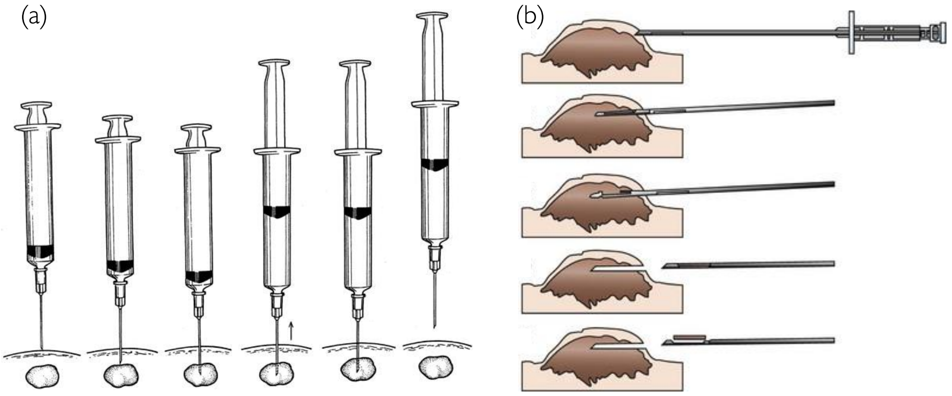

Figure 2.15: Graphics showing the procedures for (a) fine needle aspiration and (b) core needle biopsies.[94,95]

As the gold standard, breast biopsies are taken to histopathology where they are sectioned and stained for diagnosis under the microscope. The piece of biopsy tissue first undergoes gross examination, with and without a microscope. The tissue is embedded in paraffin wax, sliced to 4 μm on a microtome to visualise the cells adequately at a high spatial resolution.[96] Stains are applied to highlight different cellular features – haematoxylin stains cell nuclei blue, whilst eosin stains cytoplasm, connective tissue and other extracellular substances pink or red – for analysis under a microscope. The nature of the tissue is decided to be either benign, "uncertain" or malignant. Tissues classified as uncertain follow the same pathway as those classed as benign – leading to false negatives but also a reduction in patient over-treatment. If a malignancy is found, the molecular subtype is investigated to determine the hormone receptor status necessary for therapy.

A precedence in the importance of microcalcifications to diagnosis via histopathology has been set within the 2016 updated clinical guidance for breast cancer screening.[93] If present within the x-ray imaging, the representative microcalcifications must be demonstrated within the core biopsy specimens. Failure to do so requires a repeat biopsy or an advanced diagnostic surgical biopsy, to ensure the microcalcification is excised for evaluation. This sets a high priority and pressure on the practitioner to capture the required tissue and microcalcifications upon the first instance.

Historically, agreement of diagnosis between histopathologists is a highly-disputed matter – interobserver studies of Stage I breast carcinomas over the past twenty years has increased from a 79.5% agreement in 1995[97], to 90.3% in 2015.[98] Development of fixation techniques and an increase in knowledge and experience has led to more agreeable diagnoses. Communication between histopathologists and radiologists is key to ensuring a correct diagnosis is reached.[96]

2.5.5 Magnetic Resonance Imaging

MRI is a non-ionising imaging technique using strong magnetic fields and radio frequency (RF) pulses to analyse the motion of protons within hydrogen atoms on axial, sagittal and coronal planes. Bilateral breast coils are used to transmit and receive a homogeneous RF signal across the breast. Coils produce a high-quality image, keeping the fat signal supressed for good soft tissue contrast and reducing the SNR.[99] Contrast enhanced MRI for breast imaging uses gadolinium to speed up the relaxation time of hydrogen atoms in water, improving the clarity of lesions in the imaging and changing diagnostic decisions for up to 40% of patients.[107] Gadolinium has, however, been linked to nephrogenic systemic fibrosis (NSF), causing thickening and scarring of the skin and internal organs in patients with poor kidney function.[107] As such, the use of several gadolinium based contrast agents is restricted to patients with a high estimated Glomerular Filtration Rate (eGFR).[107] MRI images are significantly more sensitive and specific than mammography or ultrasound, 90.3% and 89.7% respectively, although this can increase the rate of false positives.[89,69] MRI is costly, at a price per patient of £216 in 2010, making it unviable for use as a screening method for the entire population.[69] However, annual surveillance is offered to women with a familial history, aged 30 years onwards.[100]

2.6 Therapeutics

Breast cancer patients with early diagnosis typically follow the route of surgery followed by a second, or adjunctive, therapy to maximise the initial treatment effectiveness. For advanced cancer patients, the adjunctive therapy is used to control tumour growth and suppress the symptoms. Radiotherapy, chemotherapy and hormone therapy can also be used as a neo-adjuvant, shrinking the tumour prior to surgery reducing risk of complications.

2.6.1 Lumpectomy or Mastectomy

Lumpectomy is breast-conserving surgery where the tumour and a radial margin of 2 mm of surrounding tissue is excised to be examined histopathologically, under the NHSBSP standards.[101] Partial mastectomy or quadrantectomy involves a larger area of breast removal – preservation of the lactiferous ducts is a high priority since surgical disruption could affect the drainage of a large area of glandular tissue. For large tumours and elevated risk patients, as previously discussed, mastectomy removes the entire breast(s) which can include the surrounding lymph nodes.

2.6.2 Adjuvant Treatment

Radiotherapy targets high energy x-ray photons directly into the tumour, disrupting the DNA within the cells and stopping proliferation. Post lumpectomy or mastectomy, radiotherapy is the most common adjuvant treatment, applied to the whole of the remaining breast or chest wall respectively. Major side effects of the combined treatment are localised skin burning, lymphoedema, reducing movement in the arm and shoulder of the affected side, and inducing increased osteoblastic and osteoclastic activity, leading to a higher risk of fragility fractures.[111]
Chemotherapy is the use of cytotoxic drugs which target highly-proliferating cells in the body, non-specifically destroying both malignant and healthy cells. Hair follicles, nail beds and the intestinal epithelium cells are most commonly affected, leading to hair and nail loss, reduction

in appetite and nausea.

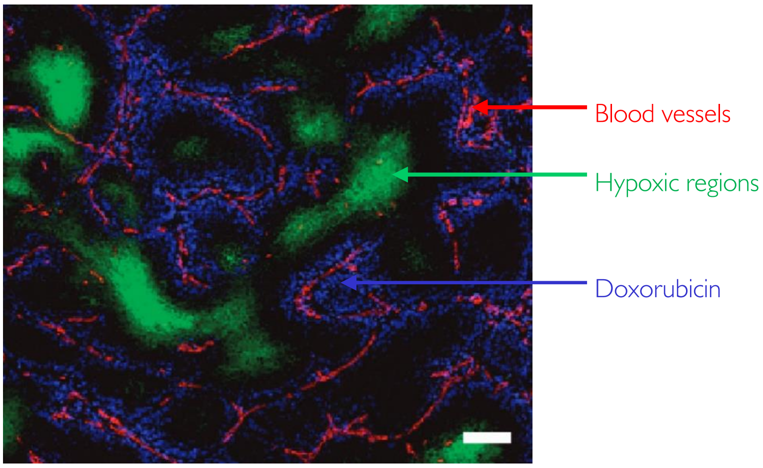

Figure 2.16: A three-colour composite fluorescence microscopy image shows scarce uptake of Doxorubicin, administered via the blood vessels, into the hypoxic regions of a breast cancer tumour.[102]

Typically, an amalgamation of two or three drugs are used to attack the cells at distinct stages of cell cycle growth. A widely used drug, Doxorubicin, has been shown to have poor penetration depth into the hypoxic regions of breast cancer tumours, as shown in Figure 2.16.[102] Chemotherapy is most effective when used in combination with radiotherapy which has the ability to penetrate deep into the tumour growth.

Hormone therapy lowers or blocks the growth effects of Luminal A and B, and HER2 cancer subtypes. Historically, the competitively-binding estrogen receptor drug Tamoxifen had been used in 75 – 80% of patients to reduce recurrence rates of ER-positive breast cancer.[112] More recently an enzyme that synthesizes estrogen from androgens has been developed into a treatment drug, Aromatase Inhibitor (AI). AIs have provided an alternative means of hormone therapy in women whose ovaries cannot produce significant amounts of aromatase.[112,113] For patients who have a Triple Negative or Basal like cancer, exhibiting no receptor expression, hormone therapy is not employed. **Targeted therapy** interrupts the pathways of, or blocks growth proteins characteristic to the breast cancer cell. Antibodies are targeted to the specific protein type, such as HER2 and epidermal growth factor receptor (EGFR), making the treatment less destructive compared to chemotherapy.

2.7 Summary

Breast cancer incidence continues to grow across the globe. Campaigns to increase disease awareness, minimize the delay between symptoms to diagnosis, and implement effective treatment has resulted in significant improvements in breast cancer survival rates across the UK. The value of detecting cancer early is clear, and significant improvements can be made in the clinical applications surrounding cancer diagnosis.

Current medical imaging techniques are inefficient in disease detection, often requiring the carcinoma to reach a late stage before visualisation can occur – even in the highly successful asymptomatic screening programme, around half of all cases present as Stage II. The ability to gain mammographic images of diagnostic quality causes procedural pain through compression, and hence lower patient return rates, due to increased rates of obesity. Ultrasound imaging caters to those patients with denser breasts, yet requires an additional, invasive biopsy. MRI is a highly sensitive imaging technique; large costs play a key role in the selectivity of patients for which the procedure can cater for, limiting its use.

False positive diagnosis is responsible for the over treatment of patients. Human error and differential diagnosis is inevitable with radiologists interpreting images and histopathologists determining the presence of malignancy within the biopsy.

Multimodality imaging allows a more thorough approach to diagnostics. It is therefore important to increase the potential of current diagnostic methods by introducing techniques which are complimentary to present procedures, providing unique and further information. Current imaging methods assess and discriminate breast tissue and cellular features on a morphological basis. The biochemical analysis of the tissue, detecting the molecular changes prior to a physiological change, is a diagnostic technique currently unexplored in the hospital setting. Moreover, the use of a diagnostic and therapeutic, or theranostic, combined technique is yet to be considered as a clinical practice.

3. Raman Spectroscopy

To gain an understanding of how vibrational spectroscopy is applicable in the analysis of biological samples, it is important to first discuss the main theoretical principles surrounding Raman spectroscopy, discussed in Section 3.1 . Surface Enhanced Raman spectroscopy (SERS), the history of which is briefly covered in the introductory chapter, is a critical technique employed within this body of work – its mechanisms and adaptations are covered in Section 3.2. Further emerging biomedical "imaging" techniques are further discussed in Section 3.3.

3.1 Theory of Raman Scattering

Light interacting with matter can be either absorbed, taking a molecule from a ground to excited state, or scattered. When an oscillating photon of light interacts with a molecule, the negatively charged electron cloud is distorted by the oscillating electric field and the molecule is shifted to a higher, virtual energy state. The oscillating molecular dipole will emit a new photon at the same frequency or wavelength to the incident one if there is no change in polarisability of the molecule during this oscillation. In this case the scattered light is equal to that of the incident light – elastic, Rayleigh scattering. However, if there is a change in the polarisability of the molecule, a discrete change in energy to the molecule can take place, changing its molecular vibrational state. The molecule can gain or lose energy from the photon, moving to a higher (Stokes) or lower (anti-Stokes) state.[103]

At ambient temperature, room or body, the lowest vibrational ground state level is prevalent. Hence Stokes' is the predominantly produced and therefore more favourable Raman scattering in the analysis of molecular content.

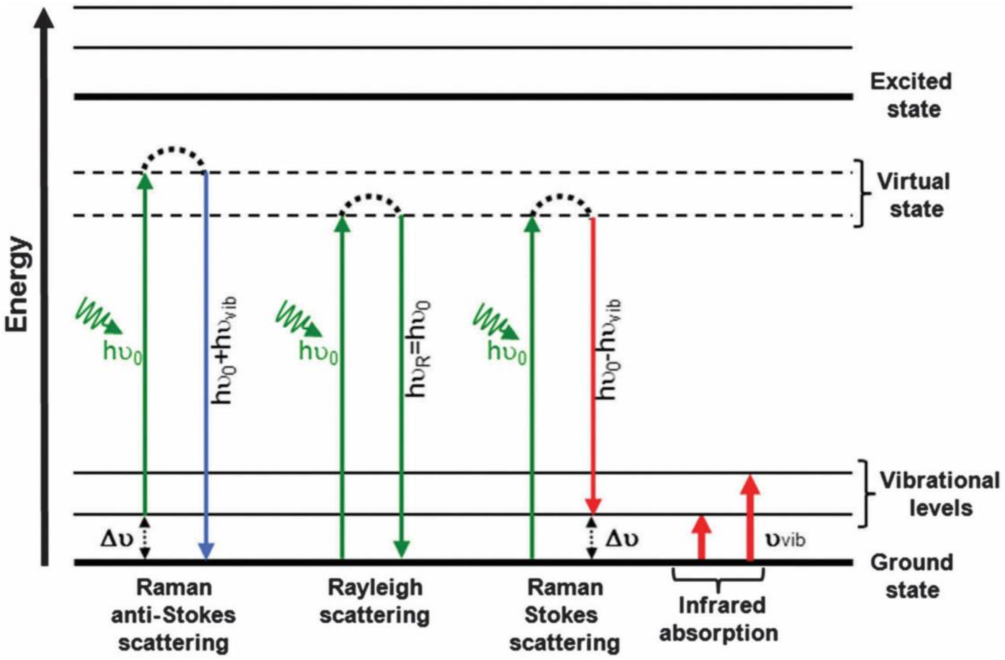

Figure 3.1: A Jablonski diagram showing the energy level transitions involved during Infrared absorption, Rayleigh, Raman Stokes and anti-Stokes scattering ($\mathbf{h}\boldsymbol{v}_{\mathbf{0}}$ = incident laser energy; $\mathbf{h}\boldsymbol{v}_{\boldsymbol{vib}}$ = vibrational energy; $\boldsymbol{\Delta v}$ = Raman shift; $\boldsymbol{v}_{\boldsymbol{vib}}$ = vibrational frequencies.)^{104}

If a molecule has a vibrational mode whereby a dipole moment oscillates at the frequency of the incident radiation absorption will occur, demonstrated in Figure 3.1 as for IR absorption in from ground to molecular vibrational levels. Mid-IR photons are highly absorbed by biological materials and are incompatible with deep *in vivo* measurements planned here forth in this thesis. Conversely Raman scattering relies on a change in polarizability of a molecule.

3.1.1 Polarizability

The ease of which a molecule can be distorted is known as the polarizability, α, which is dependent on the number of electrons and how many energy levels they occupy. Atoms with a large nucleus have a strong polarizability – the electron cloud is distant from the nucleus allowing an ease of distortion.

The principles of Raman scattering can be mathematically described. Polarizability, α, induces a dipole moment, μ_{ind}, under the applied electric field, E, as seen in Equation (1) below.

$$\mu_{ind} = \alpha \, \mathrm{E} \tag{1}$$

At a molecule's nuclear geometrical equilibrium, α_0, and at a distance away from the molecule's equilibrium geometry, Δr, the polarisability α is

$$\alpha = \alpha_0 + \frac{\delta\alpha}{\delta r}\Delta r \tag{2}$$

with the derivative

$$\frac{\delta\alpha}{\delta r} \tag{3}$$

explaining the change in polarizability depending on the change of the molecular position. If this value is equal to 0, the molecule being described does not have a changeable polarisability and is therefore not Raman active.

The Δr details the vibrations or rotations of the molecule undergoing polarization in terms of time, t, and the frequency of the vibration, v, where r_{max} is the maximum vibrational amplitude, shown in Equation (4).

$$\Delta r = r_{max} \cos(2\pi v t) \tag{4}$$

The applied electric field, E, also has a specific frequency, v_{in}, which has a maximum electric field frequency, E_{max}, as explained below:

$$E = E_{max} \cos(2\pi v_{in} t) \tag{5}$$

Both Equations (4) and (5) include the term 2π to convert the frequency and time parts of the equation into values which oscillate from 1 to 0 to -1 in a co-sinusoidal fashion, mimicking the induced molecular vibration under the applied electric field.

Substituting the Equations (2), (4) and (5) for α, Δr and E respectively allows for the Equation:

$$p = \alpha_0 E_{max} \cos(2\pi v_{in} t) + E_{max} r_{max} \frac{\delta\alpha}{\delta r} \cos(2\pi v t) \cos(2\pi v_{in} t) \tag{6}$$

The relationship between the two cosines is as shown:

$$cos\ a \times cos\ b = \frac{1}{2}(\cos(a+b) + \cos(a-b)) \tag{7}$$

where $cos\ a$ represents $2\pi v_{in} t$ and $cos\ b$ signifies $2\pi v t$. "$\cos(a+b)$" defines the Anti-Stokes scattering of Raman, where the value is the sum of the incoming light plus the vibrational frequency; "$\cos(a-b)$" is the Stokes scattering, where the incoming light minus the vibrational frequency is defined.

By substituting the product of the two cosines into Equation (6) we obtain the following Equation:

$$p = \alpha_0 E_{max} \cos(2\pi v_{in} t) + \frac{E_{max} r_{max}}{2} \frac{\delta\alpha}{\delta r} (\cos(2\pi(v_{in} + v)) + \cos(2\pi(v_{in} - v))) \tag{8}$$

From Equation (8) we can find the terms for both inelastic/Raman and elastic/Rayleigh scattering. The variable v_{in} is the frequency of the incoming light, but also describes the outgoing scattered photon of the same frequency. Therefore, the polarizability of a molecule and hence scattering of light is dependent on the frequency of the incoming light, vibrations of the molecule and applied electric field, with the derivative $\frac{\delta\alpha}{\delta r}$ giving the selection rule to whether the molecule is Raman active.

3.1.2 Hooke's Law

Within the molecule, individual atomic bonds are more readily Raman active than others. A strong double bond will allow less distortion, storing more energy compared to a single bond.

Under Hooke's law, the vibration of these individual bonds within a diatomic molecule can be described as:

$$v_m = \frac{1}{2\pi}\sqrt{\frac{K}{\mu}} \tag{9}$$

where K is the spring constant (N/m) of the bond between the two atoms. The molecular vibration, v_m, is proportional to the strength of the bond, whilst being inversely proportional to the inertial or reduced mass, μ, described as:

$$\mu = \frac{m_1 m_2}{m_1 + m_2} \tag{10}$$

where m_1 and m_2 are the masses of the atoms. Hence, both the atoms and individual bonds contribute to the characteristic, molecular vibrations. Symmetric vibrations cause the greatest distortion to the electron cloud, most commonly associated with Raman active molecules. Conversely, asymmetric vibrations cause a change in dipole and hence allow IR absorption.[103] Typical bond vibrations include stretching, rocking and wagging as seen in Figure 3.2.

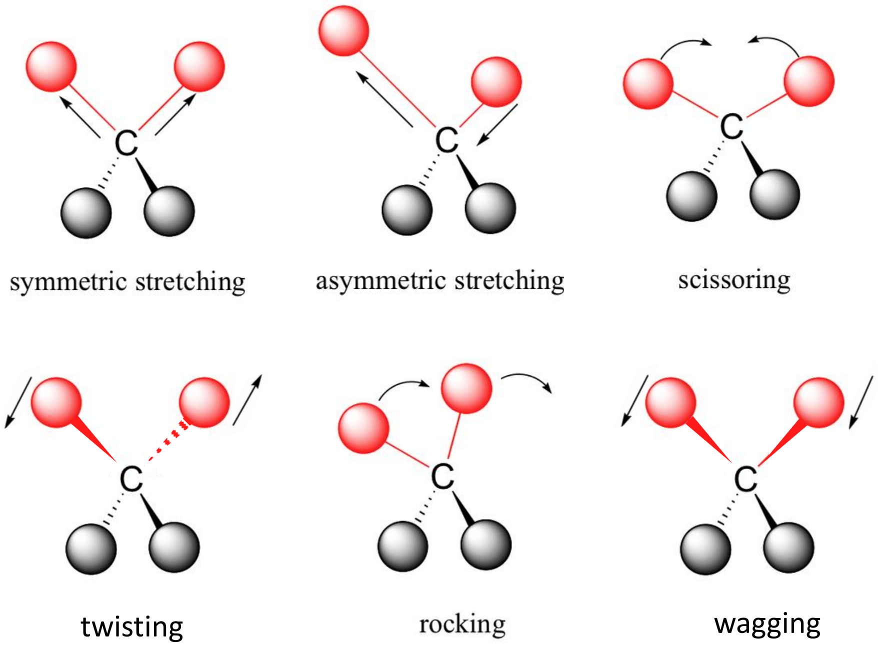

Figure 3.2: Six types of vibrational modes. Adapted from [105]

3.1.3 Raman Cross Section

Every molecule has a total Raman cross section, σ_{RS}, measured in units of cm^2 denoting the area of the molecule readily available for particle-photon interaction. This cross section defines the Raman signal, I_R, that a density of molecules per cm^3, D, can produce:

$$I_R = I_0 \sigma D dz \tag{11}$$

The excitation laser intensity, I_0, and path length travelled through the sample, dz, also affects the Raman scattering produced.[106] The relationship between the intensity of Raman signal and the wavelength of incident light can be described as:

$$P_S \propto \frac{I_0}{\lambda^4} \tag{12}$$

where it is inversely affected to the fourth power. This is known as the scattering coefficient of the material.[107] The σ_{RS} of a molecule is incredibly small, requiring large concentrations or changes in the spectroscopic technique and hence optical set-up, such as coherent anti-stoke Raman scattering (CARS) and stimulated Raman scattering (SRS), to provide sensitive measurements.[108,109] The use of surface enhanced Raman spectroscopy (SERS) enables low analyte concentrations to garner a large σ_{RS}, whilst keeping the Raman system unaltered.

A typical, modern Raman spectroscopy system is generally comprised of: a monochromatic laser source; an arrangement of optics guiding and focussing light to and from a sample; a spectrometer collecting and detecting the Raman photons; and computer aided analysis of the detector results. A Raman spectrum displays the biochemical, molecular “fingerprint” of the sample. Known as Raman shift, measured as a function of energy in units of wavenumbers (cm^{-1}). The intensity of the signal is proportional to the number of Raman active bonds within the sample – which can be increased by orders of magnitude with the introduction of metallic nanoparticles for SERS.

3.2 Surface Enhanced Raman Spectroscopy Theory

As discussed in the introductory chapter, SERS can be broken down into two processes: electromagnetic enhancement as proposed by Jeanmaire and Van Duyne; and chemical enhancement suggested by Albrecht and Creighton.[9,10] This section delves into the theory behind SERS, and how the technique can be adapted to suit an array of biomedical applications.

3.2.1 Mie Theory and Localised Surface Plasmon Resonance

Colloids have historically been utilised since the fourth century (AD). The most visible example today is stained glass within churches and cathedrals. The process involved medieval artists mixing gold and silver metallic salts into the molten silica compound. The respective metals created red and yellow panes of glass as light shone through, as seen in Figure 3.3. Varying the size of metal NPs to "give rise to a variety of colours" was theorised by Michael Faraday in 1856.

Figure 3.3: 14th century medieval stained-glass window at Troyes Cathedral, France.

This could not be fully established however until the turn of the twentieth century. The optical properties of colloids theorised in 1908 by German physicist, Gustav Mie, through his solution of Maxwell's equation.

The eponymous theory is used to describe the absorption, scattering and extinction cross section of a spherical NP. The interacting photon distorts the electron cloud forming a collective, sinusoidal oscillation of the free electrons, altering the Raman cross section. Mie theory holds two assumptions: both the surrounding media and the NPs are dielectric in nature; and the radius of the NP is smaller than that of the incident light wavelength (λ).

The extinction cross section (C_{ext}) of NPs suspended within a medium is calculated as[110]:

$$C_{ext} = \frac{24\pi^2 r^3 {\varepsilon_m}^{3/2}}{\lambda} \frac{\varepsilon_i}{(\varepsilon_r + 2\varepsilon_m)^2 + {\varepsilon_i}^2} \tag{13}$$

The dielectric constants of the real and imaginary parts of the metal is described as ε_r, or real, and ε_i, imaginary, respectively; ε_m describes the medium. The dielectric constants and the size of the NP are the main variables affecting C_{ext}.

Further, the extinction of the light is separated into two areas: scattering (C_{sca}) and absorption (C_{abs}) cross sections. The relationship can be described as:

$$C_{ext} = C_{abs} + C_{sca} \tag{14}$$

Equations (15) and (16) breaks down C_{abs} and C_{sca}. In the equations, k describes the direction and magnitude of light through the sample ($k = 2\pi/\lambda$), whilst the nanoparticle volume is defined by r:

$$C_{abs} = 4\pi k r^3 \, Im\left[\frac{\varepsilon_{np} - \varepsilon_{media}}{\varepsilon_{np} - 2\varepsilon_{media}}\right] \propto \frac{r^3}{\lambda} \tag{15}$$

$$C_{sca} = \frac{8\pi}{3} k^4 r^6 \left|\frac{\varepsilon_{np} - \varepsilon_{media}}{\varepsilon_{np} - 2\varepsilon_{media}}\right|^2 \propto \frac{r^6}{\lambda^4} \tag{16}$$

Whereby ε_{np} and ε_{media} are the dielectric constants of the NP and surrounding media, respectively.

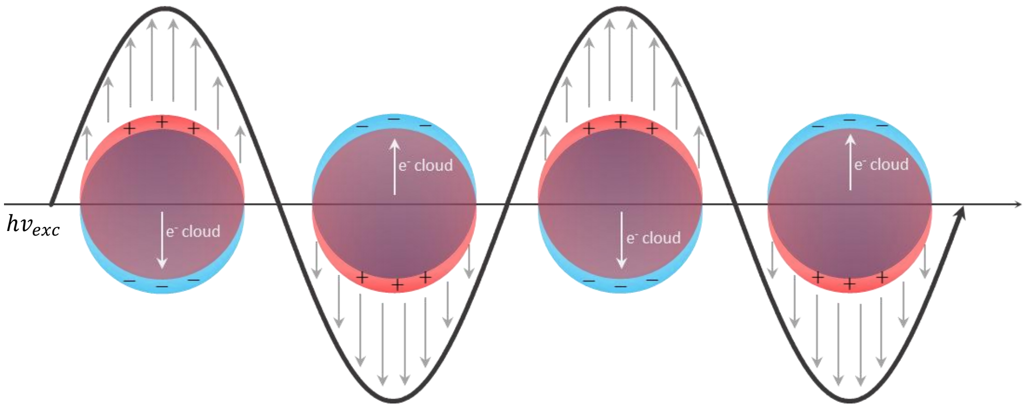

Figure 3.4: Localised surface plasmon resonance – free electron cloud oscillation occurring upon the NP surface, within the interacting wavelength ($\boldsymbol{hv_{exc}}$), enhances the local EM field.

This shows both scattering and absorption cross sections increase proportionally to NP size, hence the number of free electrons upon the NP surface, with C_{abs} increasing at half the rate to C_{sca}. This phenomenon of electromagnetic enhancement, known as localised surface plasmon resonance (LSPR), is visually interpreted in Figure 3.4.

Adsorption of a molecule to the NP surface, distance Angstrom in length, creates a further chemical enhancement, Figure 3.5.

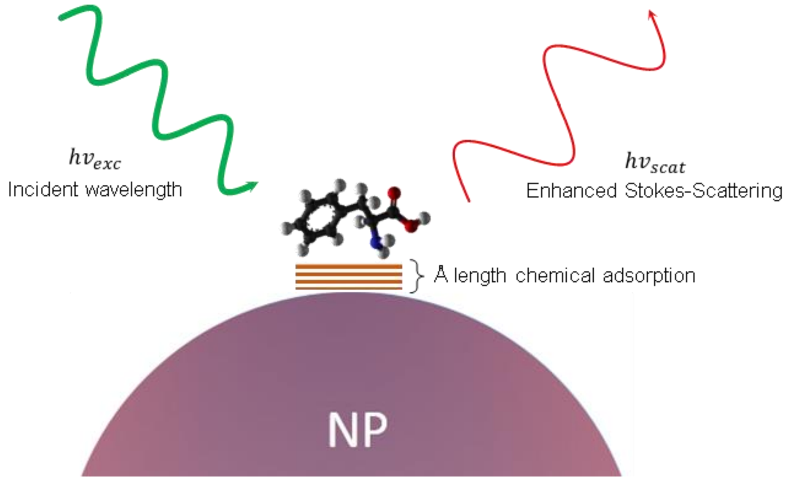

Figure 3.5: Molecule adsorbed to or orientated within Angstrom length near to NP produces chemical enhancement. Adapted from [114]

Contributing factors to the signal enhancement include: the change of molecular polarizability once adsorbed; a charge-transfer between the analyte and metal complex; and molecular resonance with the LSPR.[111–113] Van der Waals forces leading to this physisorption upon a NP surface affects molecular symmetry, vastly changing the Raman spectrum. This is dependent upon the newly found vibrational modes of the molecule, and the molecular orientation.

The enhancement factor (EF) of a molecule within SERS is denoted by the following equation:

$$SERS\ EF = \frac{I_{SERS}/N_{SERS}}{I_{RS}/N_{RS}} \tag{17}$$

whereby I_{SERS} denotes the SERS Raman intensity, whereas I_{RS} relates to the normal Raman intensity; N_{SERS} and N_{RS} correspond to the number of molecules under the respective conditions.[115] Electromagnetic enhancement accounts for signal increase by a factor of 10^4 – 10^6, whilst the magnitude of chemical enhancement accounts for a factor of $\sim 10^2$. Single molecule measurements have been shown to create enhancements of up to 10^{14}.[116,117] This is generally not well understood.

In utilising the SERS technique, adjustments to NP composition and morphology allows the adaptation of the LSPR to be fit for purpose in terms of the illumination wavelength and material to be analysed.

3.2.2 Plasmon Tuning

The two most common metals used for SERS techniques are gold (Au) and silver (Ag). This is due to the real dielectric function contributing to C_{abs} and C_{sca}, from Equations (15) and (16), of both metals being highly enhanced at resonance with the incident wavelength – known as the Fröhlich condition.[118] The NP dielectric constant, ε_{np}, is controlled by changing the size, shape and material, as seen in Figure 3.6. This effectively changes the plasmon absorption, and hence scattering, tuning the LSPR.[109] Binding events lead to a slight change in the surrounding medium, ε_{media}, with the resulting change in refractive index, which also affect the LSPR causing a red-shift – this in itself can be used as a LSPR sensor, biomolecule detection method.[119] Ag inherently surpasses Au as a SERS substrate due to higher absorption at the

LSPR region. However, for biomedical applications of SERS, the red-shifted LSPR position of AuNPs makes them a preferred plasmonic substrate, further discussed in Section 3.3.[120]

In selecting laser wavelength, maximum enhancement is observed when wavelength is red-shifted with respect to the LSPR, in order to achieve electromagnetic enhancement of both the incident and radiated fields.[121,122]

In increase in the overall radius of spherical NPs achieves a resonant enhancement red-shift, as seen by the LSPR peak shift of gold and silver nanospheres in Figure 3.6. Elongation of these spherical NPs to a rod-like shape creates a secondary, further red-shifted plasmon peak, corresponding to the shorter longitudinal and longer transverse axes.[123] Anisotropic particles with sharp surface features, such as nanorods and prisms, possess the "lightening rod" effect, whereby the localised electromagnetic enhancement can increase up to a hundred fold.[124]

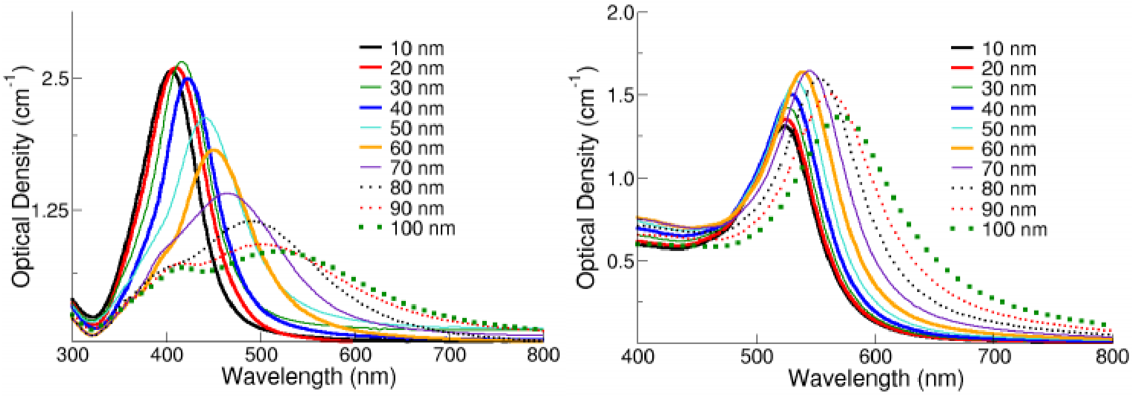

Figure 3.6: Graphs to show the optical density, attenuation of scattered and absorbed light, of silver (left) and gold (right) spherical NPs increasing in diameter size. This shows the tunability of the LSPR of NPs depending on the size and material used.[130]

The dipole moments of NPs can be capitalised upon in the form of "hot spots". NPs placed within the formation of dimers, with an interparticle gap of 0 – 1 nm, was found to red-shift the LSPR with approximately 2 orders of magnitude greater enhancement, known as "dipole coupling".[120,125] Structures with sharper tips present greater maximal enhancements, such as triangle NPs, which can be shaped into bowties, garner the maximum dipole coupling.[126,127]

Dipole coupling, however, as the enhancements are highly localized to the region, drop off rapidly with distance.[128,129] Requiring uniform positioning, the trait is often reproducibly exploited within a NP array setting.

Another large area of development is the use of core/shell NPs. Specifically in multimodal imaging, iron oxide core/Au-shell NPs: harnessing the superparamagnetic properties for MRI use and magnetic guidance through the body, whilst using the inert gold surface as a biocompatible material with scope for further surface functionalisation.[131–135] The use of an Au shell also affects the LSPR in the form of a red-shift. Multifunctionality in AuNPs opens a wide range of imaging possibilities, including the use of extrinsic SERS and therapeutic capabilities.

3.2.2.1 Raman Reporters for Extrinsic SERS

Intrinsic SERS is the direct enhancement of a desired molecule. Conversely, extrinsic SERS is the NP surface chemisorption of molecules having inherently strong Raman active modes. These molecules are commonly referred to as Raman reporters (RRs).[12,136] RRs including aromatic compounds are most widely used, with the ring breathing mode of benzene recognised as a highly sensitive marker. Extrinsic SERS has a number of advantages over intrinsic: the technique is extremely sensitive, negating the need to enhance low concentration biomolecules; a protective and/or targeting layer, such as silicon and polyethylene glycol (PEG), and/or antigens and receptor molecules can be used to encase the reporter NP, encouraging biocompatibility; and a number of distinctive reporters may be used concurrently for multiplexed Raman imaging capabilities. [12,128,136–138]

The mechanism of Raman-reporter-to-colloid-surface attachment commonly used is covalent bonding. Most studies use -thiolated RR due to the chemical stability against competing molecules, however nitrogen and isothiocyanate terminal group RR are also used, having an affinity to the gold colloid surface.[139,140] AuNPs of larger diameters (≥50 nm) have been shown to adsorb Raman reporter molecules, 2-NT and 4-MBA, with increasing efficiency and signal intensity, up to an enhancement factor of 10^3, as the nanoparticle size increased.[110]

Several sets of RR-AuNPs allow for multiplexed use within a single system.[12,138] Coupled with individual and specific targeting capabilities, each RR would signal distinct areas of disease in either highlighting benign or malignant regions, or determining the molecular subtype of a carcinoma for tailored therapy.

3.2.2.2 Nanoparticle Theranostics

Theranostics are considered valuable techniques, allowing clinicians to diagnose and treat simultaneously within one patient visit. The intrinsic nature of NPs can be exploited in creating a theranostic NP probe. In tuning the laser wavelength to the maximum resonance of the NP (λ_{max}) , laser irradiation can occur, causing heating of the NPs in a technique known as photothermal therapy.[141–143]

As described in Equations (15) and (16), the efficiency of absorption, $\frac{r^3}{\lambda}$, dominates over the scattering efficiency, $\frac{r^6}{\lambda^4}$, especially with smaller NPs. As seen in

Figure 3.7, from the study by Jain et al, nanospheres and nanorods of a smaller diameter and effective radius and nanoshells composed of a greater shell ratio, are more efficient at light absorption and hence photothermal therapy techniques.[144]

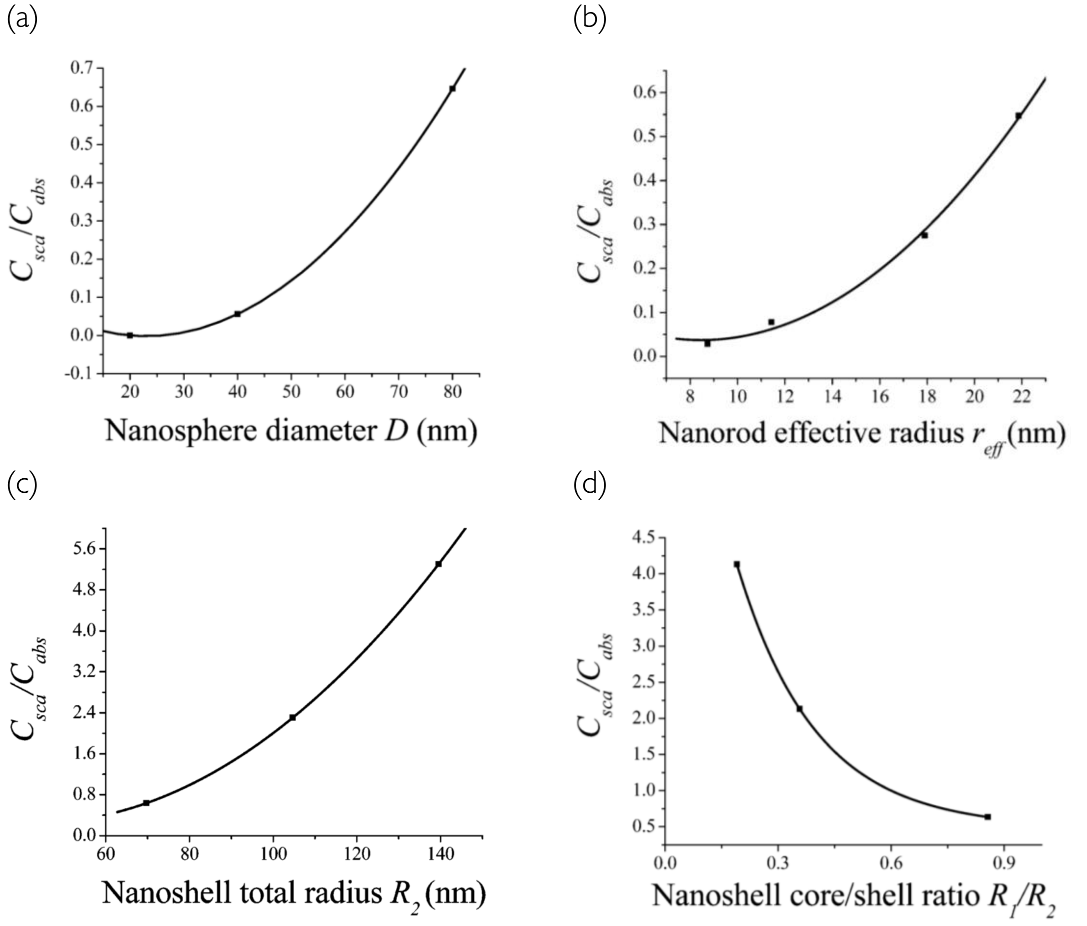

Figure 3.7: Tunability of the ratio of scattering to absorption of nanoparticles. Variation of $\boldsymbol{C_{sca}/C_{abs}}$ with (a) nanosphere diameter *D*; (b) nanorod effective radius r_{eff} at fixed aspect ratio $R = 3.9$; (c) nanoshell total radius R_2 at fixed $R_1/R_2 = 0.857$; and (d) nanoshell core/shell ratio R_1/R_2 at fixed $R_2 = 70$ nm.[144]

AuNP mediated photothermal therapy of human breast epithelial carcinoma (SK-BR-3 cells) by means of silicon core/Au shell (100:10 nm core/shell ratio) nanoshells, was first studied by Hirsch et al..[145] Thermally induced cell death, via loss of cell membrane integrity and protein denaturation, occurred in tuning the laser wavelength to the $\lambda_{max} = 820$ nm. The composition of a smaller nanosphere diameter favours the C_{sca}/C_{abs} efficiency for photothermal therapies; however for diagnostic purposes, the λ_{max} must be taken into consideration when selecting the laser wavelength and NP size in respect to the NIR "biological window".[144,145]

3.3 Spectroscopic Bioimaging Techniques

Spectroscopic techniques for the analysis of biological samples requires both the illumination and collection wavelengths to lie within the NIR region between 650 – 900 nm.[148]

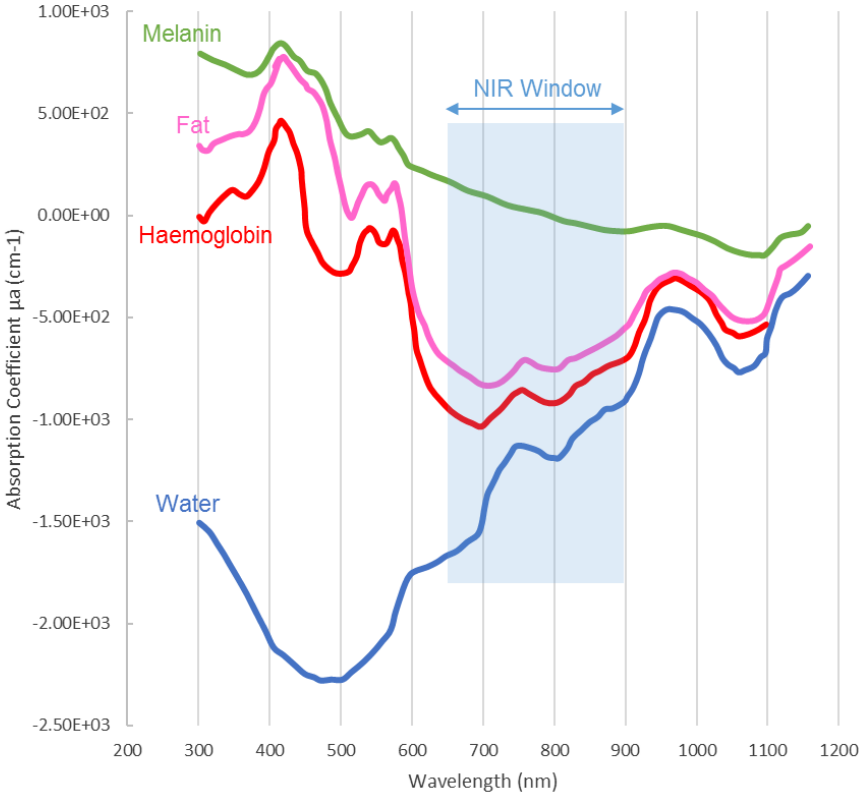

Figure 3.8: Absorption coefficients of biological molecules and the NIR window which allows photons to enter and exit the media with increased ease. Adapted and modified from [146,147]

This spectral region is the “biological window”, whereby water, haemoglobin, and most relevant to breast tissue, fat, are at the lowest absorption coefficients, as seen in Figure 3.8.[147,149] To maximise the efficiency and penetration depths of spectroscopic techniques, selection of the illumination wavelength is an important factor. The illumination wavelength, which in turn affects the sample collection wavelengths, must both sit within the NIR window to avoid the absorption of photons allowing the maximum number Raman photons to be created and collected from the system. The absorption profile of eumelanin which is black-brown, is inherently greater than that of pheomelanin, red-yellow, which is represented in Figure 3.8. This is an unavoidable variance between patients and wavelength selection.

Propagation of light through a biological medium is dictated by the scattering and absorption coefficients of the sample, μ_s and μ_a respectively, measured in units of cm^{-1}. Adding the two coefficients leads to the total attenuation coefficient of the media.

Absorption in biological tissues is due to water and macro-molecules, such as fats, melanin and haemoglobin.[107] The inverse of μ_a, I_a, defines the mean penetration depth into the absorbing medium.

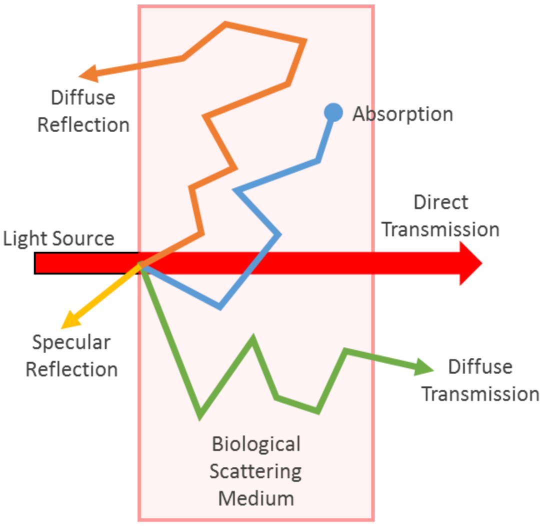

Figure 3.9: Possible photon pathways through tissue. Adapted from [150]

In biological media, light scattering is generally anisotropic, g, whereby light propagates in a continuous, forward direction.[151,152] This diffusion of light through a biological sample is known as the reduced scattering coefficient, described as:

$$\mu_s' = \mu_s(1 - g) \tag{18}$$

Figure 3.9 shows the diverse ways photons can be scattered or absorbed within biological media.

Optical scattering within a homo- or heterogeneous biological layer, such as skin tissue, is due to particles refracting light to varying degrees of efficiency. The inverse parameter of μ_s, $1/\mu_s$ (cm), is known as the mean free path (MFP). Combining mean penetration depth and MFP length statistically predicts a photon scattering potential. For example, at ~650 nm skin tissue has a penetration depth of ~50 μm, and MFP of 5 mm; hence, single photon absorption occurs after 100 scattering events.[153]

Laser wavelengths employed in biological sample studies range from 532 – 830 nm, and most typically 785, 808 or 830 nm, allowing penetration and collection of inelastic light with minimal photodamage occurrence.

Research into biological specimens is vast, with the main area of study concerning carcinomas. The Raman fingerprint of biological tissues generally ranges between 400 – 2000 cm^{-1}, and sometimes into the higher wavenumbers between 2,700 – 3,500 cm^{-1} most commonly associated with the CH_2CH_3 symmetric stretch of lipids and proteins.[154] Disease changes significantly alters the ratio of intensity, peak broadening or peak shift within the characteristic Raman spectrum.

3.3.1 Micro-Raman Spectroscopy

The technique of micro-Raman spectroscopy utilises a microscope objective to both focus and collect the scattered light, termed as backscattering geometry, at a 180° angle. Samples are mounted onto slides for analysis. The most commonly used substrate is quartz, having no photoluminescence addition to the Raman spectrum, present in standard glass microscope slides.

The disease change and progression of neoplasia in various regions of the body, such as within brain, breast, bladder, colorectal, larynx, lung, lymph node, oesophageal, prostate, uterine and cervical tissues, is usually presented as fixed histopathological tissue slices or tumour micro arrays (TMAs).[155] The major obstacle with micro-Raman spectroscopy of biological specimens is the sole reliance upon the native signal of the tissue. Low concentrations of the desired biomolecule, or too much interference from auto-fluorescent molecules, is a major obstacle intrinsic to micro-Raman spectroscopy.

3.3.2 Deep Raman

Deep Raman is an umbrella term for a range of techniques developed for layered turbid sample analysis, from the micro to millimetre scale.

Spatially offset Raman spectroscopy, or **SORS**, relies on the collection of diffusely scattered Raman photons to form depth measurements.

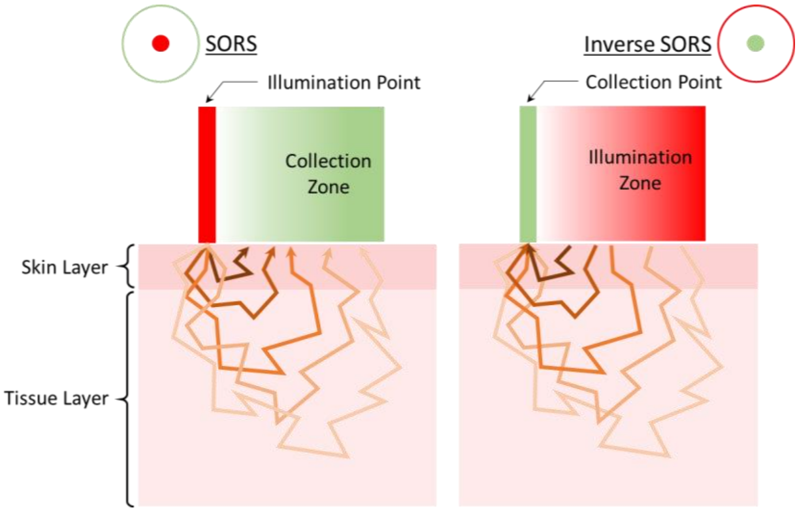

Figure 3.10: Schematic of the two varieties of spatially offset Raman spectroscopy: standard SORS, single illumination point and adjustable ring collection zone; and inverse SORS, single collection point and ring illumination for distribution of photons across a larger area, reducing burning and allowing an increased laser power.

As seen in Figure 3.10, photons are illuminated and collected in a point to ring fashion, or inversely. Principally, photons with longer scattering pathways travel a greater depth and breadth through biological media. Hence, a collection point distanced further from the illumination point will collect Raman scattering from the greatest z-direction.

Inverse SORS is the reverse, with the illumination distributed across the ring area, allowing for higher and sustained laser power over the region without the issue of tissue irradiation occurring. SORS and inverse SORS can be achieved either in an open optics set-up using an axicon lens, or in a closed system as a point-to-ring fibre optic bundle, discussed further in Section 3.3.3.

Another type of deep characterisation method is Transmission Raman spectroscopy, or **TRS**, whereby the collection point is positioned on the opposite face from the illumination point, obtaining Raman scattering through the sample. Unlike SORS, media layers are unable to be distinguished as the sample is measured as a whole. This is the technique which will be employed for the measurement of the turbid, phantom samples.

Surface Enhanced Spatially Offset Raman spectroscopy, or **SESORS**, combining deep Raman with the SERS technique opens the possibility of examining areas of disease far deeper within tissue – currently at a maximal transmission of ~47 mm through chicken breast tissue.[12]

3.3.3 Fibre Optic Probes

The use of fibre optic probes within the medical community is common place, allowing flexibility in traversing through the body and providing a safer imaging option for both patient and practitioner. Fibre optic probes are a precise technique with the ability to directly hone in on areas of interest, markedly improving the signal gained of low concentration biological molecules of interest.

The inclusion of Raman fibre optic probes has been studied within current practices, such as colorectal, cervical and lung endoscopy.[156–158] Recently, a novel techniques for brain tumour margin determination using a Raman fibre optic probe, and lymph node characterisation with an internalised needle probe have been proven as a significant diagnostic possibilities.[159,160]

Photoluminescent emissions inherent to fibre optics cause disruption across the whole fingerprint region.[161] Filtering or separately allocated illumination and collection fibres are two techniques employed in the avoidance of subsequent signal loss from this type of fluorescence.

Fibre optic probes are also an inherently invasive diagnostic technique, requiring the probe to traverse into the body, respectively requiring local or general anaesthetic in either breaking the skin barrier or entering the body anally or orally.

Other Techniques

In vivo near-infrared diffuse reflectance spectroscopy (NIRS) was developed in 1977 by Frans Jöbsis as a bulk, biological analytical technique, able to non-invasively detect cerebral and myocardial oxygenation levels.[162] NIRS relies on the transparency of tissue within the biological water window allowing the transmission and reflectance of scattered photons to the detector. As seen in Figure 3.8, haemoglobin, water and fat absorbs near-infrared light, as does other chromophore molecules such as glucose. The level of these chromophores within the tissue causes differential attenuation levels, allowing the prediction of blood glucose levels or neovascularisation synonymous with tumour growth, for example.[163,164]

As a comparative non-invasive technique to SESORS, NIRS is a highly insensitive technique unable to fully distinguish the biochemical make-up of the tissue. This is a major drawback in the identification of disease type present, hindering the ability to tailor the patient's treatment pathway or stage a cancerous legion.

3.4 Summary

The fundamentals of Raman spectroscopy theory have been outlined within this chapter. When considering the use of Raman spectroscopy within a clinical setting, several parameters must be met.

Biomedical Raman imaging techniques requires thought into the selection of laser wavelength. Both the illumination wavelength and Raman shifted photons must avoid lying within the region of absorption outside the NIR window, allowing a greater amount of light into and out of the biological system. Moreover, the avoidance of patient skin burning through the tempering of laser power and acquisition time must also be met.

The selection of the Transmission Raman technique aligns with the current diagnostic technique of mammography. By capitalising on the compressed, and hence thinner, nature of the breast required for this diagnostic technique, the Raman photons have a shorter distance to travel, increasing the possibility of photon collection in comparison to absorption. Moreover, the use of AuNPs during mammographic imaging act as a contrast agent, increasing the sensitivity of the technique. Incorporating new techniques within existing practices streamlines diagnostic pathways.

In the employment of SERS, plasmon tuning in terms of the selected material, and the size and shape of the nanoparticles is key in delivering large signal enhancement. It can be seen in Figure 3.6 that the overall enhancement of Ag as a NP material is greater than that of Au. Despite this, in a biomedical imaging setting gold is a better candidate due to its stable nature and ease of surface chemistry for functionalisation.[109]

The nature of extrinsic SERS is suitable in the exploitation of multiplexed imaging, a useful technique in the development of disease distinct AuNP targeting probes employed simultaneously. AuNPs of larger diameters ($\geq$50 nm) have been shown to adsorb RR molecules, such as the commonly used 4-Mercaptobenzoic acid and 2-Naphthalenethiol, with increasing efficiency and signal intensity, up to an enhancement factor of 10^3, as NP size increased.[110] As such extrinsic SERS with AuNPs of a $>$50 nm size were selected for use within this thesis.

Consideration into the AuNP shape was still required. The ability to utilise nanoshell NPs as theranostic agents through their photothermal capabilities further increases their benefit for medical use.

As such, the toxicology of AuNPs in relation to humans is explored in the following Chapter. NP material, size and shape selection is examined – nanoshells can be exploited as theranostic agents, however their robust size may be unfit for biomedical purpose – plus further functionalisation possibilities for use within this thesis.

4. Nanoparticle Biocompatibility

Nanoparticle interaction within the body, pharmacodynamics, and hence nanoparticle metabolism by the body, pharmacokinetics, amounts to vast areas of research crucial to the ongoing effort towards in vivo use of nanoparticles for theranostic purposes.

Several current imaging techniques use contrast agents to highlight areas of diagnostic interest. Computed Tomography (CT), Positron Emission Tomography–CT (PET–CT) and MRI utilise contrast agents, iodine, F–fluoro–2–deoxy–D–glucose (F–FDG) and gadolinium respectively. They can however be non-specific and toxic in nature. Intravenous iodine has a short imaging time, produces poor contrast in obese patients, and can cause nephropathy. F-FDG highlights unspecific areas of tissue with high-turnover-rates which efficiently take up glucose – this includes not only tumours, but also areas of inflammation and the heart. Gadolinium affects the magnetic field of nearby water molecules enhancing image quality. Though rarely inducing side effects, many gadolinium products have been discontinued due to concerns over toxicity. Yet contrast agents such as these are in use within the hospital setting. A precedence of importance in identifying patients who can metabolise nanoparticles efficiently should be applied to the field moving forwards.

This chapter considers the effects of NP adaption, relating to cell clearance and tumour targeting efficiency. Section 4.1discusses the metabolic pathway of nanoparticles within the body. The selection of material, size and shape of the NPs required for effective clearance is evaluated in Section 4.2. Section 4.3 considers how NP pH and dispersion affects cell interactions. Protein corona formation, altering the likelihood of phagocytosis, is considered in Section 4.4. An established method for tackling an immune response is through surface modification using polyethylene glycol (PEG), further discussed in section 4.5. Section 4.6

considers the best method for achieving intercellular NP uptake – targeted or untargeted. Finally, a consideration of all factors in tailoring nanoparticles of high biocompatibility is summarised in Section 4.7.

4.1 Pharmacokinetics

The metabolic pathway of nanoparticles is through the mononuclear phagocyte system (MPS), or reticuloendothelial system (RES), consisting of macrophages located in the reticular connective tissue of the RES organs. Nanoparticle clearance takes place mainly within the Kupffer cells of the liver. A study by Sadauskas et al found that 40 nm AuNPs could remain within the Kupffer cells of a mouse model up to six months after the primary injection.[165]

Figure 4.1 displays the intravenous route of AuNPs, considering the size of NPs able to be metabolised out of the body through the liver, kidneys and spleen, or lodge within the cells of different regions within the lungs.

Nanoparticle pharmacokinetics are dose dependent – low and medium doses, ~0.01 and ~0.1 mg/Kg respectively, have been proven to reduce cytotoxicity within rat models, deemed as suitable comparatives to humans due to the relative liver to body weight ratio.[166,167]

Biocompatible NPs are required to be engineered with specific performance characteristics, allowing a long blood circulation lifetime to increase uptake probability, whilst triggering a delayed, post-diagnostic or therapeutic immune response, prompting cell clearance to reduce cytotoxicity.[168] The upcoming sections within this chapter detail the five areas where tailoring colloids can lead to a level of optimal biocompatibility.

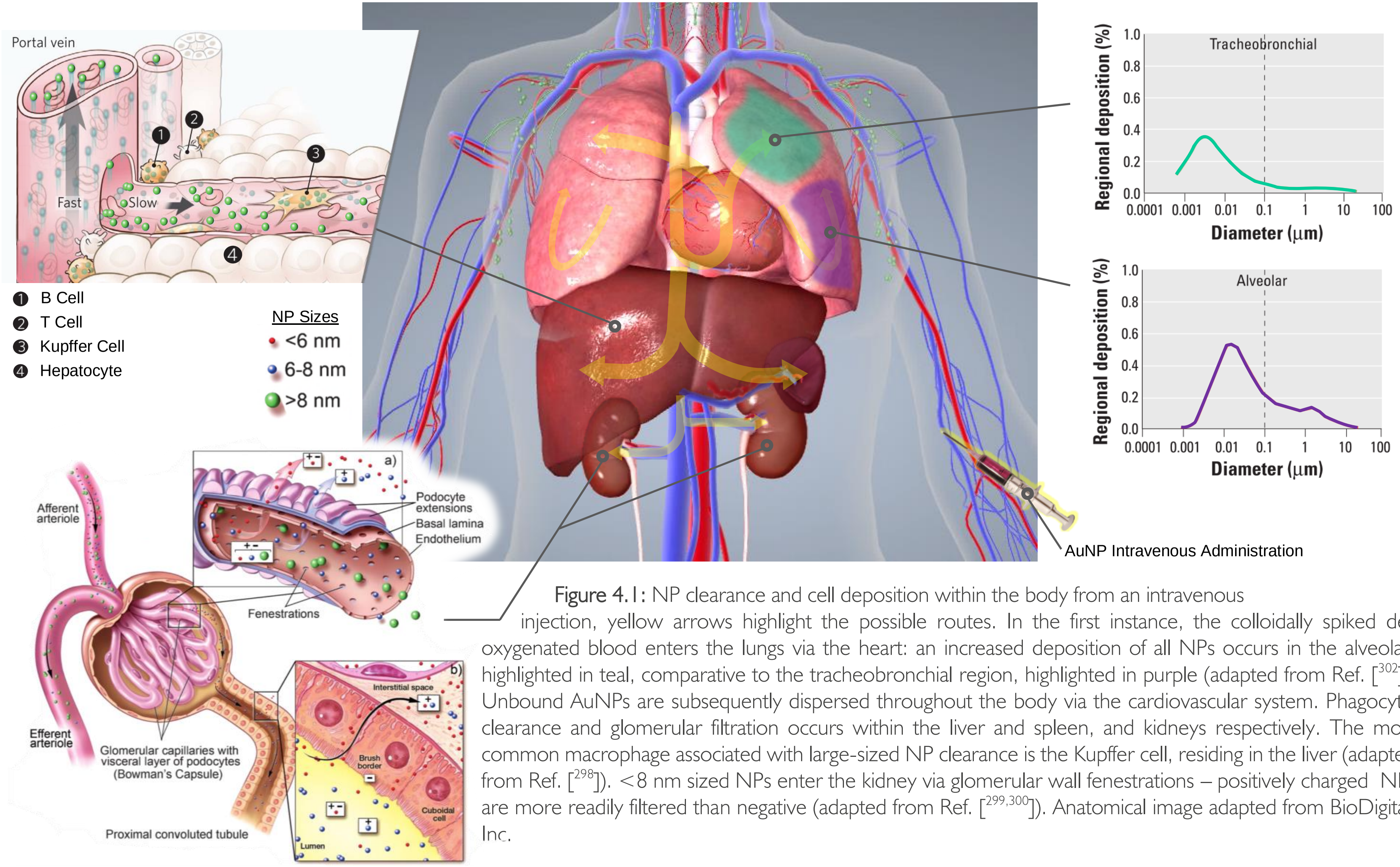

Figure 4.1: NP clearance and cell deposition within the body from an intravenous injection, yellow arrows highlight the possible routes. In the first instance, the colloidally spiked deoxygenated blood enters the lungs via the heart: an increased deposition of all NPs occurs in the alveolar, highlighted in teal, comparative to the tracheobronchial region, highlighted in purple (adapted from Ref. [302]). Unbound AuNPs are subsequently dispersed throughout the body via the cardiovascular system. Phagocytic clearance and glomerular filtration occurs within the liver and spleen, and kidneys respectively. The most common macrophage associated with large-sized NP clearance is the Kupffer cell, residing in the liver (adapted from Ref. [298]). <8 nm sized NPs enter the kidney via glomerular wall fenestrations – positively charged NPs are more readily filtered than negative (adapted from Ref. [299,300]). Anatomical image adapted from BioDigital, Inc.

4.2 Material, Size and Shape

Nanoparticle material choice forms the basis of biocompatibility. Seemingly unreactive carbon nanotubes, championed as strong candidates for drug delivery,[169] have been found to spear through macrophages and cause pulmonary toxicity, not dissimilar to high levels of asbestos contact.[170,171] Quantum dots, highly regarded as excellent bioimaging tool, have also been found to have a high toxicity potential.[172]

Inert, inorganic compounds, such as silica and gold, have been widely studied as strong candidates for therapeutics, including drug delivery, and diagnostics, specifically as shells, containing bio-toxic materials. As found by Shukla et al, gold has a low production level of reactive oxygen and nitrite species, reducing proinflammatory cytokine secretion, making them suitable candidates for nanotheranostics.[173] Other metals, such as silver, give way to reactive and antibacterial properties, less suitable for *in vivo* use.[174,175]

NP size also plays a significant role – as seen in Figure 4.1, NPs <8 nm in diameter, including nanorods, undergo glomerular filtration, whilst Kupffer cells within the liver expunge larger sized NPs from circulation. Accumulation within these organs has been most commonly associated with AuNPs sized either ≤ 30 nm and >100 nm.[176–181]

Biocompatible sized NPs can lead to cytotoxicity when administered in large doses, with low doses generally considered as ~ 0.01 mg/Kg.[176] In a study by Mironava et al, however, NPs which had been internalised were transferred during cell division, effectively decreasing the number of NPs within the overall cell population over time.[182]

4.3 Dispersion State

Colloidal stability is governed by the electrokinetic potential of surface-ion accumulations, which in turn is influenced by pH.[183] This potential, known as Zeta potential (ζ-potential), denotes the level of electrostatic repulsion, characterising the dispersion stability and interfacial chemistry of the NPs, including aggregation level, ligand chemistry success, and cell disruption.[184–187] ζ-potential is a measurement of the electric double layer of the NP, comprised of the stationary "stern" layer and moving "slipping plane", bordering the bulk solution.[184]

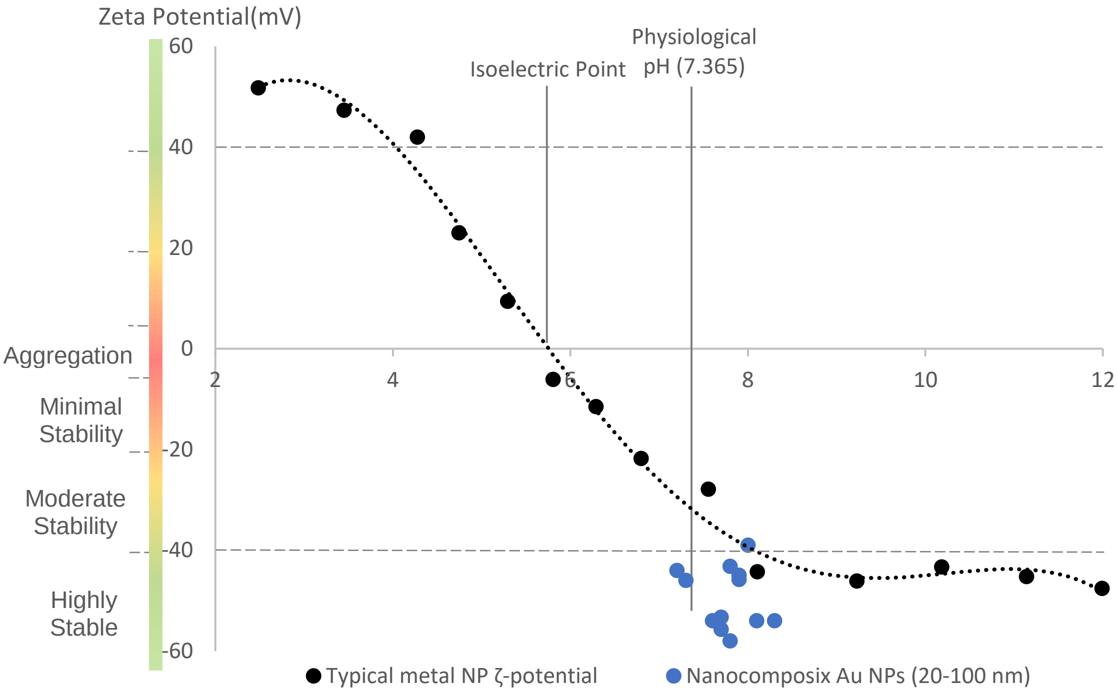

Figure 4.2: A graph showing the relationship of ζ-potential to colloidal pH. The magnitude of ζ-potential is denoted as aggregation between 0 – ±5 mV, of minimal stability between ±5 – ±20 mV, of moderate stability between ±20 – ±40 mV, and high stability ≥ ±40 mV. Values of commercially purchased AuNPs, Nanocomposix (San Diego, USA), ranging from 20 nm to 100 nm are displayed. The physiological pH value of 7.365 is marked. Typical metal NP values adapted from[186,188]

As seen in

Figure 4.2, a decrease in H^+ ions leads to a basic NP environment, creating an electrostatic force greater than the Van de Waals forces of attraction, gaining dispersion stability.[186,187] For biocompatible intracellular interactions, minimal levels of NP aggregation and limited cell membrane disruption must occur – commercially purchased NPs used throughout this thesis are plotted on the graph in Figure 4.2, showing high stability levels and conformation around the physiological pH point.

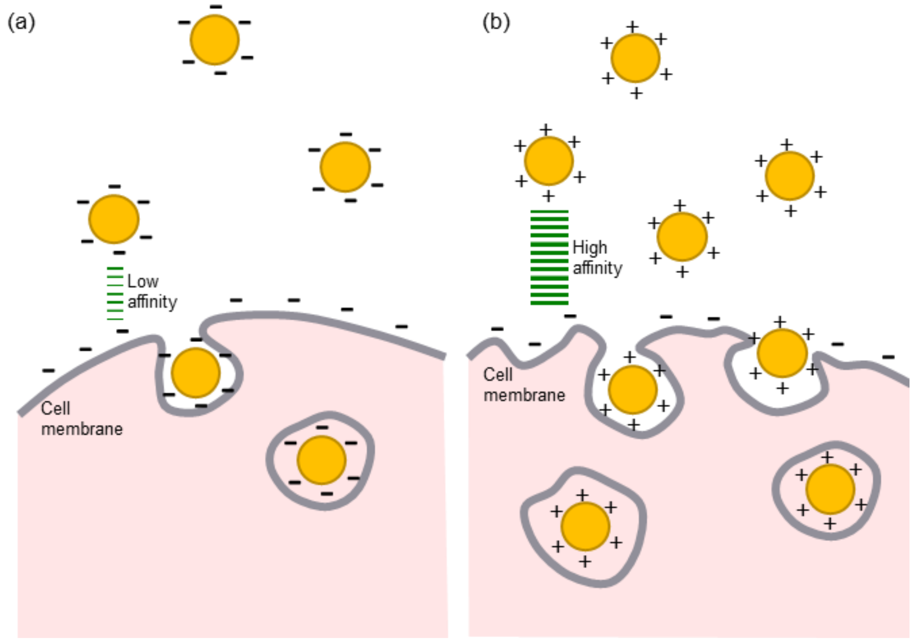

Figure 4.3: Endocytosis and cell membrane interaction of different NP surface charges: (a) anionic NPs such as citrate capped or PVA coated; (b) cationic NPs including cetyltrimethylammonium bromide coated. Adapted from [189]

Figure 4.3 shows the interaction differences between cationic, (b), and anionic, (a), NP surfaces. Cationic surfaces, such as cetyltrimethylammonium bromide (CTAB) capped nanorods, have a high affinity to the cell membrane, increasing the rate of endocytosis into cells. They have been seen, however, to cause disruption to cell membranes, mitochondria and red blood cell morphology, leading to apoptosis.[180,190] Conversely, anionic NPs, such as citrate capped, show little disturbance to cell biology with relatively less cell uptake.

Despite a generally neutral pH across the body, the pH level within solid breast tumours is lowered. A recent study by Rong et al capitalised on this fact, developing NPs functionalised with pH sensitive cleaver links which, once residing within the acidic tumour environment, release doxorubicin, the triple negative breast cancer drug.[191] Desired localisation of NPs within the body through intravenous injection is met with difficulties in the first instance. Studies have shown that once NPs have been introduced to plasma fluids, ζ-potential values tend to trend towards 0 mV, with up to a ±21.8 mV change.[192,193] This is attributed to the surface interaction of biomolecules, specifically in the formation of the protein corona.

4.4 Protein Corona & Opsonisation

A major hurdle in site-specific NP targeting for diagnostics and drug delivery is in ensuring an extended blood circulation life-time and the efficacy of targeting ligands. Protein corona formation cloaks any targeting ligands present on the NP surface, preventing target site recognition, whilst presenting a biological shell for opsonins to attach, flagging the particle for phagocytosis.

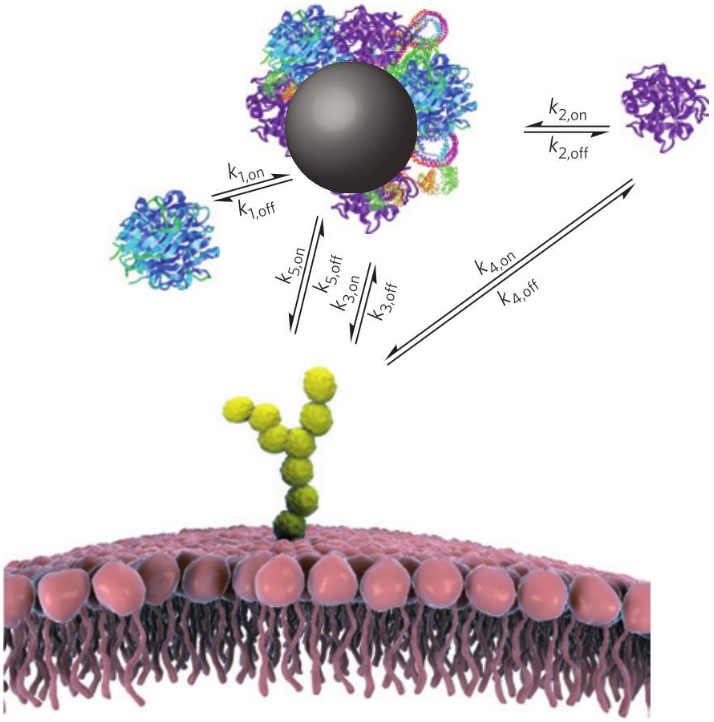

Figure 4.4: Relevant processes (arrows), in both directions (on/off), for a nanoparticle interacting with a receptor. Biomolecules in the environment adsorb strongly to the bare nanoparticle surface (k1), forming a tightly bound layer of biomolecules, the 'hard' corona, in immediate contact with the nanoparticle. Other biomolecules, the 'soft' corona, have a residual affinity to the nanoparticle–hard-corona complex (primarily to the hard corona itself), but this is much lower, so those molecules are in rapid exchange with the environment (k2). If sufficiently long-lived in the corona, a biomolecule may lead to recognition of the nanoparticle–corona complex as a whole by a cell-membrane receptor (k3). The same biomolecule alone can also be recognized by the receptor (k4). If present, the bare surface of the nanoparticle may also interact with cell surface receptors (k5) or other constituents of the cell membrane.[194]

NPs delivered via intravenous administration encounter proteins highly abundant in blood plasma, such as albumin, fibrinogen, and apolipoproteins, which are primarily adsorbed. This initial surface formation is replaced by low concentration proteins with a higher affinity to the

NP surface, leading to a “hard” corona. The surrounding, loosely bound proteins form a low affinity, highly changeable “soft” corona.[195]

Corona formation increases the likelihood of opsonisation – whereby opsonins attach to the NP-corona, flagging the particles as foreign bodies to be removed from the body through the MPS. Particle size, and hence surface curvature, dictates the amplitude of protein adsorption and conformation upon the NP surface.[196] With proteins such as albumin and fibrinogen, NPs < 30 nm in diameter possessing a large surface area and greater curvature, a reduced level of interaction occurs; pseudo-flat surfaces, characteristic to nanoparticles > 60 nm, absorb these proteins more readily.[197] However, high surface curvature allows proteins to retain their original conformation, with NPs ≤ 50 nm undergoing vast protein saturation with strongly formed hard coronas.

The phenomenon of opsonisation through protein corona formation can be capitalised upon. One such technique assumes that, once taken up by the phagocytes, the NPs will be transported to an area of inflammation, hence accumulating within the tumour tissue.[198] Another involves the engineering of a biomolecule specific protein corona; creating specialised targeting capabilities, whilst remaining resistant to immune response. An example of such is the use of platelet fragments in targeting dysmorphic vasculature found in tumours.[199,200] Conversely, cloaking mechanisms can be employed, such as the use of polyethylene glycol (PEG), as discussed in the next section.

4.5 Polyethylene Glycol

Polyethylene glycol (PEG) is a hydrophilic, ethylene repeating polymer, creating a passive NP surface reducing interactions with biofluid molecules, creating a “stealth” NP.[201] PEG and PEG-ylated NPs have been widely accepted for clinical use, having low toxicity and provoking minimal immune response, with over 35 US FDA-approved preclinical studies, for both imaging and therapy purposes, in progress.[201,202]

Surface modification of AuNPs with PEG for biological purposes has become a staple technique. Examples include it's use within enhanced anti-tumour drug delivery,[203] photothermal therapy,[190,204] distal end tethering of targeting ligands[205], and use within *in vivo* Raman reporter SERS studies.[206]

The density and length of PEG molecules on the NP surface greatly affects the blood circulation half-life. A high density of short chain PEG molecules leads to a brush-like formation; lower densities, or longer chains able to fold, creates a less effective mushroom formation.[207,208]

A mouse model toxicology study of PEGylated AuNPs by Zhang et al discovered that NPs of 60 nm in size reflected the lowest concentration within the heart, liver, spleen and kidneys, comparative to the 5, 10 and 30 nm AuNPs.[176] Unlike other un-PEGylated biocompatibility studies however, there were no discernible growth effects or changes to the major organs at every AuNP size.

4.6 Passive vs Active Targeting

Enhanced vascular permeability has been observed in solid tumours leading to an EPR effect, as briefly discussed in Chapter 2, Section 2.3.1. The key mechanisms allow NPs between 10 – 100 nm to extravase to a higher level within carcinoma, comparative to healthy tissue vasculature, and to be retained within the diseased area.[201,209] The blood flow within tumour tissue, already encouraging permeability due to the immature nature of the vasculature, increases dramatically with a higher blood pressure level. This fact can be exploited using an angiotensin II to induce hypertension: whilst having no effect on normal tissue blood flow, the lack of smooth muscle within tumour vasculature creates elevated extravasation, vastly increasing the EPR effect.[39,210] Which begs the question, does this mechanism alone provide sufficient passive, tumour targeting, or is active, receptor-mediated targeting required also?

Many studies have employed disease specific biomolecules targeting ligands, such as anti-HER2 (Human Epidermal Receptor), Tumour Necrosis Factor (TNF), and Vascular Endothelial Growth Factor (VEGF), which have been successful in NP-cell interactions, in both *in vitro* and *in vivo* studies.[203,204,211,212] Designing the fixed-orientation of these targeting ligands is crucial in gaining highly effective and consistent conjugation.[213] A study by Salvati et al discovered that the optimal design for 50 nm silica NPs cell penetration consisted of a targeting ligand attached distally upon a PEG molecule. However, a level of bio-identity was still lost once in contact with PBS with protein corona formation.[214]

4.7 Summary

In understanding how the tailoring of NPs affects biocompatibility, the development of near to non-cytotoxic NP probes can be achieved. Figure 4.5 displays a heat map, summarising how the level or inclusion of specific NP features may affect biocompatibility.

The composition of the NP itself, in terms of size and shape, is the major factor in determining the success of an *in vivo* NP probe. Not only in terms of inaccessible site-location, mainly due to inability to traverse through tight vasculature for larger NPs, but also the heightened levels of pharmacokinetics through the kidneys or liver. As such, a size between 60 – 100 nm and hence a nanospherical shape was selected for this study. With nanospheres

In relation to previous studies performing *in vivo* SERS and biocompatibility experiments, spherical AuNPs 60 – 100 nm have been found to produce an enhanced Raman signal whilst causing low levels of cytotoxicity.[206,215–222]

NP stability, and hence circulation half-life, is crucial factor in ensuring enhanced permeability and retention is achieved at an efficient and elevated level. Ensuring a highly positive/negative

Zeta potential, alongside an organic pH level, are two key factors in gaining biological stability. The use of a "cloaking agent" such as PEG or also enforces stability, however the choice of chain-length and density must be considered in terms of the disease targeting specifications of the NPs. A biologically engineered protein corona can also be used; however, this omits the use of disease-specific ligand surface modification, which has also been proven to increase the desired site location of AuNPs.

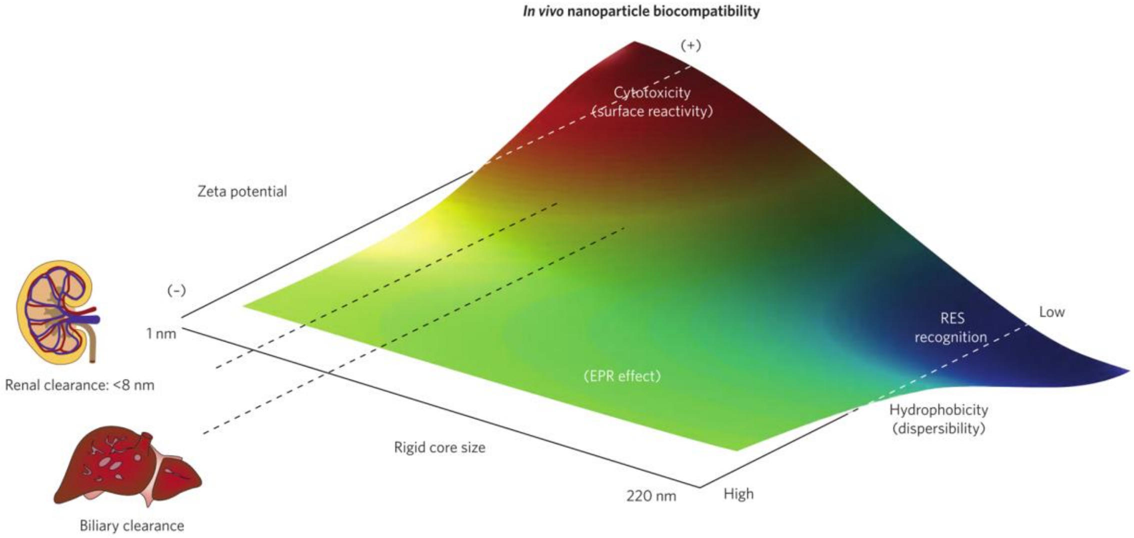

Figure 4.5: Physical characteristics of nanoparticles determine in vivo biocompatibility. The three-dimensional phase diagram displays the qualitative biocompatibility trends revealed after in vivo screening of around 130 nanoparticles. The main independent particle variables that determine the in vivo biocompatibility are size, zeta potential and hydrophobicity. Biocompatibility is reflected in the colour spectrum, with red representing likely toxicity, blue likely safety and blue–green–yellow intermediate levels of safety. Small, cationic particles with high surface reactivity are most likely to be toxic (red hue) compared to than the larger relatively hydrophobic or poorly dispersed particles, which are rapidly and safely (blue hue) removed by the reticuloendothelial system (RES). Particles that promote enhanced permeation and retention (EPR) effects—and are therefore optimal for cancer theranostics — generally have mid-range sizes and relatively neutral surface charges.[168]

Targeted delivery of drug-bearing or theranostic NPs allows site-specific treatment, avoiding the overall toxicity induced by chemotherapy and eliminating the use of ionising radiation required for radiotherapy.[234] For example, the PEGylated liposomal encapsulation of Doxorubicin has been shown to improve uptake by up to 300-fold within ovarian and breast carcinomas, effectively improving bioavailability and reducing costs.[235] However, when considering the use of nanoparticles in vivo, it is important to weigh up the risk versus benefit on an individual patient basis. Much like the required eGFR assessment with iodine contrast use in CT for example, patients with non-alcoholic fatty liver disease (NAFLD) have a reduced Kupffer cell functionality, which would affect the clearance rate of circulating NPs $>8 - <100$ nm.[236] Pharmacokinetic reducing factors such as this would reduce patient eligibility for SESORS, further constricting its use as a specialist technique.

Hence, the key factors ensuring an elevated level of site-specific NP delivery include the size, shape and zeta potential, engineered to allow the EPR effect to take place, with the addition of a PEG-ylated and targeting functionalisation, for extra circulation and homing capabilities.

Thesis Aims

The use of optical spectroscopic techniques within the clinical arena is a fast-developing area of biomedical application. The need for early diagnosis, especially within symptom presenting diseases, is vital in combating high mortality rates associated with extended referral times from initial patient assessment. The amalgamation of novel techniques within current diagnostic techniques can lead to an improvement in the sensitivity of the original method, and/or lead to a reduction of patient wait time between assessments, streamlining the diagnostic pathway.

The aims of this thesis, in relation to the transferability of the SERS Transmission Raman technique within a clinical setting, are as follows:

- Highlight the need to develop novel, spectroscopic techniques with a mind to incorporate with, rather than replace, current diagnostic methods.
- Cement the use of turbid, PDMS phantoms as viable optical tissue replicas. Incorporation of tissue layers, and even occlusions, within the phantoms elevates the optical and morphological representation.
- The use of RR-AuNPs in combination with mammographic imaging to provide further depth information, highlighting the cancerous region independently, with use with Raman spectroscopy, or within x-ray imaging as a contrast agent.
- Explore the use of these RR-AuNPs as a more biocompatible probe, able to actively target biomarkers synonymous with highly malignant breast carcinomas – microcalcifications.

Experimental Design

Synthesis and Functionalisation of Gold Nanoparticles

Optical Phantom Construction

SESORS of Breast Phantoms: Experimental Design

5. Synthesis and Functionalisation of Gold Nanoparticles

5.1 Introduction

Exploration into the synthesis of gold nanoparticles (AuNPs) leading to Raman reporter labelling, and hence further functionalisation, with the necessary biocompatibility measures accounted for, is detailed within this Chapter.

The chemistry and characterisation, via TEM imaging and UV/Vis analysis, of the initially synthesised AuNPs is discussed in Section 5.2. Leading on from this, the Raman reporter labelling of the commercially purchased AuNPs is explored in Section 5.3. The characteristic SERS signals gained from the three reporter labels (2-Naphthalenethiol, 4-Acetamidophenol and 4-Mercaptobenzoic acid) are detailed, with the binding mechanisms of each compared. The full functionalisation of the AuNPs is described in Section 5.4 with three separate components: a Raman reporter label, polyethylene glycol (PEG) and a hydroxyapatite targeting bisphosphonate molecule. The design, carbodiimide chemistry and characterisation of these AuNPs is discussed. A summation of all findings within the Chapter are presented in Section 5.5.

These experiments form the basis of the Raman reporter AuNPs (RR-AuNPs) and active targeting AuNPs (2-NT-PEG-BP AuNPs) employed in the proceeding Chapters 8 and 9, respectively.

5.2 Synthesis of Gold Nanoparticles

Initially, AuNPs were synthesised using the traditional method developed by Turkevich, et al..[223] The formation of gold nanospheres occurs via the addition of aqueous trisodium citrate to an aqueous solution of tetrachloroauric acid ($HAuCl_4$). The citrate acts as both a reducing agent and stabilizer of the NPs. The multi-step chemical reactions which take place are described below.[224] Prior to synthesis, all glassware used was washed with Aqua Regia (1 part nitric acid to 3 parts hydrochloric acid molar ratio), rinsed thoroughly three times with DI water, and placed in a glass drying oven until bone-dry.

The $HAuCl_4$ salt disproportionates upon its addition to water:

$$H_2O + HAuCl_4 \rightarrow AuCl_3 + H^+ + Cl^- \tag{19}$$

This initial solution, starting out as a straw-yellow colour, is placed in a round bottom flask and placed in a heating mantle. The solution was stirred at a constant rate to approximately 90°C, cautious not to bring to the boil.

Separately, the aqueous trisodium citrate solution is formed. Water causes the citrate to oxidise, producing dicarboxy-acetone and carbon dioxide as a by-product:

$$H_2O + \mathrm{C_6H_5O_7}^{-3} \rightarrow C_5H_6O_5 + CO_2 + H^- + 2e^- \tag{20}$$

The dicarboxy-acetone has a further reaction in the aqueous solution forming acetone:

$$2H_2O + C_5H_6O_5 \rightarrow C_3H_6O + 2CO_2 + 2(OH)^- \tag{21}$$

The citrate solution is slowly added to the tetrachloroauric acid solution, where the acetone reduces the auric salt ($AuCl_3$) to aurous salt ($AuCl$):

$$AuCl_3 + 2e^- \rightarrow AuCl + Cl_2^- \tag{22}$$

Facilitated by remaining dicarboxyacetone, the aurous salt forms a complex ($3AuCl$), allowing a second disproportionation causing the nucleation of the Au NPs:

$$3AuCl \rightarrow 2Au^0 + AuCl_3 \tag{23}$$

The nucleation sites continue grow as more Au is adsorbed onto the surface. The reaction is held under reflux for 30 minutes, turning the solution to a deep, ruby red. Remaining citrate particles form a negatively charged monolayer capping the NPs, giving the colloid electrostatic stability reducing the potential of aggregation. The colloidal solution is then slowly cooled to room temperature. Tin foil wrapped glass storage jars were used, protecting the colloid from direct light, and stored in the fridge at 4°C to prolong shelf life.

A slight deviation to the Turkevich method was made in pursuit of “dumbbell” or peanut-like AuNPs. 20% of the initial $HAuCl_4$ stock volume was heated, and then refluxed with the total volume of citrate solution. This created initial points of nucleation. After 20 minutes of reflux, the remaining 80% $HAuCl_4$ stock solution was added, and refluxed for a further 30 minutes, turning the solution ruby red. This process allowed two separate nuclei to form, grow and adjoin. The NPs were cooled and stored in a similar fashion as previously set out.

All NP preparation required the use of a **centrifuge**, Mikro 22 (Hettich, Germany), and **deionised water** (18.5 MΩ), Arium Mini (Sartorius, Germany); especially in the removal of supernatant and washing of the NPs between functionalisation steps, removing excess conjugate from the colloidal solution.

Once synthesised, the crystal lattice, size and dispersity of colloids were investigated using Transmission Electron Microscopy (TEM) and Ultraviolet-Visible spectroscopy (UV/Vis).

To characterise the structure of nano-sized particles **Transmission Electron Miscroscopy (TEM)**, JEM-2100 LaB6, JEOL (Tokyo, Japan), is employed. A high powered electron beam is passed through the sample under vacuum. The crystalline lattice of the sample structure acts as a diffraction grating – the electron beam waves are diffracted through the lattice causing interference patterns, forming the density based image. The NP samples are prepared in several steps. First, a 1 mL volume of colloid is concentrated via centrifugation, removing 0.8 mL of supernatant.

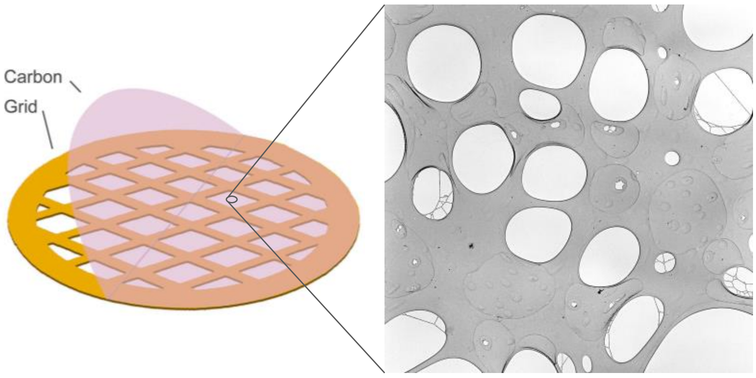

Figure 5.1: Agar Scientific Carbon Film 300 Mesh Copper TEM grid – an illustrative representation of the grid with a highlighted area visualised with TEM.[225]

A micropipette is used to transfer 0.1 mL the colloidal concentration onto a carbon film 300 mesh copper grid, AGS160-3H, Agar Scientific (Stansted, UK). The TEM grid is dried for up to 48 hours in a sterile environment, reducing contamination and ensuring stable imaging. A limitation to TEM is the propensity for NP aggregation during sample preparation.

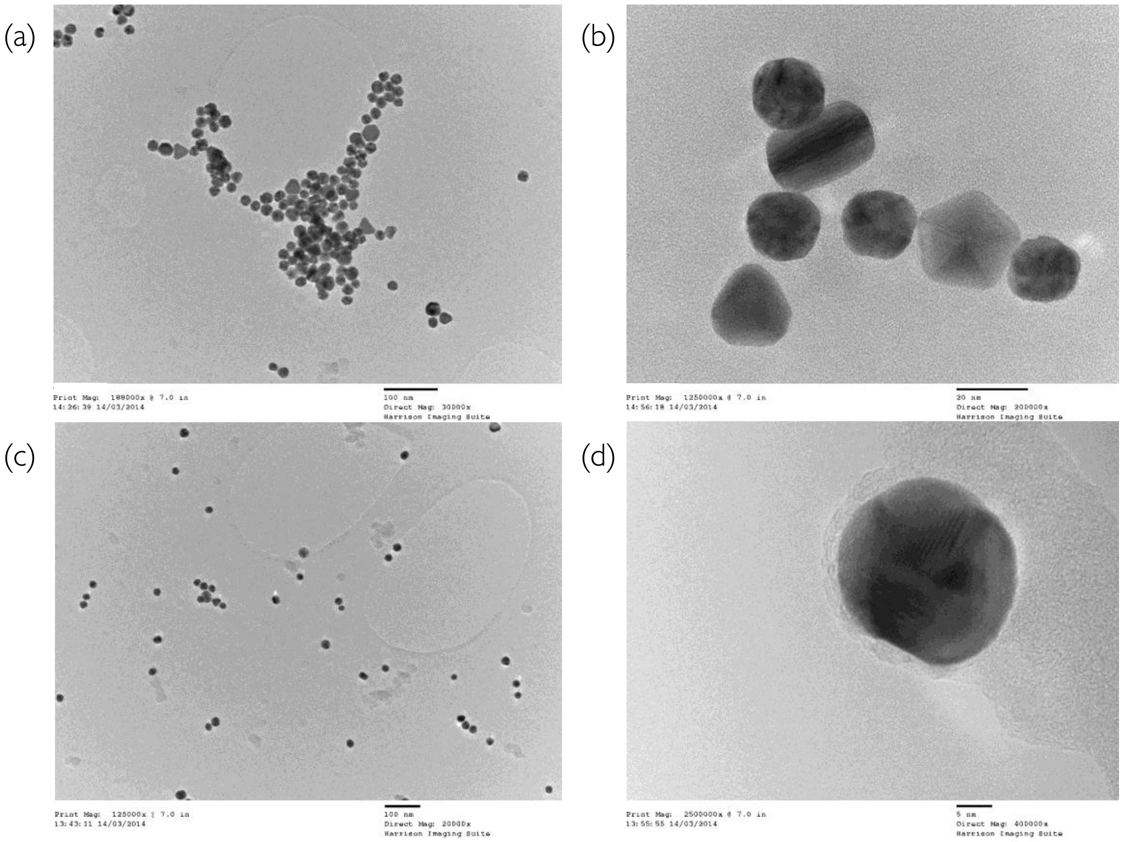

Figure 5.2: TEM images of AuNPs synthesised from standard Turkevich method: (a) and (c) display a wide field view of the polydisperse NPs; (b) shows a near-field variety of AuNP shapes, namely spherical, pentagonal, and two truncated triangular nanoplates, which have been synthesised within the same batch; (d) a spherical, poly-lattice NP, averaging 20 nm in diameter.

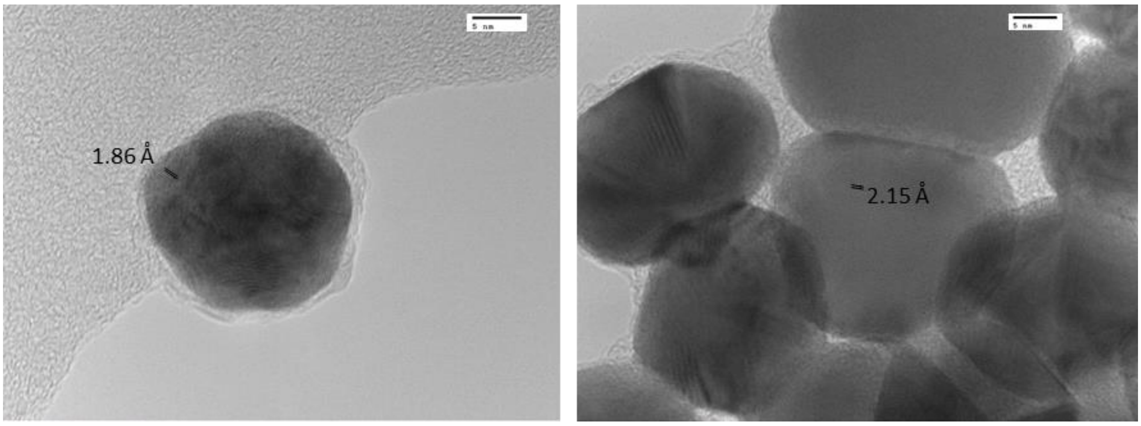

Figure 5.3: A spherical, 20 nm AuNP with a compact poly-lattice; A truncated triangular plate with wider D-spacing, and a single lattice synonymous of non-spherical nanoplate. Scale bars are to 5 nm.

From

Figure 5.2 (a), the standard Turkevich synthesis method mainly produced pseudo-spherical NPs, cuboctahedron in structure, with an average size of 20 nm.[226] In several batches, a variety of shapes such as pentagons and truncated triangular nanoplates were also produced, as seen in

Figure 5.2 (b). The crystal lattice is further investigated.

The formation of the crystallographic planes indicates the nature of the NP shape: a tight, poly lattice is suggestive of spherical shape, whilst plate type NPs have a more open, single lattice, as

Figure 5.3 displays.

The modified synthesis method led to the formation of "peanut" like NPs, as seen in

Figure 5.4 (a) and (b). The joined-double-spherical shape of the NP prompted a pursuit of this method. As discussed in the Chapter 3, Section 3.2, large hot-spots induced by the proximity of two NPs is a highly sought-after attribute.

The lattice was investigated to ensure the two nucleation points had cross-lattice joined, which can be clearly seen in Figure 5.5.

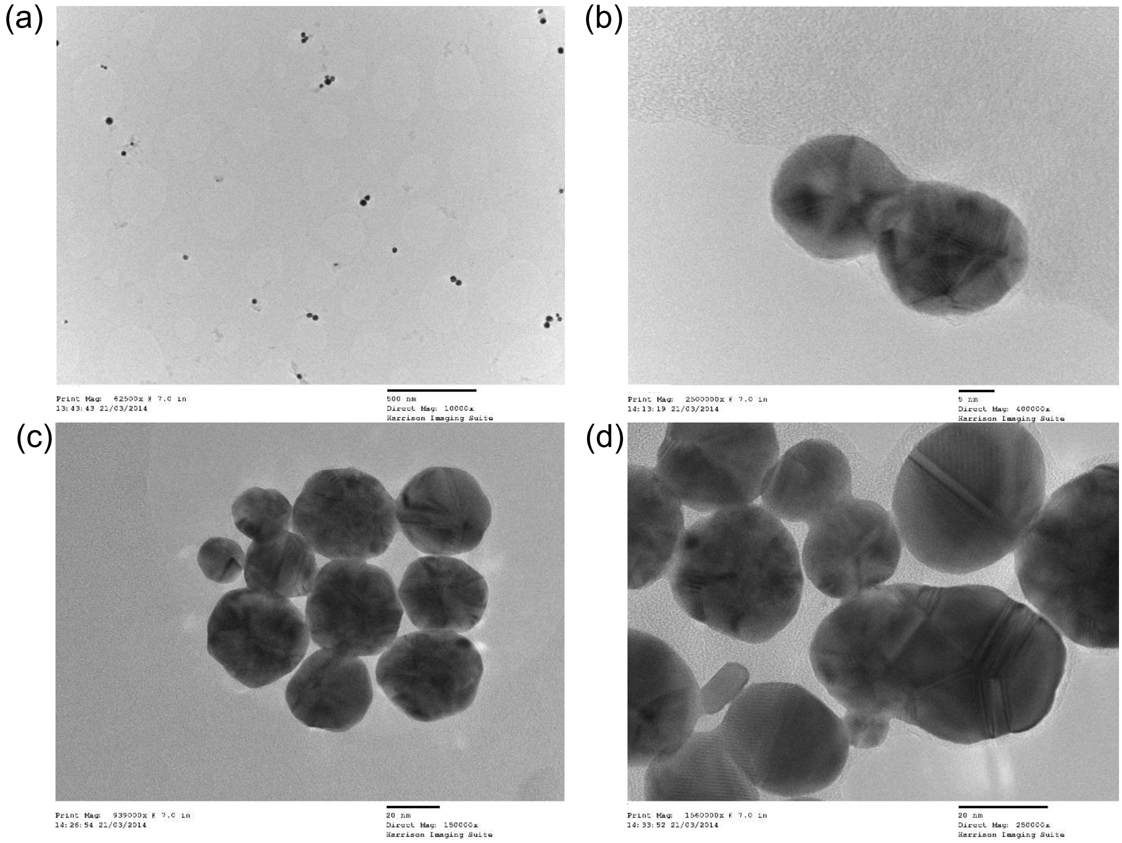

Figure 5.4: TEM images of the peanut-like/doublet AuNPs synthesised from the modified Turkevich method: (a) wide field of view display of the AuNPs, most are seemingly paired closely with a few individual NPs; (b) a near-field view of a singular doublet AuNP – the width of the adjoining nucleation point neck was ~5 nm, with the average dimensions of a successful doublet synthesis being 20 x 50 nm; (c) and (d) display the variations in NP synthesis within the batches, creating larger diameters of 40 nm ±10 nm, or elongated almost rod like NPs.

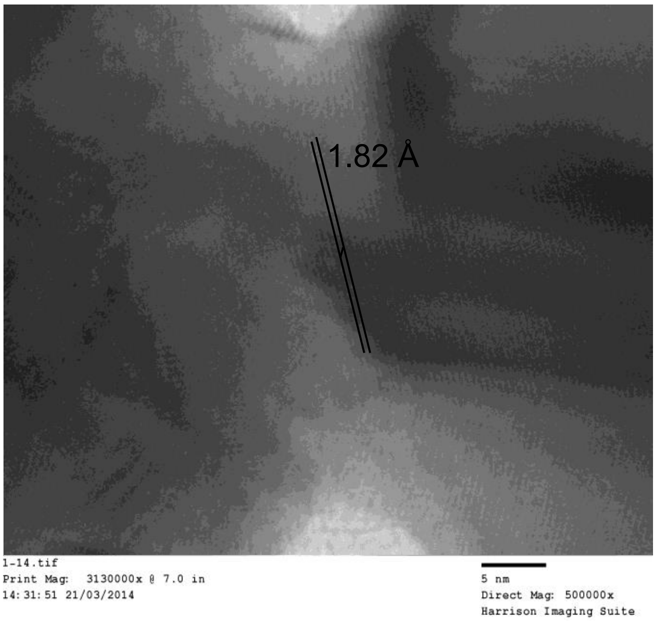

Figure 5.5: TEM image of a peanut-like AuNP cross-nucleation point confirming the presence of a compact poly-lattice structure adjoining the two spherical NPs, creating a singular doublet.

An **Ultraviolet/Visible Absorbance Spectrophotometer**, Evolution Array, Thermo Fisher (Massachusetts, USA), is used to analyse the absorbance of materials, including the LSPR and stability of NPs. with an effective measurement range between of 185 – 1100 nm. The UV/Vis is equipped with a durable tungsten lamp and a photodiode array for illumination and collection respectively. A blank sample of DI water is run initially to gain a normalised absorbance spectrum, prior to further sample measurements.

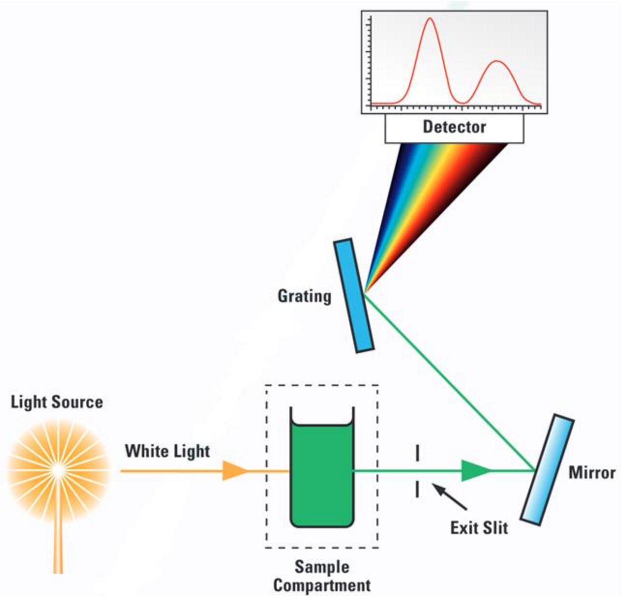

Figure 5.6: Thermo Fisher Evolution Array UV/Vis Absorbance Spectrometer – simplified optical set-up schematic of the equipment.[227]

UV/Vis testing determined the LSPR of the AuNP batches, displayed in Figure 5.7, in relation to a reference peak of commercially purchased 20 nm spherical AuNPs. The plasmon resonance of the doublet AuNP batches were expected to contain a second absorption peak not dissimilar to that of Au nanorods, however this did not appear for either batch.

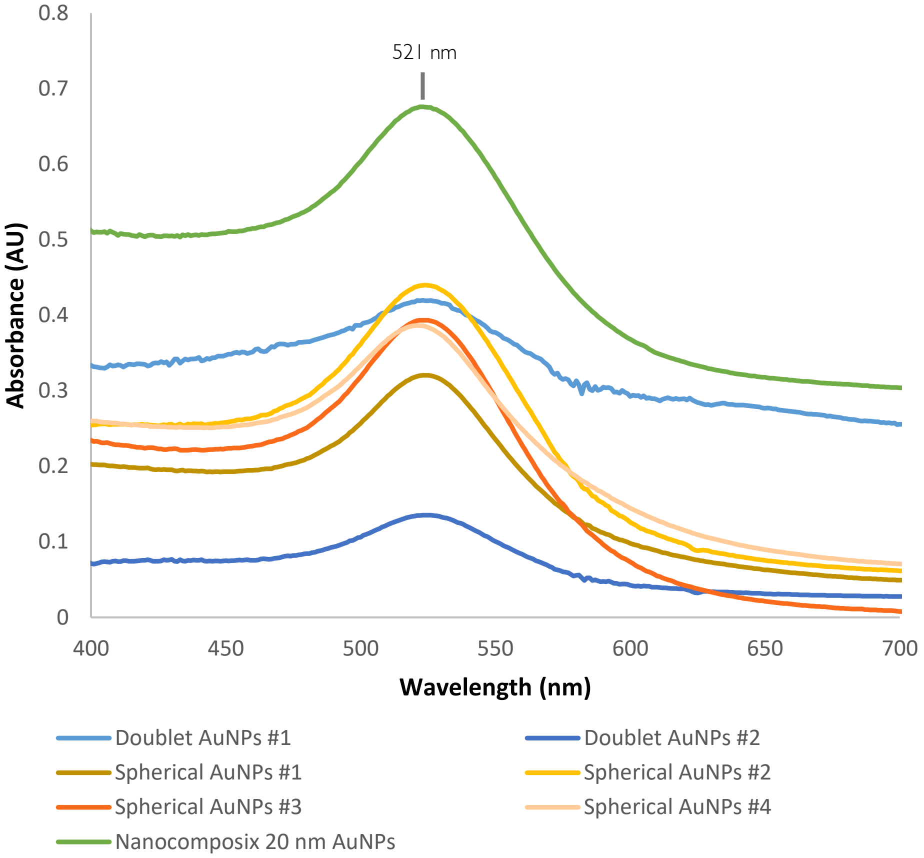

Figure 5.7: UV/Vis spectrum of all synthesised AuNP batches, four standard Turkevich method spherical AuNPs and two modified Turkevich method doublet AuNPs, and a reference spectrum of Nanocomposix 20 nm spherical AuNPs. Spherical batches #1 – 3 matches similarly to the reference spectrum, confirming a ~20 nm diameter average; batch #4 has a $\boldsymbol{\lambda_{max}}$ of 520 nm, relating to a smaller average diameter. Doublet batches #1 and #2 both have a broadened LSPR peak, confirming the presence of elongated AuNPs, however a secondary, red-shifted peak was unexpectedly not present, confirming a low overall volume of doublets within each of the batches.

Inconsistency in AuNP concentrations between batches affected the ability to determine the overall size and aggregation status of the batches. Hence, a normalised optical density chart, Figure 5.8, for solely spherical AuNPs was produced. A direct comparison of doublet AuNPs to the reference peak could not be made due to the difference in shape and size. The graph shows the synthesised AuNPs were not aggregating but were not reduced enough to form an overall batch size of 20 nm. Instead, a wide range of AuNPs were formed in each batch, on average smaller than 20 nm. Over time, AuNPs in an aqueous solution can release gold ions from the surface which can aggregate to form smaller AuNPs within the original batch, leading to further narrowing and an overall blue-shift in LSPR.

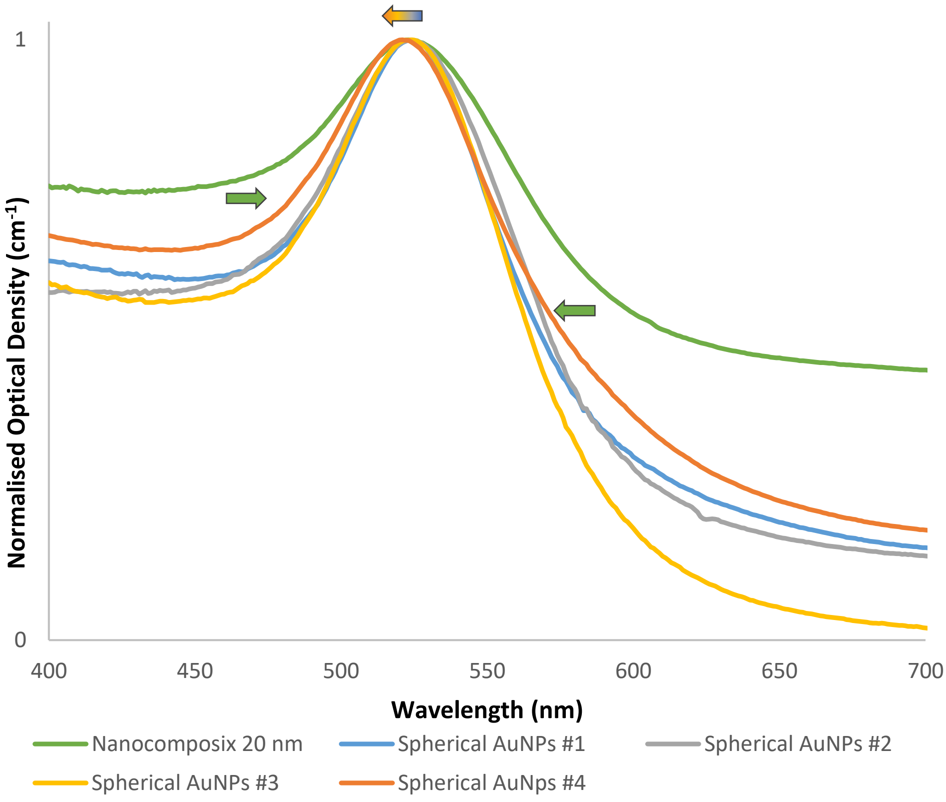

Figure 5.8: Normalised optical density UV/Vis spectrum of the synthesised Turkevich method AuNPs in relation to the reference spectrum of Nanocomposix 20 nm spherical AuNPs. The two green arrows denote the narrowing of the synthesised AuNPs in comparison to the reference peak indicative of a size distribution. The gradated left arrow denotes the blue-shift in LSPR by 1-2 nm for each of the synthesised batches.

Consecutive batches following the Turkevich and adjusted synthesis methods produced a varied and desirable range of NP size and shapes. Achieving a consistency of spherical or doublet NPs between batches was problematic, with several batches aggregating prior to completion. Adjustments were made to stabilise colloids – a decrease in citrate salt concentration for greater nanoparticle size formation and diligence in maintaining a consistent synthesis temperature were two main attuned parameters. Consistency and successful synthesis issues were still met however. With the modified method, additional $HAuCl_4$ would increase the growth size of original nucleation sites rather than conduct new formations, as seen in Figure 5.4 (c) and (d). Human error in not thoroughly cleaning the glassware is also a factor affecting successful synthesis.

Ensuring monodispersity and consistency between self-synthesised AuNP batches could not be guaranteed. Synthesis of AuNPs inconsistently produced NPs larger than ~20 nm.

To ensure experimental consistency in the following experiments, a pragmatic decision was made to purchase commercially available 80 nm colloids from Nanocomposix (San Diego, USA). Each batch is mass produced under consistent conditions and supplied with a data sheet providing information on Zeta potential, a size distribution histogram and absorbance spectrum. All purchased batches of colloids were cross checked with UV/Vis and TEM imaging on site and found to be concordant with the given results. As a wholly accessible and viable option, further experimentation with AuNPs were performed using the NanoXact bare gold nanospheres, 0.05 mg/mL, in aqueous 2 mM sodium citrate solution.

5.3 Labelling with Raman Reporters

In preparation for multiplexed depth measurements within breast phantoms, the optical response of the Raman reporter labelled AuNPs was assessed. The following materials were obtained: 80 nm spherical AuNPs (Nanocomposix); 2-Naphthalenethiol (2-NT), 4-Acetamidophenol (4-ATP), more commonly known as paracetamol, and 4-Mercaptobenzoic acid (4-MBA) (Sigma Aldrich, USA) diluted into 10 mM ethanol stock solutions, where subsequent aliquots were diluted to 4 μM solutions ready for conjugation. For micro-Raman experiments a stainless-steel slide was used for drop-drying analysis.

For consistency, 0.5 mL of colloid was transferred via micropipette into a triple DI water rinsed Eppendorf, followed by the dropwise addition of the reporter solution at a $1:0.3$ volumetric ratio. During this process, the colloid solution was placed upon an Eppendorf mixing platform, Vortex VariMix (SciQuip, UK), and consequently thoroughly mixed for five minutes. Upon resting the colloid solution at room temperature for ten minutes to aid full binding confirmation, the NPs were centrifuged at 2700 RPM for 7 minutes. Once the supernatant was removed and the NP pellet re-suspended in DI water, the process was repeated a further two times. To increase shelf life, the Raman reporter stock solutions and reporter-conjugated AuNPs were stored in dark conditions at 4°C.

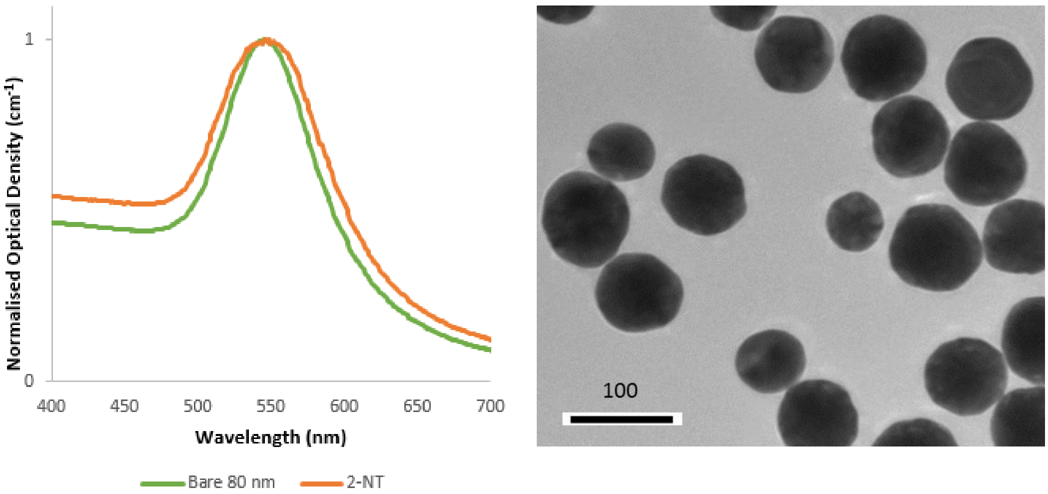

Figure 5.9: UV/Vis and TEM imaging examples of the 2-NT RR AuNPs, with the reference bare citrate-capped absorbance spectrum displayed in the UV/Vis imaging figure.

For each reporter, a complete surface coverage under a non-aggregating, stable reporter-to-colloid ratio was determined and followed in subsequent experiments. The size of the AuNP also affected the ratio in terms of concentrations: a concentration of 9.7×10^9 nanoparticle per mL. Variations between purchased AuNP batches were noted and adjusted for.

The SERS spectrum of each reporter AuNP was analysed via point spectra of the drop dried solutions on a stainless-steel slide. The system used for point-spectra, and micro-Raman mapping, was a Renishaw InVia Reflex (Renishaw, Wotton-Under-Edge, UK). A diagrammatic of the optical set-up can be seen in Figure 5.10.

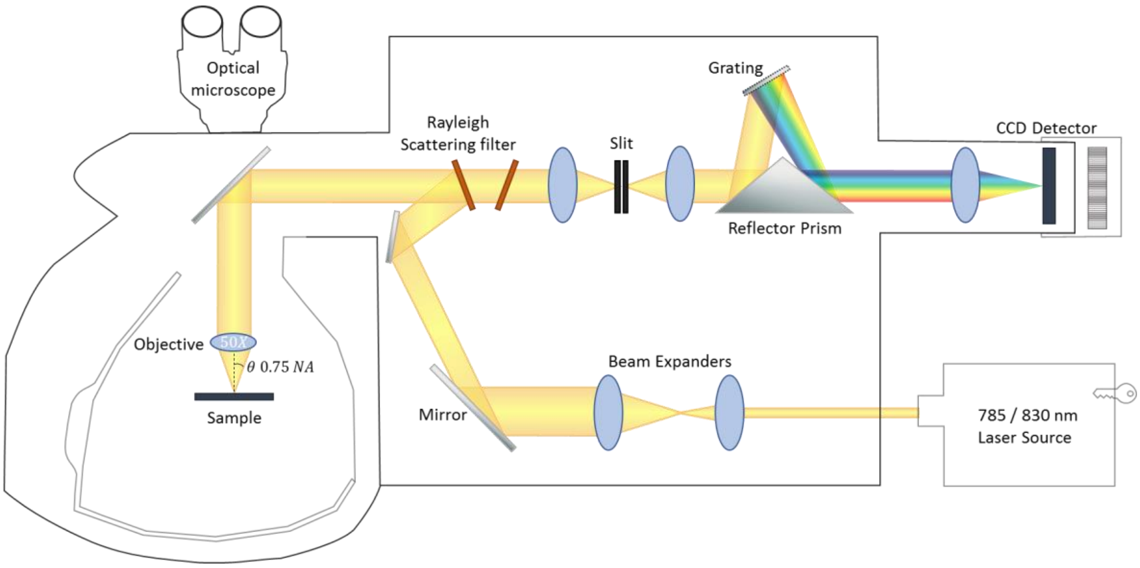

Figure 5.10: Renishaw InVia Reflex optical set-up – the illumination source passes through beam expanders allowing the small, collimated beam to fill the optics; mirrors guide the beam to the objective, 50X magnification displayed here, and onto the sample; the scattered light is collected and passed through Rayleigh scattering filters and a slit to clean the wavelength of the beam; a reflector prism guides the beam onto the grating, where the light is dispersed, and CCD detector array for computer analysis.

Two NIR lasers at 785 and 830 nm, reaching 140 mW power at sample illumination, are built into the system. Two Leica microscope objectives, both with a 200 mm working focal length, were used: 5X/0.12 NA (numerical aperture; inversely related to working distance) for large area surface montages, and 50X/0.75 NA for small area montages, mapping, and point spectra. The laser focused spot size, assuming uniform illumination, can be described as:

$$Spot\ Size = \frac{1.22\lambda}{NA} \tag{24}$$

Hence, for the two working objectives and laser wavelengths, the spot sizes are:

Objective	NA	Spot Size (µm) 785 nm	830 nm
5x	0.12	7.98	8.44
50x	0.75	1.28	1.35

Table 5.1: The variability of microscope objective (5x and 50x) spot sizes depending on the selected wavelength (785 and 830 nm) and the intrinsic numerical aperture.

The spatial resolution of the system is in the order of 1 μm. Governed by the diffraction limit of light, spatial resolution it is dependent on the laser wavelength and the NA of the objective in use, and can be described as

$$Spatial\ Resolution = \lambda/2NA \qquad (25)$$

Hence, an 830 nm laser wavelength through a 0.75 NA objective has a 675 nm spatial resolution. A shorter wavelength and a higher NA will increase the spatial resolution closer to the diffraction limit.

Scattered photons are guided from the sample to the Rayleigh scattering filters. Holographic notch filters are used to retain a high level of Raman scattering intensity. The selected Raman signal travels through a 50 μm slit, is dispersed with a 600 line/mm grating and detected with the -70°C Peltier cooled, deep depletion CCD array (1024 x 256 pixels). The spectral resolution of the system is ~2 cm^{-1} (600 mm/l grating). Spectral resolution dictates the number of resolvable peaks a system can produce. CCD pixel quantity and size, the diffraction grating density, and slit size are the main factors affecting spectral resolution. A minimum of three pixels are required to resolve a single peak, hence a CCD array with a high quantity of small pixels increases resolution. The use of high density line/mm grating increases resolution but decreases spectral range and strength. Similarly, a small slit increases optical resolution but decreases signal strength. Laser wavelength also plays a crucial role – a shorter wavelength will increase Raman scattering efficiency, but also increase the risk of fluorescence and sample burning, reducing quantifiable Raman signal.

The samples are placed on an automated stage, enabling an ease of surface montage imaging and mapping.[108] The system was calibrated by taking a spectrum of a silicon wafer and using the reference peak of 520 cm^{-1}. Arbitrary intensity Raman spectra for each of the Raman reporters is seen in

Figure 5.11.

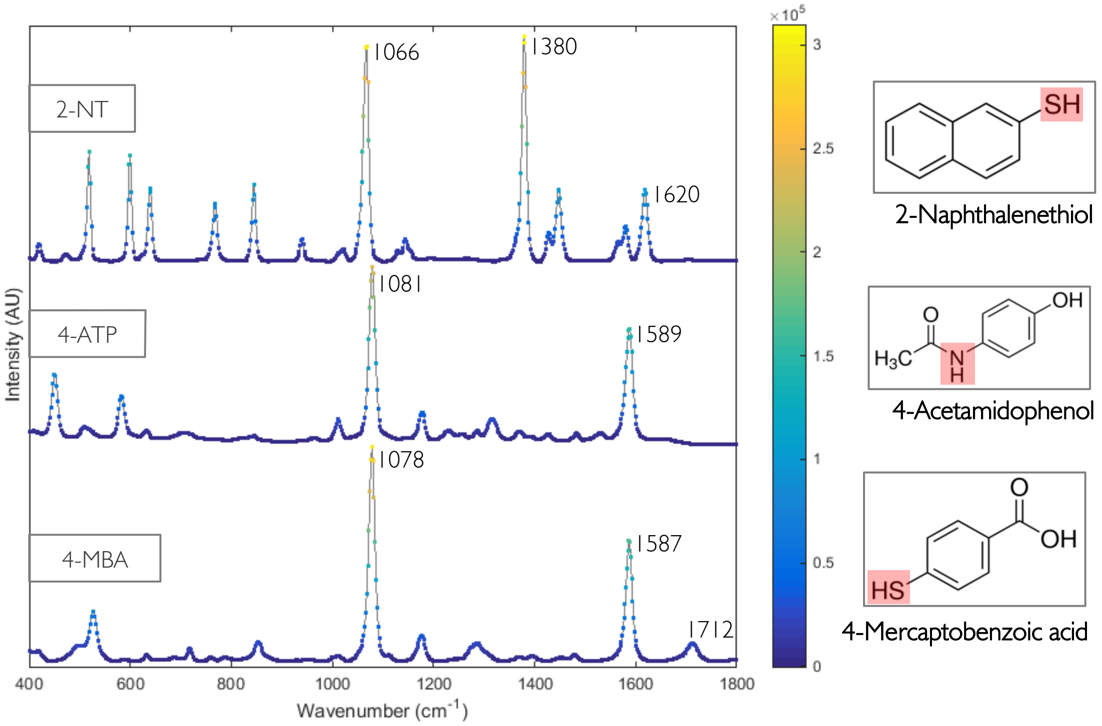

Figure 5.11: Micro-Raman spectrum of the three 80 nm reporter-AuNPs and the corresponding molecular structure of the reporters: 2-NT, 4-ATP and 4-MBA, from top to bottom. The signal intensities plotted across each spectrum is plotted in relation to the colour bar. The AuNP surface binding point for each of the reporter molecules is highlighted in red. The acquisition for each measurement was at a 70 mW sample illumination power, 2 seconds and 5 accumulations.

As Figure 5.11 shows, the three types of reporter molecule have distinct, yet similar, spectral features. The main, characteristic peak assignments when measured under the outlined SERS conditions are classified as follows:

Peak Position (cm^{-1})	Vibrational Mode Reporter Assignment		
	2-NT	4-ATP	4-MBA
1066	Benzene ring symmetric stretch		
1078			$\nu 12$ Benzene ring symmetric stretch
1081		Out-of-plane C–C skeletal stretch	
1380	Benzene ring symmetric stretch		
1587			$\nu 8a$ Benzene ring symmetric stretch
1589		δ N-H bending	

1618	Benzene ring symmetric stretch		
1712			C=O stretch

Data for the characteristic peaks of 2-NT taken are from the papers by Alvarez-Puebla et al.[228,229]; of 4-ATP from the book section by Cinta Pinzaru and Pavel[120]; and 4-MBA from Michota and Bukowska paper.[230]

4-MBA and 2-NT bind to the NP surface via a gold-thiolate bond. Conversely, the 4-ATP is bound via the acetamido nitrogen present. The reporter binding angle affects the orientation of the molecule, perpendicular or parallel to the NP surface, the latter being the case with 4-ATP as seen in Figure 5.12. The significant enhancement of the C-C skeletal stretch at 1081 cm^{-1} supports this suggested orientation.[120]

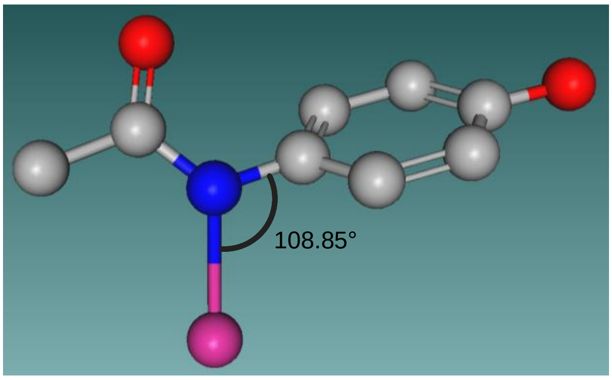

Figure 5.12: Orientation of the 4-ATP Raman reporter molecule when bound to a gold surface, represented in pink. The bond angle of 108.85° between the gold-thiol and benzene ring is also displayed.

The comparable intensity of the 4-MCBA and 2-NT is owed to the increased number and compact nature of the reporter molecules bound to the AuNP surface. A excess of approximately 82,700 RR molecules per AuNP was used.

5.4 Active Targeting Functionalisation

The development of a highly specific targeting agent for breast malignancy is critical for early detection and diagnosis. Research into breast cancer relevant ligands primarily study antibodies and receptors. A relatively untapped, relevant marker of disease is microcalcifications, which when present, contain higher levels of hydroxyapatite (HAP) shown to be synonymous with malignant DCIS, discussed in Chapter 2 Section 2.3.3. Bisphosphonates (BP), a widely-used molecule for targeting HAP, is discussed in sub-section 2.3.3.1.

Cole et al have a number of studies into AuNPs labelled with a type of BP, alendronate, to target bone tumours and microcalcifications, acting as a contrast agent for CT imaging.[59,231,232]

Deciding upon the ligands necessary to achieve a strong SERS signal, effectively target HAP, and remain biologically inert was a crucial initial step. Hence, the targeted AuNPs were made up of three constituent parts to satisfy the needs: a strong, carbodiimide chemistry inert Raman reporter 2-naphthalenethiol (2-NT) was selected, 2,000 Da polyethylene glycol (PEG) to ensure stability and a high binding molecule affinity, and the targeting BP, alendronate. To achieve the full potential of the three components, the configuration and positioning upon the surface of the NP was essential.

5.4.1 Raman Reporter, PEG and Alendronate Conformation

As previously discussed in Chapter 4 Section 4.4, in terms of biocompatibility and avoiding protein corona formation, the most effective conformation of PEG is in a brush-like orientation. The overall most effective conformation of both PEG and targeting ligand is visualised in Figure 5.13 (c).

Using a high grafting volume of 2,000 Da PEG results in a conformation as in

Figure 5.13 (a) occurring. The ideal tethering is seen in

Figure 5.13 (c): the targeting BP attached upon the distal end of a dense, brush-like PEG barrier. Furthermore, it has been shown that distally tethered binding moieties have a significantly enhanced target-specific avidity of up to 4.5 orders of magnitude through multivalent interactions.[234,235] The use of the shorter 2-NT molecule required for SERS could lead to a conformation similar to

Figure 5.13 (d), leading to the BP molecule being buried within the PEG.[233] As such, the ratio of 2-NT: PEG requires tempering.

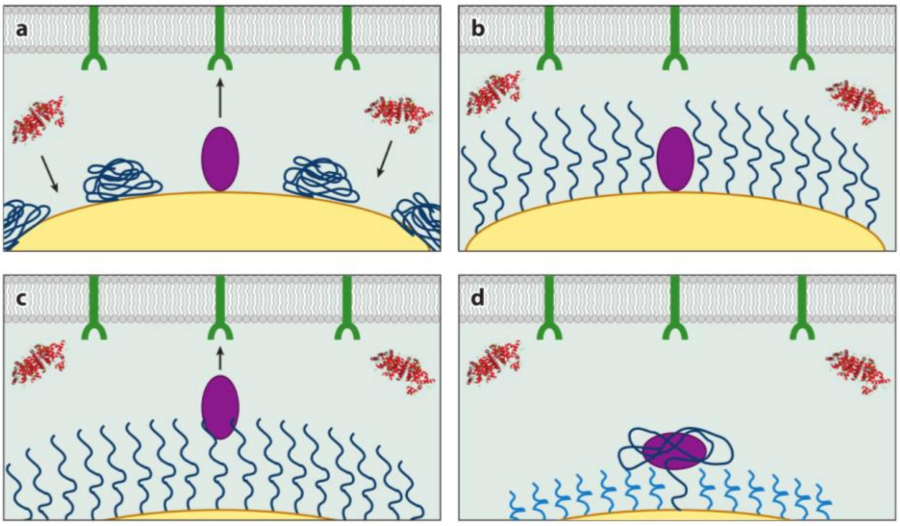

Figure 5.13: PEG and targeting ligand NP surface attachment variations: (a) PEG in a mushroom-like conformation with the targeting molecule anchored to the surface of the AuNP; (b) higher PEG grafting densities lead to a brush-like conformation which blocks the target molecule from binding; (c) anchoring the targeting ligand to the distal end of the brush-like PEG; (d) shorter neighbouring molecules can cause the PEG molecule to relax back into a mushroom-like conformation.[233]

Ensuring the alendronate molecules have little steric hindrance, occurring within large molecular groupings preventing targeted binding of smaller molecules, is key to increasing their ability to locate the binding points within HAP. The role of PEG tether length affecting steric hindrance is explored by Cole et al.[232] The assumption of a longer chain length increasing the binding ability of distally-attached bisphosphonates has been disproven both in vitro and in vivo. Long PEG tethers can provide too much distance between the BPs, leading to distant and low concentrations.[236] Further investigations by Cole et al. found an ideal tether length of 2,000 Da, resulting in a greater binding affinity in vitro compared to 1,000 and 5,000 Da.[232] The design outline of the active targeting AuNP is seen in Figure 5.14.

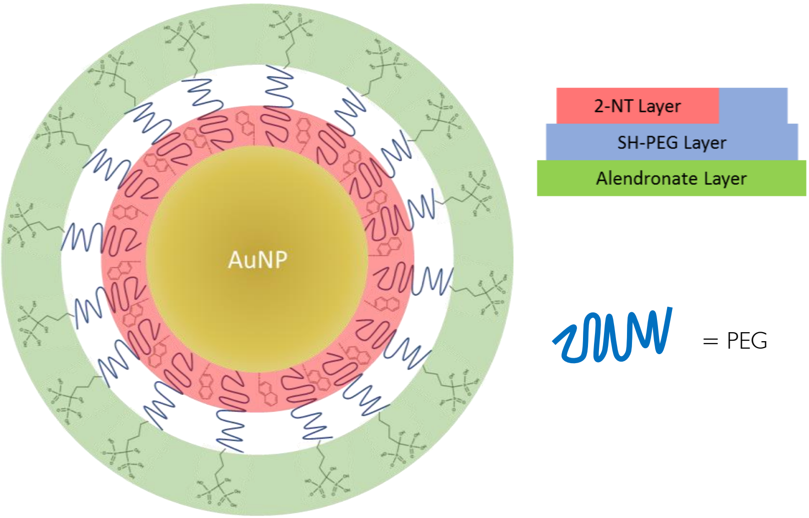

Figure 5.14: An image portraying the overall design of the targeting NPs: 2-NT and PEG layers attached directly to the AuNP surface, alendronate fixed at the distal end of the PEG molecule.

5.4.2 2-NT to PEG Ratio

The necessity of both the 2-NT and the PEG to readily bind to the NP surface with little competition required the use of thiolated PEG. The ratio of 2-NT to PEG molecules also needed to satisfy two specifications: a high enough level of 2-NT molecules to gain a significant SERS signal; and an appropriate amount of PEG to gain a brush-like conformation. The preparation method was adjusted from Qian et al. to deliver an optimization of surface coverage.[206]

A 4 μM ethanol solution of 2-NT and a 10 μM aqueous solution of 2,000 Da PEG was prepared. NPs : 2-NT : PEG was added as a ratio of $1 : 0.1 : 0.2$. Initially, 100 μL of 2-NT solution was added dropwise to 1 mL of colloid, then shaken vigorously for 5 minutes. 500 μL of PEG solution was then added dropwise and again shaken to ensure complete coverage of the NPs. The colloid solution was centrifuged at 3000 RPM for 7 minutes, supernatant removed, and washed with DI water – repeating three times to remove any remaining, unattached -thiols. Prior to attachment of alendronate, the 2-NT-PEG NPs were analysed using UV/Vis to determine whether aggregation had occurred, detailed in Section 5.4.4.

Under successful conjugation conditions, an approximate ratio of 2,474 2-NT molecules to an excess of 58,978 PEG molecules per 80 nm nanoparticle could be attained.

5.4.3 Carbodiimide Chemistry

In conjugating targeting molecules to a PEG layer, one of the most common coupling techniques is carbodiimide chemistry.[237,238] In this process a carbodiimide cross linker and a stabilizing ester facilitates a zero-length, carboxyl-to-amine reaction. Hence, a distal PEG group of -COOH is required.

The two most commonly used carbodiimide structures are 1-ethyl-3-(-3-dimethylaminopropyl) carbodiimide (EDC) suitable for aqueous crosslinking, and N',N'-dicyclohexyl carbodiimide (DCC) for organic synthesis methods. With the pre-prepared 2-NT-PEG NPs suspended in DI water, EDC was chosen. The carbodiimide reacts with the carboxyl group, forming the intermediate, active ester o.-acylisourea – Figure 5.15.

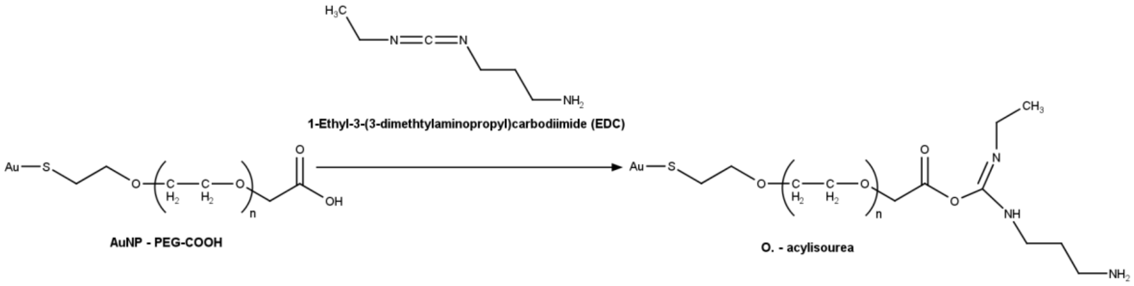

Figure 5.15: Reaction pathway of initial -COOH PEG with EDC: C=N reacts to the receptive -OH group, forming the intermediate O.-acylisourea.

When in aqueous solution, o.-acylisourea is unstable. If left destabilised, hydrolysis can occur. Hydrolysis deactivates the binding site, regenerating the carboxyl group. This significantly reduces the number of reaction sites available, decreasing overall yield. Carboxylate activation with EDC is most efficient at pH 3.5 – 4.5.[239] However, the rate of hydrolysis at this level of acidity is estimated to be 2 – 3 s^{-1}.[240]

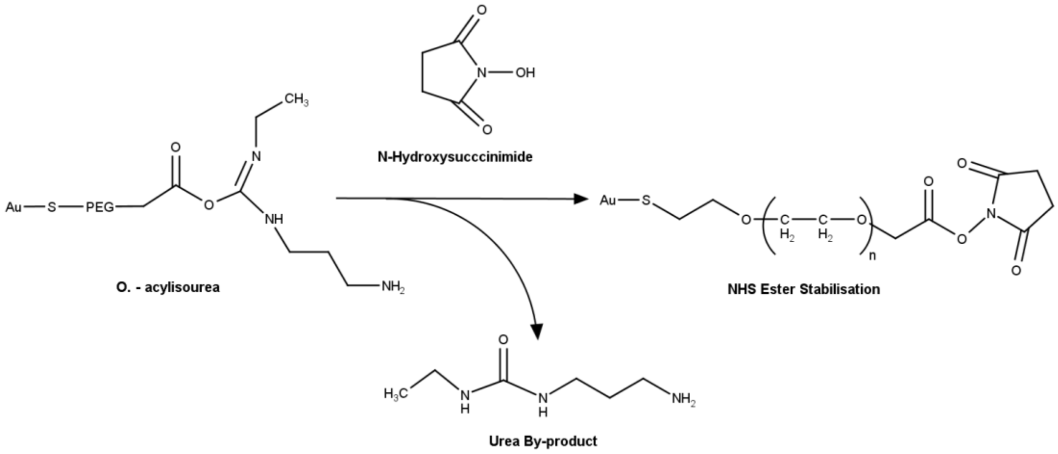

Figure 5.16: Reaction pathway of O.-acylisourea with NHS to form a stabilised platform for amine group bonding. A non-toxic urea by-product is formed through the reaction.

Avoiding yield loss and hydrolysis requires the use of a hydrophilic, stabilising ester: *N*-hydroxysuccinimide (NHS), chemical reaction pathway seen in Figure 5.16.

EDC used in conjunction with NHS at pH 7.5, retains a high yield and significantly increases hydrolysis rate to 40 minutes.[241] 0.1 M phosphate-buffered saline (PBS) at pH 7.4 was used for the EDC, NHS and alendronate solutions – amine deprotonation occurs at an acidic pH halting further reactions. The final reaction pathway conjugating the alendronate to the PEG is seen in Figure 5.17.

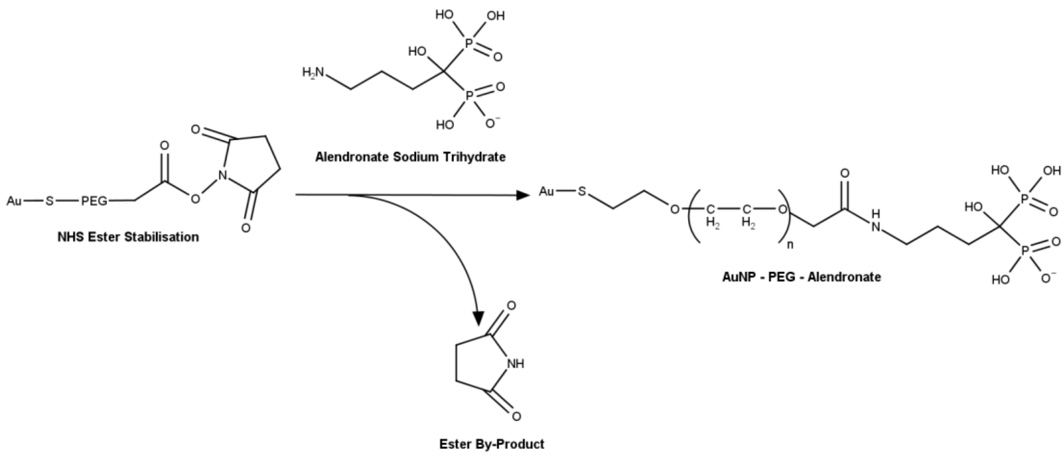

Figure 5.17: Reaction pathway of NHS stabilized PEG with alendronate amine group forming final resultant of carbodiimide chemistry; ester by-product is substituted in the reaction.

The process began with 4 mL of 2-NT-PEG NP colloid decanted into a flask with a magnetic stirrer. PBS solutions of NHS (20 mg/mL) and EDC (15 mg/mL) were added in unison, at a 1:2 parts ratio, to activate the carboxylic group. The solution was stirred at a constant rate for 20 minutes. A PBS solution of alendronate (1 mg/mL) was then added at a 1:1 molar ratio of alendronate:PEG, and left to gently stir at room temperature for up to 3 hours. The final product (2-NT-PEG-BP NPs) was centrifuged at 2,500 RPM for 7 minutes, and rinsed with DI water, three times.

Post-labelling, the 2-NT-PEG-BP NPs were stored at 4°C in foil wrapped, sealed glass containers. Characterisation of the NPs with UV/Vis and TEM was then carried out.

5.4.4 UV/Vis and TEM Analysis

UV/Vis measurements were taken at each step of NP labelling: bare, with 2-NT Raman reporter, 2-NT with PEG, and fully functionalised with alendronate, as seen in Figure 5.18.

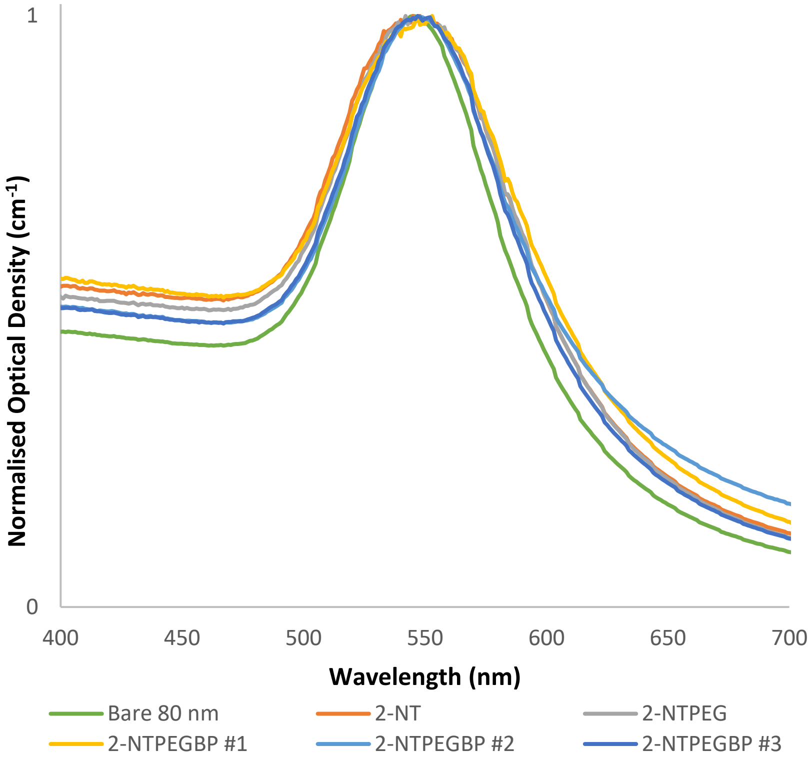

λ_{max} (nm)	545	545	542	553	547	547

Figure 5.18: Normalised UV/Vis spectra of each labelling step from bare NPs to fully targeting. Three batches of the targeting NPs were measured to check consistency in the carbodiimide chemistry. Apart from the fully functionalised batch #1, minimal aggregation occurred at all steps.

Crucially, at each labelling step the peak width remained consistent that of the bare AuNPs, verifying that little aggregation had occurred at each stage of labelling. The slight red-shift of the peaks following each stage confirmed that further surface modification had been successful, or that an overall increase in NP size had occurred. Both the 2-NT-PEG and 2-NT-PEG-BP colloids were imaged with TEM to clarify the NP labelling at each crucial step.

The 2-NT-PEG NPs are visualised with TEM imaging in

Figure 5.19. As can be seen, the PEG molecules appeared to have conformed upon the NP surface into a mushroom-like formation. This brought doubt upon the success of the carbodiimide chemistry in both carboxyl-to-amine binding, and effectiveness of HAP targeting thereafter. Analysis of the 2-NT-PEG-BP NPs brought light to the situation.

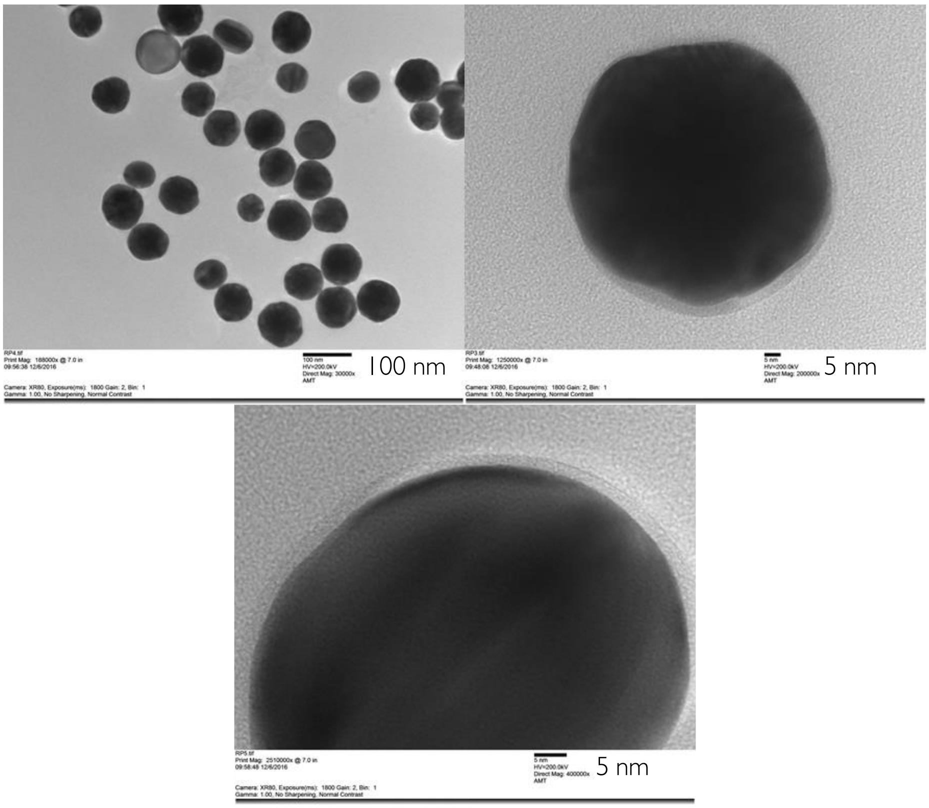

Figure 5.19: A range of TEM images displaying the features of the 2-NT-PEG NPs, clustered and individually. Larger annotations of the scale bar added for clarity.

Figure 5.20 characterises the PEG as a brush-like conformation post-carbodiimide chemistry. Slight thinning of the conjugated layer on one side of the NP relates to the orientation of the NP with regards to the microscope. Across the main bulk of the targeted NPs viewed with TEM, successful labelling had occurred remaining disperse in nature. However as seen in Figure 5.21, success was varied. Several NPs showed levels of aggregation; and whilst some achieved a “patchy” formation others failed to undergo successful conjugation of any type. PEG disassociation or non-binding also occurred, evident in the mottled background effect created by these lone, aggregate molecules present in Figure 5.20 and Figure 5.21 TEM images.

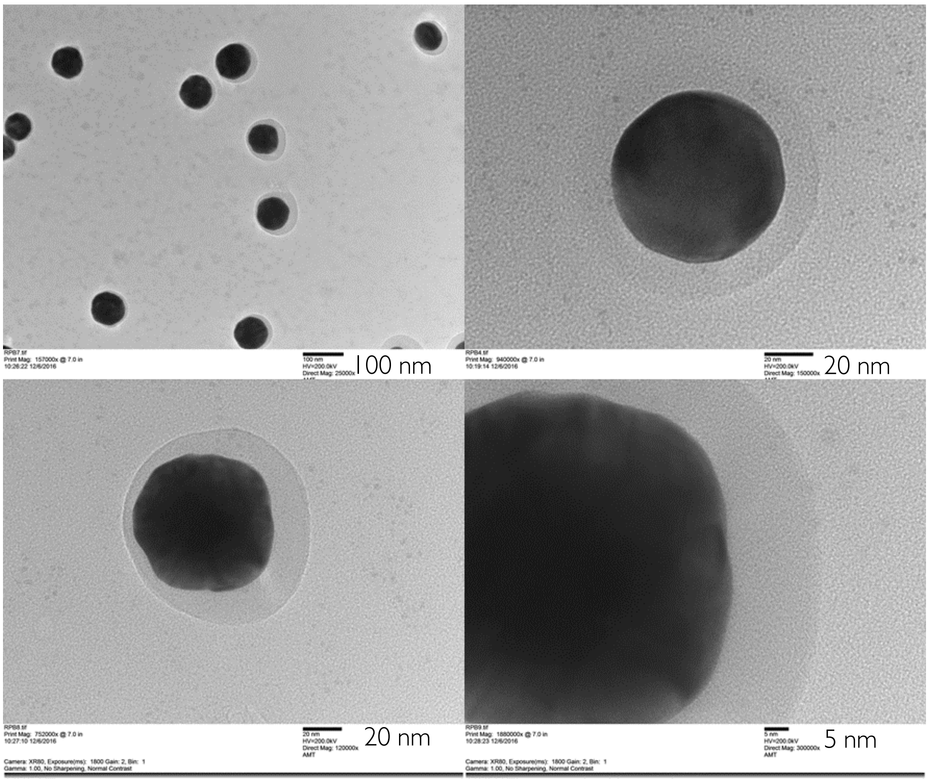

Figure 5.20: TEM images of singular 2-NT-PEG-BP NPs displaying a brush-like conformation, from magnification levels 100 – 5 nm. Larger annotations of scale bars added for clarity.

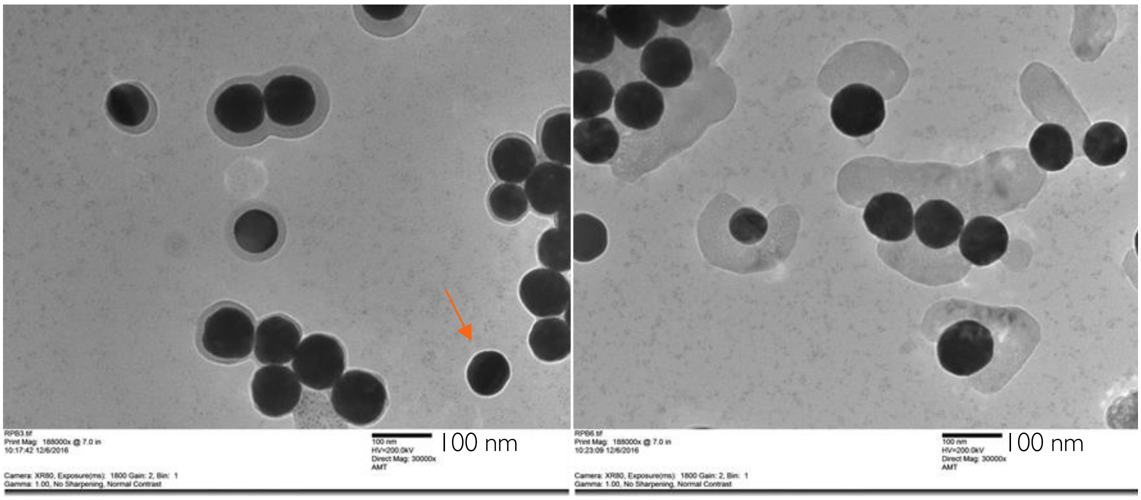

Figure 5.21: TEM images displaying occurrences of unsuccessful carbodiimide chemistry. Highlighted by the orange arrow is a PEG-only labelled NP. Larger annotations of scale bars added for clarity.

As seen in the UV/Vis spectra in Figure 5.18, little overall aggregation had occurred within the bulk of the colloid – this highlights the propensity of aggregation occurring during TEM preparation.

5.5 Discussion and Conclusions

The nature of gold colloid production on a small scale resulted in a prominence of polydispersity, with a low level of batch reproducibility. Consistency in SERS requires uniformity in AuNP size with monodispersity.[109,115] As such, to ensure reproducible experiments in SERS commercially available AuNPs were obtained. The batch specific properties supplied on a data sheet were cross checked using TEM imaging and UV/Vis to ensure validity.

Persistence in the production of the peanut-shaped AuNPs could have been made, however consistency in synthesis was lacking and difficult to reproduce due to the need to temper the two nucleation points. This may be an interesting avenue to pursue for future work.

The selection of 80 nm AuNPs falls within the remit of biocompatibility, with a higher known success rate of RR binding to the colloidal surface and hence extrinsic enhancement. RRs 2-NT and 4-MBA are two of the most commonly used as RRs due to the thiolated binding mechanism and highly Raman active benzene ring within the molecules. 4-ATP, more commonly known as paracetamol, is less widely used, and generally selected as a Raman standard.[106] The difference in binding mechanisms and angles between the acetamido nitrogen of 4-ATP, and -thiols of 4-MBA and 2-NT is a point of interest moving forwards in terms of the signal intensity garnered from each.

The actively targeting AuNPs are next considered. To be effective, NPs must avoid clearance from the body through the liver, achieving long circulation times with passive, EPR effect and active targeting mechanisms enabling tumour retention. The necessary steps were taken to considerate the functionalisation design: use of the 2-NT Raman reporter as a carbodiimide chemistry inert molecule; the length of PEG chain for optimal brush-like coverage; and the tethering of the actively targeting alendronate molecule at the distal end of the PEG to reduce steric hindrance.

An increase in the chain length of the PEG, plus an increase in the ratio of spacer Raman reporters on the colloid surface, may provide a brush-like formation in the first, non-targeting functionalisation step. Other BPs with a greater HAP binding affinity, such as risedronate and zolendronic acid, could also be tested in place of the alendronate molecule. This brings up the possibility of using a different PEG binding mechanism other than the amine, which is known to be the main binding site to the HAP.

The ability to test the RR-AuNPs at depth required the manufacture of optically representative breast tissue phantoms, the remit behind the material selection and consideration of the required shape for transferability of experimental results into a clinical setting is explored in the next Chapter.

6. Optical Phantom Construction

6.1 Introduction

The use of optical and morphologically representative "tissue-mimicking" phantoms was first experimentally proposed in the 1980s, detailing the trans-illumination of the phantoms with infra-red light as a potential new method for breast cancer diagnosis.[242,243] Henceforth, key factors enabling the use of optical phantoms, other than crucially representing the scattering and absorption factors of the desired tissue type over clinically useful wavelengths, include the stability, homogeneity and reproducibility in phantom formation.[243]

Within this chapter, Section 6.2 considers the optical matching properties of various phantom materials relating to breast tissue at an 830 nm wavelength. The fabrication of polydimethylsiloxane (PDMS) phantoms is detailed in Sections 6.3 and 6.4. Section 7.4 is broken down into two key areas: 6.4.1 describing optically representative breast phantoms of a semi-infinite form, and 6.4.2 which considers optically and morphologically representative breast phantoms; both utilising additive manufacturing in mould creation. The latter sub-section considers the transferability of the deep Raman technique into a hospital setting, in combination with mammography. This required a notable change of the optical phantoms in becoming representative of a breast in a compressed state.

6.2 Postmenopausal Breast Tissue Optical Property Matching

Graphs pertaining the results from the breast optical properties studies of pre- and post-menopausal women have been plotted in Figure 6.1 and Figure 6.2. The vertical, dark grey dotted line marks the 830 nm wavelength selected for experimental use in this study; the vertical, light grey dotted line marks the collection wavelength of the benzene ring, predominant across all RR-AuNPs.

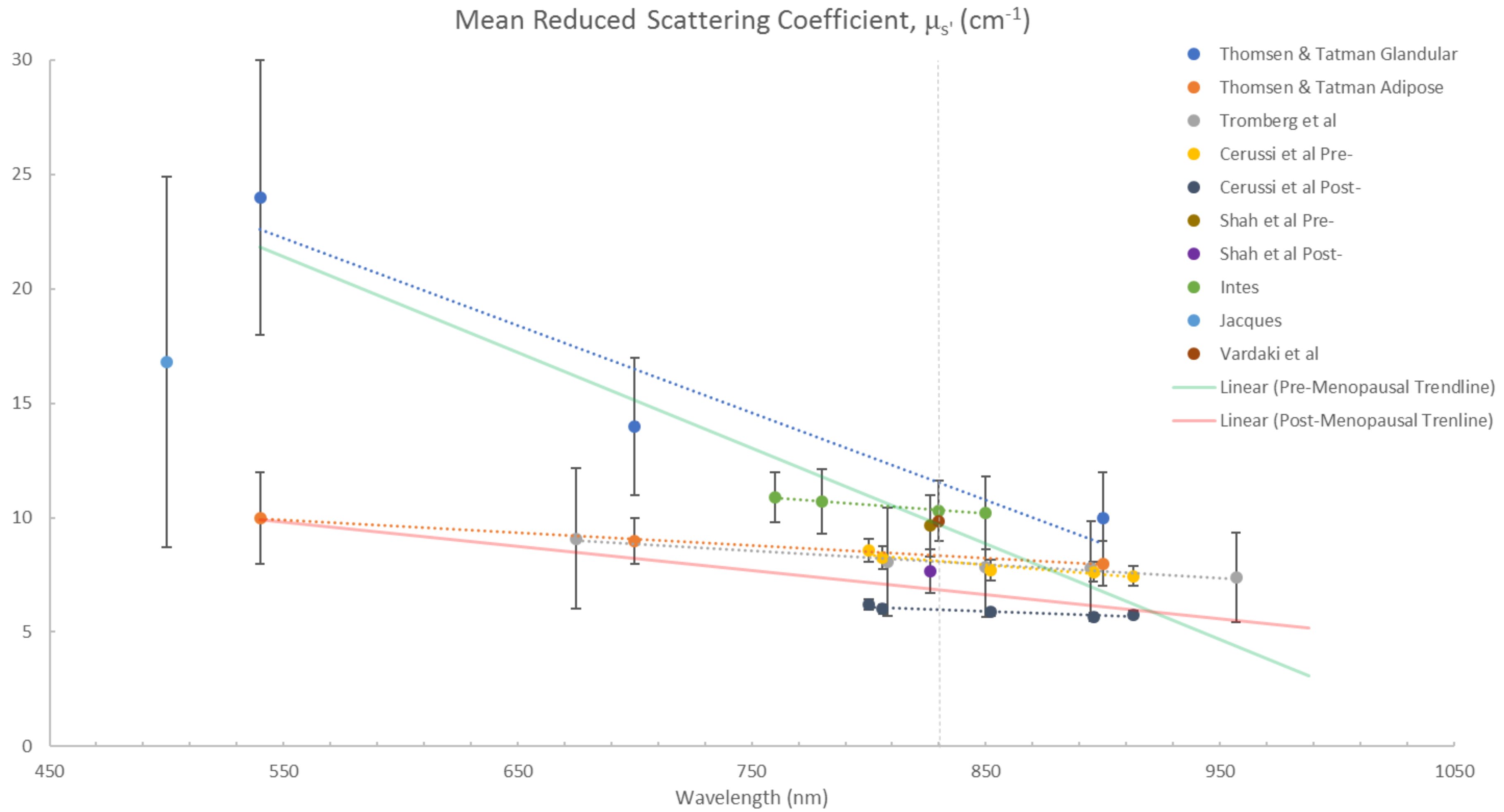

Figure 6.1: A graph to show the mean reduced scattering coefficient (cm^{-1}) values from three reviews and four studies, focussing on pre- and post-menopausal women as the main identifiers. Tromberg et al[303] and Intes[247] study values are representative of both groups, averaging an age of 46.5 and 57.2± 9.6 respectively. The glandular breast values from the Thomsen & Tatman[304] review were selected for the pre-menopausal group; the adipose values selected for the post- group. Hence, pre- and post-menopausal values from Thomsen & Tatman, Cerussi et al[248] and Shah et al[245] studies were selected to form the two averaged trendlines, green and red respectively.

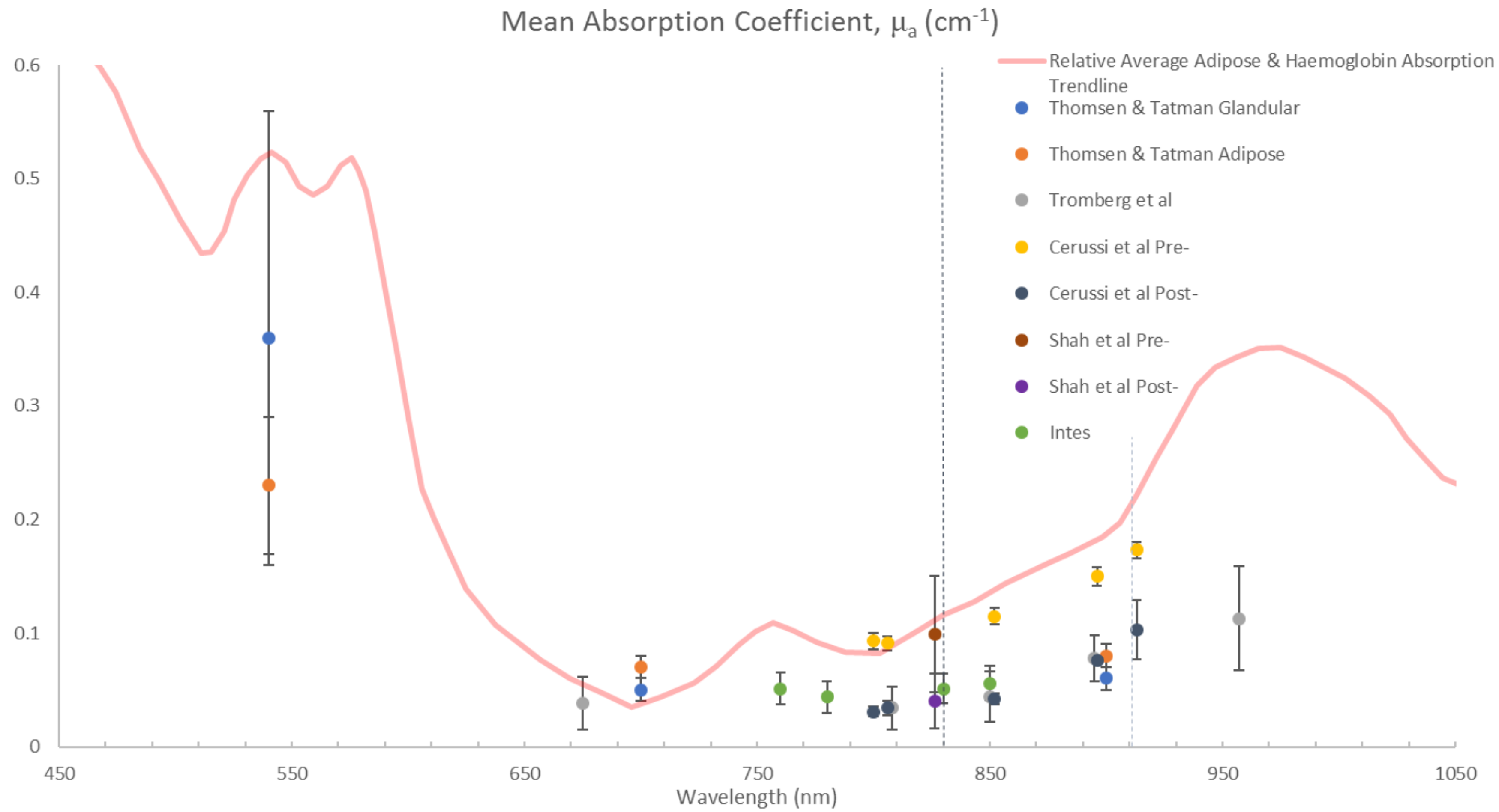

Figure 6.2: A graph to show the mean absorption coefficient (cm^{-1}) values from one review and four studies, focussing on pre- and post-menopausal women as the main identifiers. Tromberg et al[303] and Intes[247] study values are representative of both identifying groups, with the average ages of 46.5 and 57.2 ± 9.6 respectively. The glandular breast values from the Thomsen & Tatman[304] review are deemed representative of the pre-menopausal group, with the adipose values typical for post-menopausal. The red trendline is a combined average of adipose and haemoglobin adsorption coefficients selected from the Jacques[147] review, factored down to profile the plotted values.

Appreciable differences in the optical properties of breast tissue during the phases of the menstrual cycle, due to the physiological changes in haemoglobin concentration (oxy- and deoxy-), and oxygen and water saturation, have been documented.[244–247] This increased variation is highlighted by the standard deviation values for pre-menopausal women in the studies by Cerussi et al and Shah et al.[245,248]

In relation to the epidemiology of this thesis, predominantly women over 45 years of years undergoing or post-menopausal, these cyclical factors can be disregarded. A slowing of hormonal and glandular activity in menopausal breast tissue leads to a reduction in vascular requirements. A lower blood volume effectively reduces the absorption and reduced scattering coefficients, by approximately 230 – 300 % and 16 – 22% respectively.[245]

Pre- and post-menopausal μ_s' trendlines – indicative of Cerussi et al, Shah et al and Thomsen & Tatmen (considering the glandular tissue values for pre-menopausal, and adipose tissue for post-menopausal) – intersect 830 nm at 9.702cm^{-1} and 8.852 cm^{-1} respectively.

From Figure 6.2, averaged haemoglobin and adipose values derived from the Jacques review paper[147] were factored by ~4.6 times to be relative to the plotted results, forming the absorption trendline.

At 830 nm for post-menopausal breast tissue, the mean reduced scattering coefficient value of ~8.8 cm^{-1}, and the average absorption coefficient of approximately 0.056 cm^{-1}, were selected for use.

6.3 Optical Phantom Fabrication Techniques

In the creation of turbid phantoms for spectroscopic diagnosis, both $\mu_{s'}$ and μ_a must be taken into consideration.[249] Materials historically used for optical phantoms in a biomedical setting include intralipid, agarose, and animal substitutes, such as porcine fat and muscle. Whilst the porcine tissues can be layered, the liquid phantom is unable to create inhomogeneous layers of realistic complexity within itself. Though the optical density of diluted Intralipid is closely related to that of tissue, the scattering anisotropy value of $g = 0.8$ is decreased from that of tissue ($g = \geq 0.9$).[250] Another drawback is the unstable nature of these materials, having a short working life-span – for intralipid and agarose this can be no more than two months, whilst porcine tissue is around only three days, with adequate refrigeration between measurements. Requiring substitutions, repeatable measurements of the initial phantoms cannot take place over a long-time period.

Solid materials, such as polytetrafluoroethylene (PTFE) and polyurethane (PU), hold long term optical stability and a greater freedom in morphological representation. PTFE and PU supplied as blocks, sheets or rods, can be machined to size. Castable liquids, such as polydimethylsiloxane (PDMS), give an extra element of flexibility, with the stability of a 10-year shelf life. The optical nature of the solid polymers is rudimentary, however, much like the agarose and intralipid phantoms, scattering and absorbing agents can be added to the PDMS to vary the optical properties. The refractive index of PDMS, 1.40 – 1.42, which sits within the mammalian soft tissue range, between 1.35 – 1.48.[251]

Titanium dioxide (TiO_2) and aluminium dioxide (Al_3O_2) are the two most common scattering agents used for optical phantoms, whilst an array of inks, such as India or Nigrosin, can be used to create further absorption within the PDMS material if required.[249,252] The anisotropy of TiO_2 of $g = 0.93$ is more characteristically aligned with the scattering profile of tissue.[253]

The solid, reproducible phantom material PDMS with scattering agent TiO_2 was investigated. The reduced scattering and absorption coefficients of these materials, in comparison with post-menopausal breast tissue and Caucasian skin tissue, is given in Table 6.1. The optical values for pork fat, muscle and dermis are also given, as a representative of breast adipose, glandular and skin tissue, respectively. PTFE was also measured as a possible alternate solid phantom.

Material	Reduced Scattering Coefficient (μ_s') cm^{-1}	Absorption Coefficient (μ_a) cm^{-1}
Human Breast tissue	8.8	0.056
Human Skin tissue [254]	15.2	0.38
Pork Muscle[255]	2.7	0.11
Pork Adipose[256,257]	4.5	0.8
Pork Dermis [258]	10.8	0.3
PTFE [259]	161	>0.01
PDMS [260]	~0.01	~0.01

Table 6.1: The reduced scattering ($\boldsymbol{\mu_s}'$) and absorption ($\boldsymbol{\mu_a}$) coefficients of human tissues, comparative to the phantom materials of porcine tissue, PTFE and PDMS.

The values for the PDMS are negligible as the material possesses no inherent scattering or absorption properties.[260]

In determining the thickness limitation of the optical phantoms, the SESORS study by Stone et al. was considered: the group were able to gain a transmission signal of Raman reporter AuNPs at a depth of ~47 mm.[12] However, to determine the SESORS technique within turbid phantoms as a proof of concept, phantoms of a reduced thickness, between 23 – 33 mm, was selected.

6.4 PDMS with Titanium Dioxide Phantoms

The suitable scattering and absorption coefficients to optically match the pre-menopausal breast tissue properties, as defined in Section 6.2, were selected. Although molecular densities change person to person, an average blood and fat content value was used to represent the absorption coefficients, as in Figure 6.2.[147] In terms of a quasi-skin layer, melanin content varies with ethnicity – for this study, the focus is on developed world groups, represented mainly as Caucasian.

In creating the quasi-skin layer, a study by Pope et al. determined the breast skin thickness of the superior (0.7 – 2.3 mm), inferior (0.7 – 2.7 mm), medial (0.6 – 2.4 mm) and lateral (0.5 – 2.1 mm) quadrants.[261] This led to the average across all quadrants of 1.5 mm. Hence, this determined the constant thickness required for the quasi-skin layer.

The TiO_2/PDMS phantoms were produced in the same way. The preparation was modified from the studies by de Bruin et al and Iping Petterson et al, following the latter in the use of rutile TiO_2, Sigma Aldrich (Missouri, USA), to provide uniform scattering at a wavelength of 830 nm.[262,263] The volume of PDMS, and hence quantity of TiO_2 to provide the required reduced scattering coefficient value, was calculated to the total required mould volume. Table 6.2 describes the required ratios, adjusted to an 830 nm wavelength from the study by Greening et al.[264]

Phantom Type	PDMS Ratio (mL) (10:1 base:curing agent)	TiO_2 Quantity (g)
Breast tissue	56 : 5.6	48 mg/mL = 2.957
Skin	9 : 0.9	74 mg/mL = 0.731

Table 6.2: The ratio of PDMS base to curing agent required to fill the semi-infinite tray mould, alongside the respective quantities of TiO_2 required to fulfil the optical scattering properties of the post-menopausal breast and skin tissue.

According to the defined ratios, the TiO_2 was added to the PDMS curing agent, Dow Corning (Wales, UK), and sonicated to ensure an even particulate distribution. The PDMS base was then added to the mixture and stirred for 10 minutes until homogeneous. After placing under vacuum to remove bubbles, the de-gassed TiO_2/PDMS liquid was poured into the moulds, and cured in an oven at ~85°C for one hour. Rapid cross-linking of the PDMS through curing minimises the "fall-out" of TiO_2, improving the optical homogeneity across the whole phantom section.[252] Multiple phantoms were cast from the same batch of breast tissue/skin matching TiO_2/PDMS to reduce inter-sample variation.[249]

6.4.1 Semi-Infinite Breast & Skin Phantoms

The desired block phantom proportions were required to consist of a semi-infinite-geometry. The longitudinal dimensions of the phantom must be representative of a large volume medium and hence ≥45 mm, reducing the lateral dissipation of photons from the system.[265–267] Transferability of experimental measurements to a clinically viable, *in vivo* setting is made feasible when measuring semi-infinite phantoms with an optical axis thickness greater than 20 mm.[265,268]

As such, a tray with four mould insertions was 3D printed. **Additive manufacturing**, or 3D printing, of models designed in Autodesk Inventor were completed using the Form 2, Formlabs (Massachusetts, USA) and the MakerBot Replicator+, MakerBot (New York, USA).

The lateral dimensions of each mould within the tray was set at 50 x 45 x 10 mm. 1.5 mm depth skin phantoms, a combination of 10 and 5 mm thickness breast phantoms were cast. The combination of these layers allows the formation of semi-infinite phantoms, smallest thickness of 23 mm (1.5 mm skin | 10 mm breast | 10 mm breast | 1.5 mm skin), increasing by a depth diameter of 5 mm. The 3D printed tray mould and a 33 mm phantom combination is seen in Figure 6.3.

Of the breast tissue phantoms, a single hole was driven in at half phantom depth using a cork borer, ø5 mm, creating a centrally positioned chamber for an AuNP containing NMR tube inclusion. Further breast phantom pieces remained whole, allowing layering and depth variation possibilities to be explored.

The use of silicone releasing agent spray ensured mould reusability, granting consistency in both breast tissue and skin phantom production.

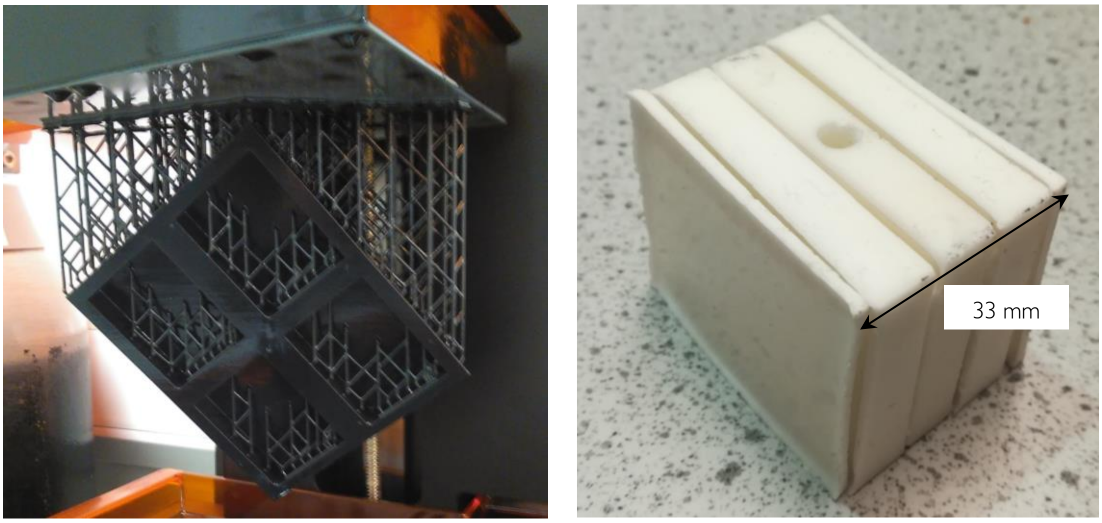

Figure 6.3: Left image: 3D printed mould tray, 50 x 40 x 10 mm section dimensions, to be cast. The mould is seen here post additive manufacturing, yet to be removed from the base plate within the Form2 3D printer. Right image: The completed breast tissue and skin block phantoms, arranged with the inclusion space in the middle of the phantom (11.5 mm depth) at a thickness of 33 mm.

6.4.2 Morphologically Representative Whole Breast Phantoms

As with endoscopic Raman fibre optic probes, as discussed in Chapter 3, Section 3.3.3, incorporation of new techniques within existing ones allows the diagnostics process to be efficiently streamlined, eliminating patient wait times between tests and hence delaying disease progression. Post-menopausal patients susceptible to breast cancer undergo mammographic imaging via referral, or through triennial screening. Capitalising on this current diagnostic pathway would create minimal disruption to current procedure. Also, with the breast in a compressed state, tissue penetration depth required when using TRS is minimised, with the possibility of spot compression further reducing breast thickness and raising the ease of Raman photon collection.

6.4.2.1 Exploration of Breasts in a Compressed State

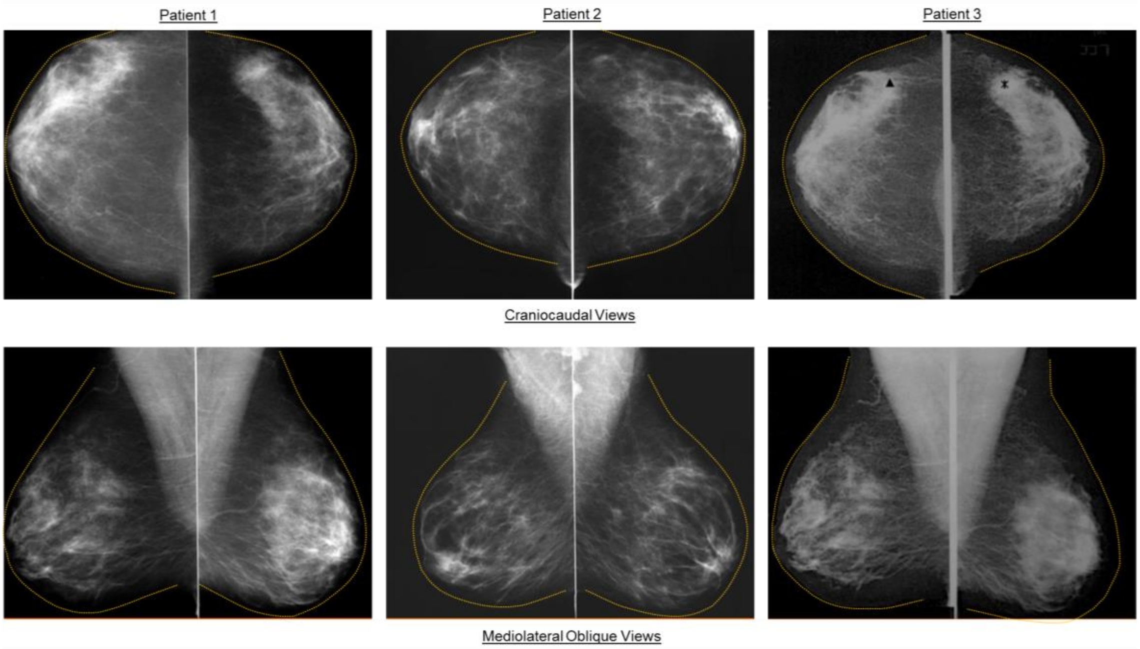

Figure 6.4: Standard, two-view mammogram images of both left and right breasts - craniocaudal, top level, and mediolateral oblique, bottom level - of three patients under a screening program, above 40 years of age. The dashed yellow line marks the margin, and hence general shape, of the breasts under compression of a diagnostic quality. [269]

Modelling morphologically representative compressed breast moulds required image analysis of mammograms, taking into consideration differences in breast volume and variation in pressure applied across the compression paddle. Gaining this understanding of breast shape under mammographic compression was an important first step prior to mould making.

The general, guideline shape can be seen in both craniocaudal and mediolateral oblique mammographic images of

Figure 6.4. To produce a radiographic exposure with consistency in contrast, the compression paddle applied must create an even thickness across the whole of the breast, from chest wall to nipple. Following this knowledge and the guideline shape, whilst taking into consideration the 177.8 mm NMR tubes requiring stable inclusions, a flat sided, elongated, "D" shape was chosen. The 3D model and phantom casting process is seen in Figure 6.5.

6.4.2.2 Formation of Breast Phantoms

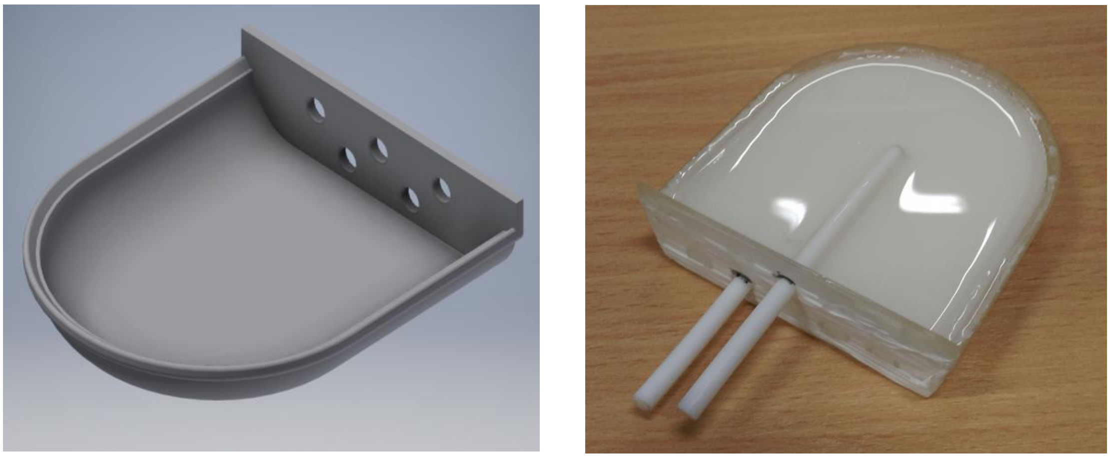

Figure 6.5: Left image: The 11 mm half breast mould design in Autodesk Inventor; Right image: Casting progress of one half of the 22 mm breast tissue phantom. The two rows of holes positioned at the back of the mould are covered using PTFE tape to avoid leaks. Two ø 5 mm PTFE rods are pushed through and affixed into position at a depth of 60 mm into the phantom.

Breast tissue phantoms sized 25 mm, 27.5 mm and 30 mm were selected. 3D models of the breast moulds were created using Autodesk at three, half sizes: 11 mm, 12.25 mm, and 13.5 mm. This allowed the two halves of the phantom to be made individually in the reusable moulds, avoiding as much TiO_2 planar fall-out as possible. Hole positioning using ø 5 mm PTFE rods was selected prior to casting, forgoing the need to bore inclusions post-cure. Due to the thin walled nature of the moulds, “High Temperature” resin was used to minimise the effects of heat shrinkage when placed within the curing oven.

6.4.2.3 Quasi-Skin

An encompassing quasi-skin layer was produced, representative of the optical properties of skin and the morphological nature of the breast. Large tray moulds, similar to that of the study by Saager et al, were 3D printed at a 1.5 mm fillable depth, as an average breast skin thickness.[270] An excess of quasi-skin was cast to ensure an even, un-stretched layer over the tissue phantom. A bidirectional spirit level was used, as seen in Figure 6.6, as the nature of a thin TiO_2/PDMS layer requires precise, even curing.

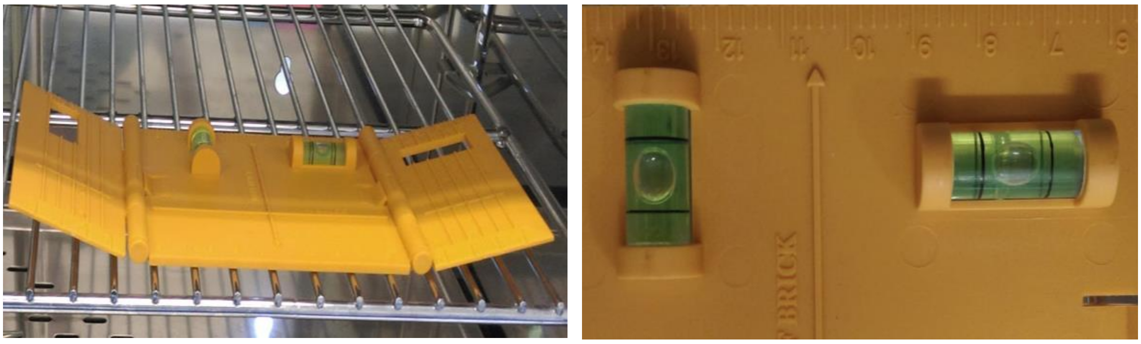

Figure 6.6: The bidirectional spirit level placed within the oven; a close-up of the centred bubbles.

The quasi-skin was required to wrap round the curved features of the breast phantom as seamlessly as possible. An area of the quasi-skin was required to be removed. This was calculated by subtracting the filleted surface area of the breast phantom from the assumed cuboidal area, detailed in Figure 6.7.

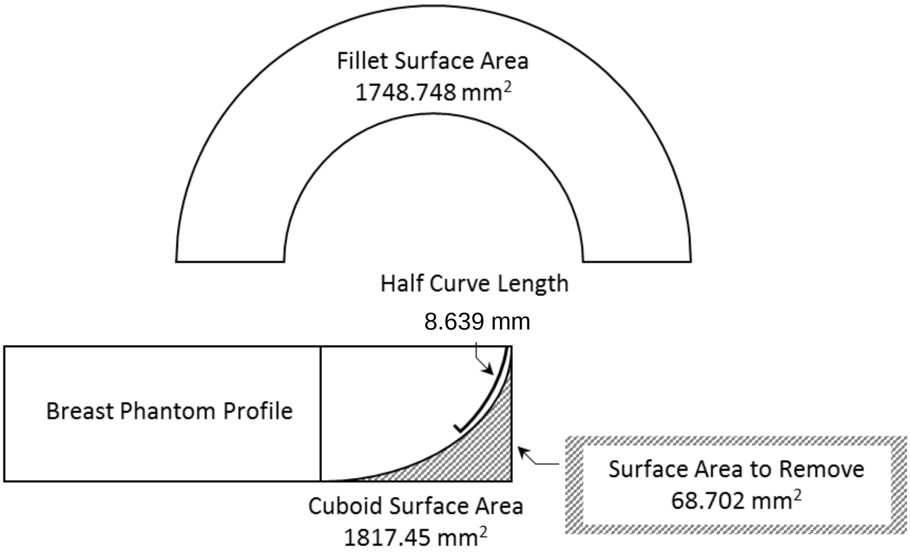

Figure 6.7: Quasi-skin template sector removal maths. The filleted surface area considers the skin thickness of 1.5 mm.

The 68.702 mm^2 area for removal was distributed over seven sectors, placed evenly across the fillet in 22.5° segments, equalling a total area of 9.815 mm^2 per sector. The sector shape geometry was calculated in three steps: finding the individual length of each sector, the angle of the sector and consequently the sector arc length.

To create a smooth surface layer, the sector length was required to begin half way along the length of the curve. As such, the half curve length was calculated:

$$\begin{gathered} Curve\ Length = \left(\frac{2\ \pi\ r}{4}\right) \\ \left(\frac{2\ \pi\ 11}{4}\right) = 17.278\ mm \\ \frac{17.278}{2} = 8.639\ mm \end{gathered} \tag{26}$$

The angle of the sector could then be derived from the area and length:

$$\begin{gathered} Sector\ Angle = \frac{Sector\ Area}{\pi\ r^2} \\ \frac{9.815}{\pi\ 8.639^2} = 7.534° \end{gathered} \tag{27}$$

Hence, the arc length could be calculated:

$$\begin{gathered} Sector\ Arc\ Length = \frac{Sector\ Angle}{180} \times \pi\ r \\ \frac{7.534}{180} \times \pi\ 8.6395 = 1.136\ mm \end{gathered} \tag{28}$$

The full template design could therefore be produced using the 2D plotting software in Autodesk, see Appendix for all three templates. The annotated template is seen in Figure 6.8.

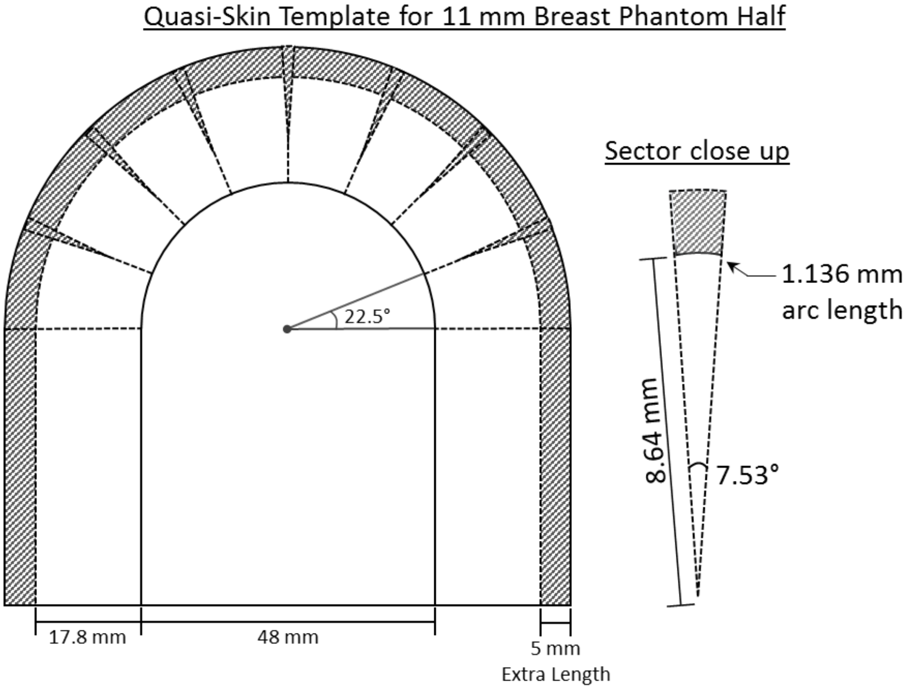

Figure 6.8: Final template for 25 mm breast phantom half quasi-skin. The dotted lines highlight the cut-out segments, with the shaded area denoting areas to be removed, including a 5 mm area of provision.

Once precisely cut to shape, the quasi-skin was affixed to the tissue, initially with double-sided tape and then more robustly with a thin layer of PDMS. This process was repeated for the 12.25 mm and 13.5 mm breast phantoms halves. The final 25 mm breast phantom can be seen in Figure 6.9.

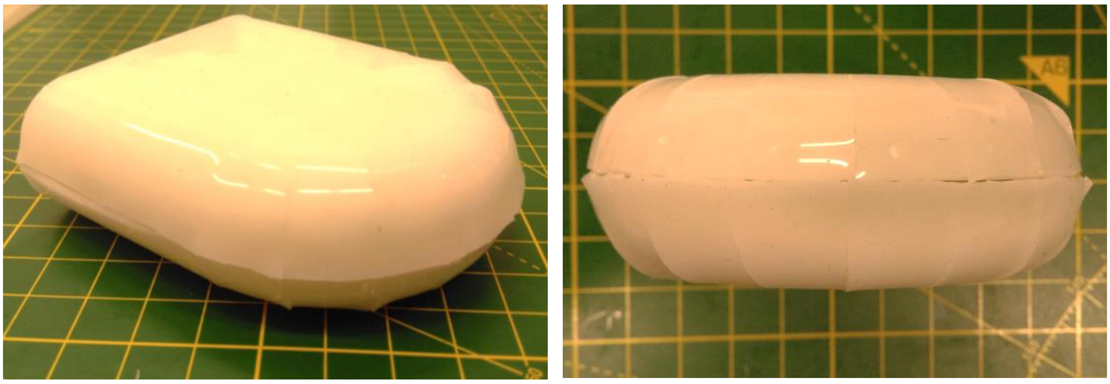

Figure 6.9: Two views of the completed 25 mm optical breast phantom, displaying the continuous nature of the quasi-skin on the surface.

6.5 Scattering and Absorbance Plots

The scaling of light scattering in terms of phantom thickness was measured in relation to pork fat and muscle tissue, as a commonly used optical phantom representative of breast tissue. Though mice are traditionally used as disease models, for toxicological and pathological studies porcine tissues are being chosen as an alternative over dog or monkey due to their similar anatomical functionalities to humans.[269,285,286]

For consistent characterisation and comparison across the materials, semi-infinite layers were produced in sections of 10 mm thickness, with an experimental standard of 1.5 mm quasi-skin also measured.

The Transmission Raman set-up, detailed in Section 7.2, and a power meter PM100D, Thorlabs (New Jersey, USA), with a 400 – 1700 nm, 500 mW, silicone photodiode power sensor, S121C, Thorlabs (New Jersey, USA) was selected for the characterisation of the phantom materials. At each thickness, several power meter measurements were recorded (6 ± 3) and averaged up to a 40 mm thickness. This value was divided by the laser power at the sample illumination point (300 mW) to calculate the logarithmic value (I/I_O) for each phantom. The results for the TiO_2/PDMS breast and skin phantoms against PTFE, and pork adipose and muscle tissue is presented in

Figure 6.10.

The grey shaded area behind each of the materials denotes the highest and lowest intensity measurements at each thickness point. Variability between measurements was considerably higher for all pork tissue samples, with the PTFE and TiO_2/PDMS phantoms remaining largely consistent throughout testing. However, due to the variability of measurements of highly scattering materials the quantity of light detected by the power meter either great, as with the 1.5 mm skin phantom, or very little, with the breast phantom at 40 mm. This leads to inconsistencies. Another factor leading to variability is the nature of the material. Unlike the rigid polymer structure of PTFE, pork tissues are inherently disorganised, leading to a wide-ranging measurement catchment.

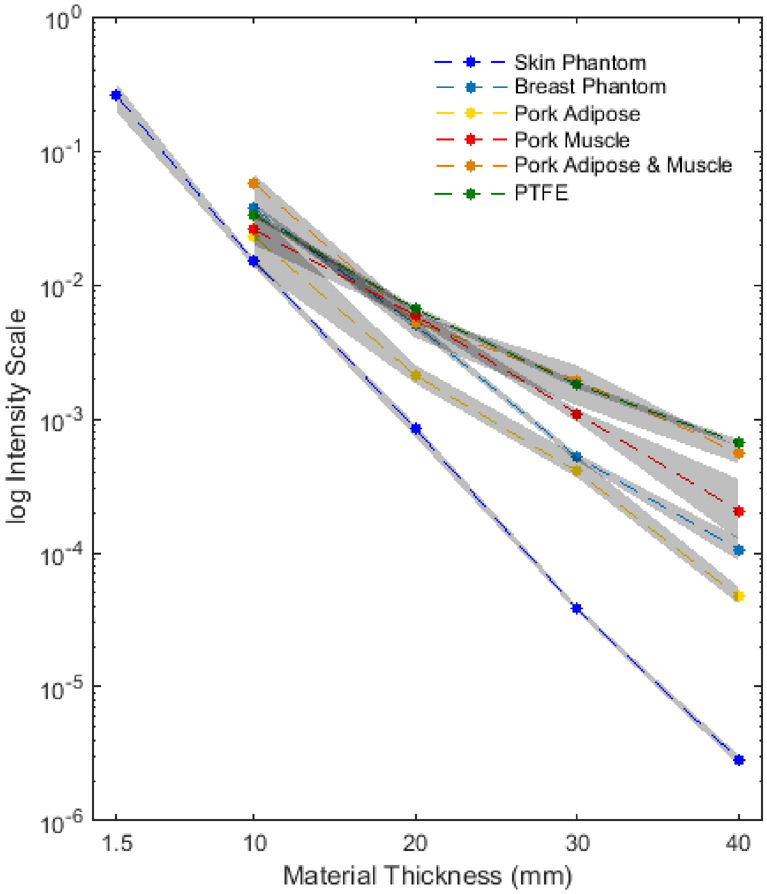

Figure 6.10: A logarithmic intensity scale graph of the breast and skin phantoms, ranging in thickness from 1.5 to 40 mm, against PTFE, and a combination of pork adipose and muscle. The shaded grey areas map the highest and lowest intensity points for each of the materials power meter measurements.

At a 10 mm thickness, the breast tissue phantom closely optically matches density of the pork muscle. As the thickness increases to 40 mm, the values trend towards the pork adipose measurement. This is representative of post-menopausal breasts at variable sizes – with an overall increase in breast thickness, the ratio of glandular to adipose tissue increases, trending towards "fattier" breasts. The skin phantom values are of a greater optical density than either the pork fat or muscle, as expected with the highly scattering characteristics. The absorbance of the PDMS at increasing mg/g concentrations of TiO_2 was also assessed using the UV/Vis

Spectrophotometer, details of which can be found in Section 5.2. The results are displayed in Figure 6.11.

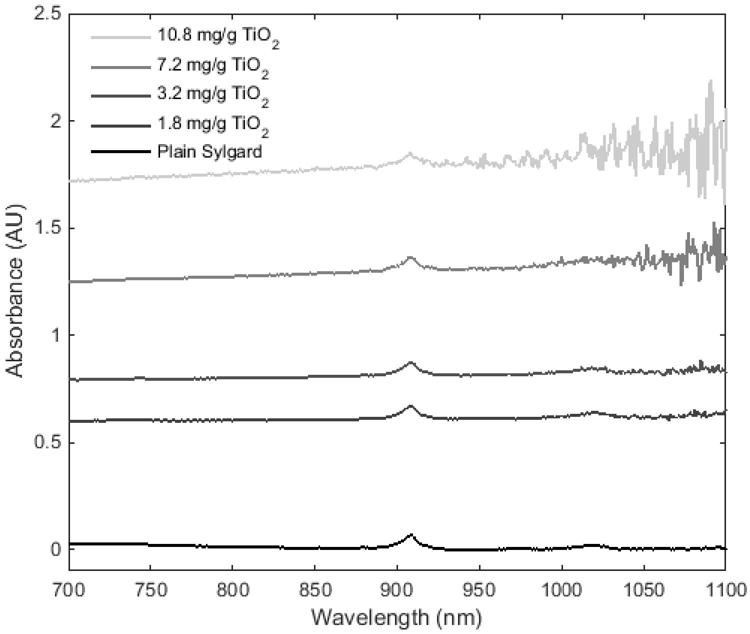

Figure 6.11: Absorbance spectra of Sylgard with increasing quantities (mg/g) of TiO_2 within the PDMS. The inherent absorbance of plain PDMS is minimal at around 0.001, with an absorption peak at 908 nm. The scattering nature of the TiO_2 causes the absorbance intensity to increase.

The absorbance of plain PDMS (Sylgard 184) is minimal, extending above 0.01 AU at two separate points – a peak at 908 nm and a smaller "extended" peak area across 1008 – 1030 nm. These inherent absorbance peaks remain with the addition of TiO_2 (mg/g) to the PDMS, with an overall trend of an increasing absorbance value due to the highly scattering nature of the material.

6.6 Discussion and Conclusions

An understanding of the inherent material properties of the PDMS and how the concentration of TiO_2 determines the characterisation of the phantom for both post-menopausal breast tissue and skin tissue optical properties were explored. The PDMS material desirable qualities of higher optical stability and prolonged shelf-life, comparative to liquid phantoms, dictated its use as the scattering agent vehicle.

The relation of the phantom logarithmic intensities in comparison to porcine adipose and muscle tissue values confirmed the desired optical properties had been met for each. The skin phantom displayed the desired highly scattering properties, whilst the breast phantom had a low level of absorption and scattering matching closely to the values of the pork adipose tissue. This denoted optical property matching comparable to that of post-menopausal breast tissue.

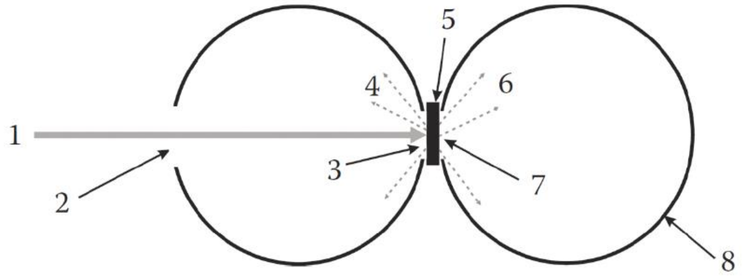

Figure 6.12: Double integrating sphere for simultaneous transmittance and reflectance measurement: (1) incident beam, (2,7) entrance port, (3) exit port, (4) diffuse reflected photons, (5) sample, (6) transmitted photons, (8) integrating sphere.[271]

Calculation of the absolute absorption and reduced scattering coefficient values of the phantoms can be made using of a single or double, visualised in Figure 6.12, integrating sphere, determining the total transmittance and reflectance of a sample.

This technique requires the use of a microtome, as the sample thickness must be reduced to one MFP length, or 0.1 mm. Structural integrity of the material post-microtome is a major area of concern, with possible weak or breakage points being incorporated into the sample. Furthermore, the mathematical modelling of the phantom optical properties requires the use of the inverse adding–doubling algorithm within a robust Monte Carlo simulation.[107] This level of optical density specificity was beyond the scope of this thesis. Unlike the sourced values of μ_a and μ_s', there is limited transferability of published results from single/double integrating sphere studies.

To gain smoother depth transition possibilities, the dimensions of semi-infinite phantom sections could be reduced to a 2 mm thickness. This however brings inconsistencies into phantom reproducibility, which is more easily avoidable with the manufacture of ≥5 mm sections. Additional layers of subcutaneous adipose tissue between the skin and breast tissue would add another dimension of realism to the phantom. The adoption of a spin-coating technique, as used by Lurie et al in the creation of bladder phantoms, could be adopted to circumvent pouring discrepancies and establish additional tissue (glandular/adipose) layering.[272] Moreover, future work into manufacturing phantoms with tumour or microcalcification occlusions present, as with 3D anatomical training models, could also be investigated. This level of phantom manufacture did not fall within the remit of possibility for this thesis.

Additional absorption properties derived from the inclusion of India Ink within the phantom was not explored within this thesis. Undoubtedly this is an area which could be improved upon. Furthermore, changing the absorption properties of the skin layer to represent distinct levels of pigmentation would increase phantom applicability across different races.

The effect of compression upon the breast could not be mechanically represented. This is an area of interest as compression forces may vary comparatively to stationary optical density values. This has been previously studied using freeze-thawed polyvinyl alcohol phantoms for realistic simulation of compression, however repeatability issues occurred with prolonged storage.[273]

The use of PDMS/TiO_2 phantoms within the Raman/SERS field is minimal, with turbid phantoms of this nature more widely used in the realms of X-radiation dosimetry characterisation[249,274], diagnostic imaging (both x-ray and ultrasound) studies[150,231,243,252,270], and optical coherence tomography (OCT)[262,272,275]. The incorporation of optical biomedical techniques within the current diagnostic remit is essential to ease clinical transferability. The production of morphologically representative phantoms, presented as within the imaging modality setting, is therefore key. With the foundations for the depth analysis of RR-AuNPs set, the experimental design and set-up for the two phantom types is pursued within the following Chapter.

7. SESORS of Breast Phantoms: Experimental Design

7.1 Introduction

This chapter explores the incorporation of the reporter labelled AuNPs within the turbid breast phantoms at defined inclusion positions. Point measurements of singular inclusions forms the depth intensity profile for each of the Raman reporters, whilst Raman mapping with several inclusions determines the ability to distinguish the depth position of the AuNPs in phantoms of increasing thickness. The experimental design and data analysis of such is investigated in separate Chapters – Chapter 8 and Chapter 9 respectively.

Several components and design constraints needed to be met prior to experimentation. Section 7.2 details the deep Raman Transmission set-up. Section 7.3 covers the hardware (7.3.1), software (7.3.3) and electrical (7.3.2) elements required for the design and development of an automated stage, permitting motorised and semi-autonomous transmission Raman mapping. Section 7.4 explores the theory and implementation of a dielectric bandpass filter, or "photon diode", incorporated into the experiments using purpose-designed and 3D printed instrument holders. The concentration of NPs (NPs/mL) for experimental use was adjusted and monitored in relation to previous biocompatibility dose studies, ensuring the viability of *in vivo* transferability is upheld, explored in Section 7.5. The summarisation of all sections is followed up in Section 7.6.

7.2 Deep Raman Spectroscopy – Transmission Set-Up

The system used for transmission Raman spectroscopy of large, turbid samples consisted of optics from Thorlabs (Newton, New Jersey, USA), a spectrometer from Kaiser Optical Systems (Ann Arbor, Michigan, USA), and a CCD detector array from Andor (Belfast, UK).

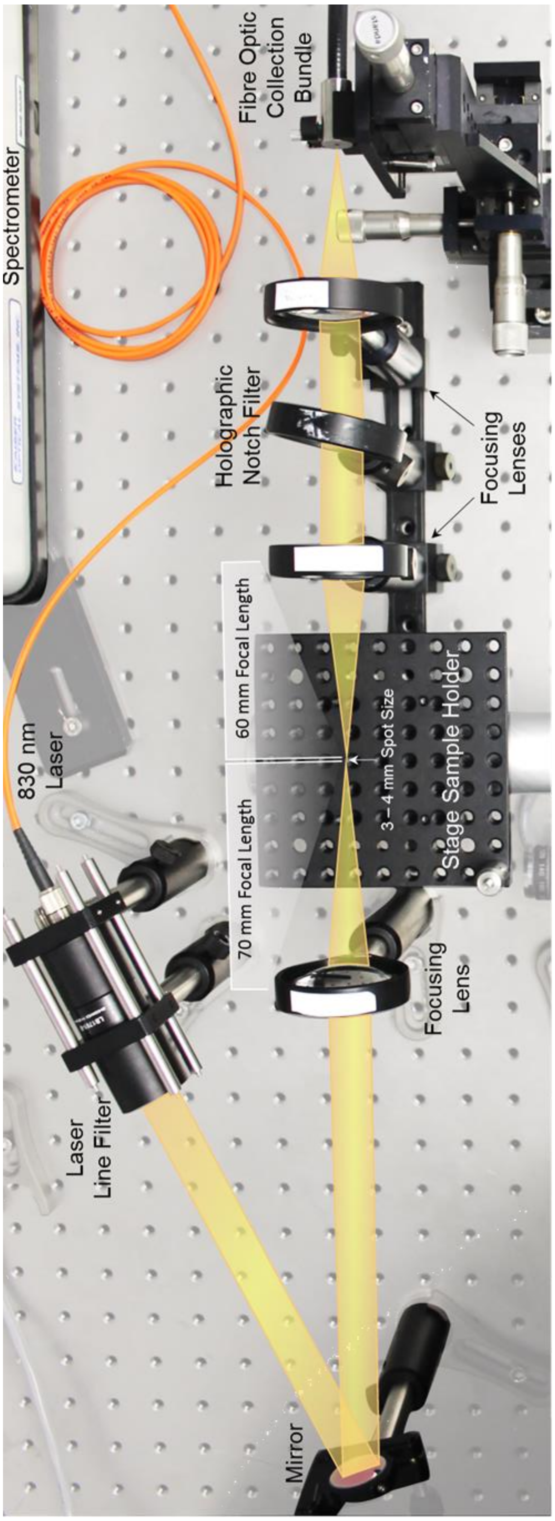

Figure 7.1: Labelled image of Transmission Raman set-up detailing the equipment used outside of the spectrometer – the 830 nm wavelength laser travels through a laser line filter, directed by a mirror through a focusing lens to the sample; transmitted scattering is focused through a notch filter before entering a fibre optic bundle leading to the spectrometer.

Unlike the micro-Raman, the initial optical set-up is completely open, allowing adjustments and versatility in sample orientation and measurement. This initial zone is depicted in Figure 7.1.

A monochromatic, 830 nm laser (Innovative Photonic Solutions), with ~300 mW sample illumination power, is used. To supress spectral deviation, laser line filters (FL830-10, Thorlabs) ensures a wavelength centred illumination source, collimated to 25 mm.

Focal lenses direct the light through the sample and to the holographic notch filter removing Rayleigh scattering. The inelastically scattered light is focused to a fibre optic collection bundle, configured in a "round to linear" formation. This increases the coupling efficiency to the spectrometer allowing a high throughput of light, retaining resolution whilst gaining sensitivity and SNR.

The spectrometer and CCD set-up is depicted in Figure 7.2. The linear collection fibre bundle is orientated to match alignment with the 100 μm entrance slit, positioned after a second holographic notch filter, removing any stray elastically scattered light which may have entered the system.

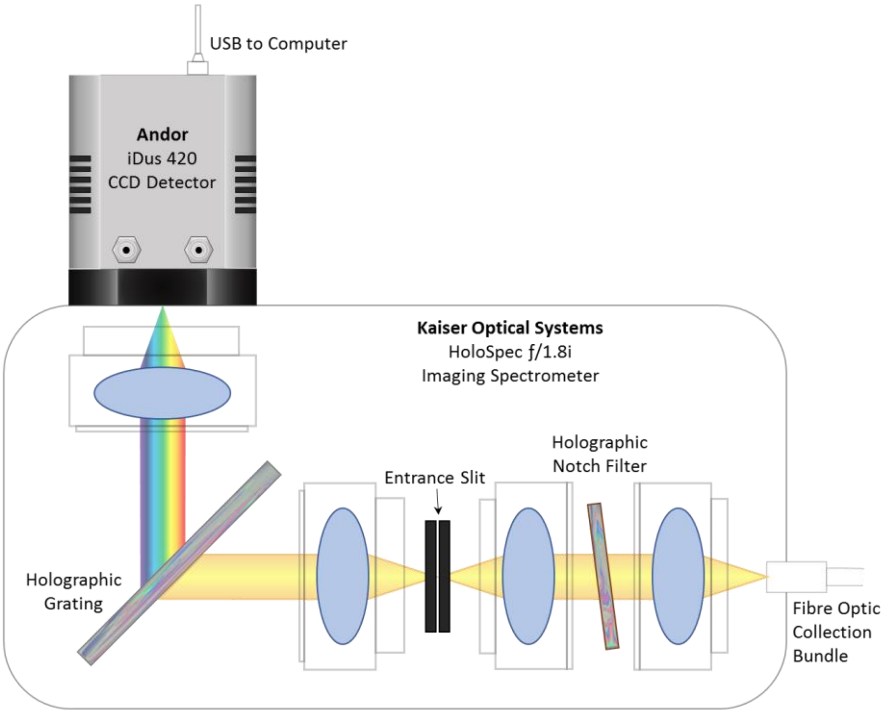

Figure 7.2: Kaiser Optical Systems HoloSpec ƒ/1.8i Spectrometer and Andor iDus 420 CCD – the collected light passes through the holographic notch filter, removing Rayleigh scattering; an entrance slit collimates the beam; a holographic grating disperses the Raman signal directly onto the CCD array.

A transmissive holographic grating is used to efficiently disperse the wavelengths of light. Spectrometer efficiency is very high. Comprised of a low f-number (1.8), with high etendue, a large fraction of the collected light can be measured. The CCD array is comprised of 1024 x 256 pixels, sized 26 x 26 μm, and is thermoelectrically cooled to -75°C. Deep deletion permits a high quantum efficiency, whereby the likelihood of photon to photoelectron production is at a peak of 95%.

Prior to single-point measurements or mapping, the system is calibrated using the characteristic spectral peaks of pure aspirin (acetylsalicylic acid). The intensity of the laser at both the immediate illumination point and sample illumination point was collected using a **power meter**, PM100D, Thorlabs (New Jersey, USA), with a 400 – 1700 nm, 500 mW, silicone photodiode power sensor, S121C, Thorlabs (New Jersey, USA). The data was logged for quality assurance purposes.

An **infrared conversion viewer**, IRV2, Laser2000 (Cambridgeshire, UK), was used for necessary optical realignment and through the deep Raman experiments to ensure laser position upon the turbid samples.

7.3 Stage Set-Up and Automation

7.3.1 Hardware – Optomechanical Stage Set-Up

To map the AuNPs positioned within the phantoms required the design of an x,y movement motorised stage (Standa, Lithuania) with an adaptable sample holder attachment for versatility. Prior to purchase, the required optomechanical components (Thorlabs, New Jersey, USA) were mapped out using SolidWorks, as in Figure 7.3, to ensure workability within the optical constraints of the deep Raman set-up.

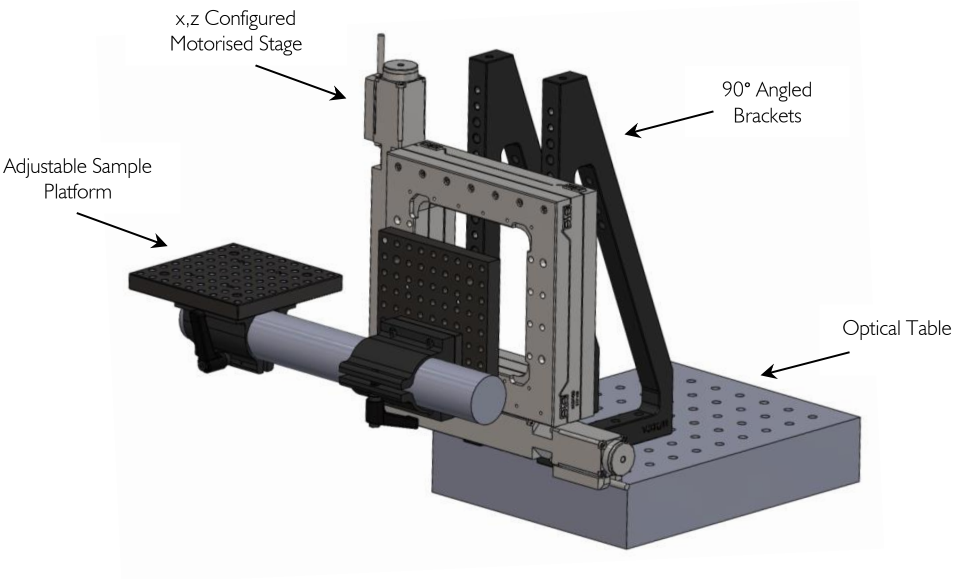

Figure 7.3: Solidworks curated, digitally planned stage design schematic of the motorised stage (Standa, Lithuania), in light grey, configured to an x,z movement range utilising angled brackets (Thorlabs, New Jersey, USA); other optomechanical components (Thorlabs) were used in the creation of the adaptable sample platform. The design is laid out as if upon the optical table.

After physical stage set-up, the mechanisation of external CCD triggering in response to stage movement was required. This would allow automated Raman mapping, requiring only the computerised set-up prior to Raman measurement.

7.3.2 Electrical Hardware – 5V Pulse Amplifier

Getting the stage to "speak" to the CCD required some electronics and circuitry building. Using a multimeter, the voltage of the initial pulse from the stage registered at 3.29V. To trigger a spectral capture response, the CCD required a pulse of ~5V. Hence, an n-p-n transistor diode, consisting of silicon doped with boron/aluminium (p-type) sandwiched between arsenic/phosphorus doped silicon (n-type) was used. Triggering the gate with the initial stage pulse enabled the higher potential difference (4.84 V) applied to the terminals of the transistor to be applied to the external CCD trigger. The circuit design in principal and actuality is seen in Figure 7.4.

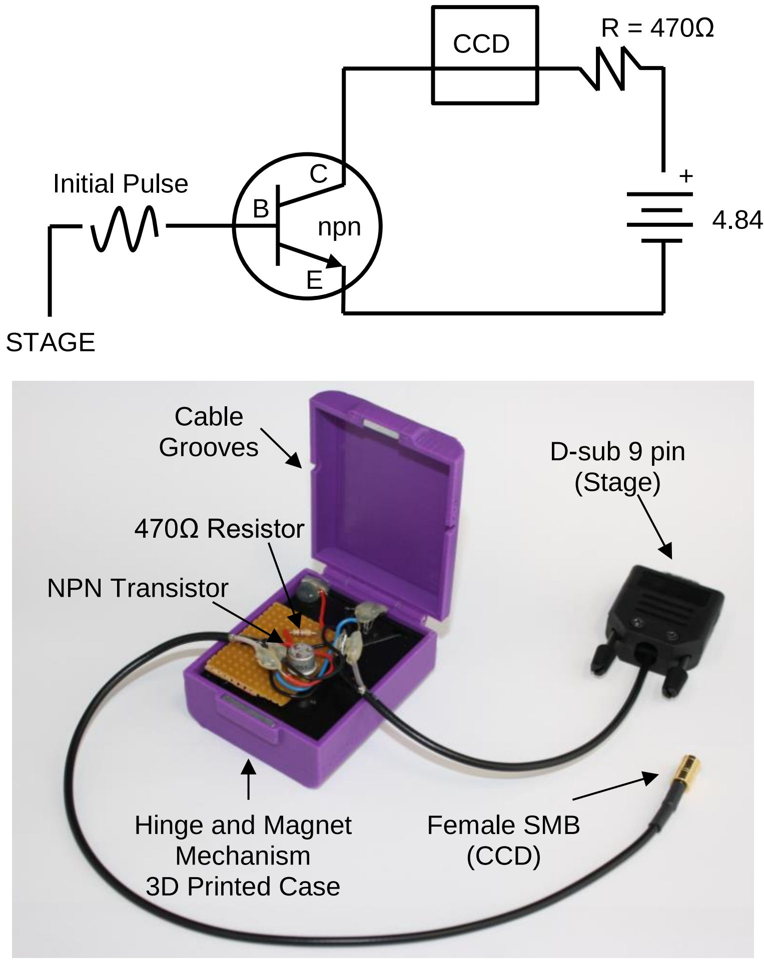

Figure 7.4: Top image: circuit design of the 5V pulse amplifier. The npn transistor connects to 4.84V from 3 AA batteries, with a resistor, R, of 470Ω was used for impedance. Bottom image: the completed pulse amplifier circuit within the 3D printed box with a hinge and magnetic closing mechanism. The electronic components were soldered onto a copper circuit board. A battery pack was used to keep the AA batteries together. Once the connector cables were soldered, a dab of hot glue was applied for longevity.

When connected to three AA batteries, forming 4.84V, and a 470**Ω** resistor, creating impedance strong enough to protect the transistor and circuitry, a pulse amplification strong enough to trigger the CCD was garnered. After initial circuit testing using a breadboard with LED output substitutes, the components, cables and battery pack were soldered to a copper circuit board. The configuration for the D-sub 9 pin stage connector was soldered to the synchronisation output (8) and ground (9) pins. A 3D printed box housing the circuit and battery pack was designed and manufactured, encapsulating the circuitry with the female SMB and D-sub 9 pin able to freely connect to the CCD and motorised stage, respectively.

7.3.3 Software – Andor SOLIS and Matlab Programming

Mapping of the desired area under specific acquisition measures were parameters required to be adjustable for flexible use of the automated stage. Internal programming within the Andor SOLIS for Spectroscopy software and an outward Graphical User Interface (GUI) MATLAB program were developed to define the measurement and stage movement specifications respectively. An example of the two programs can be seen in Figure 7.5.

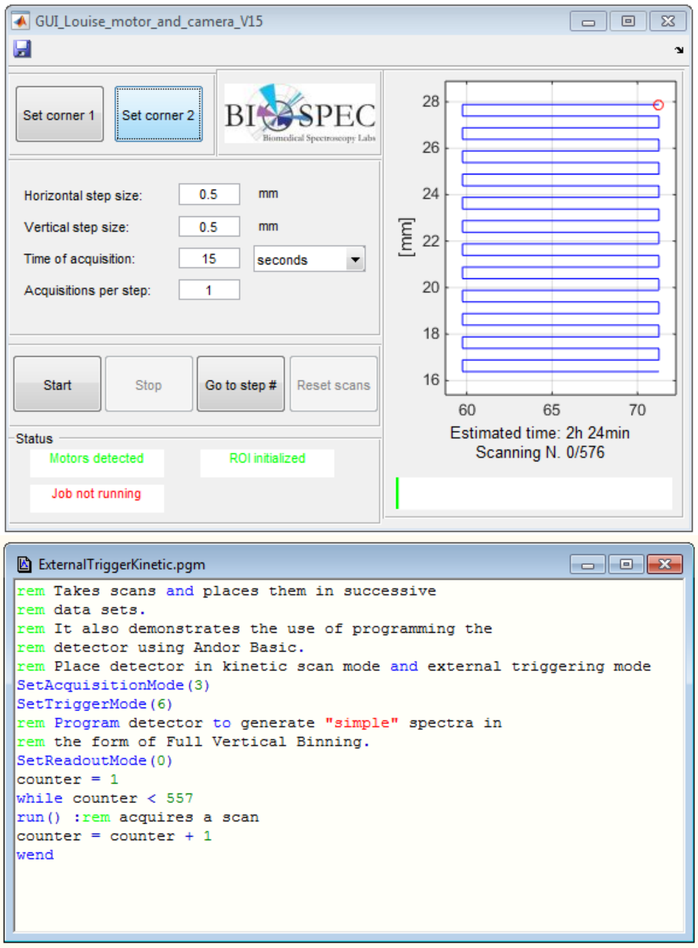

Horizontal step size: 0.5 mm
Vertical step size: 0.5 mm
Time of acquisition: 15 seconds
Acquisitions per step: 1

Estimated time: 2h 24min
Scanning N. 0/576

```
rem Takes scans and places them in successive
rem data sets.
rem It also demonstrates the use of programming the
rem detector using Andor Basic.
rem Place detector in kinetic scan mode and external triggering mode
SetAcquisitionMode(3)
SetTriggerMode(6)
rem Program detector to generate "simple" spectra in
rem the form of Full Vertical Binning.
SetReadoutMode(0)
counter = 1
while counter < 557
run() :rem acquires a scan
counter = counter + 1
wend
```

Figure 7.5: An example of the MATLAB GUI program and internal Andor SOLIS program for kinetic mapping from an external start trigger source.

The MATLAB program observes the translation range limits of the motorised stage. When the stage is positioned at the uppermost distal point of the desired map area, the button "Set Corner 1" is pressed. The lowermost point in diagonal relation is manually translated to where "Set Corner 2" is pressed, applying the blue line-raster within the GUI map area under the set horizontal and vertical step size. The red circle defines the current position of the stage, with the estimated mapping time length and number of scanning points detailed below.

The acquisition parameters, measurement time, number of accumulations and auto-save file names, are defined within the main Andor software. The curated internal program defines the trigger as an external source [SetTriggerMode(6)] and ensures the acquisition is run under the kinetic scan mode [SetAcquisitionMode(3)]. The kinetic scan mode required the pulse amplifier start signal to be used to begin the scan, rather than at every scan point. This reduced the amount of electrical noise within the system, increasing the sensitivity and hence SNR of the collected spectra.

The number of scanning points, plus one, is entered within the run counter ensuring the whole of the map scan points are saved. The "Time of acquisition" within the GUI is adjusted with extra 1 second time length to ensure the measurement is complete prior to stage movement.

7.4 Photon Diode

7.4.1 Background and Theory

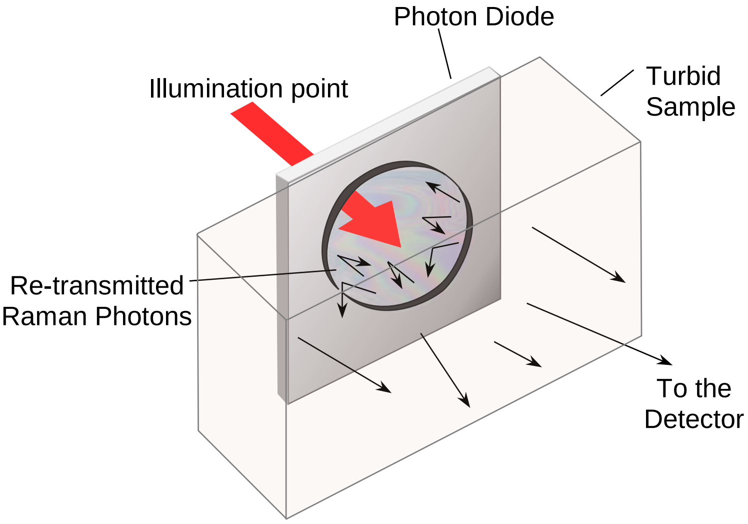

Figure 7.6: Diagrammatic of the dielectric bandpass filter, or photon diode, in transmission against a turbid sample. As seen, photons rarely pass back through the unidirectional mirror which retransmits most Raman photons to the detector.

The use of a dielectric bandpass filter, or photon diode, enables light which has been backscattered at an acute angle to the laser source to be reflected back into the system.[276–278] This increases the number of interacting light photons and hence the potential for Raman signal to be collected.

A 25-mm photon diode centred at 830 nm with a bandwidth of 3.2 nm, Max Laser Line Filter LL01-830-25, Semrock (New York, USA) was placed over the laser beam deposition area on the sample. The filter has a transmission at 830 nm of >90%.[265] If the angle of incidence changes, the wavelength of light possible to pass through the filter is shifted, as seen in Figure 7.7. Keeping the photon diode perpendicular to the optical axis is important in enabling maximum laser transmission and off axis backscattered reflection.

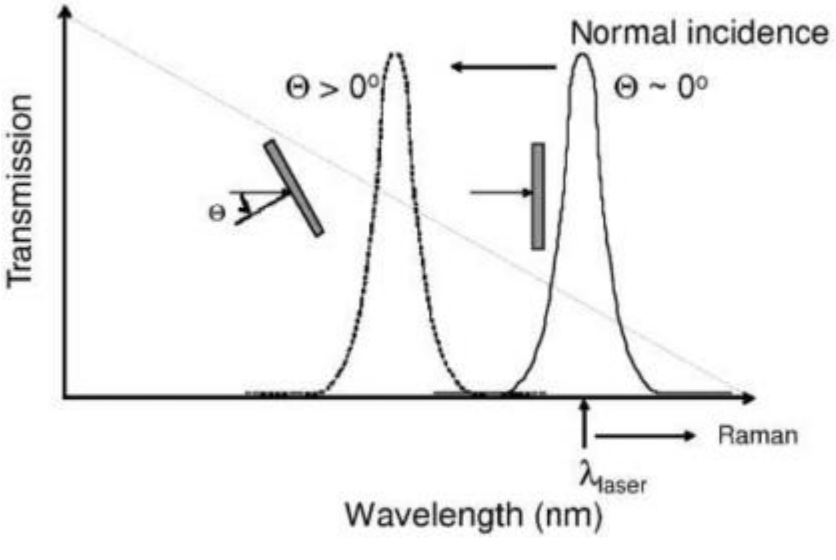

Figure 7.7: A graph to show the importance of the photon diode remaining perpendicular to optical axis: transmission versus wavelength for normal and oblique incidence, whereby the wavelength shifts with a change in angle.[265]

Minimal air-gap interface between the phantom and photon diode is another key aspect. The majority of laser photon losses occur at the air-sample interface, which increases with highly scattering samples.[277] As such, positioning the photon diode with a minimal air-gap interface to the optical phantom reduces unwarranted photon loss, increasing the effectiveness of the technique.

7.4.2 3D Printed Photon Diode Holders

As discussed, the key factors in ensuring optimal photon diode use include a constant perpendicular angle to the optical axis, and a very minimal air-gap interface. To ensure both factors were consistently met for individual point spectra and mapping purposes, photon diode holders were designed in Autodesk Inventor and manufactured using the MakerBot and Form 2 3D printers.

The point measurement photon diode holder was designed to securely slide onto the base component of the motorised stage arm. This was then locked into place on the underside of the platform base using two sets of nuts and bolts, as seen in Figure 7.8. The motorised stage was configured to an x,y formation, allowing the focal length to be adjusted depending on the phantom thickness.

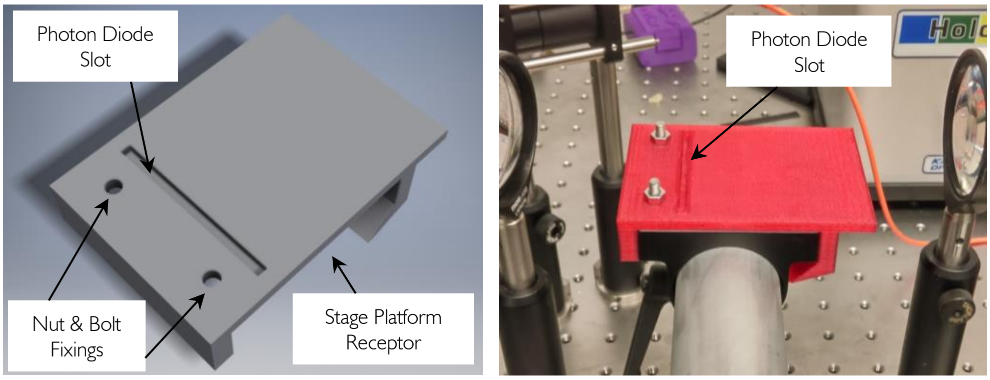

Figure 7.8: Left image: The point-measurement photon diode holder designed in Autodesk Inventor. The gully slot measures 4 mm in depth, safely securing the photon diode; Right image: The 3D printed holder slid into place on the x,z motorised stage arm and secured with two sets of nuts and bolts.

As shown in Figure 7.9, levelling of the holder platform was ensured using a bidirectional spirit level, and the 90° position of the photon diode checked with a metal rule. This design did not require any extra fixings to hold the photon diode at a constant perpendicular angle.

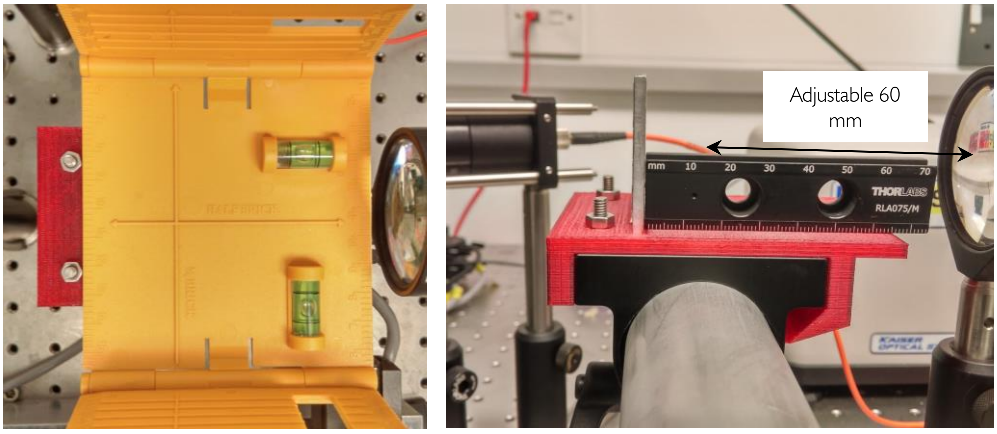

Figure 7.9: Left image: bidirectional spirit level confirming the stage platform is balanced; Right image: the photon diode positioned within the slot – the solid metal rule confirms the 90° angle of the photon diode. The x,y motorised stage allows the 60 mm focal length to be adjusted dependent on phantom thickness.

On the other hand, the mapping photon diode holder was required to remain in a fixed position within the optical axis, without interference of motorised stage movement. Hence, the model was designed to affix atop an optomechanical post using a screw within a counter bored hole. This eliminated illumination path interference. The optical post was secured to the optical rail between the two focusing lenses, affront the breast phantom.

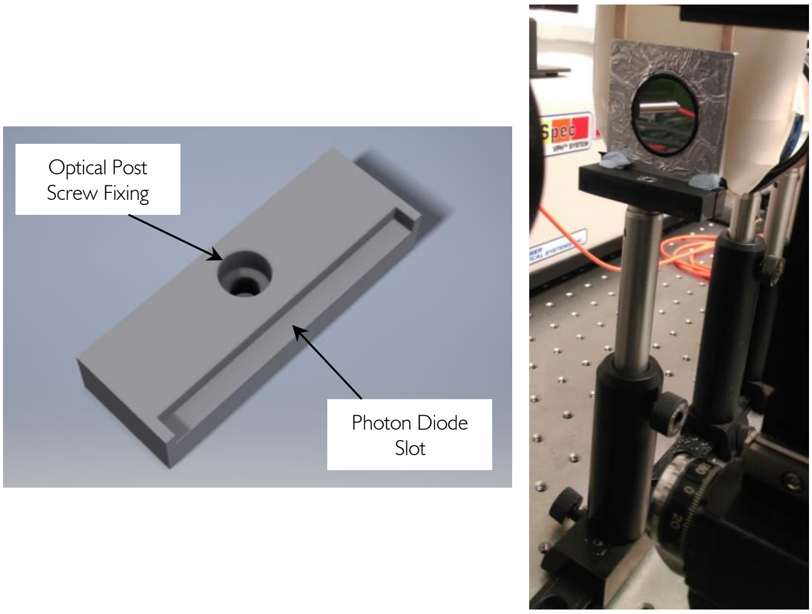

Figure 7.10: Left image: The mapping photon diode holder designed in Autodesk Inventor. A counter bore was designed to accommodate the cap head of the screw into the optical post. The 25 x 3.5 mm recess encompasses three sides of the photon diode, allowing a minimal air gap phantom interface; Right image: The 3D printed holder with photon diode secured to the optical post, in line with the illumination path. Extra blu-tack pieces were used to ensure stability.

The Autodesk Inventor design and complete set-up, including the breast phantom with a mid-centrally located NMR tube, is seen in Figure 7.10 and Figure 7.11.

Respective 3D printers were used due to the difference in the nature of the additive material. The MakerBot printer, used in the creation of the single point measurement PD holder, utilises Fused Deposition Modelling (FDM) whereby a heated plastic filament is extruded, building upon the previous additive layer.

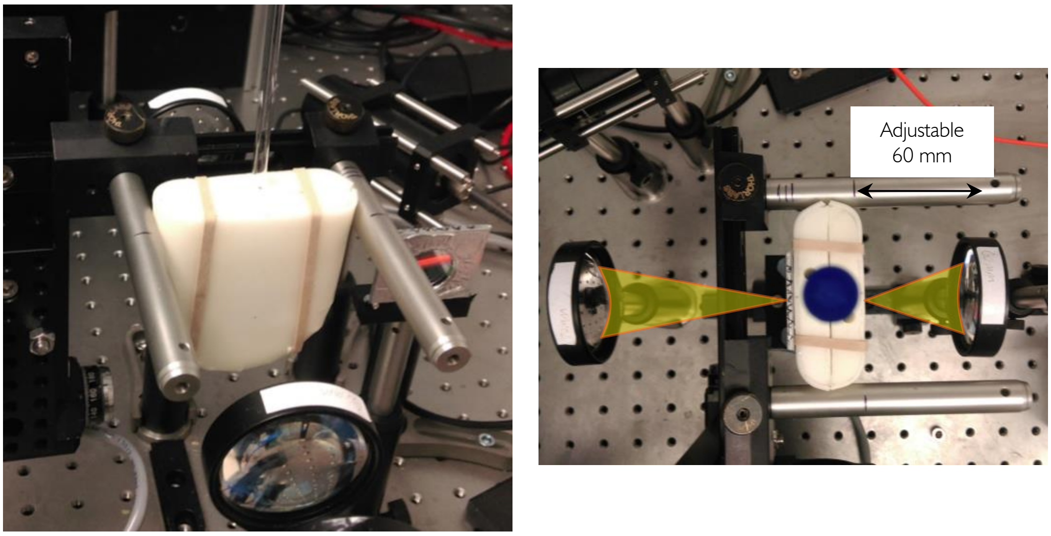

Figure 7.11: Transmission Raman set-up of the morphologically representative breast phantom including the photon diode. Left image: Two metal arms, clamped to hold the phantom in position, fixed to the x,z stage allows the full range of movement for photon diode enhanced mapping to occur; Right image: A top-down view including an NMR tube within the middle breast phantom hole. Each phantom is adjusted to adhere to the 60 mm focal length.

The mechanical properties of this macro layered structure provide a surface by which the photon diode can be inserted into a gully and “gripped” by the material, requiring no extra supportive features. Comparatively, the Form2 3D printer, for the mapping PD holder, operates using vat photopolymerisation. This method creates micro layers of hardened plastic via a UV laser projecting upon the photosensitive, liquid polymer resin. This technique provides a smooth surface finish to the build, decreasing the drag of the material across the phantom interface. Blu-tack was required against the back of the photon diode, seen in Figure 7.10, required to maintain the 90° angle between the laser and phantom interface.

7.4.3 Optical Phantom Power Meter Plots with Photon Diode

The efficiency of the photon diode against the two TiO_2/PDMS phantom types of skin and breast tissue, seen in Figure 7.12.

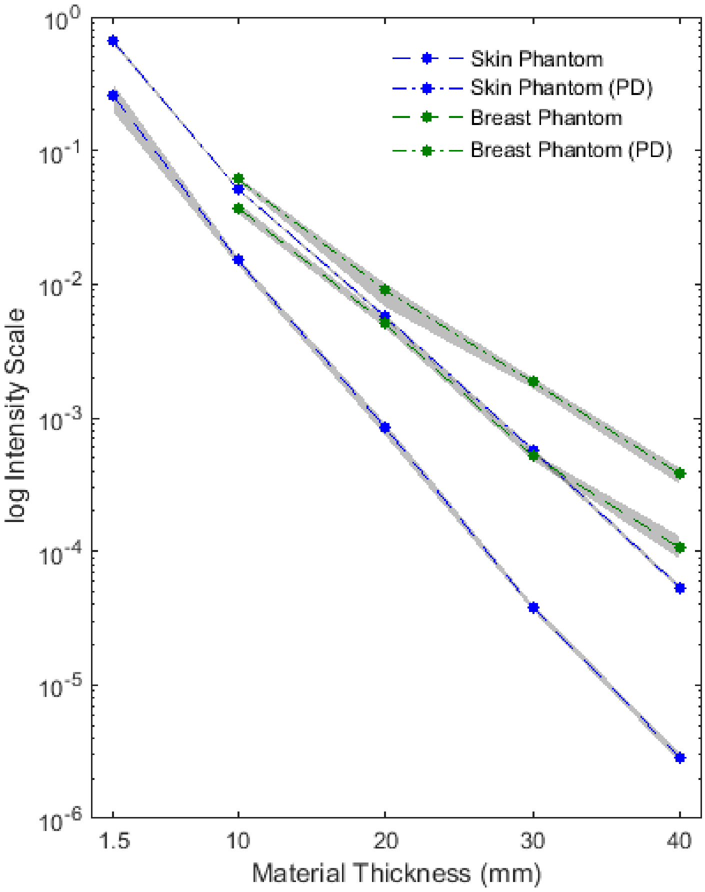

Light Transmission Increase with Photon Diode (%)

Width (mm) Phantom Type	1.5	10	20	30	40
Breast Tissue	N/A	61.26	80.65	258.61	236.80
Skin Tissue	152.85	132.68	588.68	1438.60	1778.62

Figure 7.12: A graph to show the logarithmic, power meter intensities of the breast and skin phantoms, with and without a photon diode, measured in transmission; and a table to show the percentage change of light intensity produced with a photon diode present. The standard laser intensity at the sample illumination point, 300 mW, was selected.

As previously discussed, at each thickness four measurements were logged, averaged, and divided by the laser power at the illumination point (300 mW) to calculate the logarithmic value (I/I_0) for each phantom, up to a 40 mm thickness. The boundaries of the grey shaded areas at each point represent the maximum and minimum values recorded. Overall, the variation in sample measurement decreases for both the skin and breast phantoms with photon diode use, with an increase in light transmission by up to 2 orders of magnitude.

7.5 AuNP Inclusions and Dose Biocompatibility

The optical phantom design required accessible and dispensable vessels for containment and positional flexibility, with the added benefit of storage ease. As such, borosilicate glass NMR tubes, ColorSpec NMR tubes (ø5 mm × 177.8 mm), Sigma Aldrich (Missouri, USA), were selected for use.

The photoluminescent nature of the 1 mm combined wall thickness of borosilicate glass, alongside quartz (a standard Raman neutral material commonly used), stainless steel (used to analyse the drop dried nanoparticles under micro-Raman), and the Raman spectrum of an Eppendorf tube, is seen in Figure 7.13.

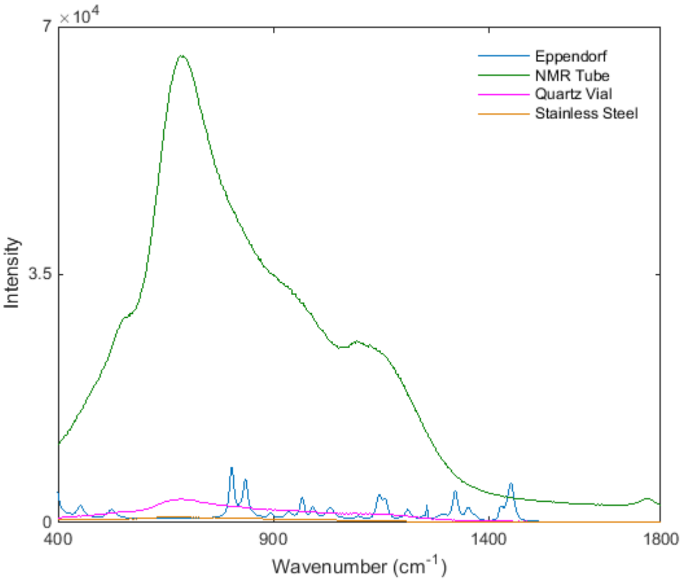

Figure 7.13: Photoluminescent and Raman (Eppendorf) spectrum of four sample holder materials – stainless steel slide was used in Chapter 6 for the micro-Raman testing of the AuNPs.

The ideal material for encasing the NPs for the following experiments would be quartz. Despite this, quartz is an impractical material comparative to the economic and replaceable nature of borosilicate glass NMR tubes. The pre-processing techniques used to reduce the spectral contribution of the NMR tube photoluminescence, increasing the SNR of the AuNPs, is discussed in Chapter 9, Section 8.2.

The ability to garner a Raman signal of the AuNPs at large depths required consideration as to the ideal NPs/mL concentration, with nanoparticle dose presenting as the biocompatible limiting factor.

Mouse model toxicology studies of PEGylated AuNPs delivered at an ~4 mg/kg dose confirmed little to no adverse growth effects, with accumulation and acute inflammation mainly sited within the liver.[176,178]

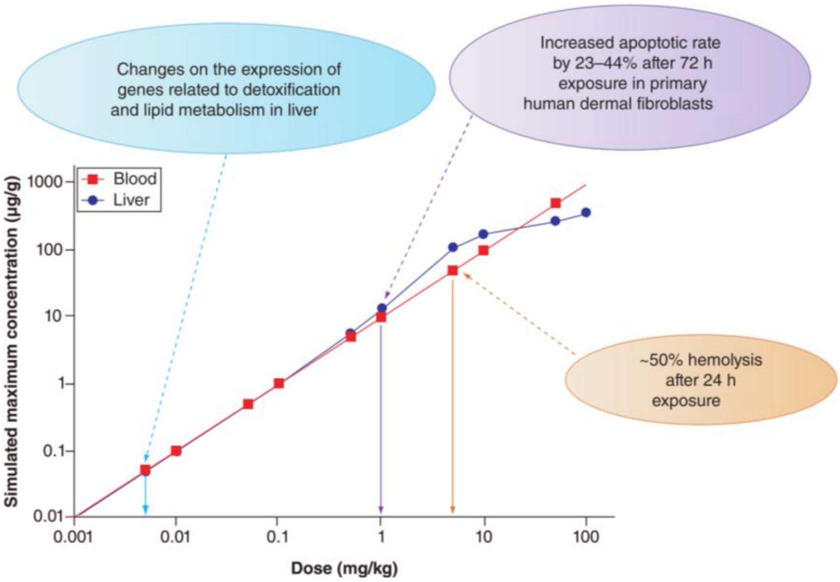

Figure 7.14: In vitro to in vivo extrapolation and species extrapolation of doses and toxicity of gold nanoparticles. Blue and red lines represent model-predicted maximum concentrations of gold nanoparticles in the liver and blood, respectively, of humans after intravenous injection (0.001–100 mg/kg). The dashed arrows point to where liver toxicity (0.01 mg/kg) was observed in rats (blue); in vitro cytotoxicity (13 µg/ml) of primary human dermal fibroblasts (purple); and haemolysis (50 µg/ml) of red blood cells (orange). The solid arrows point to the model-predicted human equivalent dose (HED) associated with the reported in vitro cytotoxicity (HED = 1 mg/kg), haemolysis (HED = 5 mg/kg) and in vivo toxicity (HED = 0.005 mg/kg). Adapted from[167]

Due to the similarity in liver to body weight ratio, the results from rats and pigs is considered to have a greater transferability to humans. As such, dose models and the related toxicological effects adapted from the review by Lin et al have been selected as reference for the study. The known toxicological effects from both *in vivo* and *in vitro* experimental work of rats and human cells, and computational pig models, have been plotted to the human equivalent dose (HED), seen in Figure 7.14.[167]

Hence, it is generally considered that a low, safe AuNP HED model is ~0.01 mg/Kg. The average female body weight within the UK, at time of writing, is 70.2 Kg, relating to an AuNP dose of 0.702 mg. The concentration of the 80 nm AuNPs is 0.052 mg/mL. After depth testing for a sufficient enhanced Raman signal at a low acquisition time (10 seconds), the AuNP concentration of 0.156 mg/mL, or a dose of 0.156 mg/g, was found to be ideal. This is equivalent to 2.91×10^{10} NPs in 1.2 mL, after centrifugal concentration from 3 mL. This concentration of AuNPs is representative of the mg/mL dose required within the area the of the breast tumour.

Tumours of an ellipsoid geometry which lie between the T1/T2 classification of early breast cancer (≤2.5 cm) have been found to have a volume between 1.257 – 5.12 cm^3.[279–282] Under the assumption that tumour tissue density lies closer to that of muscle (1.057 g/cm^3)[283] than adipose tissue (0.9 g/cm^3)[284,285], the mass of a stage T1/T2 tumour is approximately 1.328 – 5.412 g. Therefore, 0.207 – 0.844 mg of AuNPs of the 0.702 mg HED would be required to accumulate within the tumour. Remaining on the conservative end of tumour volume and considering a high percentage of AuNP uptake, the experimental dose selected is sufficiently biocompatible.

7.6 Summary

Several features of the experimental design set-up required for depth analysis of the three RR-AuNPs have been outlined.

Success with the optomechanical design and automation of the translated x,y motorised stage put several skill sets to use – hardware, software and electronic circuitry were all required in the completion of the project. Automation of the mapping process allowed a rapid and efficient workflow, enabling a diversification and increase in the possible work load one could undertake – an unavailable luxury prior to the design and implementation of the pulse amplifier and GUI mapping system. This automated design may be taken as a protocol for future mapping systems within open optical set-ups.

The benefit of photon diode use lies within the preservation of laser photons within the system, increasing the likelihood of Raman photon creation and hence transmission to the collection system and the CCD. The purpose designed 3D printed PD holders were manufactured with two key factors in mind – the need for a constant perpendicular angle to the optical axis, and a minimal air-gap-interface. The design of the singular point measurements successfully meets both criteria. The technicalities introduced with mapping (requirement of a fixed position isolated from stage movement; the moving phantom interface whilst mapping; staying in-line with the optical axis whilst avoiding unwanted interaction with the stage) presented a challenge. The trade off in material properties allowed the interface to smoothly traverse but hindered the security and fixed angle of the PD. This was countered with the use of fixing agents; however, a more robust design/solution could have been found.

Another possibility which could have been explored, especially with the morphologically representative phantom, would have been the use of a fully encasing uni-directional mirror.[276]

This approach could eliminate photon losses from the system, apart from at the transmission exit point. This would be an interesting idea to pursue in future works.

Optimising the RR-AuNP concentration (NP/mL) required consideration of a biocompatible, low dose model, whilst garnering an enhanced Raman signal at depth. These measures were met with a tumour specific dose of 2.91×10^{10} NPs in 3 mL, equating to a maximal dose of 0.012 mg/Kg, remaining within the remit of a low HED model.

Replaceable RR-AuNP inclusions were implemented with the use of borosilicate glass NMR tubes. The photoluminescent contribution to the spectrum of these NMR tubes can be eliminated, along with cosmic rays and inherent background noise, using pre- and post-processing techniques. This improves the SNR, "amplifying" the inherent RR-AuNP signal. The techniques applied for this purpose, and the resulting analysis of the experimental findings, are discussed in the next Chapter.

Experimental Results

SESORS of Breast Phantoms: Results and Analysis

Breast Microcalcification Targeting Gold Nanoparticles

8. SESORS of Breast Phantoms: Results and Analysis

8.1 Introduction

Following on from the experimental design set-up from the previous Chapter, the analysis of results is discussed here forth.

Section 8.2 details the pre- and post-processing techniques used across the data, and the importance of such methods in the analysis of both point spectra and maps. The first depth profiling experimental results using semi-infinite breast phantoms of increasing thickness and a consistent AuNP inclusion step size depth is explored in Section 8.3. Section 8.4 follows on from this with the use of the morphologically representative breast phantom in a mammographically compressed state – the depth position of three 2-NT-AuNP inclusions is evaluated. The discussions and conclusions, Section 8.5, assesses the capabilities of un-targeting reporter NPs, concluding on future works necessary to develop a targeted probe for deep Raman applications.

8.2 Data Analysis: Pre- and Post-Processing Techniques

All data analysis was completed using MATLAB R2014b, The Mathworks Inc. (Massachussetts, USA) with occasional graphs plotted in Excel, Microsoft (New Mexico, USA). All PCA was completed using the research group developed MATLAB programming and GUI.

Single-point micro and deep Raman measurements are pre-processed using subtraction and baseline removal techniques, the advantages of which can be seen in Figure 8.1. The phantom spectrum undergoes **subtraction** from the AuNP inclusion measurement, allowing the spectral features of the RR-AuNPs within the NMR tube to remain. The photoluminescence garnered from the NMR tube, discussed in Chapter 8, Section 7.5, is then removed using the **baseline subtraction**. This technique uses a polynomial fit below the spectral line to remove the background noise and photoluminescence, allowing the underlying RR-AuNP spectral features to feature more predominantly.

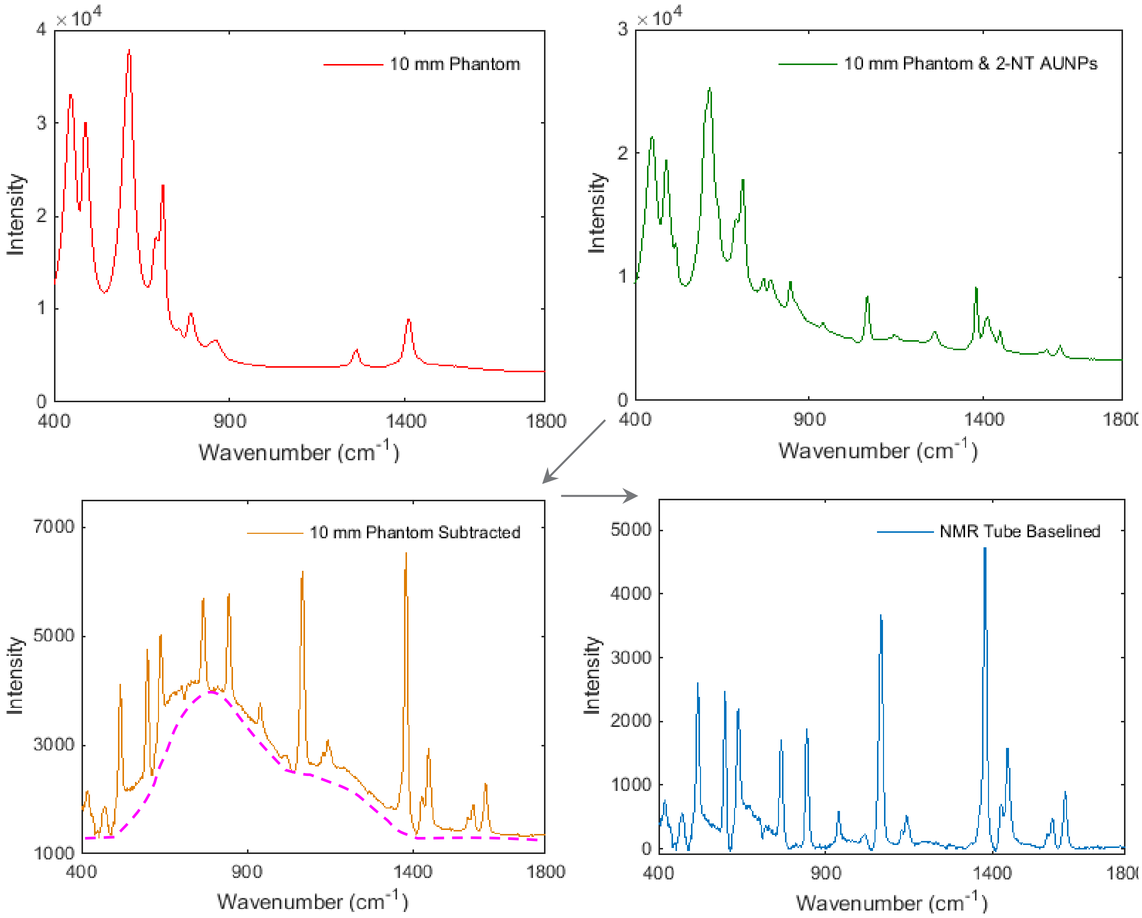

Figure 8.1: 3 mL concentrated 2-NT AuNPs within NMR tube, within 10 mm breast phantom pre-processing techniques. Top Left: the standard 10 mm breast tissue phantom spectra; Top Right: 10 mm breast tissue phantom with 2-NT AuNP in NMR tube occlusion; Bottom Left: the breast tissue phantom subtracted spectrum – the photoluminescence from NMR tube within the can be seen, with the polynomial baseline subtraction represented by the pink dashed line; Bottom Right: subtracted and baselined spectrum – the photoluminescent contribution is significantly reduced. The acquisition for each measurement was 2 seconds at 5 accumulations.

When determining the objective signal to noise ratio (SNR) of a peak intensity of a Raman band, the following equation can be used:

$$SNR = \frac{S}{\sigma_y} \tag{29}$$

whereby the average peak height above the baseline, S, is divided by the standard deviation of the peak height, σy. The SNR is most accurately calculated by acquiring several iterations of the sample spectrum for the average single peak height.[117]

Maps were pre-processed prior to multivariate analysis using a combination of a set wavenumber range, cosmic ray removal, vector normalisation and mean centring.[286] By applying a **set wavenumber range**, this reduces the size of the data set of further analysis, effectively streamlining the spectra to the wavenumber range of interest. **Cosmic ray removal** is a required technique in reducing the variance of the resulting uncharacteristic spectral spikes from the eponymous phenomenon. A 3x3 mask median filter is applied to "smooth" the peaks to the averaged neighbouring pixels. A limitation to this technique is the resulting loss of spatial resolution. **Vector normalisation** reduces the effects of sample sourced variation, such as photon path length differences or intensity fluctuations. The normalised data is then **mean centred**, calculating the mean intensity of each wavenumber within the sample spectra and subtracting the difference away, placing all wavenumbers around the zero point.

Post-processing in the form of **Principal Component Analysis** (PCA), a multivariate analysis technique, is then performed on the collected maps. PCA improves the SNR of a data set by reducing the dimensionality of the interrelated variables into their principal components (PC). A such, the first PC is the largest variant change within the data set, the second PC is the next largest change in variance, uncorrelated to the previous, and so on.[287] Each PC has a corresponding spectral loading, detailing the spectral origin of the variance, and false colour map, which plots the regional differentiation between the corresponding (bio)molecules.[288]

8.3 Depth Profiling – Semi-Infinite Breast Phantom

Acquisition parameters for the signle-point transmission Raman measurements were set at the parameters of 2 seconds and 5 accumulations, with a sample illumination intensity of 300 mW.

Initial point measurements of the 2-NT, 4-ATP and 4-MBA within the 10 mm breast phantom NMR tube inclusion are plotted in Figure 8.2. The inherent intensity of each reporter is displayed along each individual spectrum.

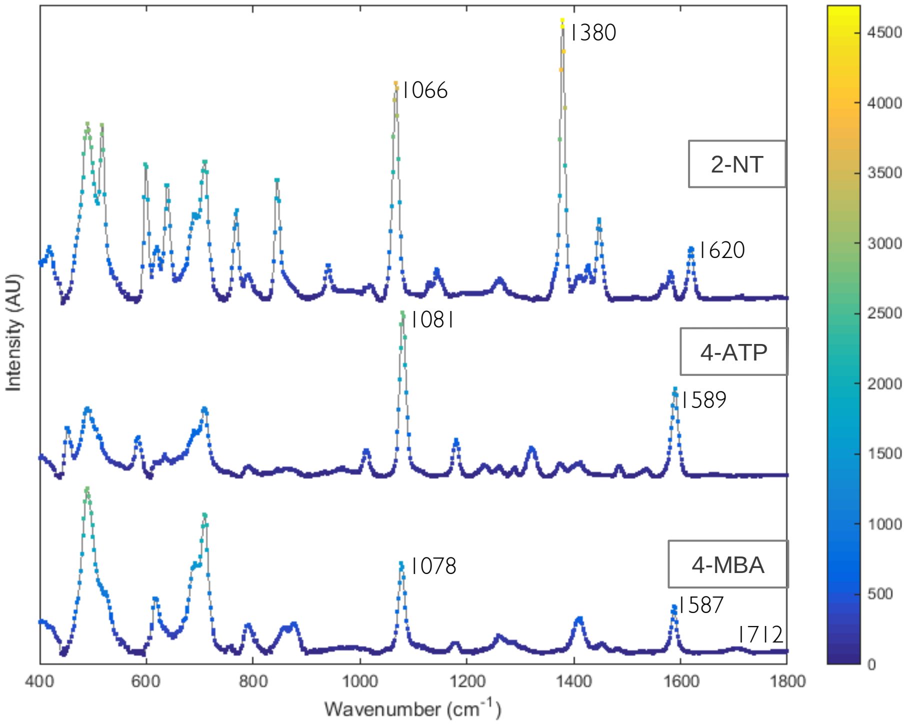

Figure 8.2: Subtracted and Raman baselined spectra of the three Raman reporter AuNPs, 2-NT (top), 4-ATP (mid) and 4-MBA (bot), within the single 10 mm breast tissue phantom block. The signal intensities plotted across each spectrum is plotted in relation to the colour bar. The acquisition for each measurement was 2 seconds at 5 accumulations.

The key characteristic peaks of each reporter are still present – with the $C = O$ stretch (1710 cm^{-1}) of 4-MBA present to further distinguish it from the 4-ATP spectrum.

Three phantom thicknesses were considered: 23, 28 and 33 mm. The position of the first inclusion was set at 6.5 mm – one 1.5 mm skin phantom layer and the 10 mm inclusion breast phantom section – increasing at a step size of 5 mm. The resulting spectra at the three (23 mm phantom thickness), four (28 mm) and five (33 mm) depth positions are plotted in the 3D graphs below. The relative peak height value of the characteristic peaks was collected using the Measure Peak MATLAB function, see Appendix for the code, and annotated upon each plot, with the resulting depth intensity profile line-plotted in black across the spectra.

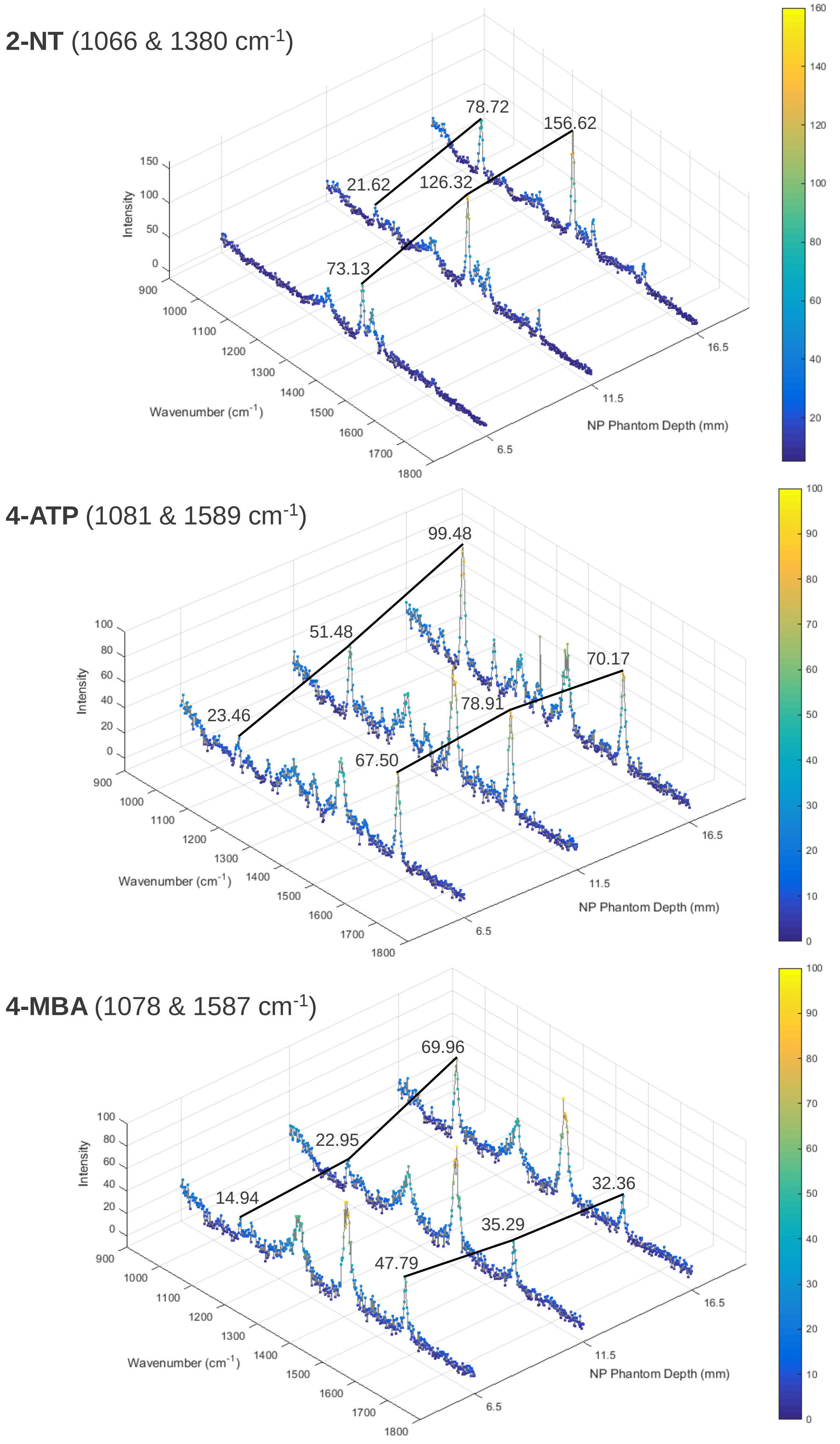

Figure 8.3: Raman spectra of 2-NT (top), 4-ATP (mid) and 4-MBA (bot) AuNPs within 23 mm of breast phantom at 5 mm intervals towards the detector. Signal intensity of the spectral peaks is plotted in relation to the colour bar. The signal intensity depth profile of characteristic peaks determined by the relative peak height is line mapped.

At 23 mm, Figure 8.3, the depth intensity profiles for each of the RR-AuNPs vary in characteristic peak ratio. The depth profiles of the higher wavenumbers (1380, 1589 and 1587 cm^{-1}) differ for each of the RR-AuNPs – the greatest signal intensity is at full depth for the 2-NT, mid-depth for 4-ATP and least depth for the 4-MBA. Conversely, the low wavenumber peaks (1066, 1081 and 1079 cm^{-1}) having comparatively lower overall signal intensity, all gain in intensity with depth progression.

At the 28 mm phantom thickness, Figure 8.4, the lower wavenumber intensity profiles remain consistent as before. The greater wavenumber intensity profile, however, forms a elongated "U" shape, whereby the signal intensity at the front-mid position (11.5 mm depth) sits at the lowest most point. This signal intensity profile is similar to the findings of Vardaki et al in which the transition of Trans-Stilbene (TS) through an Intralipid phantom presented a higher Raman intensity at the foremost and distal positions of the TS, with a decreased signal across the middle of the phantom.[289] The position at 21.5 mm garners the greatest signal intensity for the 2-NT and 4-ATP; the 4-MBA, however, has a loss of intensity at this point, aligning back to the standard characteristic peak ratio, as seen in Figure 8.2.

At a depth of 28 mm, the signal from 4-ATP and 4-MBA decreases dramatically. The increased Raman signal achieved from the 2-NT RR-AuNPs allowed depth measurements up to 33 mm, hindered by a reduction in SNR.

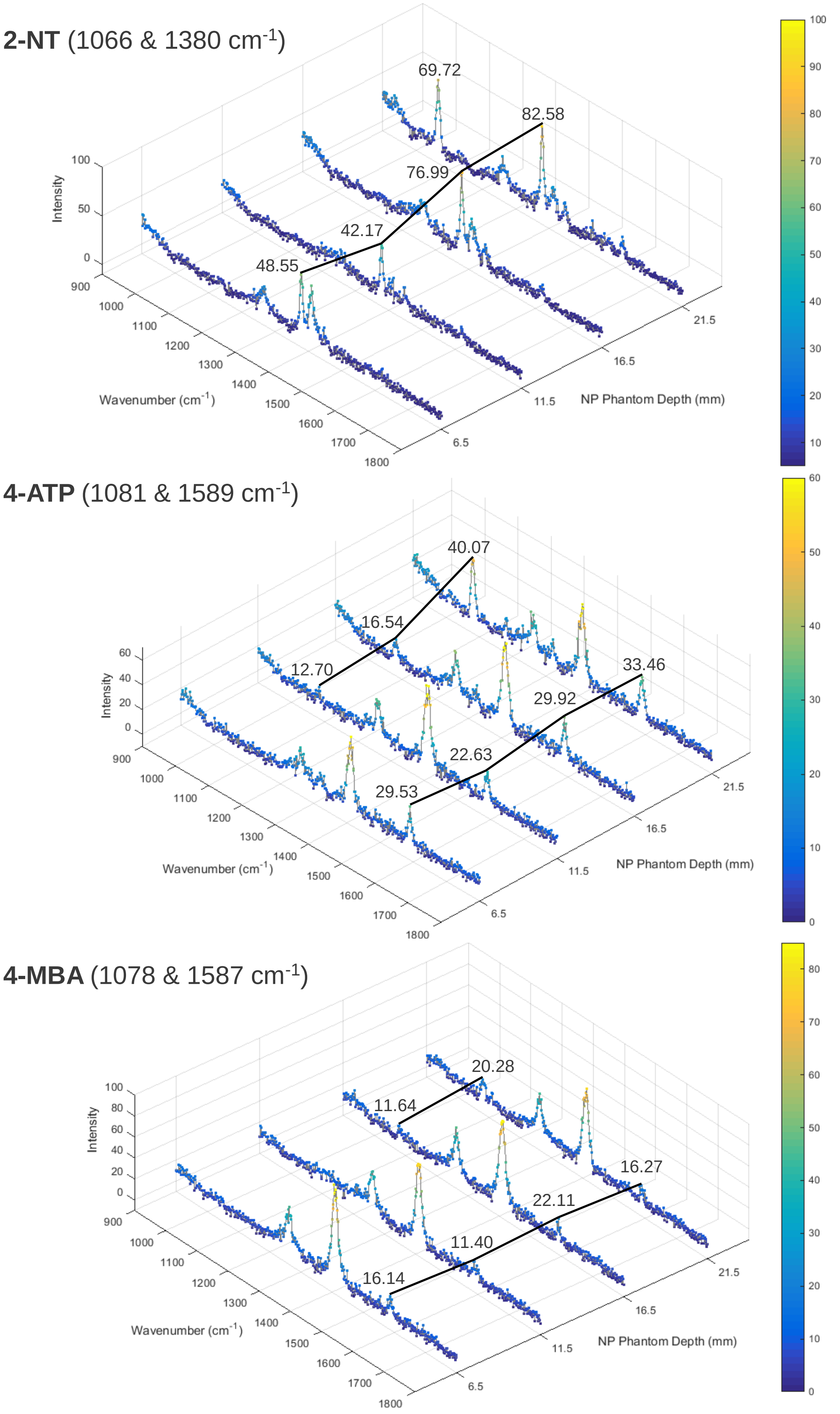

2-NT (1066 & 1380 cm^{-1})

4-ATP (1081 & 1589 cm^{-1})

4-MBA (1078 & 1587 cm^{-1})

Figure 8.4: Raman spectra of 2-NT (top), 4-ATP (mid) and 4-MBA (bot) AuNPs within 28 mm of breast phantom at 5 mm intervals towards the detector. Signal intensity of the spectral peaks is plotted in relation to the colour bar. The signal intensity depth profile of characteristic peaks determined by the relative peak height is line mapped.

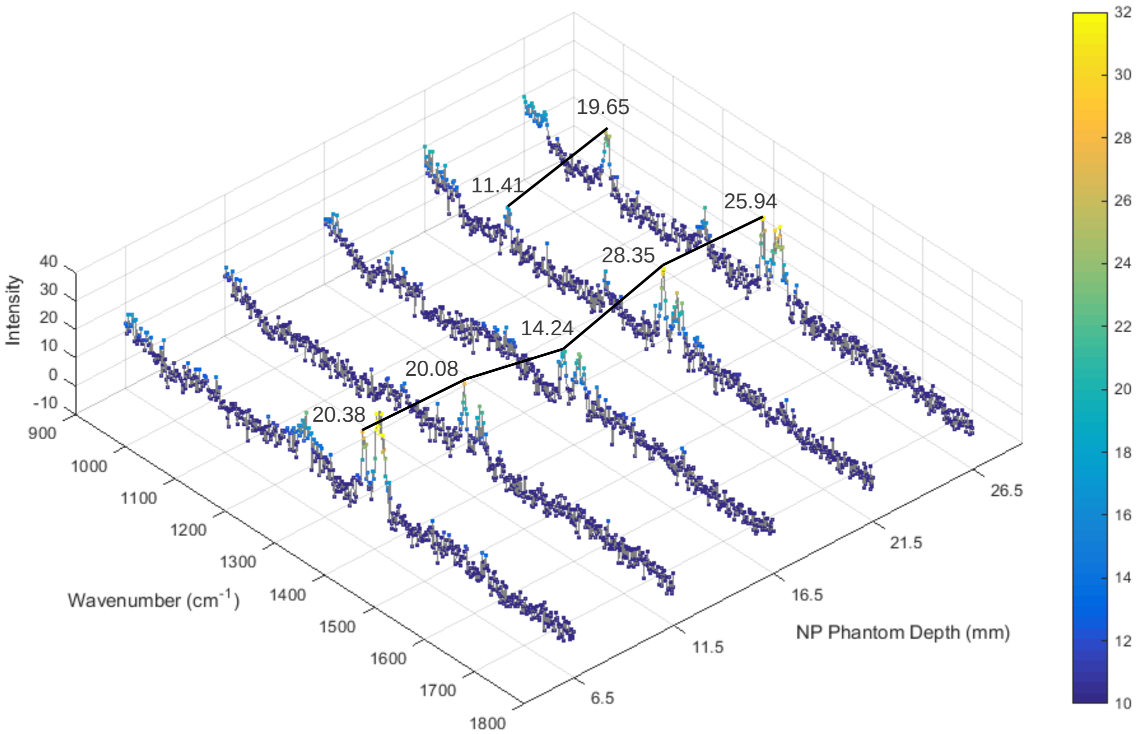

Figure 8.5: Raman signal profile of 2-NT AuNPs within 33 mm of breast phantom at 5 mm intervals towards the detector. Signal intensity of the spectral peaks is plotted in relation to the colour bar. The signal intensity depth profile of characteristic peaks determined by the relative peak height is line mapped.

The 2-NT signal intensity profiles, Figure 8.5, remains consistent to both the "U" shaped profile in the high wavenumber region and development of the lower wavenumber intensity at a greater depth within the 33 mm semi-infinite phantom.

For each of the reporters, the peak of a higher Raman shift (≥ 1380 cm^{-1}) garned an increased overall signal intensity comparative to the lower shifted, characteristic peak. The lower Raman shift peaks (1066, 1081 and 1078 cm^{-1}) gained signal intensity as the inclusion depth profile increased, moving closer towards the detector.

The relative peak position of the Raman reporter AuNPs in relation to the inherent breast phantom signal is seen in Figure 8.6.

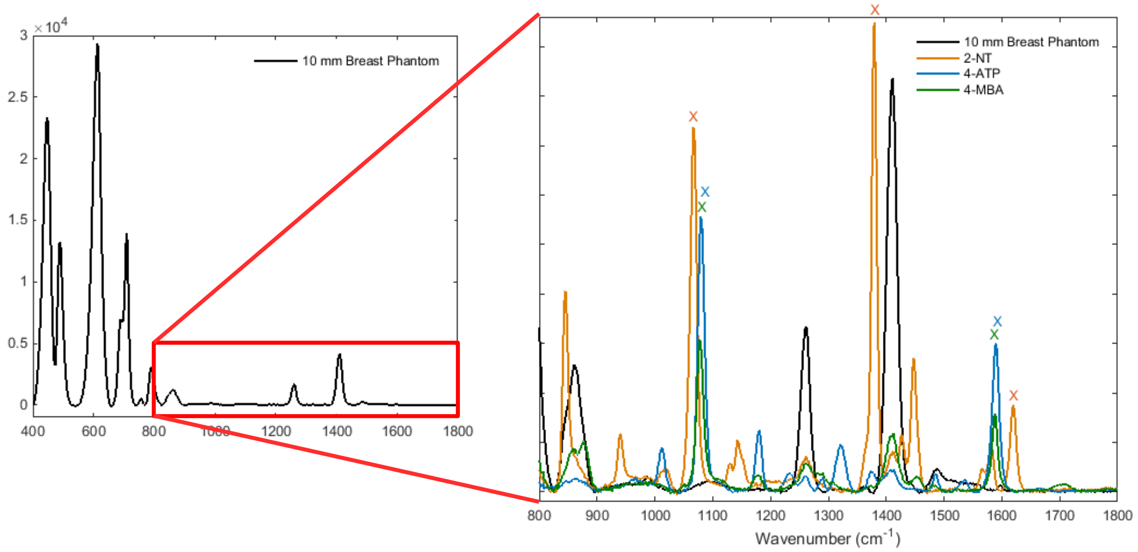

Figure 8.6: Raman spectra of the inherent phantom signal, with the exploded area of interest also containing the subtracted and baselined Raman reporters from within the 10 mm phantom. The main characteristic peaks for 2-NT, 4-ATP and 4-MBA are highlighted with an 'X' of the corresponding colour.

The lower Raman shifted characteristic peaks of all reporters, and higher shift peaks for the 4-ATP and 4-MBA are positioned upon a "blank space" area of the spectrum, having minimal influence from the inherent Sylgard phantom Raman peaks. The 2-NT peak at 1380 cm^{-1} lies directly on the shoulder of the Sylgard peak at 1410 cm^{-1}, casuing a level of intereference by increasing the overall intnesity and hence peak height. This, along with the intrinsically larger Raman cross-section, leads to the 2-NT signal collection at greater depths comparative to the 4-ATP and 4-MBA reporters.

The difference in peak height ratio across all of the reporters is made light when analysing the position of the characteristic peaks upon the Sylgard absorption spectrum. Conversion of peak values from Raman shift (cm^{-1}) to wavelength (nm) from the total wavenumbers (10248) is described in Equation (29), using 1066 cm^{-1} as an example:

$$12048 - 1066 = 10982$$
$$\frac{1}{10982} \times 10^{7} = 910.58\, nm \tag{29}$$

The results for each of the reporter characteristic peaks are plotted in Figure 8.7.

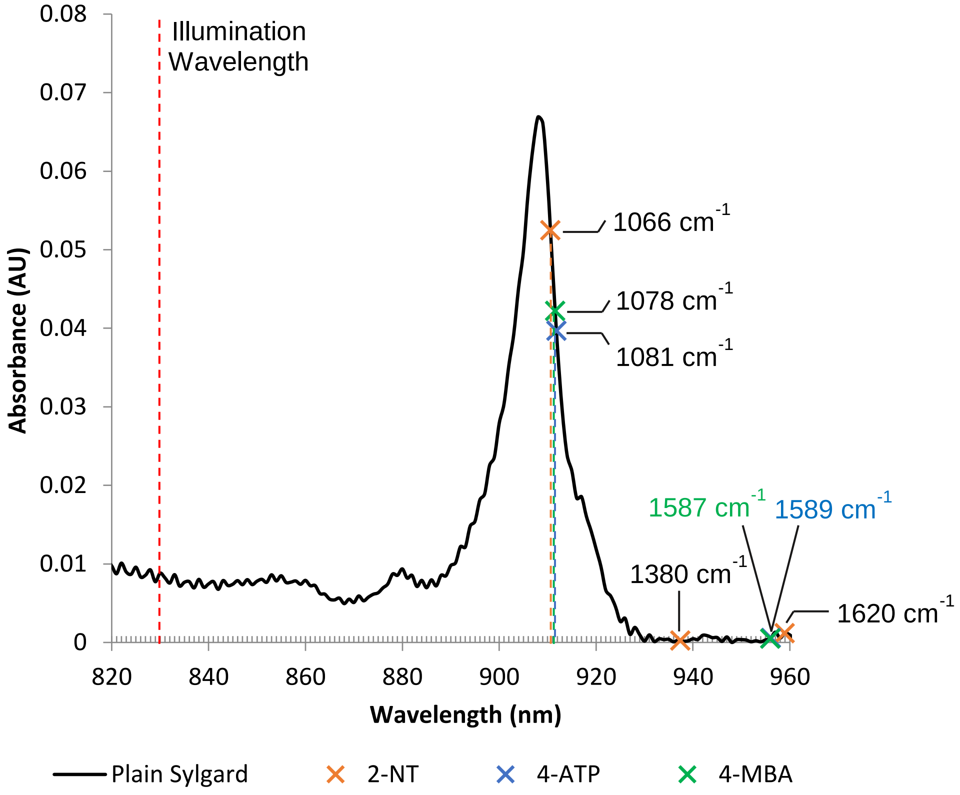

Figure 8.7: Absorbance spectra of the plain Sylgard with the characteristic peaks of the three Raman reporters (2-NT, 4-ATP and 4-MBA) plotted and labelled with the corresponding wavenumber upon the graph. The illumination wavelength of 830 nm is highlighted with a red dotted line.

The reporter peaks 1066 – 1081 cm^{-1} lie directly upon the absorption peak of the Sylgard, causing the signal intensity ratio comparative to the higher wavenumber peaks to be reduced when positioned at the lowest depth profile (6.5 mm). The greater absorption of photons creates a brevity of AuNP Raman photon contribution at the wavenumber range between 800 – 1200 cm^{-1} and hence a greater Raman signal from the Sylgard. The Raman photon contribution increases at a greater depth as the scattered photons are able to interact with the reporter AuNPs and be available for collection.

With the depth profile knowledge relating to each of the Raman reporter peaks and the relative intensity of each of them, the 2-NT was selected for depth mapping analysis within the morphologically representative breast phantoms.

8.4 Depth Mapping Analysis – Morphological Breast Phantom

For each breast phantom, the maps were measured at a sample illumination intensity of 300 mW under the acquisition parameters of 4.5 seconds with 4 accumulations, totalling 18 seconds. A step size of 0.9 mm both horizontally and vertically was set.

A visualisation of the mapped area upon the laser-phantom interface is seen in Figure 8.8.

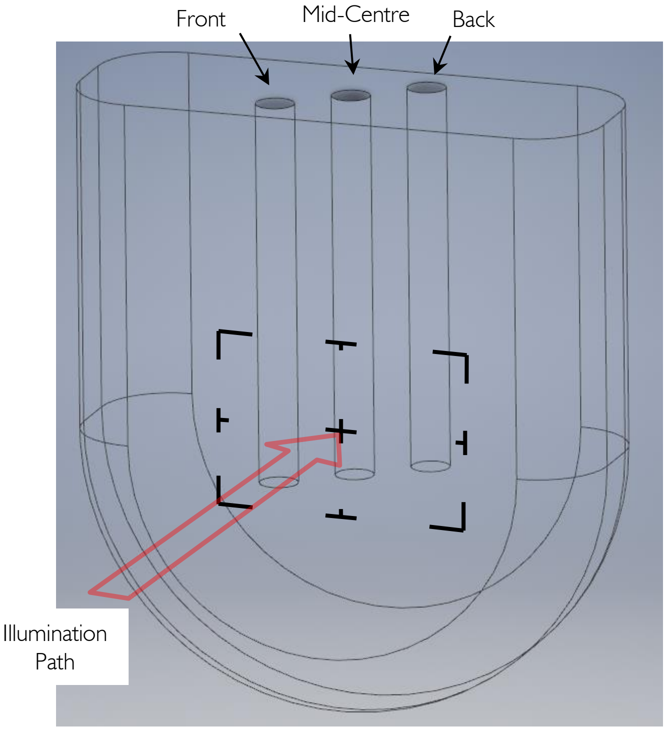

Figure 8.8: Autodesk Inventor modelled 25 mm breast phantom. The mapped area and central crosshair is outlined in black. Left to right/front to back ordering of the NMR tube inclusions are highlighted, with the path of illumination also shown (red arrow).

Initially, measurement of the 1066 cm^{-1} and 1380 cm^{-1} relative peak height using the Measure Peak MATLAB function was undertaken to provide an intensity depth profile across each of the breast phantom thicknesses. The results for the two characeristic peaks are shown in Figure 8.9.

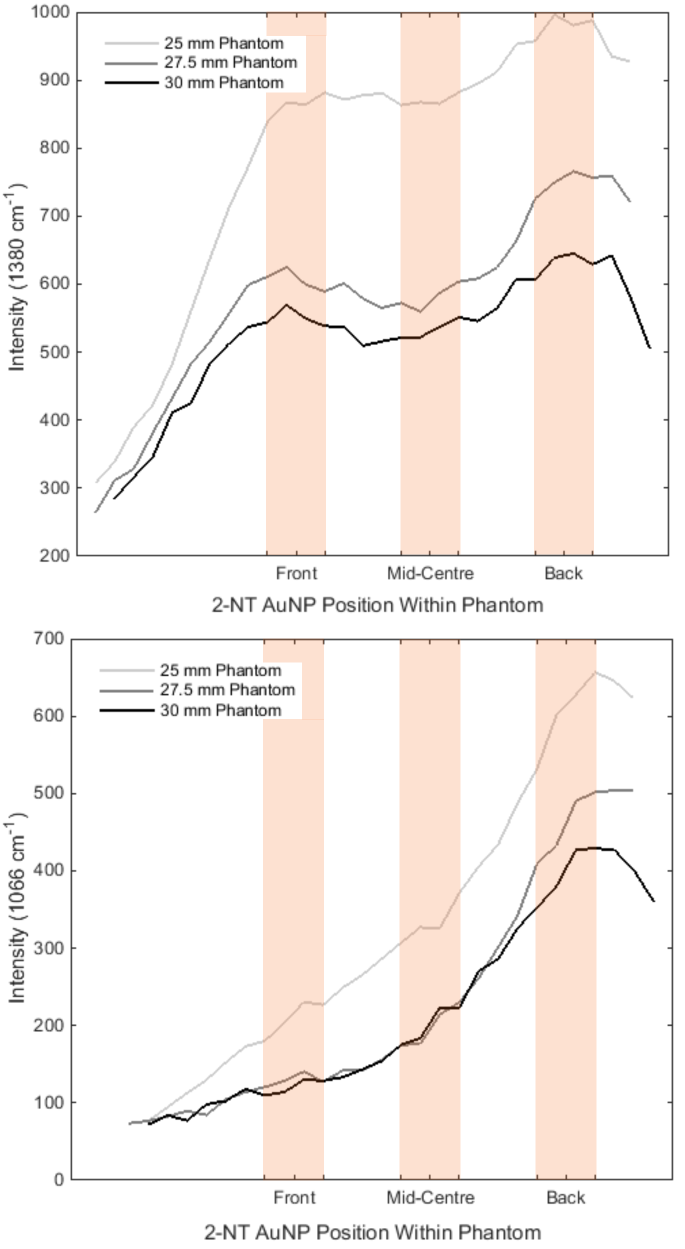

Figure 8.9: Two graphs to show the peak area intensity of the 2-NT characteristic peaks at 1380 cm^{-1} (top graph) and 1066 cm^{-1} (bottom). The generalised area of the three NMR tube positions within the breast phantoms, front, mid-centre and back, is highlighted in orange.

At a lateral distance of ≥6.4 mm from the first, front-left 2-NT AuNPs, no spectral contribution arises from the peak at 1066 cm^{-1}. Spectral contribution from the peak at 1380 cm^{-1} is seen from the starting position of the map, at a distance of 8.1 mm. This, once again, is due to the peak position upon the shoulder of the 1410 cm^{-1} PDMS peak granting perceived enhancement.

The overall intensity profile shape of both characteristic peaks are in agreeance with the previously defined profiles visualised within the semi-infinite phantom point-measurements.

PCA was utilised across all three depth maps to further analyse the intensity ratio of the 1066 and 1380 cm^{-1} 2-NT peaks at increasing depths. All maps were pre-processed with a set wavenumber range, cosmic ray removal and mean centering.

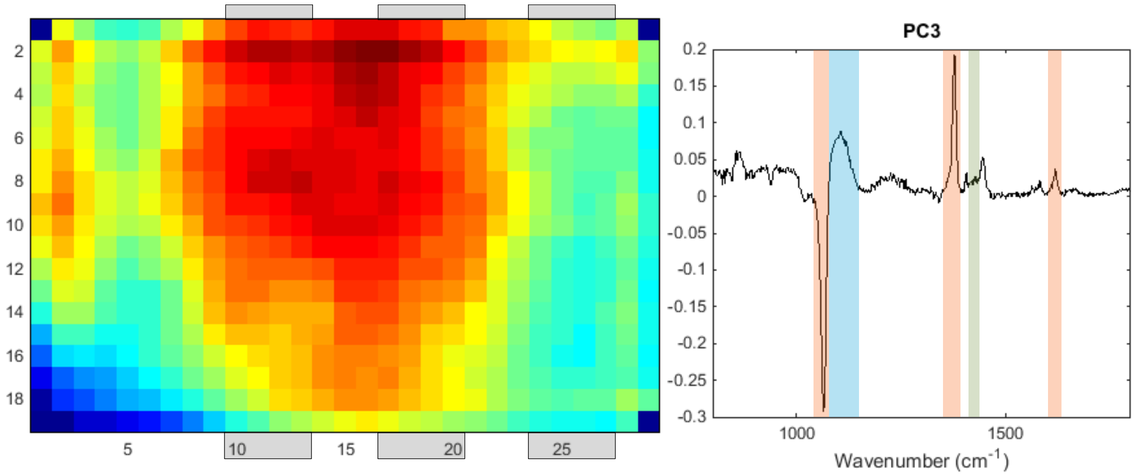

Figure 8.10: 25 mm Breast Phantom, principal component 3 map and loading: The red pixels corresponds to the ring symmetric stretch at 1066 cm^{-1} of 2-NT, the blue pixels correspond to the ring symmetric stretch at 1380 cm^{-1} and 1620 cm^{-1} of the 2-NT – all three are highlighted in orange. The PDMS peak at 1410 cm^{-1} is highlighted in green, with the NMR tube photoluminescent contribution in blue. The positioning of the AuNPs are signposted in grey above and below the pseudo-colour map. Pre-processing: wavenumber range, median filtering and mean centring.

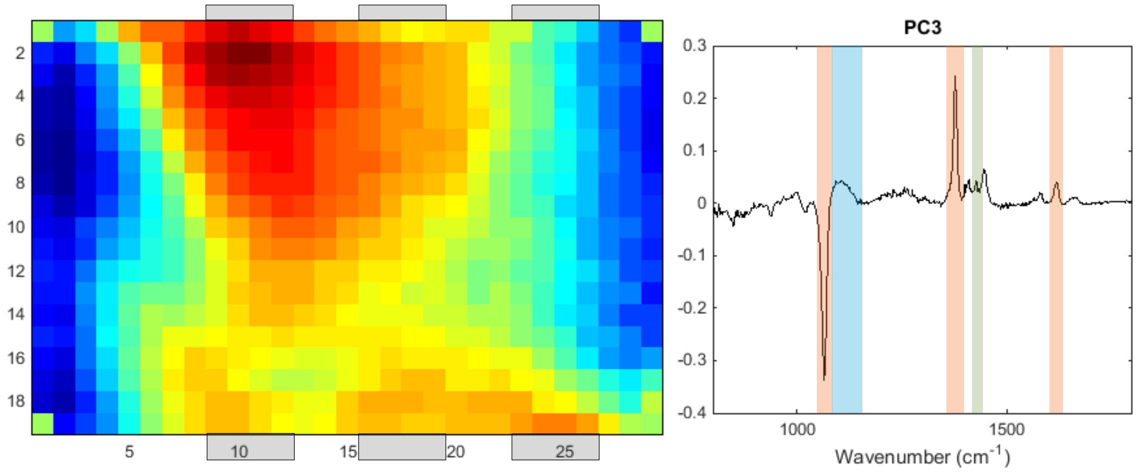

Figure 8.11: 27.5 mm Breast Phantom, principal component 3 map and loading: The red peaks correspond to the ring symmetric stretch at 1380 cm^{-1} and 1620 cm^{-1} of the 2-NT, the blue peak corresponds to the ring symmetric stretch at 1066 cm^{-1} of 2-NT – all three are highlighted in orange. The PDMS peak at 1410 cm^{-1} is highlighted in green, with the NMR tube photoluminescent contribution in blue. The positioning of the AuNPs are signposted in grey above and below the pseudo-colour map. Pre-processing: wavenumber range, median filtering and mean centring.

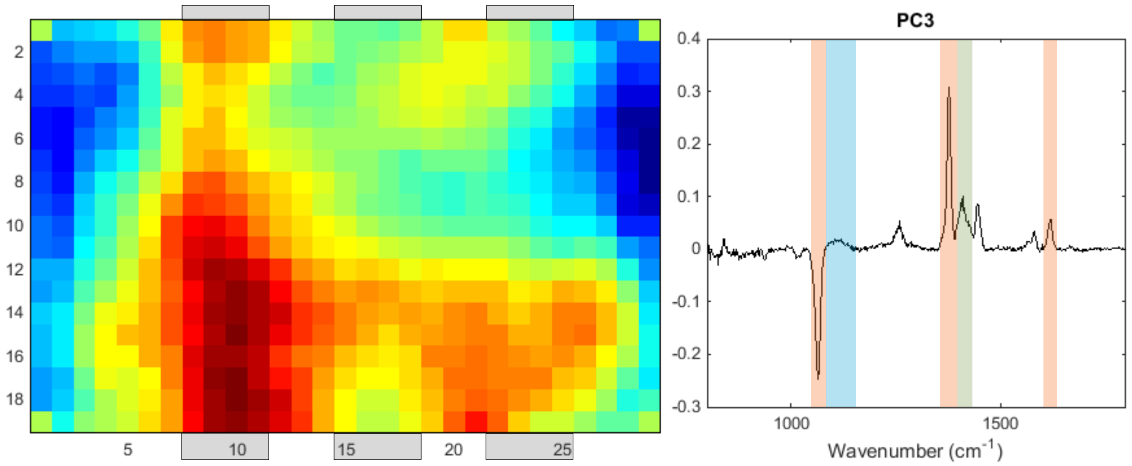

Figure 8.12: 30 mm Breast Phantom, principal component 3 map and loading: The red peaks correspond to the ring symmetric stretch at 1380 cm^{-1} and 1620 cm^{-1} of the 2-NT, the blue peak corresponds to the ring symmetric stretch at 1066 cm^{-1} of 2-NT – all three are highlighted in orange. The PDMS peak at 1410 cm^{-1} is highlighted in green, with the NMR tube photoluminescent contribution in blue. The positioning of the AuNPs are signposted in grey above and below the pseudo-colour map. Pre-processing: wavenumber range, median filtering and mean centring.

For each map, the third principal component displayed the 1066:1380 cm^{-1} intensity ratio difference, highlighted upon the spectral loadings in orange, along with the 1620 cm^{-1} peak. It can be seen that the influence of the Sylgard peak at 1410 cm^{-1}, highlighted in green, becomes more pronounced with an increase in breast phantom thickness. Conversely, the residual photoluminescence of the NMR tube, highlighted in blue, reduces in contribution.

AuNP positioning, left to right increasing in depth location, is highlighted in grey above and below the map axes. The regional differentation change displayed within the psuedo-colour maps switches peak dependance with an increase in phantom thickness. Within the 25 mm phantom, the 1066 cm^{-1} peak intensity becomes dominant at the distal location. Little differentiation, however, can be made between the frontal and mid-centrally located AuNPs intensity at 1380 cm^{-1}. At 27.5 mm, reliance on both peaks occurs: the 1066 cm^{-1} peak again becomes dominant at complete depth, but a decrease in the intensity of the 1380 cm^{-1} between the frontally and mid-positioned AuNPs is identifiable. The 30 mm phantom is no longer 1066 cm^{-1} peak dependent, with the 1380 cm^{-1} peak showing overall dominance. This follows the previously outlined depth intensity profiles of both peaks at a large depth.

8.5 Discussion and Conclusions

The depth intensity profiles of the higher wavenumber characteristic peaks from three RR-AuNP, generated from both the 28mm and 33 mm single-point depth measurements and mapping experiments, are in agreeance with the findings from Vardaki at el.[278]

Incursions to the intensity of the lower wavenumber peaks was due to the inherent absorption properties of the PDMS, minimising Raman photon collection until the depth position of the RR-AuNPs reached a minimal detector distance. It could be argued that the laser wavelength selection, in terms of the relative absorption trendline, could be adjusted from 830 nm to 808 nm. Changing the wavelength, in accordance with the biological NIR window in Figure 3.8, allows the illumination and Raman transmission photons greater access into and from the system for collection, respectively.

Within the morphologically representative breast phantoms, determination of the position of the 2-NT AuNPs at depth relied on the ratio of the relative peak height intensities of the characteristic peaks (1066 and 1380 cm^{-1}). Principal component analysis found that at a greater phantom thickness, the perception of RR-AuNP depth relied more heavily on the higher wavenumber peak (1380 cm^{-1}), unaffected by the absorption profile. Singular RR-AuNP use, in combination with mammographic imaging, has been shown as a plausible concept.

Multiplexed depth analysis within the morphologically representative breast phantom could not be perceived, due to the vast difference in intensities between the RR-AuNPs. Introducing a ratio of RR-AuNPs dependent on the signal intensity they produced would allow the multiplexed visualisation. Possible RR-AuNP configurations could be developed such as inclusion positioning combinations, or ternary colloid solutions mixed at selective ratios as studied by Jaebum Choo's group.[290,291] This required a repeat of the intensity depth profiles to determine the required RR-AuNP concentration ratios, and further breast phantom manufacturing – future work to be covered.

The development of morphologically and optically representative turbid phantoms is an area of research within the Raman community which requires further exploration. The use of mouse models is not wholly representative of human tissue in terms of both optical properties and the pharmacokinetics of AuNPs. As such, greater consideration into the use of optically layered turbid phantoms, with AuNP use adhering to a low dose model, must be made in future Raman spectroscopic works where human tissue is unavailable.

As discussed previously, the concentration of RR-AuNPs selected for experimental study falls under the remit of a low dose model. This however, would require the whole dose to accumulate within the volume of the tumour – an impossibility due to the vast clearance mechanisms within the body and recent findings that a median of 0.7% of the administered dose arrives at the desired, solid tumour destination.[308] Current contrast-based imaging, such as iodine for CT or barium in fluoroscopy, relies on the overall highlighting of vasculature or tissues to identify the abnormalities lying within the regions. This type of contrast use, despite increasing the visibility of disease, is non-specific. With NP use, the ability to target the specific disease site owes itself to further therapeutic options, such as drug delivery or photothermal ablation.[152,206,309]

As such, improvement upon the RR-AuNP design could be made in terms of the presence of active targeting ligands on the colloid surface. Hence, this was possibility was explored within the next Chapter. Additionally, consideration into the relative colloidal heating at these depths is explored to determine the utility of the NP probes as diagnostic agents.

9. Breast Microcalcification Targeting Gold Nanoparticles

9.1 Introduction

The affinity of the 2-NT-PEG-alendronate functionalised AuNPs to hydroxyapatite (HAP) is quantified within this Chapter.

In Section 9.2 the structural and biochemical features of the collagen scaffold of explored under dry and saturated conditions. The inclusion of the AuNPs within the collagen scaffold is seen in Section 9.3. Quantification of the effectiveness of the non-targeting and active-targeting AuNPs is explored using micro-Raman mapping and principal component analysis techniques within Section 9.4. The use of multivariate analysis is a necessary tool in the determination of whether selective binding of the targeted NPs to the hydroxyapatite truly occurs.

Section 9.5 considers the targeting AuNPs at depth, and their effectiveness as a diagnostic tool in relation to the colloidal heating effect. Finally, the discussions and conclusions Section 9.6 summaries the findings of this study.

9.2 Collagen Scaffold Impregnated with Hydroxyapatite

The measuring and analysis of the targeting NPs binding to HAP confirms the success of the NP labelling and design. Crystalline hydroxyapatite is soluble, making it difficult to quantify binding affinity within a colloidal solution. Hence Hydroxycoll, a HAP infused collagen which retains form once saturated, was used.

The material is produced using homogenised fibrillar collagen blended with 5 μM hydroxyapatite crystals, which consequently undergoes lyophilisation to create a scaffold-like structure.[292] The scaffold consists of holes up to 100 μM in diameter, seen in Figure 9.1, allowing permeation of the targeted NPs through the structure.

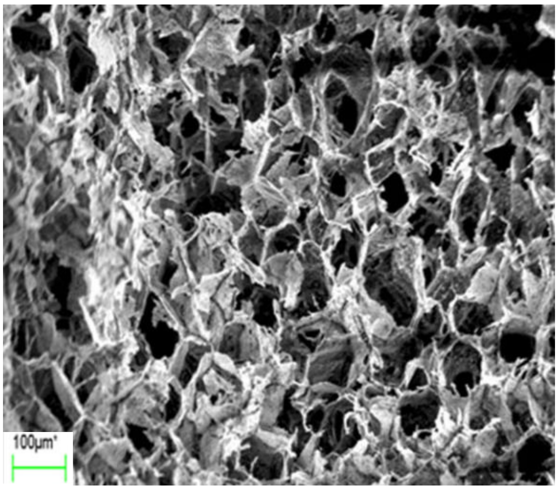

Figure 9.1: A scanning electron microscopy (SEM) image showing the pore size and structure of the Hydroxycoll material.[293]

Initially, single-point Raman spectra of the scaffold, both dry and saturated in DI water, were collected. This established the biochemical signature of the material as a bulk and gain understanding of how the structure of the collagen changes under the two conditions. Two, small 10 x 20 mm sections of the Hydroxycoll was sectioned using a cutting mat and scalpel. One remained dry whilst the other was saturated in de-ionised water. Eight Raman measurements using the 830nm laser at 100% power for 5 seconds over three accumulations were measured and equated into single mean spectra for each series.

The main peaks of interest, annotated in Figure 9.2, highlight the signal intensity change between the HAP phosphate ($-PO_4{}^{3-}$) and collagen structures as the material transitions from a dry to a hydrated state.

In the dehydrated state, peaks at 667 cm^{-1}, 1243cm^{-1}, 1343 cm^{-1}, 1667 cm^{-1} and the range over 1437-145 cm^{-1} relate to the C–S stretching of cystine, amide III, $-CH_2$ and $-CH_3$ symmetic stretch, amide I, and $-CH_2$ deformation within the collagen, respectively. The shoulder peak at 920 cm^{-1} is assigned to the C–C stretch of the collagen proline ring. Hydrating the scaffold causes a significant change in the collagen structure: breaks in cystine and proline ring structures increases the concentration of C–S and $-CH_2$ within the material. $-PO_4^{3-}$

symmetric stretching peaks at 589 cm^{-1} and 960 cm^{-1} increase in intensity as the HAP becomes exposed.

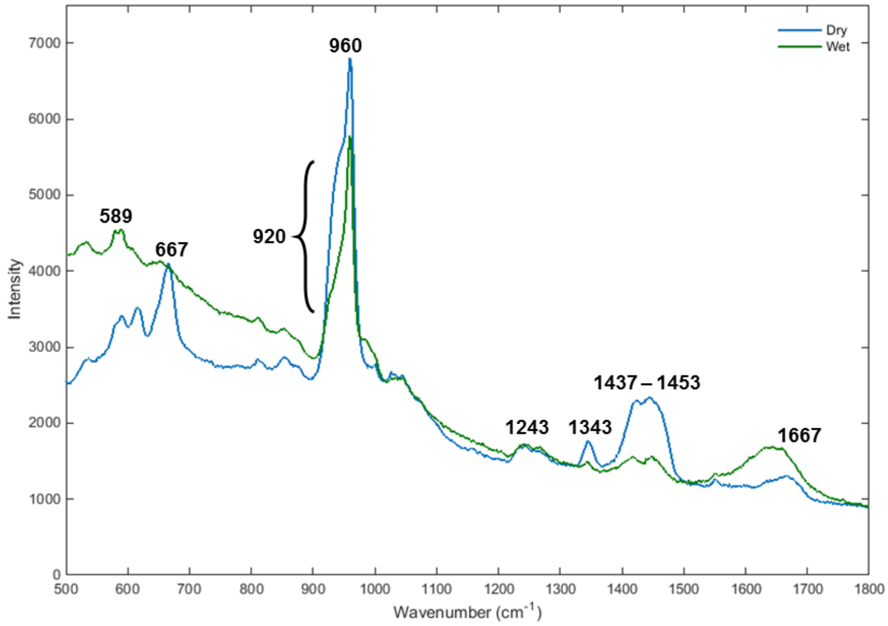

Figure 9.2: Mean Raman spectra of the HAP impregnated collagen scaffolds under dry (blue) and wet (green) conditions. Specific peak assignments have been highlighted for clarity.

The nature of the HAP in relation to carbonate substitution was explored further. The ratio between the phosphate ($-PO_4{}^{3-}$) symmetric stretch peaks at 960 cm^{-1} and 1046 cm^{-1}, and carbonate ($-CO_3{}^{2-}$) ions $-CO$ in-plane stretch at 1070 cm^{-1} determines the level of B-type substitution. This can be clinically applied to distinguish the degree of malignancy – a lesser B-type substitution, or high carbonate level, is associated with benign lesions.[49,294] A pure HAP crystal within the scaffold was micro-Raman point measured at 100% laser power for three seconds, seen in Figure 9.3:.

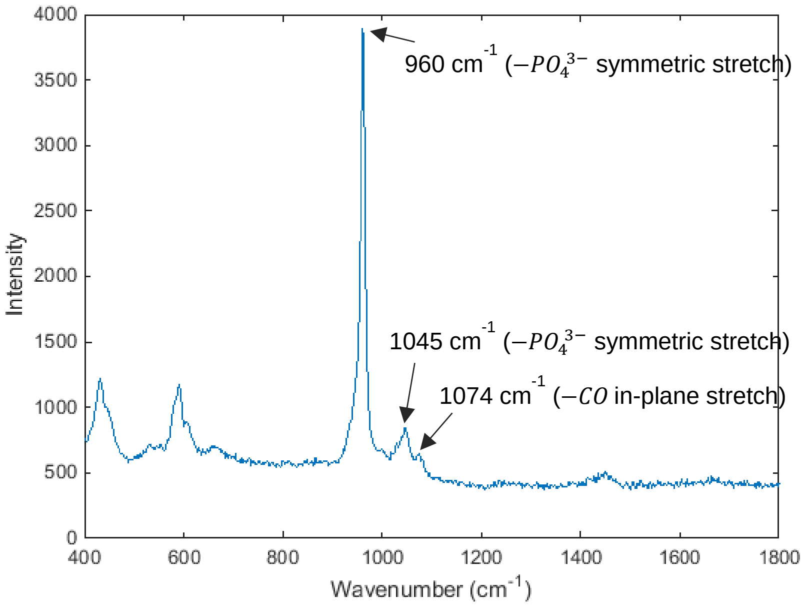

Figure 9.3: Raman spectrum of a pure HAP crystal within the dry collagen scaffold. The symmetric stretching phosphate peaks at 960 cm^{-1} and 1045 cm^{-1}, and the in-plane stretching of the $-\boldsymbol{CO}$ within the carbonate ions at 1074 cm^{-1} have been labelled. The ratio of between the two groups of peaks confirms an elevated level of B-type substitution.

Comparative to study by Kerssens et al, the intensity ratio of the carbonate peak to phosphate peaks within the HAP spectra mimics a 1.24% / 2.92% substitution level.[49] This is representative of a high B-type substitution level, equivalent to a prolific cancerous lesion, making the Hydroxycoll a suitable representative material for breast cancer microcalcifications within malignant tissue.

Next, a dry, 10 x 20 mm Hydroxycoll section was micro-Raman mapped to verify pore size and distribution of HAP throughout the collagen matrix. Due to the tiered, interlinking nature of the scaffold, surface montages collected of the scaffold, as seen in Figure 9.4, could not remain in complete focus. The highlighted area settled in focus across a complete scaffold pore, so was selected for Raman mapping. This smaller, highlighted image has been rotated to reflect the analysed colour maps below.

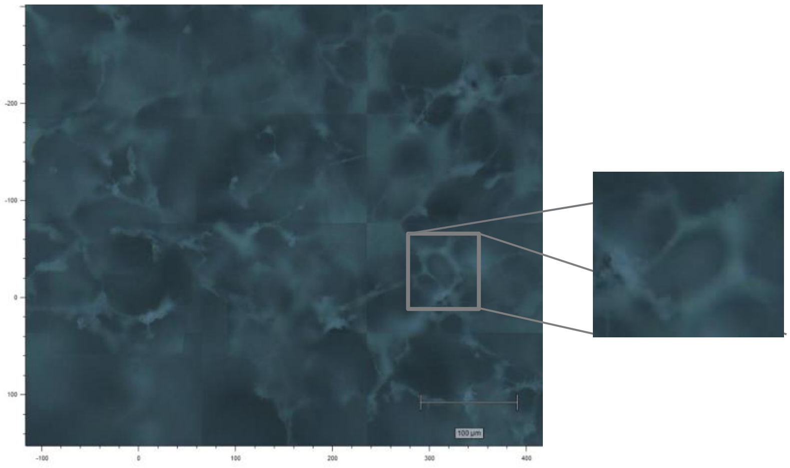

Figure 9.4: A surface montage of the dry Hydroxycoll at 50X magnification – the exploded, rotated, section highlights the area selected to be Raman mapped.

The mapping parameters consisted of 50X magnification, using the Streamline 830 nm laser at a 140 mW sample illumination intensity, with an imaging time of 30 seconds per step at a 5 μm step size. The resulting maps highlighting the peak area intensity of the collagen at 667 cm^{-1}, and at 960 cm^{-1} for HAP, is displayed in Figure 9.5.

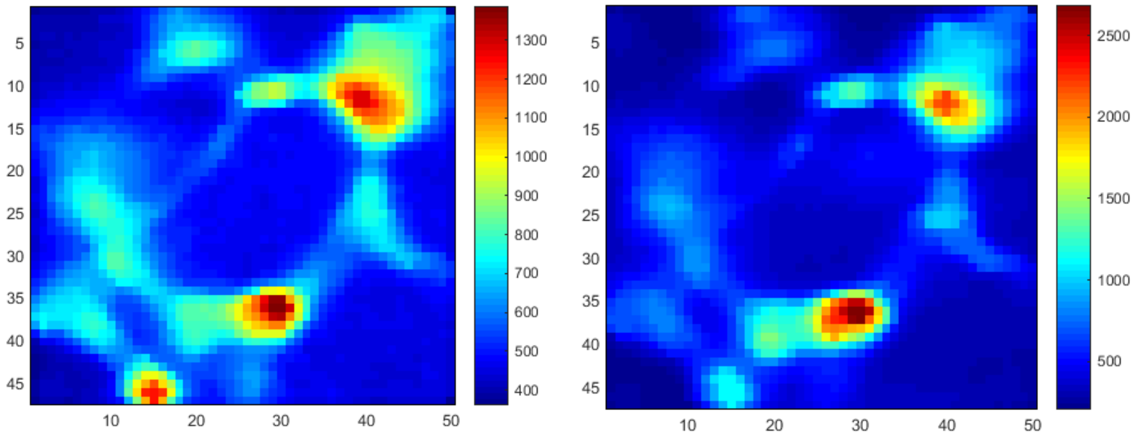

Figure 9.5: Colour maps of peak area intensities to show the distribution of: collagen (left image), identified by the selected peak at 667 cm^{-1}, $\boldsymbol{C-S}$ cysteine symmetric stretch; and HAP within the collagen structure (right image), identified by the selected peak at 960 cm^{-1}, $\boldsymbol{-PO_4{}^{3-}}$ symmetric stretch. Pre-processing: Wavenumber range and median filter for cosmic ray removal.

As seen, the HAP distribution was inclusive, but uneven, within the collagen, appearing to clump in junction areas of the scaffold. In a saturated state, however, internally bound HAP becomes more available at the surface – a crucial factor to consider when analysing the binding patterns of the targeting colloid.

9.3 Collagen Scaffold Colloid Introduction

Prior to the introduction of the NPs to the collagen scaffold, NP/mL concentrations of targeting and non-targeting NP batches were required to be consistent. Beer-Lambert Law can be used to define the absorptivity of known, and unknown, concentrations of colloids. First, known dilutions of bare AuNPs were measured using the UV/Vis spectrometer and plotted as a graph. A DI water blank set the zero-zero mark. The known standard concentration of NPs was 2.64 x 10^{-4} M, hence a half and half dilution with DI water leads to ~1.32 x 10^{-4} M. Dilutions were further halved until a 1:16 ratio was reached.

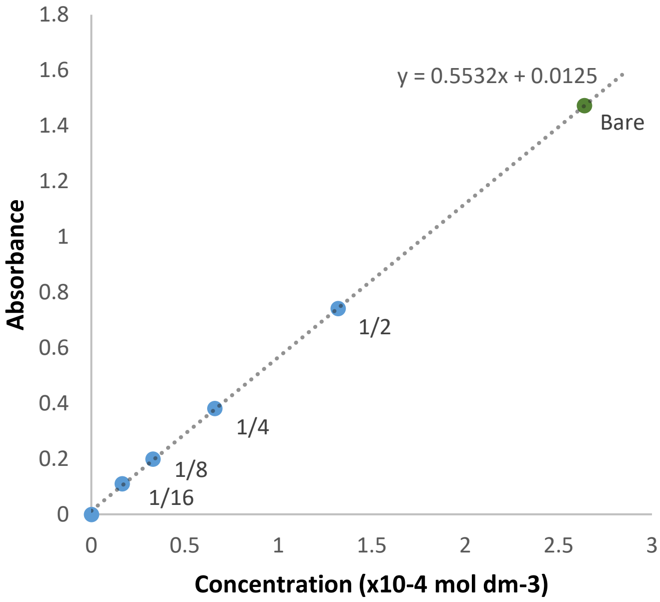

Figure 9.6: A graph to show the maximum absorbance peak value versus the known concentration of a NP dilution series.

Beer's Law is defined by the equation:

$$A = \varepsilon \, l \, c \tag{30}$$

whereby A is the maximum absorbance defined by the molar absorptivity, ε, the light path length in cm, l, and the concentration of the solution in mol dm^{-3}, c. To gain the molar absorptivity value, part of the equation can be rearranged to:

$$\varepsilon = \frac{c}{l} \tag{31}$$

Taking the equation of the line in Figure 9.6, the absorbance value can be said to be:

$$A = \ 0.5532c + 0.0125 \tag{32}$$

where the concentration, c, is now the known value of 0.5532. The cuvette width, path length is a constant value of 1.25 cm. Hence, ε was calculated to a value of 4425.6 M^{-1} cm^{-1}. The known maximum absorbance values of the labelled NPs were then calculated using Beer's Law and the values gathered from this initial concentration sampling method. The results are plotted in the graph in Figure 9.6.

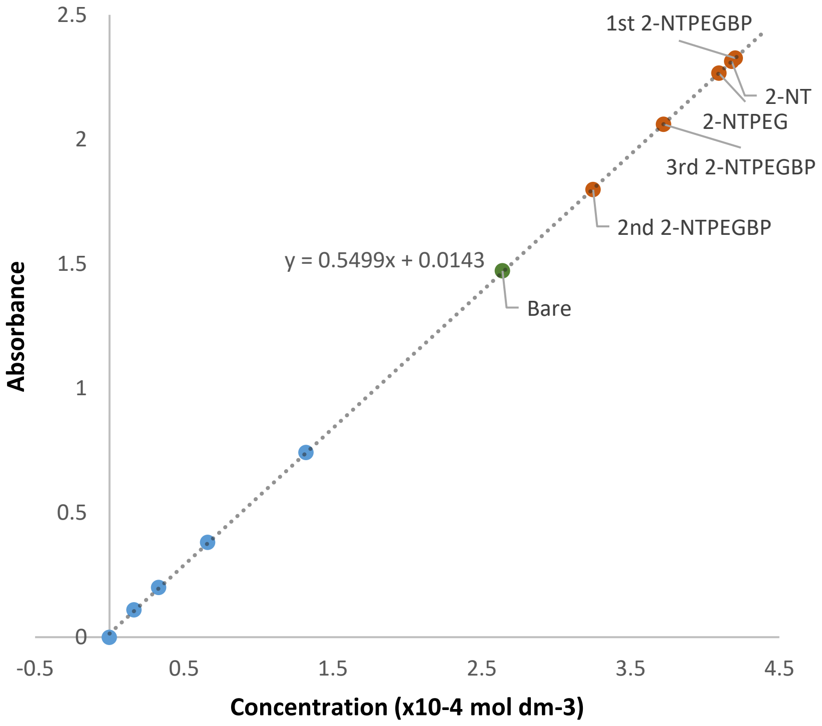

Figure 9.7: A graph to show the maximum absorbance peak value versus the known concentration of labelled NPs, found using Beer-Lambert Law.

It can be seen from the equation of the line in Figure 9.6 that a negligible amount of deviation has occurred from the initial results. This is down to several factors: the UV/Vis graph in Figure 5.18 shows asymmetry between the shape of the labelled and bare NP LSPR peak – variation of results is to be expected when measuring modified samples.

From the results garnered, the labelled NPs were diluted to the known bare NP constant molar value of 2.64 x 10^{-4} for consistent experimentation.

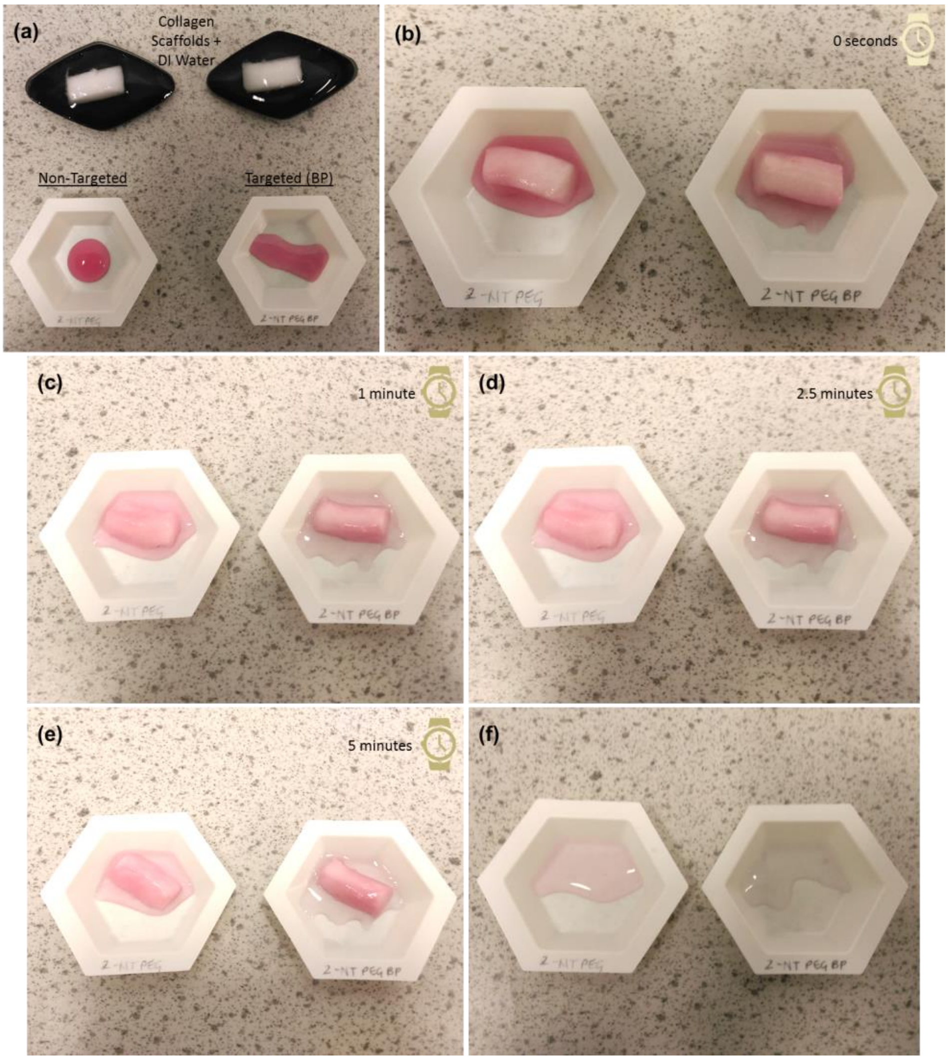

Figure 9.8: Targeted and non-targeted nanoparticle impregnation within collagen scaffold sections: (a) 0.5 mL NPs and hydrated 10 x 20 mm collagen sections prepared; (b) – (e) collagen placed and rotated in NPs for 5 minutes, progression over time seen; (f) remaining water/colloid – a slight difference of colour can be seen between the two solutions.

The introduction of targeting and non-targeting NPs to the Hydroxycoll began with the sectioning of the scaffold into regular 10 x 20 mm pieces. Two pieces were fully saturated, lightly drained of excess water and placed individually into 0.5 mL of 2-NT-PEG and 2-NT-PEG-BP colloids. To gain an even coverage, the scaffold pieces were rotated every minute for five minutes, shown in Figure 9.8. The scaffolds were removed from the colloid solution, washed three times in excess DI water, and stored in a layer of cling film to preserve saturation. The remainder colloid solution was stored in Eppendorf tubes to be later analysed with UV/Vis.

9.4 Micro-Raman Mapping and Analysis

The Micro-Raman InVia, as described in Section 5.3 was used for single-point and mapped measurements. Single-point acquisition parameters were set at a sample illumination intensity of 70 mW, at 2 seconds and 5 acquisitions. The targeting and non-targeting colloid infused scaffolds were surface montaged and mapped using the 50x magnification, using the Streamline 830 nm laser at 140 mW sample illumination power. An imaging time of 30 seconds per step at a 5 μm step size was selected. The pre- and post-processing techniques as established in Chapter 9, Section 8.2 were used again for this Chapter.

Initial point spectra of the Hydroxycoll sections saturated with the respective targeting and non-targeting nanoparticles were taken, as seen in Figure 9.9. The spectra were normalised to the 960 cm^{-1} HAP peak to succinctly compare the spectra, reducing the relative intensities from differences in photon depth collection and scattering contributions. The 2-NT-PEG colloid adsorbed section had a minimal 2-NT spectral contribution, with the collagen scaffold most prominent. By comparison, the contribution from the 2-NT reporter was greatly enhanced on the 2-NT-PEG-BP adsorbed collagen scaffold spectrum, Figure 9.9.

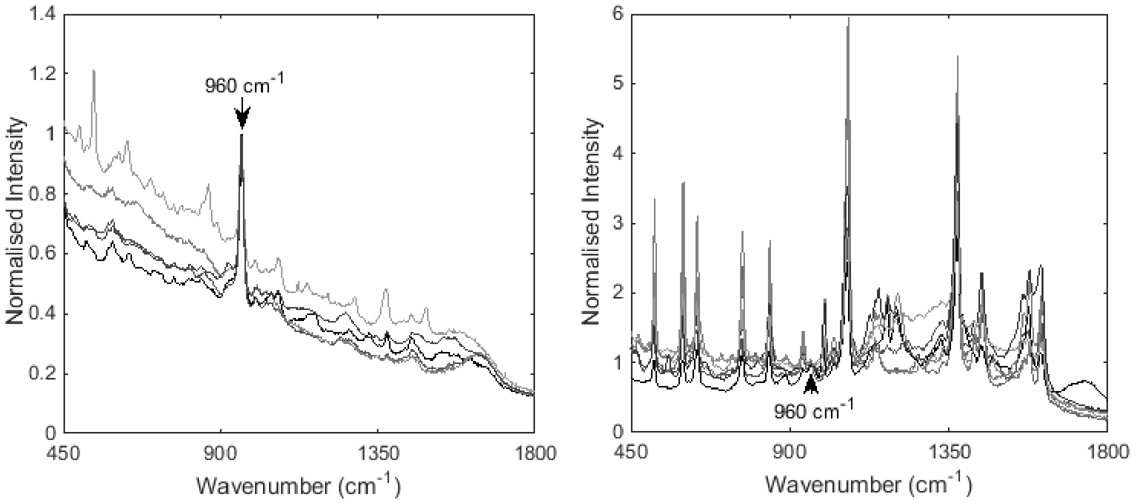

Figure 9.9: Point spectra of the surface of a 10 x 20 mm Hydroxycoll section adsorbed with 0.5 mL 2-NT-PEG AuNPs (left spectra) and 0.5 mL 2-NT-PEG-BP AuNPs (right spectra), normalised to the main HAP peak at 960 cm^{-1} ($-PO_4{}^{-3}$).

Mapping the saturated scaffolds caused several difficulties, as seen in Figure 9.10. The tiered nature of the scaffold had previously caused focussing issues; the drying rate of the wet scaffold, increased by laser heating during mapping, added an additional factor.

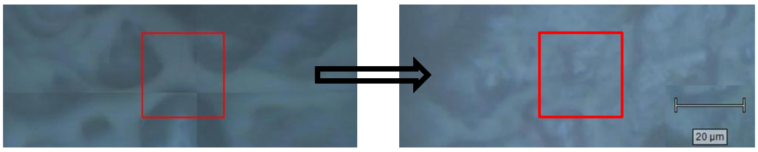

Figure 9.10: Surface montaged area before and after Raman mapping, mapped area highlighted by the red boxes. Post-mapping, the scaffold was refocused at the origin – a shift in the y and z axis of approximately 20 μm in both directions had occurred.

With a focus drop off, signal intensity similarly fell, requiring a high laser power to compensate. However, high laser intensity caused burning artefacts to the scaffold when focussed to a cluster of NPs, heating them to very high temperatures. Irregularity in focus and difficulties in selecting an appropriate laser power resulted in many unfocused or burnt mapping attempts.

9.4.1 Non-Targeting 2-NT-PEG NPs

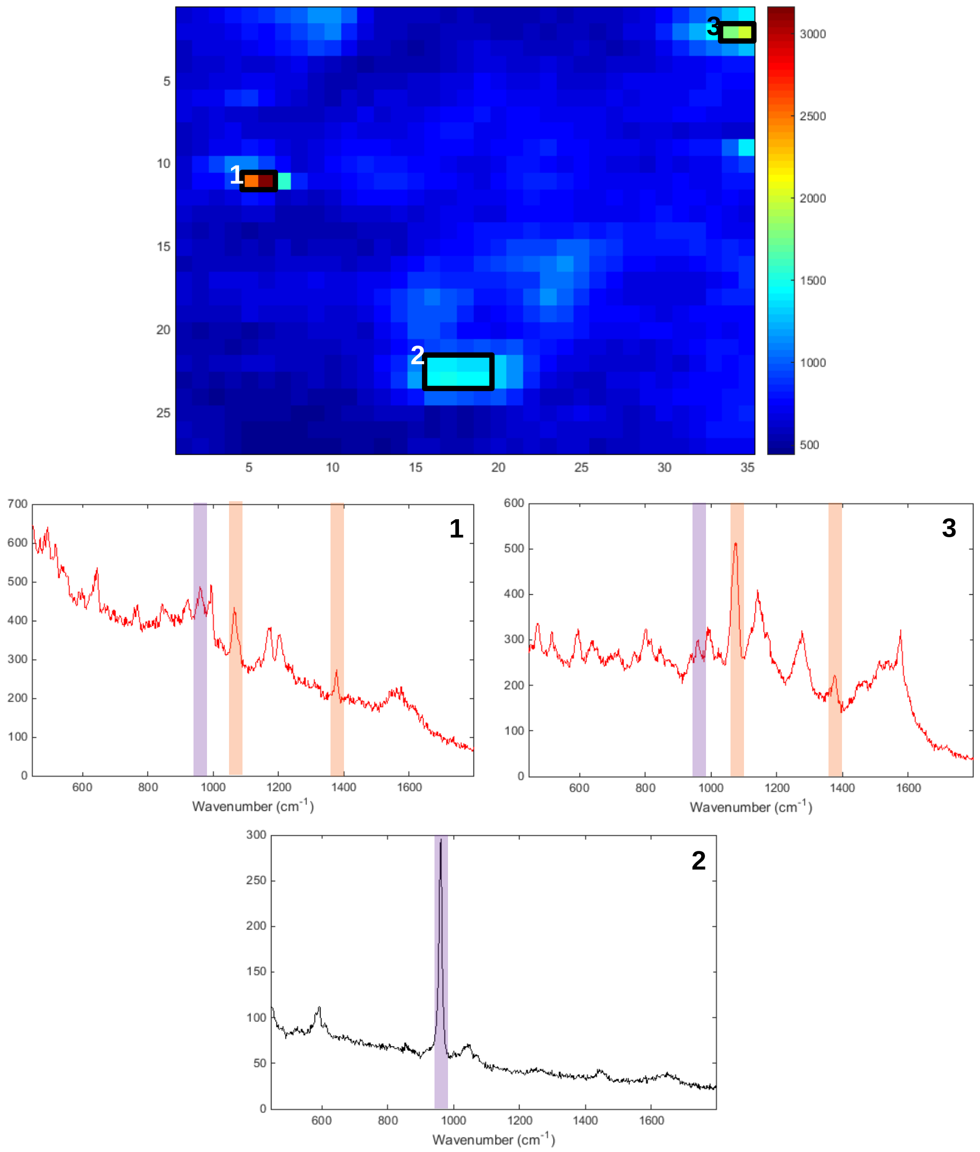

Figure 9.11: peak area @960 cm^{-1}. Highlighted areas #1 and #3 relating to the 2-NT-PEG signal; #2 is the pure HAP signal which remains free of 2-NT spectral peaks. Colour changes to annotation boxes and numbers on map for clarity only. The characteristic 2-NT peaks within the PC1 spectrum are highlighted in orange, whilst the $-PO_4{}^{-3}$ peak at 960 cm^{-1} is highlighted in purple.

Figure 9.11 shows the intensity map about the 960 cm^{-1} peak area, $-PO_4{}^{-3}$, of the 2-NT-PEG saturated collagen scaffold. Three, averaged spectral areas of interest have also been extracted from the map.

The maps three distinct areas can be categorised into two groups – the first solely highlighting the HAP-collagen scaffold structure in spectrum 2; and the second displaying the 2-NT spectral contribution in number 1 and 3. Both areas 1 and 3 contain inherent collagen scaffold spectral contribution. These areas show no strong overlap between the $-PO_4{}^{-3}$ and non-targeting AuNPs, made more apparent in the PCA map in Figure 9.12.

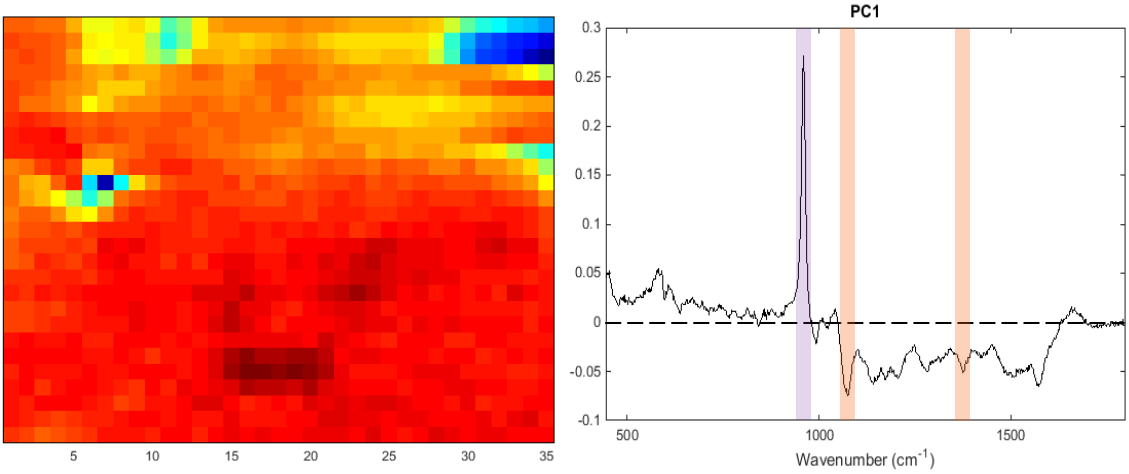

Figure 9.12: PCA map and loading confirming non-selective clustering of 2-NT-PEG AuNPs. The characteristic 2-NT peaks within the PC1 spectrum are highlighted in orange, whilst the $-\boldsymbol{PO_4}^{-3}$ peak at 960 cm^{-1} is highlighted in purple. Pre-processing: Wavenumber range, vector normalised, mean centred.

The clustered nature of the two NP areas can be attributed to aggregation occurring during drying.

9.4.2 Targeting 2-NT-PEG-BP NPs

By comparison, the alendronate functionalised targeting AuNPs show a strong affinity to the $-PO_4{}^{-3}$ within the collagen scaffold. Visualised by the peak area maps in Figure 9.13, map A for the $-PO_4{}^{-3}$ 960 cm^{-1} peak area and, B and C the signature 2-NT peaks at 1066 cm^{-1} and 1380 cm^{-1} respectively. A section of the complete scaffold pore is well visualised in map A, with the cluster of 2-NT signal occurring along the scaffold path highly resembling the clumped distribution nature of the HAP, as seen in Figure 9.5.

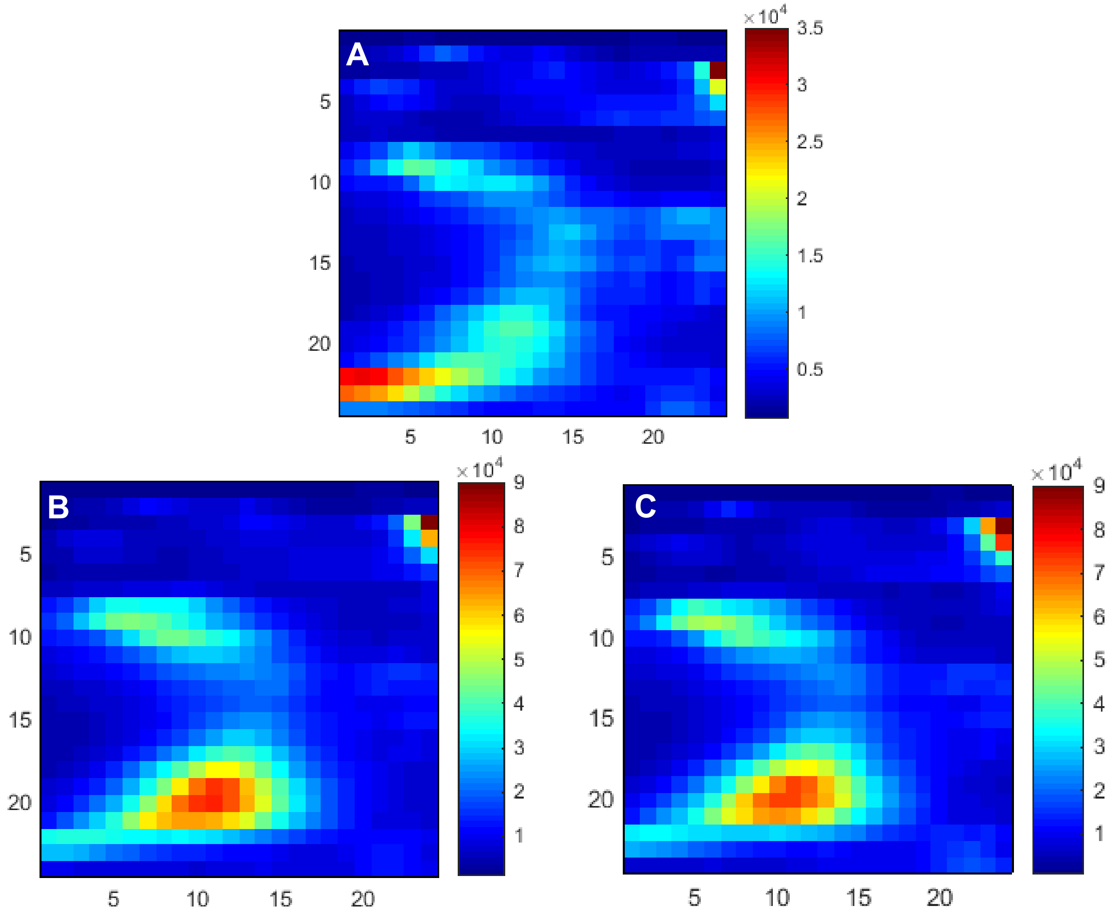

Figure 9.13: Targeting AuNPs on collagen scaffold colour map: (A) peak area at 960 cm^{-1} (B) peak area at 1066 cm^{-1} (C) peak area at 1380 cm^{-1}.

From map A, six distinct areas of interest were extracted, with the area averaged spectra displayed in Figure 9.14. The 2-NT spectrum is present in each of the interest areas to varying degrees of intensity. Section 1 displays the greatest intensity, possibly due to this area having a topographically elevated position comparative to the well-defined scaffold pore, gaining a smaller z length to the objective and hence greater focus. Section 5, of the greatest HAP intensity, has contains a large collagen scaffold spectral contribution in addition to the signature 2-NT peaks. This confirms the presence of incompletely functionalised targeting AuNPs, whereby the functionalised area containing the Raman reporter binds to the HAP, allowing the bare gold surface to interact with the collagen scaffold.

For full confirmation of active targeting with PCA, further maps were explored.

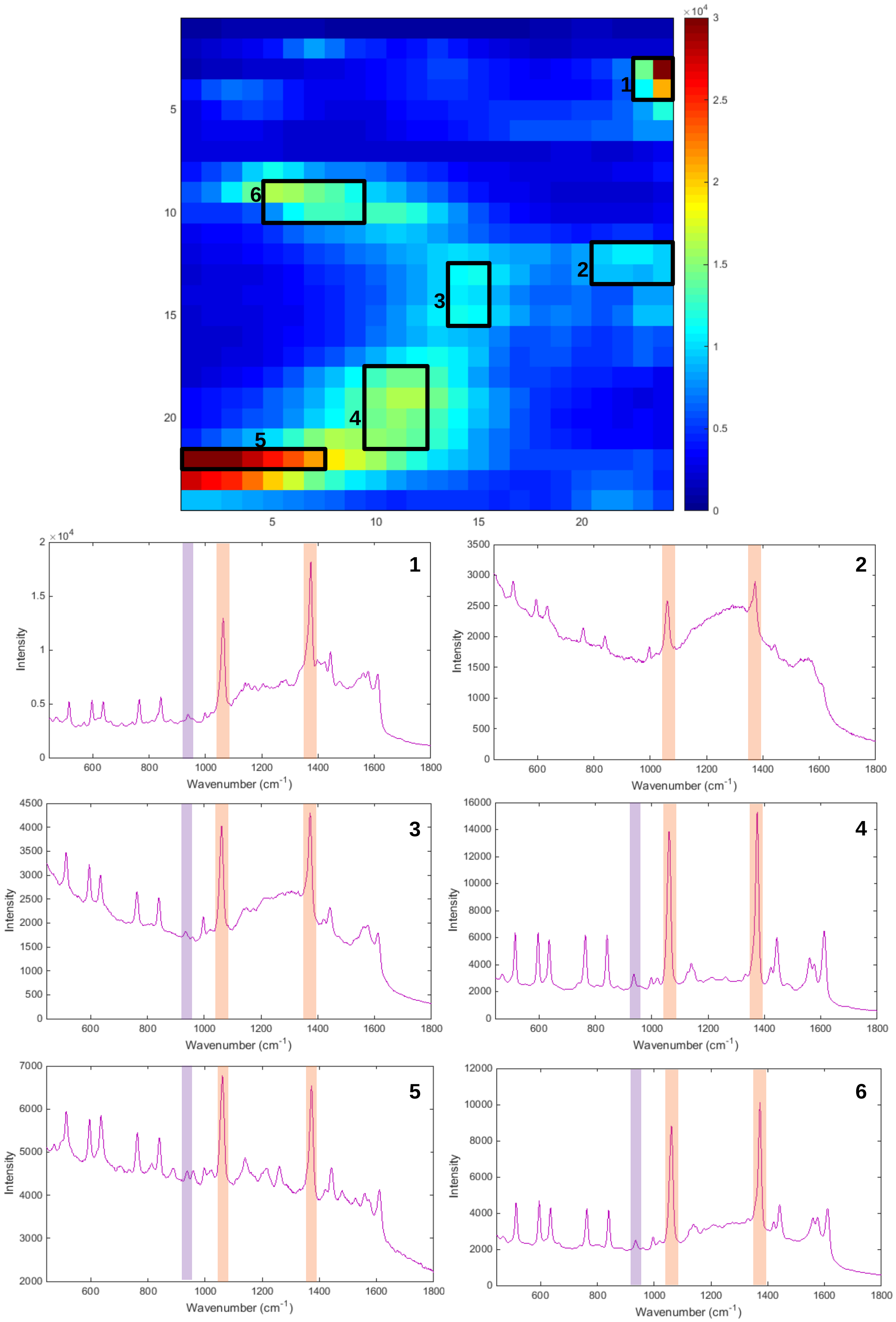

Figure 9.14: Targeting AuNPs on collagen scaffold colour map, peak area 960 cm^{-1}. Six distinct areas of interest are outlined on the map, with the averaged spectra (1-6) plotted below. The characteristic 2-NT peaks are highlighted in orange, whilst the $-PO_4^{3-}$ peak at 960 cm^{-1} is highlighted in purple.

Figure 9.15 displays the intensity maps of a new pore area, map A for the $-PO_4^{-3}$ 960 cm^{-1} peak area and, B and C the signature 2-NT peaks at 1066 cm^{-1} and 1380 cm^{-1} respectively. Once again, the clustered nature of the HAP is visualised, alongside the seemingly targeted agreeance of the signature 2-NT peaks.

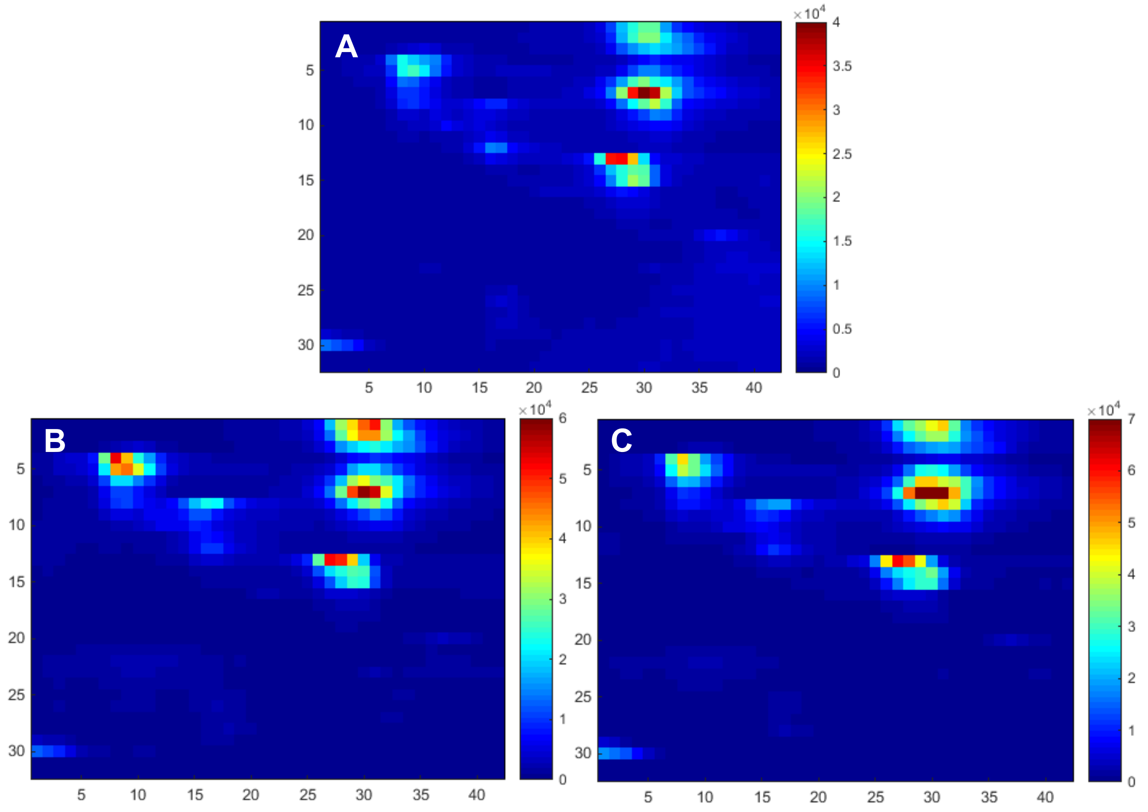

Figure 9.15: (A) peak area @ 960 cm^{-1} (B) peak area @ 1066 cm^{-1} (C) peak area @ 1380 cm^{-1}

Once again, areas of interest were extracted with the area averaged spectra displayed in Figure 9.16.

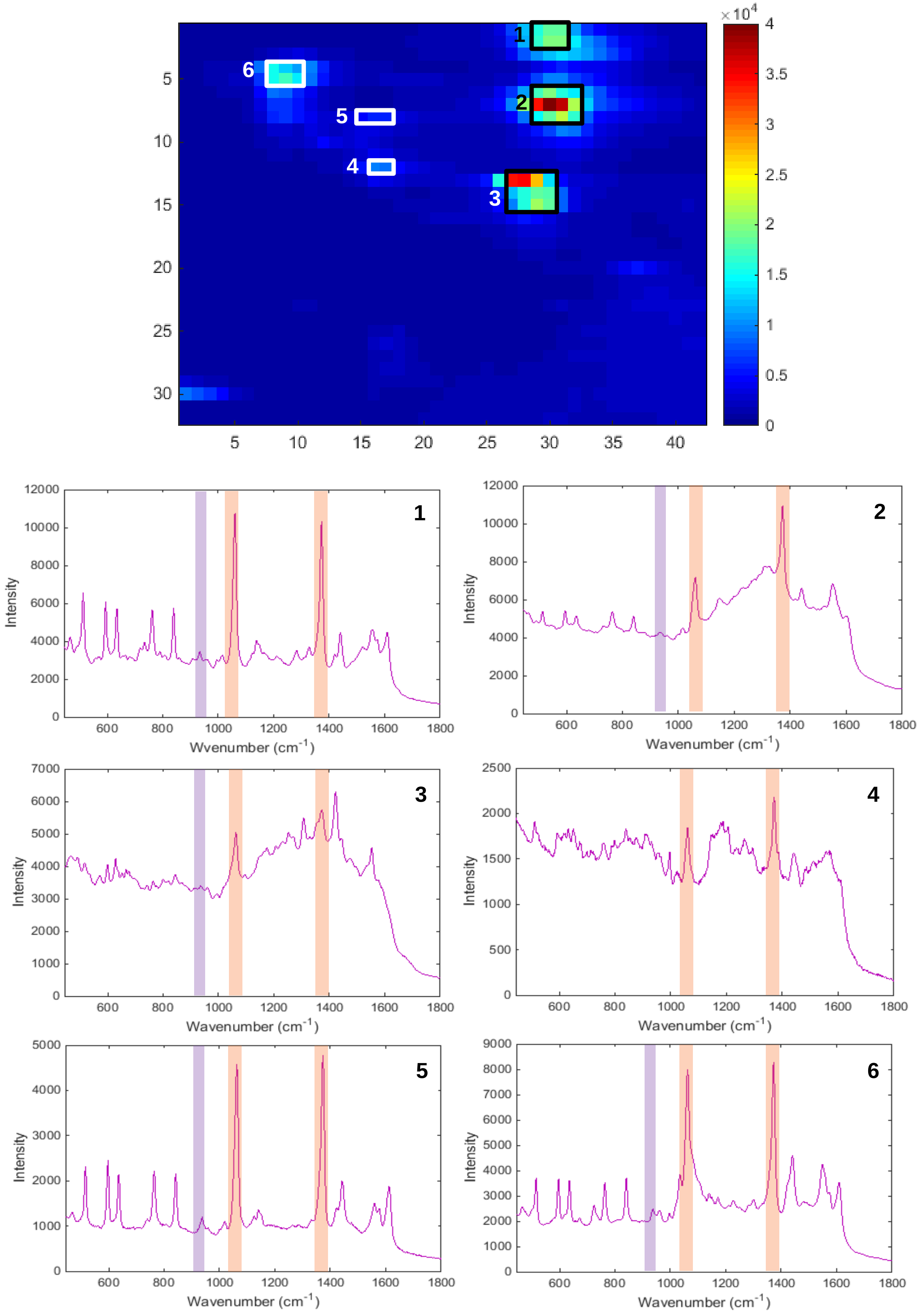

Figure 9.16: Targeting AuNPs on collagen scaffold colour map, peak area 960 cm^{-1}. Six distinct areas of interest are outlined on the map, with the averaged spectra (1-6) plotted below. Colour changes to boxes and numbers on map only for contrast/clarity. The characteristic 2-NT peaks are highlighted in orange, whilst the $-\boldsymbol{PO_4}^{-3}$ peak at 960 cm^{-1} is highlighted in purple.

All six averaged spectra confirm a presence of 2-NT. From post-processing, the second principal component map and spectra is displayed in Figure 9.17, with the areas of interest from Figure 9.16 transposed onto the map.

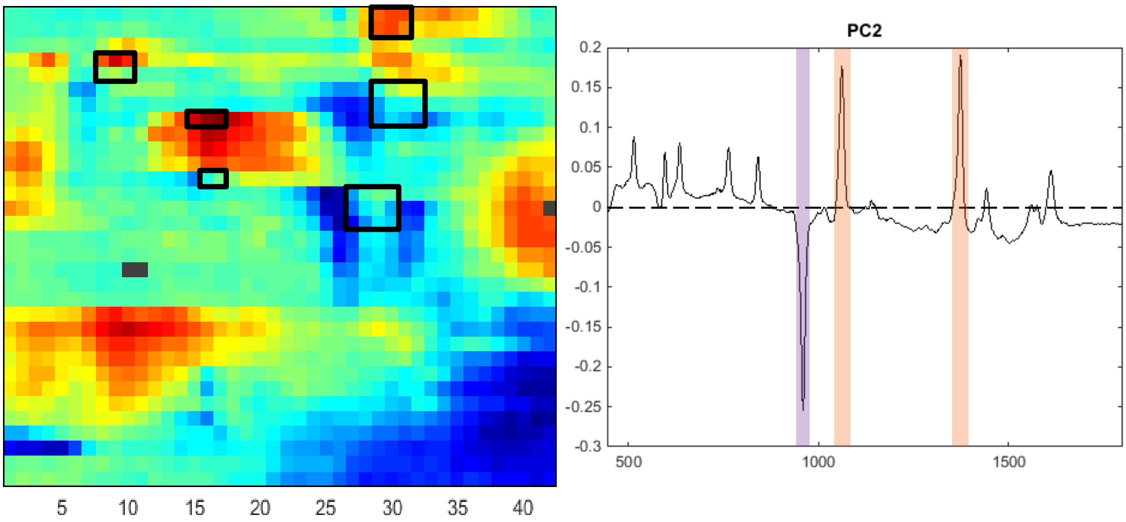

Figure 9.17: The areas of interest from Figure 9.16 have been transposed. On the PC2 spectrum, the characteristic 2-NT peaks are highlighted in orange, whilst the $\boldsymbol{-PO_4}^{-3}$ peak at 960 cm^{-1} is highlighted in purple. Pre-processing: vector normalisation and mean centring; post-processing: principal component analysis. Grey pixels = cosmic ray

Within the PC2 map, areas of interest 2 and 3, despite the 1060 cm^{-1} and 1380 cm^{-1} peak area signal intensity, shows a variance more greatly aligned to the HAP spectrum. As such, this initial map was sectioned to include areas 2 and 3 for further analysis. Figure 9.18 and Figure 9.19 displays the third and twelfth principal component colour maps and spectral loadings of the sectioned area, respectively.

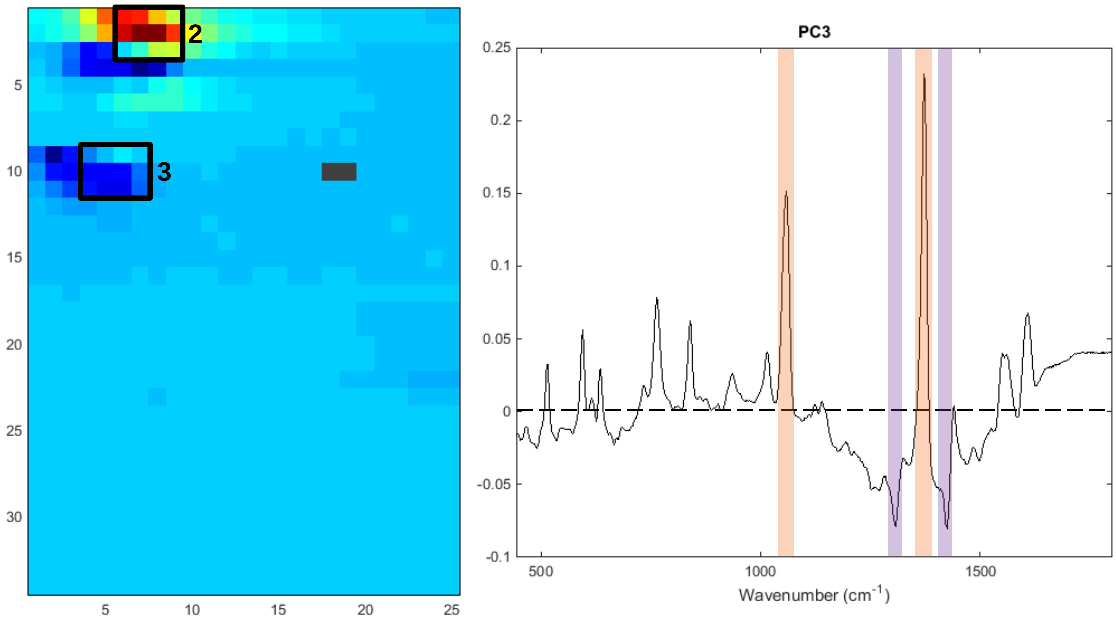

Figure 9.18: Principal component 3: colour map and loading of map resection for areas of interest 2 and 3. Red pixels correspond to 2-NT, blue pixels correspond to the $-\boldsymbol{CH_2},-\boldsymbol{CH_3}$ twisting, wagging, and/or bending at 1308 cm^{-1}, and deformation at 1425 cm^{-1} within the collagen scaffold. On the PC3 spectrum, the characteristic 2-NT peaks are highlighted in orange, whilst the $-\boldsymbol{CH_2},-\boldsymbol{CH_3}$ peaks and are highlighted in purple. Pre-processing wavenumber range, mean centring. Grey pixel = cosmic ray

In principal component analysis three, the two variable components within Figure 9.18 loading are the positive 2-NT spectrum, with the 1060 cm^{-1} and 1380 cm^{-1} peaks clearly defined. The negative peaks correspond to the $-CH_2$,$-CH_3$ twisting, wagging, and/or bending modes at 1308 cm^{-1}, and $-CH_2$ deformation at 1425 cm^{-1} within the collagen scaffold.

The presence of the $-CH_2$,$-CH_3$ vibrational modes is typical to the saturated state of the collagen scaffold; however, scaffold enhancement can only be due to the interaction between a bare AuNP surface. In relation to the PC3 map, this is specific to area of interest 3, with area 2 holding a predominantly 2-NT saturated spectral area.

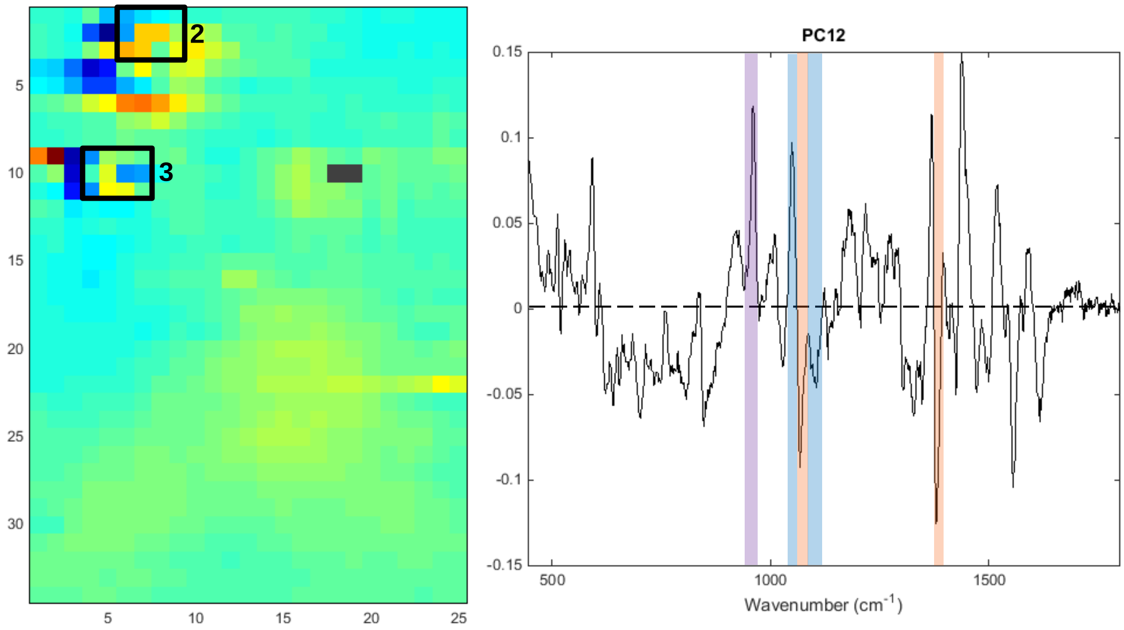

Figure 9.19: Principal component 12: map and loading of map resection for areas of interest 2 and 3. Red pixels are the 960 cm^{-1} HAP, and the blue pixels correspond to 2-NT. On the PC12 spectrum, the characteristic 2-NT peaks are highlighted in orange, the $-\boldsymbol{PO_4}^{-3}$ peak at 960 cm^{-1} is highlighted in purple, and the $-\boldsymbol{PO_4}^{-3}$ peak at 1045 cm^{-1} and $-\boldsymbol{CO}$ symmetric stretch at 1074 cm^{-1} highlighted in blue. Pre-processing wavenumber range, mean centring. Grey pixel = cosmic ray.

The twelfth principal component, pseudocolour map and spectral loading pictured above in Figure 9.19, presents the three main HAP peaks alongside the 2-NT characteristic peaks with the spectrum as a whole. The main distinctive HAP peak at 960 cm^{-1} is highlighted in purple, with the $-PO_4{}^{-3}$ peak at 1045 cm^{-1} and $-CO$ symmetric stretch at 1074 cm^{-1} highlighted in blue. Once again, the 2-NT peaks are displayed in orange, at 1067 cm^{-1} and 1379 cm^{-1}. Due to the spectral resolution of the InVia of ~2 cm^{-1}, this was not considered as a peak shift.

The presence of both the HAP and 2-NT peaks within the same spectral loading quantitively confirms the active targeting of the nanoparticles.

Further to micro-Raman mapping, the remaining colloidal solution post collagen scaffold introduction was analysed against the starting colloidal concentration. Using UV/Visible measurements and Beer Lambert Law, this determined the relative uptake for each set of colloids.

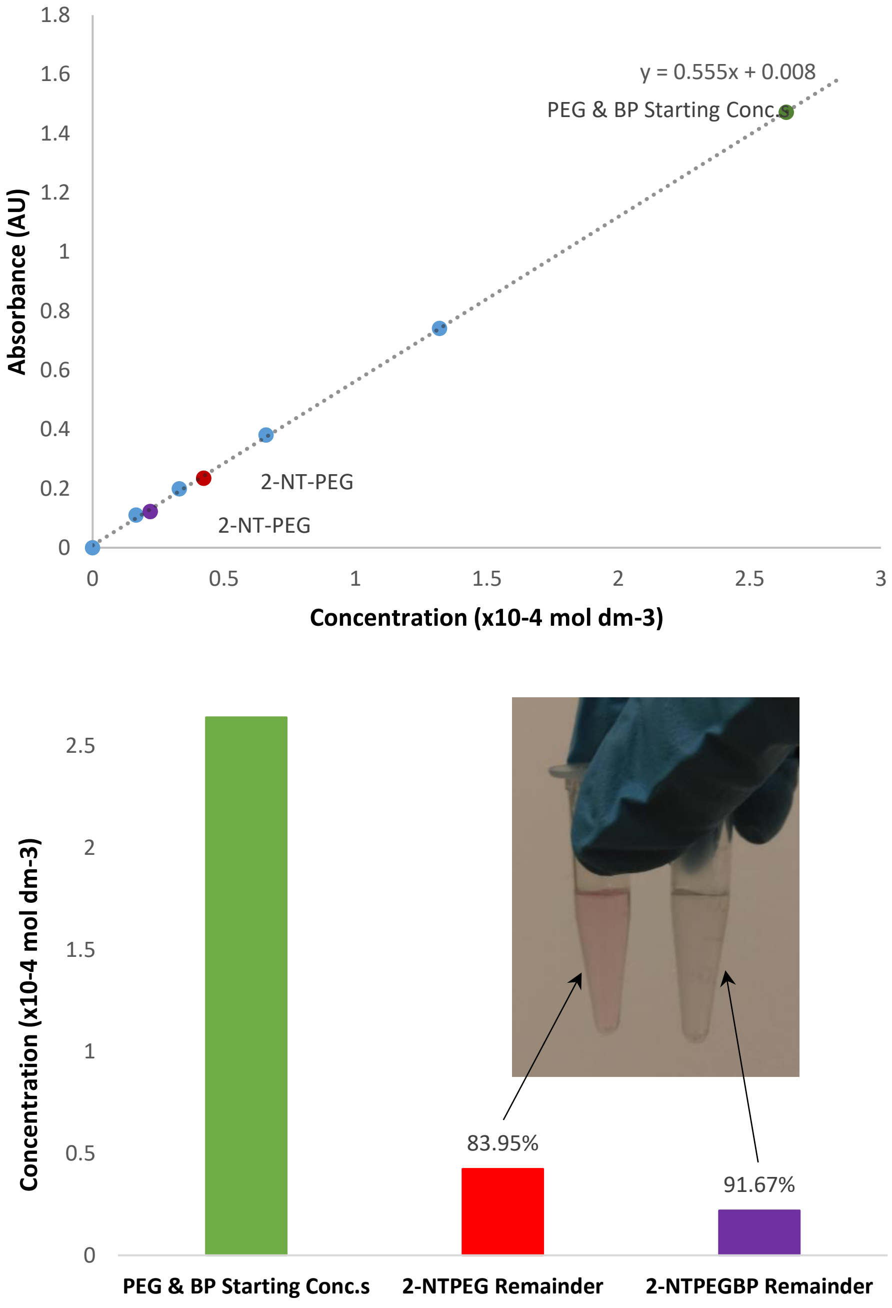

Figure 9.20: Beer-Lambert Law used to plot maximum absorbance at 546 nm against concentration; a bar graph to show the concentration of NPs remaining in solution, shown in the photo inset, with the uptake percentage added above each bar.

As seen within the insert photo in Figure 9.20, a slight colour difference between the targeting and non-targeting colloidal remains could be seen. The absorptivity defined concentration of the targeting NPs showed a 7.72% increase in collagen scaffold uptake compared to non-targeting. The sponge-like nature of the scaffold is a factor to consider in the overall colloidal uptake.

9.5 Colloid Heating

Measurement of the 2-NT-PEG NPs at depth within the block breast phantoms was unsuccessful. The relative number of 2-NT molecules on the colloid surface of the pure RR-AuNPs in comparison to the successfully functionalised 2-NT-PEG AuNPs is at a ratio of 33:1, or 81,855 molecules per AuNP to 2,474 molecules, respectively. As a point of interest, the 2-NT-PEG AuNPs were synthesised with 58,978 PEG molecules per NP. As such, the dose of functionalised NPs required for extrinsic SERS at depth would be far out of the possible biocompatible range.

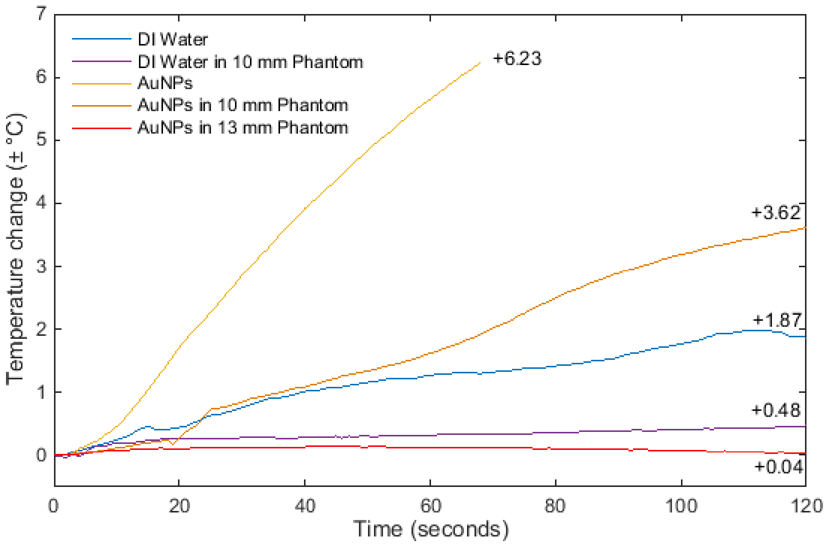

Figure 9.21: A graph to show the temperature change, in Celsius, of the functionalised nanoparticles (2.91×10^{10} NPs) outside of and within different phantom thicknesses. DI water was selected as the control. The overall change in temperature for each has been labelled next to the corresponding line.

Despite this, the diagnostic quality in terms of relative 2-NT-PEG AuNP heating, and hence unwarranted heat transfer to surrounding tissue, was considered. Figure 9.21 shows the temperate change over two minutes of solely the AuNPs (2.91 x 10^{10} NPs in 1.2 mL), and the AuNPs within 10 mm of breast phantom, and 13 mm of breast and skin phantom. DI water was selected as the control. To preserve the functionality of the NP probes, the measurement outside of the phantom was cut short after a temperature of 30°C was reached.

The dramatic decrease in 2-NT-PEG AuNP temperature from the 10 to 13 mm phantom is due to the MFP of the phantom (0.1 mm) leading to mostly scattering, reducing the light flux reaching the extended colloidal position. The change in light intensity (mW) from the laser interface (I) to the colloid location (I_O) is determined using the following equation:

$$I_O = Ie^{-(\mu_s+\mu_a)x} \tag{33}$$

whereby the intrinsic scattering and absorption coefficients (μ_s and μ_a) are multiplied by the overall change of material thickness in mm (x). The μ_s of the breast and skin phantoms are taken from the supplied literature results and calculated, from the known anisotropy of TiO_2 (0.93), to be 8.05 cm^{-1} and 13.91 cm^{-1} respectively. The μ_a of both phantoms is set at 0.05 cm^{-1}.

Hence, the change in laser intensity from the interface (300 mW) to the colloid position within the 10 mm phantom is described as follows:

$$\begin{gathered} I_{colloid} = 300e^{-(\mathbf{8.05+0.05})\mathbf{0.5}} \\ I_{colloid} = 5.23\ mW \end{gathered} \tag{34}$$

The light intensity change on the optical axis from interface to collection through the 13 mm phantom is detailed in the exploded view in Figure 9.22.

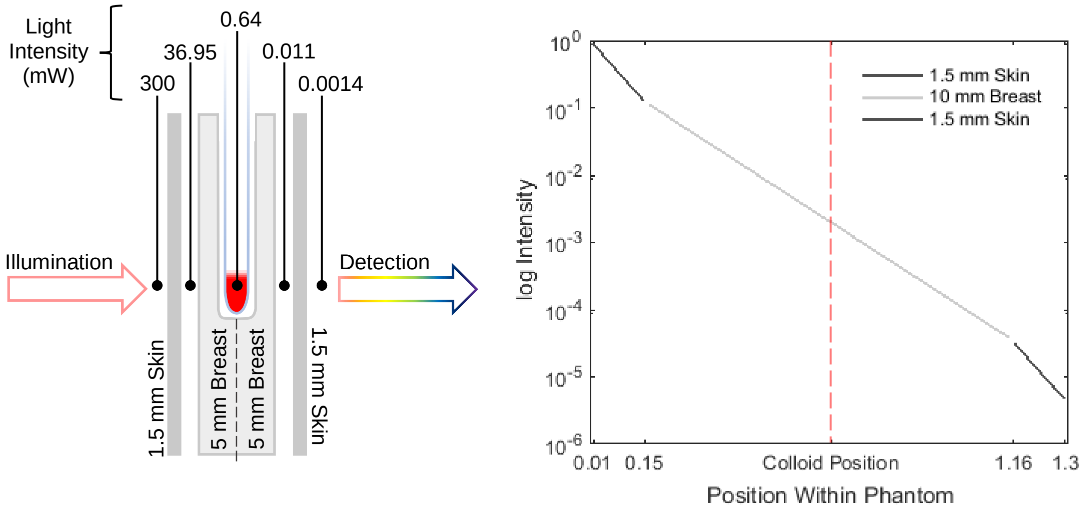

Figure 9.22: Exploded view of the 13 mm breast and skin phantom with a 2-NT-PEG AuNP NMR tube inclusion. The calculated intensity of light after each phantom layer, and at the colloidal position, is depicted above the phantom illustration. The logarithmic light intensity graph across the phantom at 0.1 mm intervals, the mean free path of the phantom, is also plotted, with the colloid position highlighted with a red dashed line.

Overall, a 4.586 mW difference in light intensity between the two phantom thicknesses is founded, clarifying the large drop-off in colloidal heating. From an initial illumination of 300 mW, only 1.4 x 10^{-3} mW transmissions through the phantom to the detector. Extrapolated to the 30 mm morphological breast phantom, the intensity is further reduced to 1.45 x 10^{-9} mW.

9.6 Discussion and Conclusions

The 2-NT-PEG-Bisphonate labelled AuNPs have been shown the actively target the hydroxyapatite biomolecules which present at elevated levels within breast microcalcifications signalling malignancy, especially within cases of DCIS. The absence of HAP binding with the 2-NT-PEG AuNPs leads to the conclusion that the affinity of the 2-NT-PEGNP AuNPs is due to the present alendronate moiety.

The synthesis of the 2-NT-PEG-BP requires adjusting, with an increased ratio of 2-NT : PEG molecules required, for the NPs to be considered for SESORS. This would require further experimentation of the synthesis recipe to garner an increased RR signal whilst maintaining a brush-like PEG formation.

A complete remodel of the NP design could increase their effectiveness at depth. For example, the use of multi-layered, nanomatryoshka AuNPs would: increase the enhancement capabilities of the RR, with the additional remit for multiplexed imaging; allow full surface PEG coverage for increased biocompatibility; and introduce a possible photothermal aspect to the NP probes.[295,296] This would vastly improve the functionality of the targeting AuNPs, a possibility to be explored within future works.

Micro-Raman mapping proved difficult in terms of laser power adjustments to reduce the evaporation speed of the collagen scaffold and likelihood of AuNP burning. The use of a low lines/mm grating to visualise the Stokes scattering would quantification of the level of temperature increase reached. This would give verification of the thermo-therapeutic capabilities of the targeting AuNPs if used in conjunction with a Raman probe, for example.

The active targeting molecule alendronate is non-specific to solely breast microcalcifications, binding to areas of osteoporosis and metastases within bone. This could be useful in ascertaining if the breast tumour has metastasised to the bone, with the nanoparticles providing excellent contrast for further x-ray imaging. The multi-faceted capabilities of these AuNPs within both Raman and X-ray imaging aligns them as a truly clinically viable, diagnostic probe.

10. Discussions, Conclusions and Future Work

The main focus of this thesis has been:

1. Nanoparticle design for diagnostic use in considering Raman signal, functionality and biocompatibility, in the selection of 80 nm gold nanospheres and the use of PEG.
2. The use of turbid, multi-layered optical phantoms as a tissue representative.
3. Demonstrating the first use of SESORS in anatomical tissue phantoms for breast imaging
4. SESORS imaging development including protocols for an automated mapping system
5. Exploring the translation requirements for the transmission Raman spectroscopy technique within the current practice of mammography, aiming to streamline the diagnostic pathway

Discussions

Prior to nanoparticle testing, a careful balance in attaining the maximum Raman signal possible within the remit of biocompatibility was required.

Initially the material, size and shape were considered. The identification of gold as an inert material with low cytotoxicity deemed it more favourable than silver, despite a reduced localised surface plasmon resonance λmax.[109,115] AuNP size and shape selection considered the LSPR peak position, with a red-shift occurring with the increase of size.[121,122,226] In focussing on the production of a diagnostic tool, the selection of the nanosphere shape, over the increased photothermal potential of the nanorods or nanoshells,[141,142,145] was made. The enhanced plasmonic effects produced by larger Au nanospheres makes them preferable for biomedical applications, whereby the selected 830 nm illumination wavelength lies within the

NIR biological window.[146–148] The adsorption affinity of Raman reporters upon the surface of AuNPs ≤50 nm was also noted in the size selection process.[110,139,140] Finally, the evaluation of the pharmacokinetics of AuNPs (≤8 nm undergoing glomerular filtration and >100 nm accumulating within the Kupffer cells of the liver)[176,177,179,180,297–300] and the favourable enhanced permeability and retention effect of NPs between 10 – 100 nm,[201,209,210] gold nanospheres 80 nm in size were selected.

To create a consistent, analytical SERS probe, the AuNPs employed need a high level of uniformity, being monodisperse in nature.[109,115] The certainty of this within the on-site synthesised AuNPs could not be guaranteed and, as such, commercially purchased, citrate-capped AuNPs were selected for use. 2-NT, 4-MBA and 4-ATP were selected as Raman reporters, known to have effective gold-thiolate and acetamido nitrogen binding mechanisms, and for previous use within NP biocompatibility studies.[110,120,206,228–230] The low levels of colloid heating at depth confirmed the diagnostic potential of these AuNPs. To further explore biocompatibility Polyethylene Glycol, as a known stealth or "cloaking" agent, [200,201] was introduced in ratio with the 2-NT RR. This combination was explored to study the effect on signal at depth, which was founded to be unobtainable.

Further development of the 2-NT-PEG AuNPs lead to an additional functionalisation with a bisphosphonate, alendronate. Bisphosphonates have a high affinity for the bone mineral hydroxyapatite, found to be present within Type II, $-PO_4{}^{3-}$ B-type substitution breast microcalcifications, most commonly associated with neoplasms.[49,50] Current literature from Cole et al has shown the successful binding of PEG-alendronate functionalised AuNPs to microcalcifications and bone tumours, which then act as an X-ray contrast agent within mammography or CT imaging.[59,231,232] The current method used in confirming the successful functionalisation and selective binding of these PEG-BP AuNPs is through the micro-CT imaging of *in vitro* and *in vivo* mouse models.

The application of the 2-NT, PEG and BP created a biocompatible, actively targeting and Raman sensitive AuNP probe – a novel combination. Consideration into the chain length of the PEG, resolved at 2000 Da,[232] and the positioning of the targeting moiety, decided upon placement at the distal end of the PEG,[233–235] was undertaken. TEM imaging confirmed the carbodiimide chemistry undertaken to adjoin the alendronate molecule had affected the gold surface, although this could not confirm the success of functionalisation. As such, a HAP infused collagen scaffold, Hydroxycoll, was obtained through a Material Transfer Agreement, see Appendix, and saturated with both the targeting and non-targeting PEGylated NPs. Micro-Raman maps, post-processed using Principal Component Analysis, quantified and confirmed (the absence of the 2-NT-PEG AuNPs in binding to the HAP) the combined presence of the 2-NT and HAP spectral features with the 2-NT-PEG-BP AuNPs. concluding that the BP molecule had undergone successful binding to the PEG distal end. Evaluation of the remaining colloidal solution using Beer-Lambert Law further solidified the binding mechanism at work, with the remaining concentration of the 2-NT-PEG AuNPs 7.72% greater. This synthesis success opens the door to further consideration into the use of RR-PEG-BP functionalised AuNPs within a combined transmission Raman spectroscopy – mammographic imaging system, especially for patients with dense breast tissue.

Requiring the NPs to remain within the biocompatible remit and the laser wavelength within the NIR range limited the level of SERS enhancement which could have been experimentally produced. As such, the transmission depths achieved within this thesis remained biologically relevant. In relation to the average compressed breast thickness of ~50 mm in the UK, over half of the population would not be sufficiently catered for under the current RR AuNP design and laser wavelength. As such, further modifications to both areas would need to be undertaken, blue-shifting the laser wavelength further into the centre of the NIR biological window and adjusting the NP size to RR ratio.

The use of turbid phantoms within Raman applications is a poorly explored area, with homogeneous Intralipid often selected for simple phantom work.[250] Having a short working life-span and inability to form realistic complexity, liquid phantoms are fast being replaced with stable, solid phantoms of polydimethylsiloxane. These can be cast to the required shape with an adjustable quantity of scattering and absorption agents added.[249,252] With this, an introduction of multiple-tissue layers, with varying optical properties, is viable, enhancing the realism of the phantoms. One such example of this is the use of spin-coating to simulate the epithelial tissue layers of the skin and bladder.[272,275] Here, the creation of both breast and skin tissue phantoms through pour-casting into 3-D printed moulds was explored and tested. As discussed previously, the use of double integrating spheres would enable the measurement of the absorption and scattering coefficients of the phantom materials. This, however, required a sophisticated Monte Carlo photon migration model to provide the coefficients following back projection of the integrating sphere measurements on carefully prepared thin samples. In its place, care was taken to use protocols found within the literature to adjust the mg/mL concentration of titanium dioxide to PDMS, providing an appropriate set of optical properties relevant to post-menopausal breast and skin tissue.

To efficiently analyse the breast phantoms within the transmission Raman set-up, a new mapping system was required. The design and implementation of the automated mapping system required several skill sets – optomechanical hardware construction, MATLAB and Andor software programming knowledge, and npn transistor electronic circuitry building. This delivered an efficient and rapid automation protocol. The main advantages of this system included an increase in workload capacity, and the production of highly specific and large data sets for further analytical "manipulation". Further and continued use of this automated set-up across institutions would cement the protocol as a highly effective solution for mapping purposes within numerous, open-optics settings.

Conclusions

The main aims of this thesis were to: confirm the use of turbid, multi-layered optical phantoms as viable tissue representatives; design and functionalise diagnostic gold nanoparticles with biocompatibility in mind; and demonstrate the potential for the incorporation of a SESORS transmission Raman spectroscopy technique within the current mammographic system, identifying the labelled AuNPs at varying depths.

The ability to produce, and reliably replicate, phantoms of both breast and skin tissue was founded. The use of high-temperature 3D printed moulds, designed in semi-infinite and morphologically representative ways, successfully enabled consistent phantom production. In adjusting the concentration of TiO_2 to satisfy the reduced scattering optical properties of post-menopausal breast and skin tissue, multi-layered phantoms could be realised.

It was concluded that within the remit of a low human equivalent dose, three Raman-reporter labelled AuNPs could be distinguished within ≤33 mm turbid phantoms. Under mammographic compression the average of breast thickness of women in the UK is ~50 mm, however this is further reduced with the use of spot compression on areas of interest.[87] As such, this proof-of-concept phantom size is within the range of applicability, although an increased thickness would translate to a larger portion of the population. The Raman signal intensities obtained from the 4-MBA and 4-ATP were markedly lower than that of the 2-NT, owing to its affinity to and compact orientation upon the AuNP surface. The relative depth signal profile of each NP probe within the sample was also established, and found to be in agreement with the findings from Vardaki at el.[278] Spectral interferences obtained from the inherent absorption and characteristic Raman peaks of the phantom material affected the RR peak height ratios between the high and low wavenumbers. As such, system adjustments concerning the preferable laser wavelength, working around the inherent material properties whilst ensuring the illumination and collection photon remain within the NIR window, must be made.

The functionalised 2-NT-PEG-BP AuNPs were confirmed to be actively targeting, with the present alendronate moiety having a high affinity to the HAP present within the Hydroxycoll collagen scaffold. This clearly demonstrates the successful creation of an AuNP probe with novel functionalisation. The multi-faceted capabilities of the 2-NT-PEG-BP AuNPs for both Raman and X-ray imaging, albeit requiring further exploration in design and biocompatibility, aligns them as a potentially clinically viable, diagnostic probe. Clearly the application of such a nanoparticle requires much greater safety analysis, considered in the Future Work sub-section of this chapter.

The integration of new techniques within the clinical setting requires a high level of diagnostic accuracy. A critical appraisal of current diagnostic techniques versus SESORS is as follows:

- MRI is a sought-after technique, providing highly sensitive images for diagnosis, although it comes at a large cost with extended waiting times. The use of gadolinium contrast is successful in increasing hydrogen relaxation times, providing enhanced clarity of lesions, however the agent is inherently toxic causing kidney tissue scarring.

- Mammography provides the gold standard of imaging; it is however an inaccurate technique for patients with dense breasts, lacks specificity in defining microcalcifications, and requires ionising x-radiation. However, the use of Digital Breast Tomosynthesis is improving the sensitivity of cancer diagnosis.

- Ultrasound is a non-ionising technique, providing rapid imaging for patients with dense breasts, with new advances into the use of higher frequency probes (~60 MHz) to detect microcalcifications which cannot be visualised within the standard frequency range. Biopsy, taken under local or general anaesthetic, is still required to definitively determine the type of microcalcification, HAP or calcium oxalate prevalent.

- Histopathology as the gold standard for micro-level tissue interpretation is gaining inter-practitioner accuracy, yet the required biopsies necessitate anaesthesia with possible repeat procedures essential if x-ray imaged microcalcifications are not represented within the specimen.

SESORS, working with extrinsic SERS AuNPs has a consistent characteristic Raman spectrum, uninfluenced by the biochemical signatures of the surrounding tissues, with multiplexed imaging capabilities using non-ionising spectroscopy. This however, is reliant on several concerns. The surface chemistry of the gold-Raman reporter bond must be impervious, and fully label the complete AuNP surface. At a in vivo level, the EPR effect must alone accumulate a high concentration of low dosed AuNPs within the malignant tissues, relying on minimal Mononuclear Phagocyte System clearance. Further biocompatibility using PEG and active targeting functionalisation requires more in-depth study to determine the success of signal recovery at depth.

This work has highlighted the need to focus on employing techniques which can be easily translated to the current diagnostic workflow. By employing transmission Raman and designing the breast phantom as if under mammographic compression, this enables detailed testing and device development to assist the easier translation of the technique as an adjunct for mammography. Incorporation of novel spectroscopic techniques within clinical diagnostic methods, as opposed to replacing them, propagates the likely acceptance into clinical practice. Furthermore, this would lessen the impact on current diagnostic pathways, reducing patient result wait times between several techniques and hence shortening disease development.[64] Other considerations crucial to evaluate for the translation of new techniques to future, clinically minded work include: health economics (Is the expense of the technique unaffordable? Would it be manageable or cost effective on a specific clinical pathway, such as familial breast cancer patients?); diagnostic accuracy (Does the SESORS technique provide highly sensitive and specific results, and is a skilled professional required to translate them?); and, in the actuation of the technique, medical device ergonomics and safety, for both practitioner and patient.

Future Work

The work of this thesis is a step on the pathway to the use of gold nanoparticles in medical diagnostics, with particular focus on SESORS. The next steps that should be considered to develop, test and translate this approach would be as follows.

Nanoparticle Development

The configuration of the AuNPs into novel designs such as those found in a multi-layered nanomatryoshka should be considered.[295,296] This would create the possibility of a more theranostically minded probe, applicable as both a diagnostic (inner AuNP) and photo-thermal therapeutic (Au shell) probe. Ultimately, this would eliminate the concerns surrounding the ratio between Raman-reporter:PEG molecules, increasing Raman signal intensity and the brush-like PEG conformation for biocompatibility simultaneously. Furthermore, the encasing of RR would allow the exploration of multiplexed imaging of cytotoxic reporters, such as malachite green isothiocyanate or crystal violet, as known reporter molecules with large Raman cross-sections. This may bring about the possibility for multiplexed depth analysis.

The exploration of colloid heating could then be analysed with the thermo-therapeutic capabilities in mind. Within the micro-Raman system, the addition of a notch filter could enable the measurement of both the Stokes and anti-Stokes lines, enabling direct quantification of the temperature increase at the NP surface level.

Returning to the current AuNP designs, the dose model used within this thesis was based upon the low Human Equivalent Dose from studies using rat and pig animal models.[166,167,176] As such, the biocompatible nature of the functionalised AuNPs could be further explored. For example, introducing the AuNPs within a metastatic breast cell 3D model, using the Hydroxycoll collagen scaffold as a support network. This would be the first step towards determining the pharmacokinetics of the AuNPs within malignant breast tissue, and hence the relative levels of biocompatibility.

Looking further forward, the clinical translation of gold nanoparticles requires an experimental testing and trail-based pathway, such as the one seen in Figure 10.1.

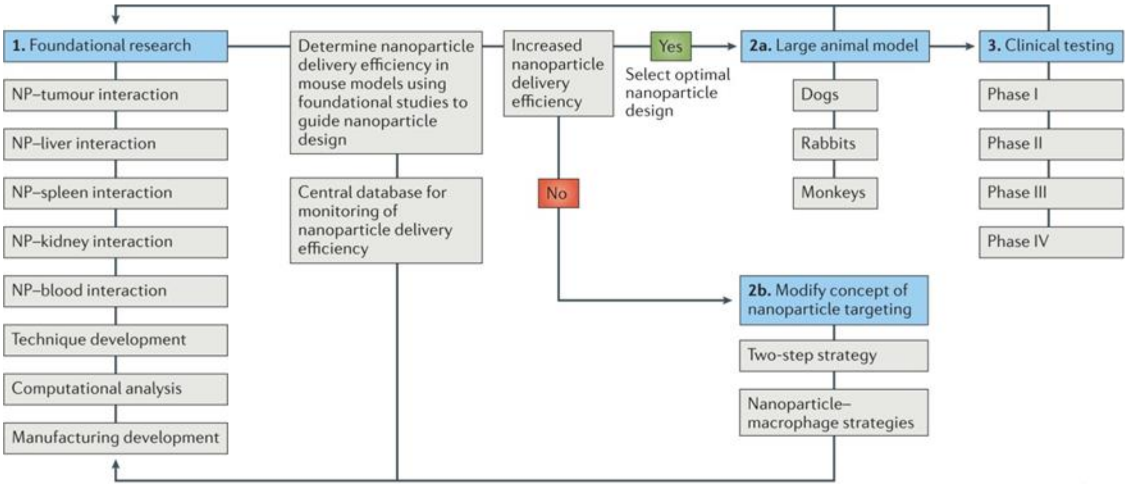

Figure 10.1: A proposed guideline strategy for nanoparticle delivery research.[308]

In developing and adjusting the delivery efficiency of a NP, the use of mouse models is paramount in determining the circulation half-life and biocompatibility of the design. As previously discussed, the use of swine for the large animal model is considered more applicable for the transferability of NPs to a Human Equivalent Dose, and as such would be considered alongside dogs, rabbits and monkeys.

Progressing to the clinical testing phase, consideration of patient suitability for the trial is of the utmost importance. Initially, patients selected for trial must fit under the "inclusion criteria" based on life expectancy, including for other medical conditions, previous treatment received and general health.[319] Patients with advanced cancers are recommended for trials involving new therapies or techniques, for example immunotherapy (the treatment of disease by inducing/enhancing/suppressing an immune response), due to the experimental nature of the therapy.[319-321] FDA approval (US) – nanomedicines (liposomes and polymer micelles) and magnetic NPs for imaging in clinical phases; estimated 5% approval rate for oncology drugs, costing $1 billion total cost to make it through all 4 Phases.[301]

Finally, the next steps in realistic phantom design for further development of the approach could be improved upon using the spin-coating technique in creating discrete layers of dermis, epidermis, adipose and glandular tissues.[272,275] Furthermore, the addition of static occlusions within the phantoms, such as HAP with varying levels of carbonate substitution for a range of microcalcifications, could also be explored.

Phantom Development

The breast phantom within this study was adjusted to represent Caucasian, post-menopausal breast tissue. Altering the absorption properties of the skin layer, representing distinct levels of pigmentation, and scattering properties of the breast tissue, to be applicable for pre-menopausal breast tissue, would increase phantom applicability across different races and patient demographics.

Testing of other clinically transferrable Raman techniques could also be explored, such as with the needle probe method.[159,160] Although a comparatively invasive technique in comparison to transmission Raman spectroscopy, this method would provide highly sensitive results in determining the presence of the targeted AuNPs. A change in phantom material selection, or silicone base to curing agent ratio, would lead to the close resemblance of the natural feel and haptic feedback of breast. This would cover the optical, morphological and tactile properties of the breast to produce hyper realistic phantoms. Additionally, the needle probe has the capability of harnessing the photo-thermal potential of the nanospheres, attainable with a close illumination-to-AuNP working distance.

Appendix

Materials Transfer Agreement

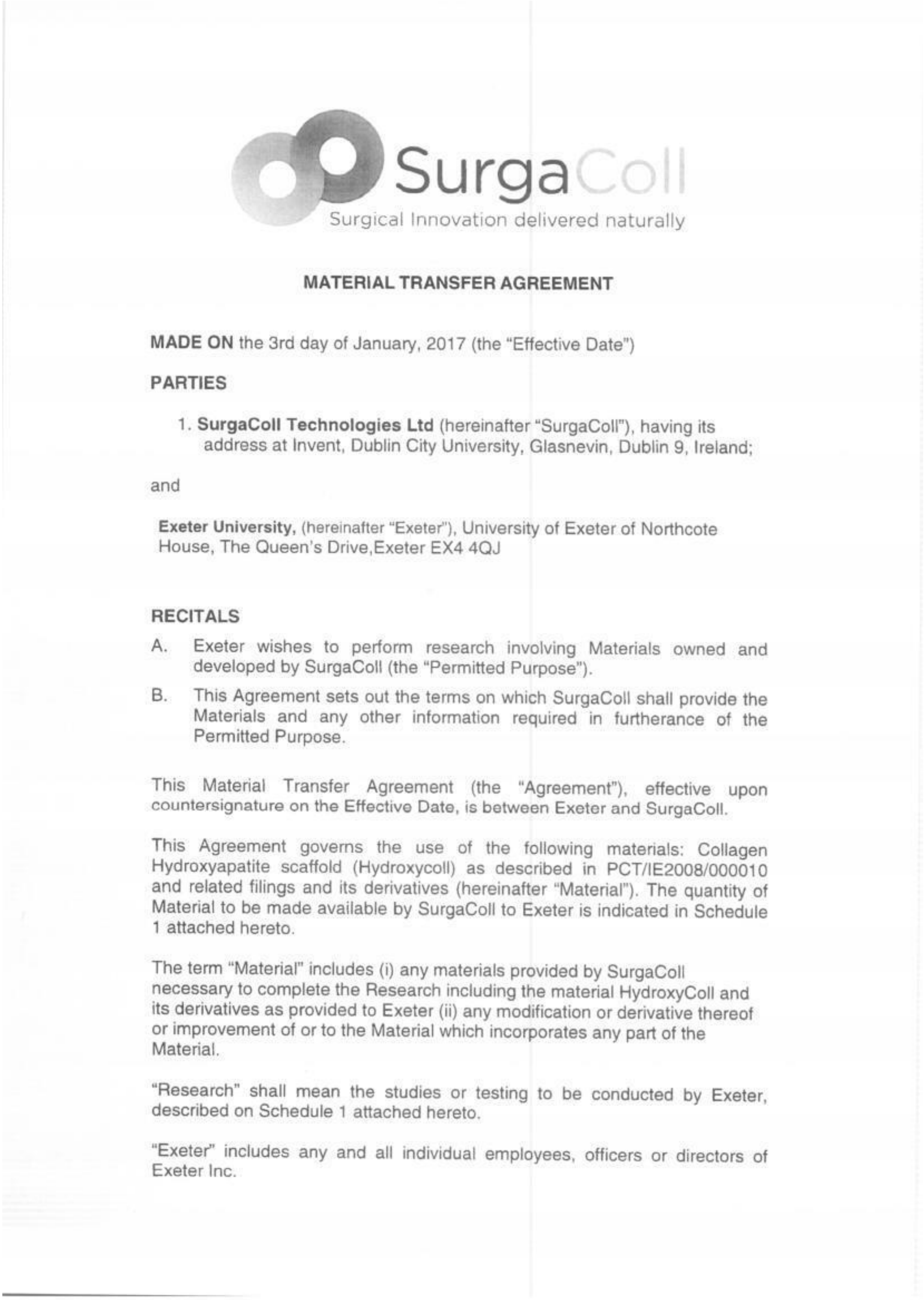

SurgaColl
Surgical Innovation delivered naturally

MATERIAL TRANSFER AGREEMENT

MADE ON the 3rd day of January, 2017 (the "Effective Date")

PARTIES

1. **SurgaColl Technologies Ltd** (hereinafter "SurgaColl"), having its address at Invent, Dublin City University, Glasnevin, Dublin 9, Ireland;

and

Exeter University, (hereinafter "Exeter"), University of Exeter of Northcote House, The Queen's Drive,Exeter EX4 4QJ

RECITALS

A. Exeter wishes to perform research involving Materials owned and developed by SurgaColl (the "Permitted Purpose").

B. This Agreement sets out the terms on which SurgaColl shall provide the Materials and any other information required in furtherance of the Permitted Purpose.

This Material Transfer Agreement (the "Agreement"), effective upon countersignature on the Effective Date, is between Exeter and SurgaColl.

This Agreement governs the use of the following materials: Collagen Hydroxyapatite scaffold (Hydroxycoll) as described in PCT/IE2008/000010 and related filings and its derivatives (hereinafter "Material"). The quantity of Material to be made available by SurgaColl to Exeter is indicated in Schedule 1 attached hereto.

The term "Material" includes (i) any materials provided by SurgaColl necessary to complete the Research including the material HydroxyColl and its derivatives as provided to Exeter (ii) any modification or derivative thereof or improvement of or to the Material which incorporates any part of the Material.

"Research" shall mean the studies or testing to be conducted by Exeter, described on Schedule 1 attached hereto.

"Exeter" includes any and all individual employees, officers or directors of Exeter Inc.

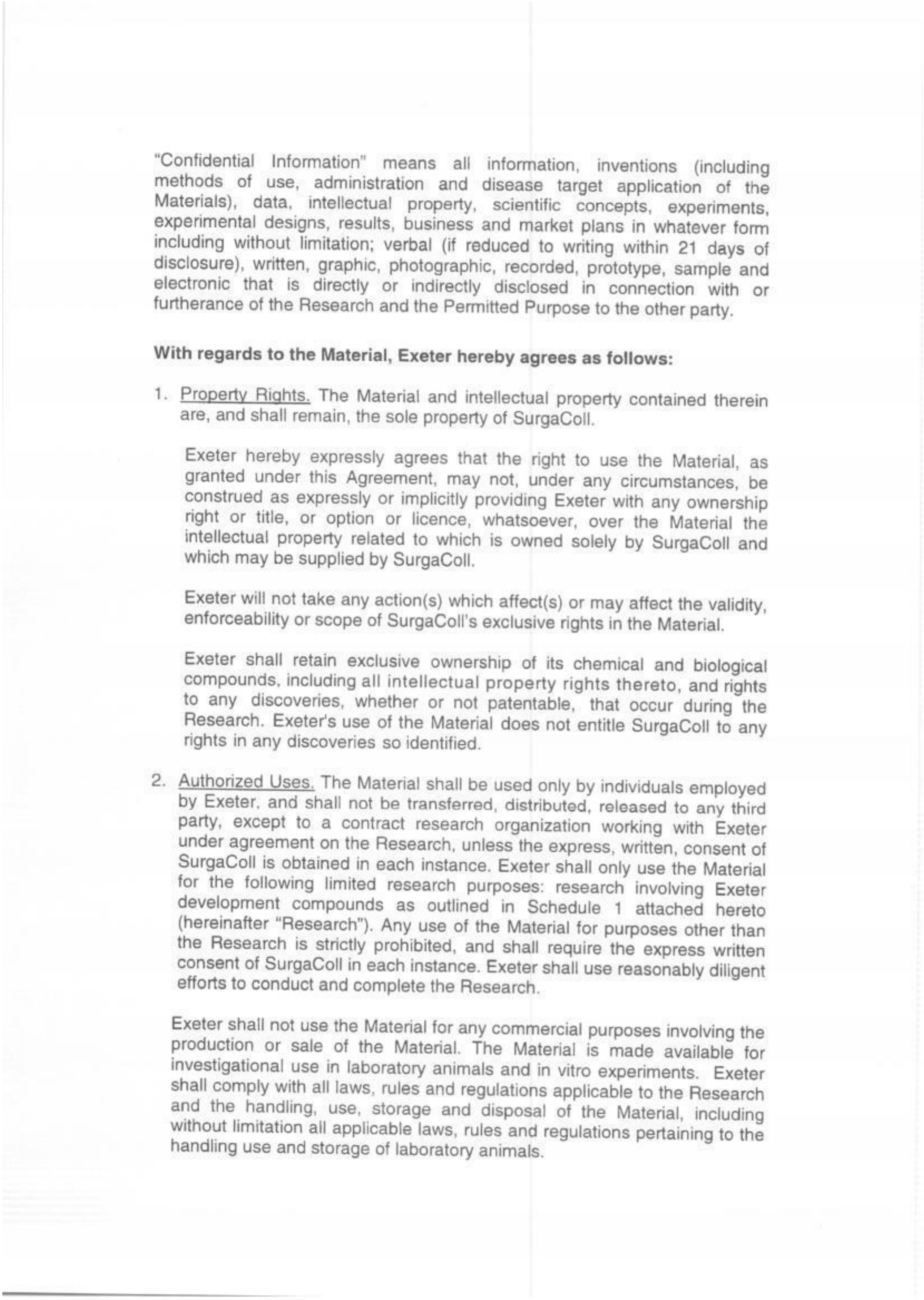

"Confidential Information" means all information, inventions (including methods of use, administration and disease target application of the Materials), data, intellectual property, scientific concepts, experiments, experimental designs, results, business and market plans in whatever form including without limitation; verbal (if reduced to writing within 21 days of disclosure), written, graphic, photographic, recorded, prototype, sample and electronic that is directly or indirectly disclosed in connection with or furtherance of the Research and the Permitted Purpose to the other party.

With regards to the Material, Exeter hereby agrees as follows:

1. Property Rights. The Material and intellectual property contained therein are, and shall remain, the sole property of SurgaColl.

   Exeter hereby expressly agrees that the right to use the Material, as granted under this Agreement, may not, under any circumstances, be construed as expressly or implicitly providing Exeter with any ownership right or title, or option or licence, whatsoever, over the Material the intellectual property related to which is owned solely by SurgaColl and which may be supplied by SurgaColl.

   Exeter will not take any action(s) which affect(s) or may affect the validity, enforceability or scope of SurgaColl's exclusive rights in the Material.

   Exeter shall retain exclusive ownership of its chemical and biological compounds, including all intellectual property rights thereto, and rights to any discoveries, whether or not patentable, that occur during the Research. Exeter's use of the Material does not entitle SurgaColl to any rights in any discoveries so identified.

2. Authorized Uses. The Material shall be used only by individuals employed by Exeter, and shall not be transferred, distributed, released to any third party, except to a contract research organization working with Exeter under agreement on the Research, unless the express, written, consent of SurgaColl is obtained in each instance. Exeter shall only use the Material for the following limited research purposes: research involving Exeter development compounds as outlined in Schedule 1 attached hereto (hereinafter "Research"). Any use of the Material for purposes other than the Research is strictly prohibited, and shall require the express written consent of SurgaColl in each instance. Exeter shall use reasonably diligent efforts to conduct and complete the Research.

Exeter shall not use the Material for any commercial purposes involving the production or sale of the Material. The Material is made available for investigational use in laboratory animals and in vitro experiments. Exeter shall comply with all laws, rules and regulations applicable to the Research and the handling, use, storage and disposal of the Material, including without limitation all applicable laws, rules and regulations pertaining to the handling use and storage of laboratory animals.

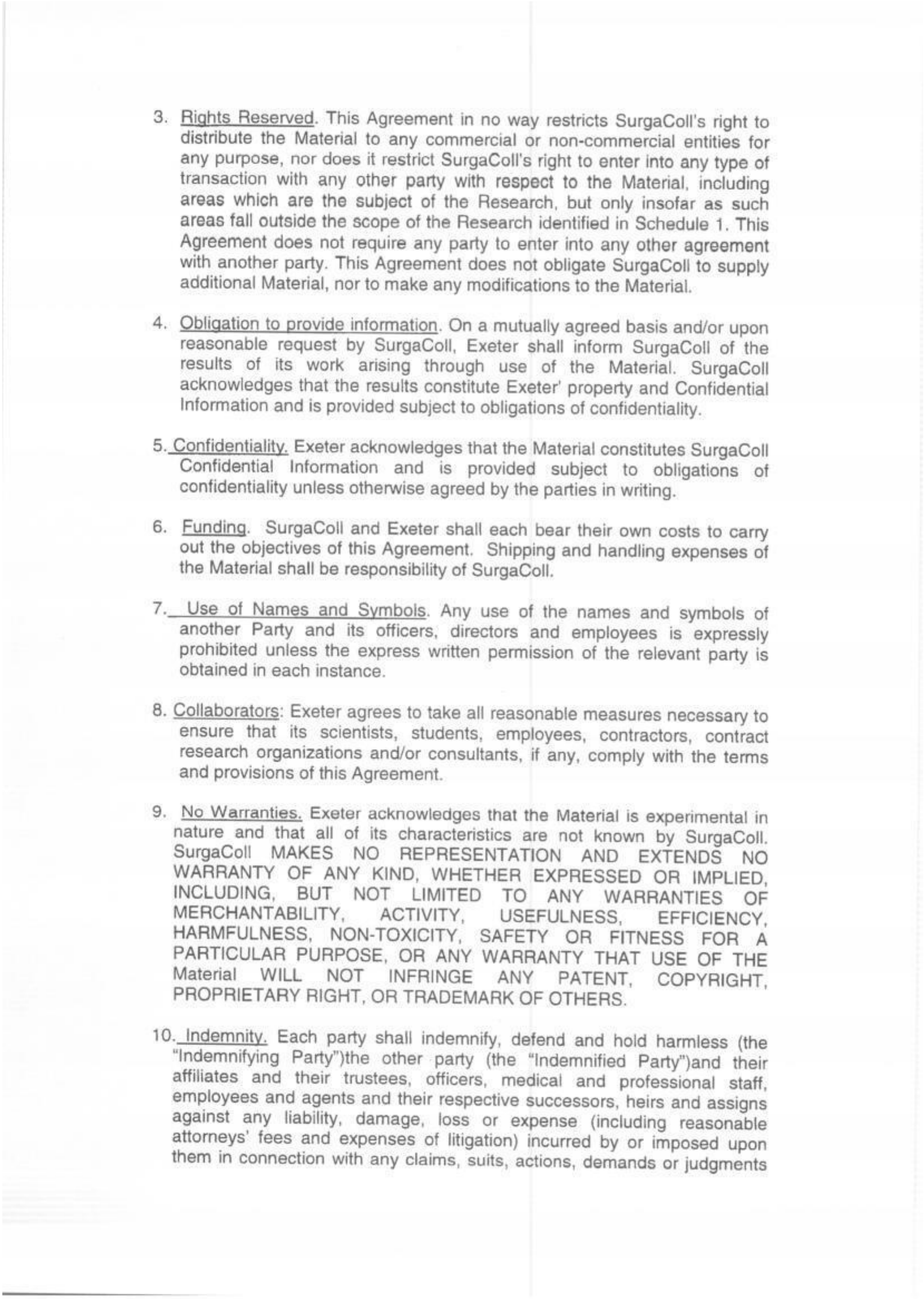

3. Rights Reserved. This Agreement in no way restricts SurgaColl's right to distribute the Material to any commercial or non-commercial entities for any purpose, nor does it restrict SurgaColl's right to enter into any type of transaction with any other party with respect to the Material, including areas which are the subject of the Research, but only insofar as such areas fall outside the scope of the Research identified in Schedule 1. This Agreement does not require any party to enter into any other agreement with another party. This Agreement does not obligate SurgaColl to supply additional Material, nor to make any modifications to the Material.

4. Obligation to provide information. On a mutually agreed basis and/or upon reasonable request by SurgaColl, Exeter shall inform SurgaColl of the results of its work arising through use of the Material. SurgaColl acknowledges that the results constitute Exeter' property and Confidential Information and is provided subject to obligations of confidentiality.

5. Confidentiality. Exeter acknowledges that the Material constitutes SurgaColl Confidential Information and is provided subject to obligations of confidentiality unless otherwise agreed by the parties in writing.

6. Funding. SurgaColl and Exeter shall each bear their own costs to carry out the objectives of this Agreement. Shipping and handling expenses of the Material shall be responsibility of SurgaColl.

7. Use of Names and Symbols. Any use of the names and symbols of another Party and its officers, directors and employees is expressly prohibited unless the express written permission of the relevant party is obtained in each instance.

8. Collaborators: Exeter agrees to take all reasonable measures necessary to ensure that its scientists, students, employees, contractors, contract research organizations and/or consultants, if any, comply with the terms and provisions of this Agreement.

9. No Warranties. Exeter acknowledges that the Material is experimental in nature and that all of its characteristics are not known by SurgaColl. SurgaColl MAKES NO REPRESENTATION AND EXTENDS NO WARRANTY OF ANY KIND, WHETHER EXPRESSED OR IMPLIED, INCLUDING, BUT NOT LIMITED TO ANY WARRANTIES OF MERCHANTABILITY, ACTIVITY, USEFULNESS, EFFICIENCY, HARMFULNESS, NON-TOXICITY, SAFETY OR FITNESS FOR A PARTICULAR PURPOSE, OR ANY WARRANTY THAT USE OF THE Material WILL NOT INFRINGE ANY PATENT, COPYRIGHT, PROPRIETARY RIGHT, OR TRADEMARK OF OTHERS.

10. Indemnity. Each party shall indemnify, defend and hold harmless (the "Indemnifying Party")the other party (the "Indemnified Party")and their affiliates and their trustees, officers, medical and professional staff, employees and agents and their respective successors, heirs and assigns against any liability, damage, loss or expense (including reasonable attorneys' fees and expenses of litigation) incurred by or imposed upon them in connection with any claims, suits, actions, demands or judgments

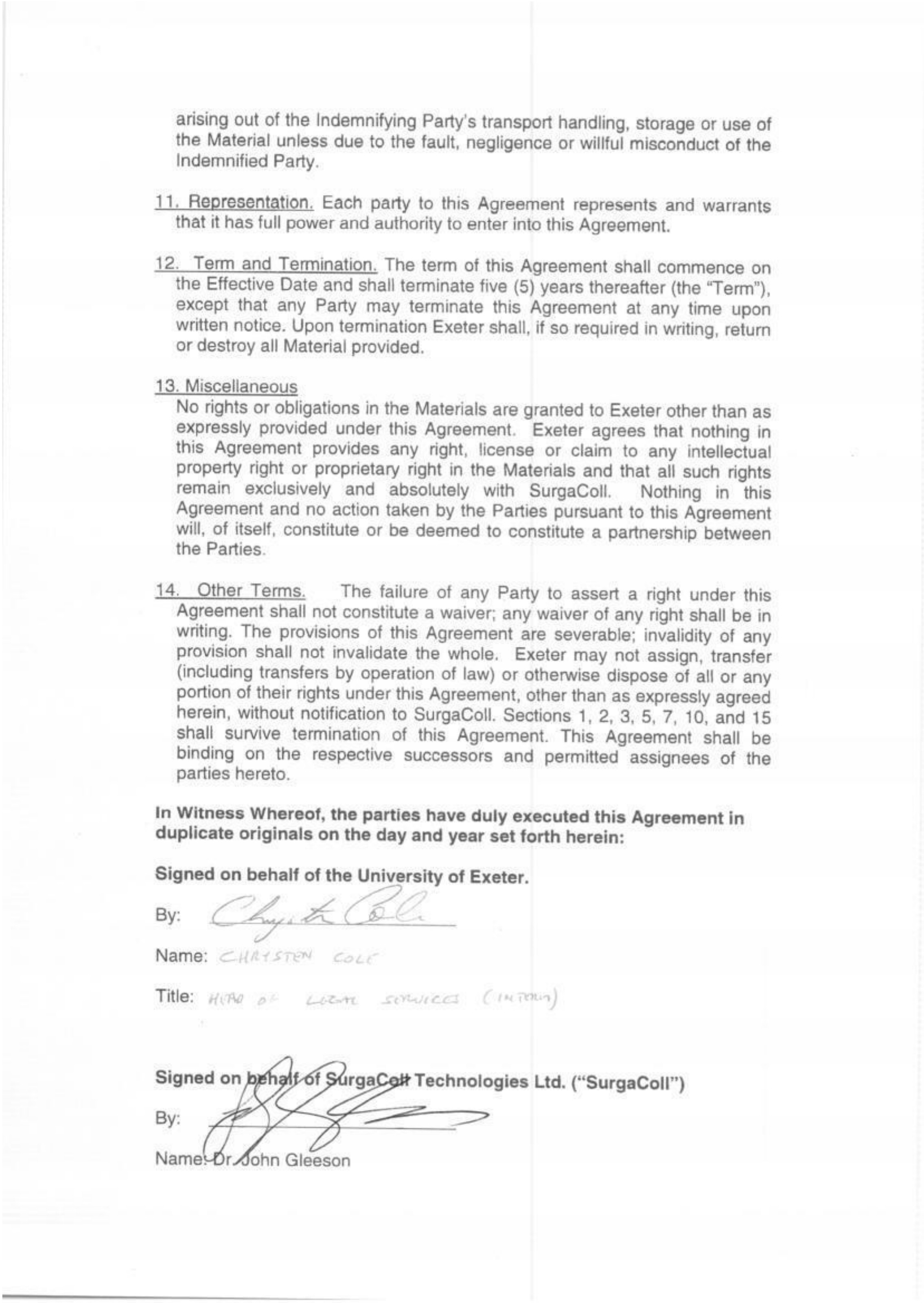

arising out of the Indemnifying Party's transport handling, storage or use of the Material unless due to the fault, negligence or willful misconduct of the Indemnified Party.

11. Representation. Each party to this Agreement represents and warrants that it has full power and authority to enter into this Agreement.

12. Term and Termination. The term of this Agreement shall commence on the Effective Date and shall terminate five (5) years thereafter (the "Term"), except that any Party may terminate this Agreement at any time upon written notice. Upon termination Exeter shall, if so required in writing, return or destroy all Material provided.

13. Miscellaneous
No rights or obligations in the Materials are granted to Exeter other than as expressly provided under this Agreement. Exeter agrees that nothing in this Agreement provides any right, license or claim to any intellectual property right or proprietary right in the Materials and that all such rights remain exclusively and absolutely with SurgaColl. Nothing in this Agreement and no action taken by the Parties pursuant to this Agreement will, of itself, constitute or be deemed to constitute a partnership between the Parties.

14. Other Terms. The failure of any Party to assert a right under this Agreement shall not constitute a waiver; any waiver of any right shall be in writing. The provisions of this Agreement are severable; invalidity of any provision shall not invalidate the whole. Exeter may not assign, transfer (including transfers by operation of law) or otherwise dispose of all or any portion of their rights under this Agreement, other than as expressly agreed herein, without notification to SurgaColl. Sections 1, 2, 3, 5, 7, 10, and 15 shall survive termination of this Agreement. This Agreement shall be binding on the respective successors and permitted assignees of the parties hereto.

In Witness Whereof, the parties have duly executed this Agreement in duplicate originals on the day and year set forth herein:

Signed on behalf of the University of Exeter.

By:

Name: CHRYSTEN COLE

Title: HEAD OF LEGAL SERVICES (INTERIM)

Signed on behalf of SurgaColl Technologies Ltd. ("SurgaColl")

By:

Name: Dr. John Gleeson

Study/Review	Age Range (Mean Age)	Breast Depth (mm)	Wavelength (nm)	Mean Reduced Scattering Coefficient (μ_s')	Mean Absorption Coefficient (μ_a)
Thomsen & Tatman, 1998 [304]				Glandular Breast	
Review			540	24 ± 6	0.36 ± 0.2
			700	14 ± 3	0.05 ± 0.01
33 frozen and thawed homogenized specimens	–	–	900	10 ± 2	0.06 ± 0.01
				Adipose Stroma	
Single Integrating Sphere			540	10 ± 2	0.23 ± 0.06
			700	9 ± 1	0.07 ± 0.01
			900	8 ± 1	0.08 ± 0.01
Tromberg et al, 2000 [303]					
Study					
			~675	9.09 ± 3.05	0.038 ± 0.023
4 subjects: 2 premenopausal	63, 67; 27, 29		~808	8.08 ± 2.37	0.034 ± 0.019
2 postmenopausal	(46.5)	10 – 25	~850	7.86 ± 2.21	0.044 ± 0.022
			~895	7.78 ± 2.04	0.078 ± 0.020
Frequency Domain Photon Migration (FDPM) Probe, multiple diode lasers			~957	7.38 ± 1.95	0.113 ± 0.046
Figures extracted from graphs					

Cerussi et al, 2001 [248]				32-year-old Premenopausal	
Study			800	8.563 ± 0.508	0.093 ± 0.007
			806	8.246 ± 0.488	0.091 ± 0.006
28 subjects: 15 premenopausal			852	7.714 ± 0.456	0.115 ± 0.007
7 postmenopausal			896	7.619 ± 0.437	0.150 ± 0.008
6 Hormone Replacement Therapy (HRT)	19 – 63 (46.6 ± 5.3)	10 – 25	913	7.452 ± 0.421	0.173 ± 0.007
				54-year-old Postmenopausal	
			800	6.206 ± 0.218	0.031 ± 0.004
			806	6.016 ± 0.210	0.034 ± 0.006
FDPM Probe, multiple diode lasers			852	5.873 ± 0.167	0.042 ± 0.005
			896	5.667 ± 0.190	0.076 ± 0.003
Figures extracted from graphs			913	5.770 ± 0.179	0.103 ± 0.026
Shah et al, 2001 [245]				Premenopausal	
Study				9.65 ± 1.35	0.099 ± 0.051
				Postmenopausal	
14 subjects: 6 premenopausal 3 postmenopausal 5 HTR	18 – 67 (~ 44.1)	10 – 25	674, 803, 849, 980 (826.25)	7.65 ± 0.95	0.04 ± 0.024
FDPM Probe, multiple diode lasers					

X. Intes, 2005 [247] *Study* 49 subjects: 13 premenopausal 23 postmenopausal 13 post-hysterectomy ‘SoftScan’ compression platform, TiSaphire laser	24 – 80 (57.2 ±13.7)	30 – 85 (57 ± 9.6)	760 780 830 850	10.9 ± 1.1 10.7 ± 1.4 10.3 ± 1.3 10.2 ± 1.6	0.051 ± 0.014 0.044 ± 0.014 0.051 ± 0.013 0.056 ± 0.015
Jacques, 2013 [147] *Review*	–	–	500	16.8 ± 8.1	–
Vardaki et al, 2016 [278] *Review*	–	–	830	9.84	0.068 – 0.102

Quasi-Skin Templates

Produced to scale on a full A3 page.

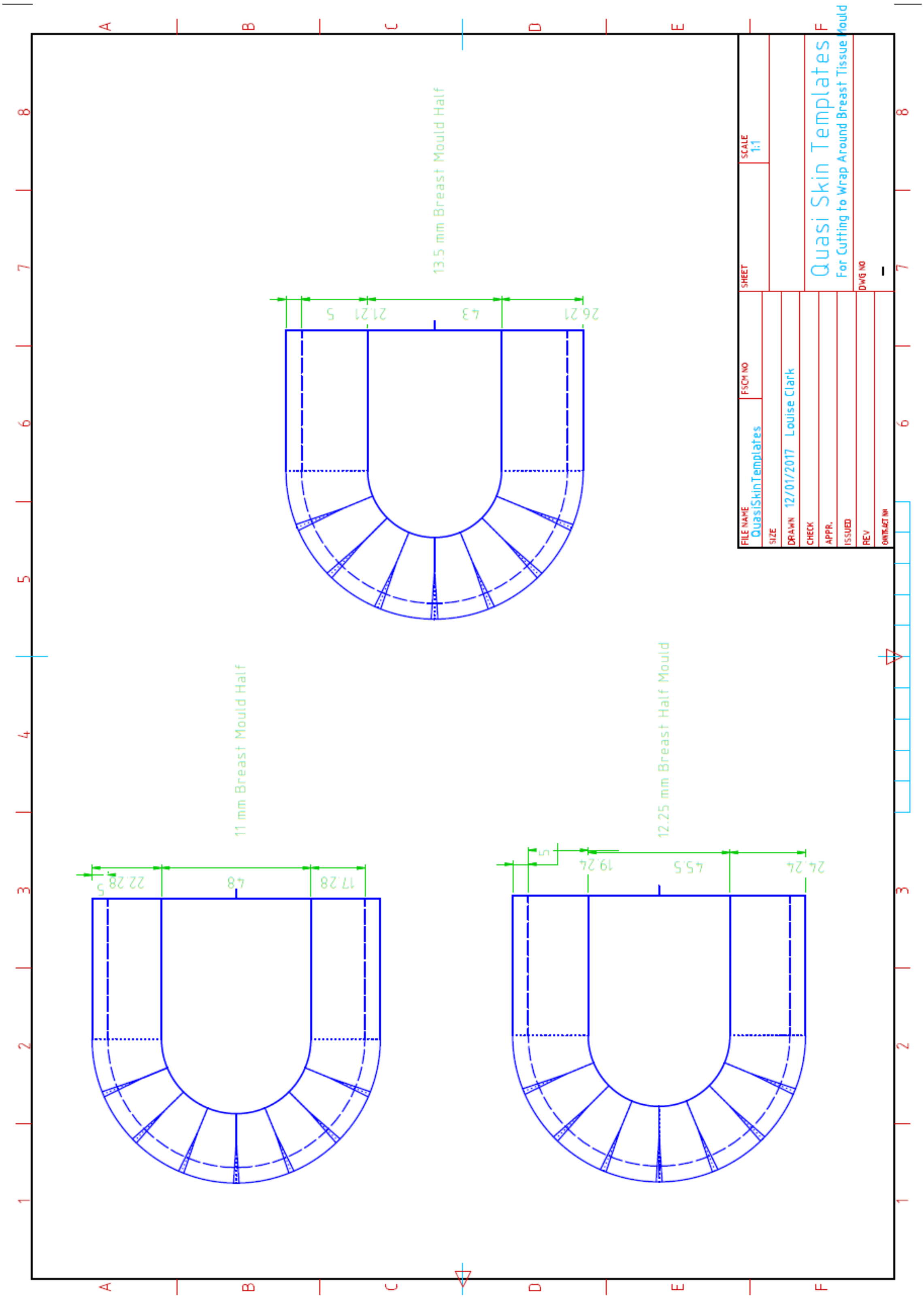

MATLAB Code

Standa Stage Automation with Andor CCD Trigger

```
function varargout = GUI_Louise_motor_and_camera_V13(varargin)
% GUI_LOUISE_MOTOR_AND_CAMERA_V13 MATLAB code for
GUI_Louise_motor_and_camera_V13.fig
%      GUI_LOUISE_MOTOR_AND_CAMERA_V13, by itself, creates a new
GUI_LOUISE_MOTOR_AND_CAMERA_V13 or raises the existing
%      singleton*.
%
%      H = GUI_LOUISE_MOTOR_AND_CAMERA_V13 returns the handle to a new
GUI_LOUISE_MOTOR_AND_CAMERA_V13 or the handle to
%      the existing singleton*.
%
%
GUI_LOUISE_MOTOR_AND_CAMERA_V13('CALLBACK',hObject,eventData,handles,.
..) calls the local
%      function named CALLBACK in GUI_LOUISE_MOTOR_AND_CAMERA_V13.M
with the given input arguments.
%
%      GUI_LOUISE_MOTOR_AND_CAMERA_V13('Property','Value',...) creates
a new GUI_LOUISE_MOTOR_AND_CAMERA_V13 or raises the
%      existing singleton*.  Starting from the left, property value
pairs are
%      applied to the GUI before
GUI_Louise_motor_and_camera_V13_OpeningFcn gets called.  An
%      unrecognized property name or invalid value makes property
application
%      stop.  All inputs are passed to
GUI_Louise_motor_and_camera_V13_OpeningFcn via varargin.
%
%      *See GUI Options on GUIDE's Tools menu.  Choose "GUI allows
only one
%      instance to run (singleton)".
%
% See also: GUIDE, GUIDATA, GUIHANDLES

% Edit the above text to modify the response to help
GUI_Louise_motor_and_camera_V13

% Last Modified by GUIDE v2.5 30-Mar-2016 14:11:25

% Begin initialization code - DO NOT EDIT
gui_Singleton = 1;
gui_State = struct('gui_Name',       mfilename, ...
                   'gui_Singleton',  gui_Singleton, ...
                   'gui_OpeningFcn',
@GUI_Louise_motor_and_camera_V13_OpeningFcn, ...
                   'gui_OutputFcn',
@GUI_Louise_motor_and_camera_V13_OutputFcn, ...
                   'gui_LayoutFcn',  [] , ...
                   'gui_Callback',   []);
if nargin && ischar(varargin{1})
    gui_State.gui_Callback = str2func(varargin{1});
end

if nargout
```

```
    [varargout{1:nargout}] = gui_mainfcn(gui_State, varargin{:});
else
    gui_mainfcn(gui_State, varargin{:});
end
% End initialization code - DO NOT EDIT


% --- Executes just before GUI_Louise_motor_and_camera_V13 is made
visible.
function GUI_Louise_motor_and_camera_V13_OpeningFcn(hObject,
eventdata, handles, varargin)
% This function has no output args, see OutputFcn.
% hObject    handle to figure
% eventdata  reserved - to be defined in a future version of MATLAB
% handles    structure with handles and user data (see GUIDATA)
% varargin   command line arguments to GUI_Louise_motor_and_camera_V13
(see VARARGIN)

    % Choose default command line output for
GUI_Louise_motor_and_camera_V13
    handles.output = hObject;


    handles = initGUI(handles);
    handles = loadConfig(handles);

    enableGUI(handles , 'idle');

    handles = initMotors(handles);
    if handles.MotorsOK == 0;
        set(handles.txMotorStatus , 'ForegroundColor' , 'r' , 'String'
, 'Motors not detected');
    end



    % Update handles structure
    guidata(hObject, handles);

% UIWAIT makes GUI_Louise_motor_and_camera_V13 wait for user response
(see UIRESUME)
% uiwait(handles.GUI_Motor_and_camera);


% --- Outputs from this function are returned to the command line.
function varargout =
GUI_Louise_motor_and_camera_V13_OutputFcn(hObject, eventdata, handles)
% varargout  cell array for returning output args (see VARARGOUT);
% hObject    handle to figure
% eventdata  reserved - to be defined in a future version of MATLAB
% handles    structure with handles and user data (see GUIDATA)

% Get default command line output from handles structure
varargout{1} = handles.output;




function handles = initGUI(handles)
```

```
    xlabel(handles.axesMain , '[mm]');
    ylabel(handles.axesMain , '[mm]');
%     set(handles.axesMain , 'XTick' , [] , 'YTick' , [] );

    handles.Corners.TopLeft     = [];
    handles.Corners.BottomRight = [];

    handles.hLinePath = [];
    handles.hCurrentPoint = [];
    handles.ScansDone = [];

    handles.hScanTimer = [];

    handles.lastSavePath = [];

    % Prepare progress bar
    axis(handles.axesProgress , [0 1 0 1]);
    box(handles.axesProgress , 'off');
    set(handles.axesProgress , 'XColor' , 'w'  , 'YColor' , 'w')

    handles.hProgressBar = rectangle('Parent' , handles.axesProgress ,
...
        'Position' , [0 , 0 , 0.01 , 1] , 'FaceColor' , 'g' ,
'EdgeColor' , 'none');




function FileNotFound(FileName)

    msgbox(['File not found : ' FileName] , 'modal')


function handles = initMotors(handles)

    scriptPath = fileparts(mfilename('fullpath'));
    NecessaryFiles = {'ximc.h' , 'ximc.h' , 'libximc.dll' ,
'xiwrapper.dll' , 'libximc_thunk_pcwin64.dll' , 'ximcm.m'};

    handles.MotorsOK = 0;
    handles.DEBUGMODE = true;   % If something goes wrong, continue as
simulation

    set(handles.txMotorStatus , 'ForegroundColor' , [204,204,0]/255 ,
'String' , 'Initializing motors...');


    % Check for necessary files
    for k = 1 : length(NecessaryFiles)
        if ~exist([scriptPath , '\' , NecessaryFiles{k}] , 'file')
            FileNotFound(NecessaryFiles{k})
            return
        end
    end



    % Load library
```

```
    [~,maxArraySize]=computer;
    is64bit = maxArraySize > 2^31;
    if not(libisloaded('libximc'))
        disp('Loading library')
            if ispc
                if (is64bit)
                        [notfound,warnings] =
loadlibrary('libximc.dll', @ximcm);
                else
                        [notfound, warnings] =
loadlibrary('libximc.dll', 'ximcm.h', 'addheader', 'ximc.h');
                end
            elseif ismac
                [notfound, warnings] =
loadlibrary('libximc.framework/libximc', 'ximcm.h', 'mfilename',
'ximcm.m', 'includepath',
'libximc.framework/Versions/Current/Headers', 'addheader', 'ximc.h');
            elseif isunix
                [notfound, warnings] = loadlibrary('libximc.so',
'ximcm.h', 'addheader', 'ximc.h');
            end
    end



    % List all functions
    % F = libfunctions('libximc','-full');
    % libfunctionsview('libximc');

    % Find devices (two motors)
    device_names = ximc_enumerate_devices_wrap(0);
    devices_count = size(device_names,2);
    if devices_count == 0
        waitfor(msgbox('No devices found - simulating movement' ,
'modal'));
        return
    end

    if length(device_names) < 2
        waitfor(msgbox('I could not find 2 motors connected to the
computer!' , 'modal'))
        return
    elseif length(device_names) > 2
        waitfor(msgbox('There is more than 2 motors connected to the
computer!' , 'modal'))
        return
    end

    handles.device_idUP = calllib('libximc','open_device',
device_names{1,1});
    handles.device_idLR = calllib('libximc','open_device',
device_names{1,2});


    handles.MotorState_UP = ximc_get_status(handles.device_idUP);
    handles.MotorStat_LR  = ximc_get_status(handles.device_idLR);





    % Get options for SYNCH OUT
```

```
    % t = struct('SyncOutFlags', 0, 'SyncOutPulseSteps', 0,
'SyncOutPeriod', 0, 'Accuracy', 0);
    % t_ptr = libpointer('sync_out_settings_calb_t', t);
    sync_settings = struct('SyncOutFlags', 0, 'SyncOutPulseSteps', 0,
'SyncOutPeriod', 0, 'Accuracy', 0, 'uAccuracy', 0);
    [result, sync_settings] =
calllib('libximc','get_sync_out_settings', handles.device_idUP,
sync_settings);


    % Specify options for SYNCH OUT and send to device
    sync_settings.SyncOutFlags  = bin2dec('00101001');  % Synch
enabled, on stop, motor steps/encoder pulses instead of milliseconds
    sync_settings.SyncOutPeriod = 100;  % ms
    sync_settings.Accuracy = 0;  % distance to the target position. As
soon as the distance to
                                 % target on approach is less than or
equal to this distance
                                 % a synchronizing pulse will be
generated if "on stop" option is used.

    result(1) = calllib('libximc','set_sync_out_settings',
handles.device_idUP, sync_settings);
    result(2) = calllib('libximc','set_sync_out_settings',
handles.device_idLR, sync_settings);

    if ~all(result == 0)
        popupErrorMessage('Error writing motor setup');
        return
    end


    % External IO mode flags
    % What I want: 00100001 (Enabled + synch when motor stop +
duration in ms)
    % SYNCOUT_ENABLED   0X01  // 00000001  // Synchronization out pin
follows the synchronization logic, if set.
    % SYNCOUT_STATE     0X02  // 00000010  // When output state is
fixed by negative SYNCOUT_ENABLED flag, the pin state is in accordance
with this flag state.
    % SYNCOUT_INVERT    0X04  // 00000100  // Low level is active, if
set, and high level is active otherwise
    % SYNCOUT_IN_STEPS  0X08  // 00001000  // Use motor steps/encoder
pulses instead of milliseconds for output pulse generation if the flag
is set
    % SYNCOUT_ONSTART   0X10  // 00010000  // Generate synchronization
pulse when movement starts.
    % SYNCOUT_ONSTOP    0X20  // 00100000  // Generate synchronization
pulse when movement stops.
    % SYNCOUT_ONPERIOD  0X40  // 01000000  // Generate synchronization
pulse every SyncOutPeriod encoder pulses
    % hexToBinaryVector('0x20')


    % structs.sync_out_settings_t.members=struct('SyncOutFlags',
'uint32', 'SyncOutPulseSteps', 'uint32', 'SyncOutPeriod', 'uint32',
'Accuracy', 'uint32', 'uAccuracy', 'uint32');
    % sync_out_settings_t       Struct Reference
    % unsigned int SyncOutFlags
    % Flags of synchronization output.
    %
    % unsigned int SyncOutPulseSteps
```

```
    % This value specifies duration of output pulse.
    %
    % unsigned int SyncOutPeriod
    % This value specifies number of encoder pulses or steps between
two output synchronization pulses when SYNCOUT ONPERIOD is set.
    %
    % unsigned int Accuracy
    % This is the neighborhood around the target coordinates, which is
getting hit in the target position and the momentum
    % generated by the stop
    %
    % unsigned int uAccuracy
    % This is the neighborhood around the target coordinates in micro
steps (only used with stepper motor)


    handles.MotorsOK = 1;
    handles.DEBUGMODE = false;

    set(handles.txMotorStatus , 'ForegroundColor' , 'g' , 'String' ,
'Motors detected');







% --- Executes on button press in btSetCorner1.
function btSetCorner1_Callback(hObject, eventdata, handles)
% hObject    handle to btSetCorner1 (see GCBO)
% eventdata  reserved - to be defined in a future version of MATLAB
% handles    structure with handles and user data (see GUIDATA)


    if handles.DEBUGMODE
        handles.Corners.TopLeft = step2mm([0 , 0]);
        updateROIstatus(handles);

    elseif handles.MotorsOK == 1
        state_UP = ximc_get_status(handles.device_idUP);
        state_LR = ximc_get_status(handles.device_idLR);

        handles.Corners.TopLeft = step2mm([state_UP.CurPosition ,
state_LR.CurPosition]);
    end

    updateROIstatus(handles);
    handles = parseInput(handles);
    guidata(hObject , handles);



% --- Executes on button press in btSetCorner2.
function btSetCorner2_Callback(hObject, eventdata, handles)
% hObject    handle to btSetCorner2 (see GCBO)
% eventdata  reserved - to be defined in a future version of MATLAB
% handles    structure with handles and user data (see GUIDATA)

    if handles.DEBUGMODE
        handles.Corners.BottomRight = step2mm([-4700 , 0]);
```

```
        updateROIstatus(handles);

    elseif handles.MotorsOK == 1
        state_UP = ximc_get_status(handles.device_idUP);
        state_LR = ximc_get_status(handles.device_idLR);

        handles.Corners.BottomRight = step2mm([state_UP.CurPosition ,
state_LR.CurPosition]);
    end


    updateROIstatus(handles);
    handles = parseInput(handles);
    guidata(hObject , handles);



function updateROIstatus(handles)
    % Lights up the ROI indication in the status bar

    if isempty(handles.Corners.TopLeft) &&
isempty(handles.Corners.BottomRight)
        set(handles.txROIInitialized , 'ForegroundColor' , 'r' ,
'String' , 'ROI not initialized');
    elseif xor(isempty(handles.Corners.TopLeft) ,
isempty(handles.Corners.BottomRight))
        set(handles.txROIInitialized , 'ForegroundColor' ,
[204,204,0]/255 , 'String' , 'One corner initialized');
    else
        set(handles.txROIInitialized , 'ForegroundColor' , 'g' ,
'String' , 'ROI initialized');
    end



function x = step2mm(x)
    % Transforms motor steps in mm
    % 53942 steps = 100 mm

    x = x / 53942 * 100;


function x = mm2step(x)
    % Transforms mm in motor steps
    % 53942 steps = 100 mm

    x = round(x * 53942 /100) ;




function [handles , Nscans] = buildPath(handles)

    Nscans = [];

    [handles , inputOK] = checkInput(handles);
    if inputOK ~= 1;   return;    end
```

```
    % Builds the motor paths from the input data
    % Startij point
    xpos0 = handles.Corners.TopLeft(1);
    ypos0 = handles.Corners.TopLeft(2);

    % Ending point
    xlim = handles.Corners.BottomRight(1);
    ylim = handles.Corners.BottomRight(2);

    % Check if user indicated a single line
    if xpos0 == xlim
        button = questdlg('Are you trying to scan a single vertical
line?','Single line scan alert','Yes','No','Cancel','Yes') ;
        if strcmpi(button , 'No') || strcmpi(button , 'Cancel')
            setappdata(handles.GUI_Motor_and_camera , 'MotorPath' ,
[]);
            setappdata(handles.GUI_Motor_and_camera , 'ScansDone' ,
[]);
            return
        end

        handles.StepSizeHorizontal = 0;
        set(handles.txHorizontalStep , 'String' , '0');

    elseif ypos0 == ylim
        button = questdlg('Are you trying to scan a single horizontal
line?','Single line scan alert','Yes','No','Cancel','Yes') ;
        if strcmpi(button , 'No') || strcmpi(button , 'Cancel')
            setappdata(handles.GUI_Motor_and_camera , 'MotorPath' ,
[]);
            setappdata(handles.GUI_Motor_and_camera , 'ScansDone' ,
[]);
            return
        end

        handles.StepSizeVertical = 0;
        set(handles.txVerticalStep , 'String' , '0');
    else

    end

    % Steps
    xstep = handles.StepSizeHorizontal;
    ystep = handles.StepSizeVertical;


    % Check if steps make sense
    if (xstep == 0  &&  xpos0 ~= xlim)  ||  (ystep == 0  &&  ypos0 ~=
ylim)
        msgbox('You indicated a zero-size step, which is only valid
for single line scans!','Wrong step size');
        setappdata(handles.GUI_Motor_and_camera , 'MotorPath' , []);
        setappdata(handles.GUI_Motor_and_camera , 'ScansDone' , []);
        return
    end


    % X and Y coordinates of all points
    if xlim < xpos0
        xstep = -xstep;
    end
```

```
    if ylim < ypos0
        ystep = -ystep;
    end


    X   = (xpos0 : xstep : xlim + xstep)';
    Y   = (ypos0 : ystep : ylim + ystep)';

    if isempty(X);    X = xpos0;    end
    if isempty(Y);    Y = ypos0;    end

    LX = length(X);
    LY = length(Y);
    Nscans = LX * LY;

    % Assemble motor path
    MotorPath = zeros(Nscans , 2);
    for k = 1 : length(Y)
        if mod(k,2) == 1
            MotorPath((k-1)*LX+1 : k*LX , :) = [X , repmat(Y(k) , LX ,
1)];
        else
            MotorPath((k-1)*LX+1 : k*LX , :) = [flipud(X) ,
repmat(Y(k) , LX , 1)];
        end
    end



    % Repeat acquisitions at each step if necessary
    if handles.AcquisitionsPerStep > 1
        X = MotorPath(: , 1)';
        Y = MotorPath(: , 2)';

        X = repmat(X , handles.AcquisitionsPerStep , 1);
        Y = repmat(Y , handles.AcquisitionsPerStep , 1);
        X = X(:);
        Y = Y(:);
        MotorPath = [X , Y];
    end

    Nscans = size(MotorPath , 1);
    setappdata(handles.GUI_Motor_and_camera , 'MotorPath' ,
MotorPath);
    ScansDone = zeros(Nscans , 1);
    setappdata(handles.GUI_Motor_and_camera , 'ScansDone' ,
ScansDone);

    handles = updateGraph(handles) ;




function handles = updateGraph(handles)

    ScansDone = getappdata(handles.GUI_Motor_and_camera ,
'ScansDone');
    currentPoint = find(ScansDone , 1 , 'last');
```

```
    MotorPath = getappdata(handles.GUI_Motor_and_camera ,
'MotorPath');

    if isempty(currentPoint);  currentPoint = 1;   end

    if isempty(handles.hLinePath)
        handles.hLinePath = plot(handles.axesMain, MotorPath(:,1) ,
MotorPath(:,2) , 'b-');
        hold(handles.axesMain , 'on');
        handles.hCurrentPoint = plot(handles.axesMain ,
MotorPath(currentPoint,1) ,...

MotorPath(currentPoint,2) , 'ro');
        grid(handles.axesMain , 'on');
    else
        set(handles.hLinePath , 'XData' , MotorPath(:,1) , ...
                                'YData' , MotorPath(:,2))
        set(handles.hCurrentPoint , 'XData' ,
MotorPath(currentPoint,1) , ...
                                    'YData' ,
MotorPath(currentPoint,2))
    end

    xstep = handles.StepSizeHorizontal;
    ystep = handles.StepSizeVertical;

    % change step size just for drawing
    if xstep == 0; xstep = 1; end ;    if ystep == 0; ystep = 1; end

    axis(handles.axesMain, [min(MotorPath(:,1)) - xstep*2 , ...
                            max(MotorPath(:,1)) + xstep*2 , ...
                            min(MotorPath(:,2)) - ystep*2 , ...
                            max(MotorPath(:,2)) + ystep*2]);

    xlabel(handles.axesMain , '[mm]');
    ylabel(handles.axesMain , '[mm]');




function txHorizontalStep_Callback(hObject, eventdata, handles)
% hObject    handle to txHorizontalStep (see GCBO)
% eventdata  reserved - to be defined in a future version of MATLAB
% handles    structure with handles and user data (see GUIDATA)

% Hints: get(hObject,'String') returns contents of txHorizontalStep as
text
%        str2double(get(hObject,'String')) returns contents of
txHorizontalStep as a double
    handles = parseInput(handles);
    guidata(hObject , handles);


% --- Executes during object creation, after setting all properties.
function txHorizontalStep_CreateFcn(hObject, eventdata, handles)
% hObject    handle to txHorizontalStep (see GCBO)
% eventdata  reserved - to be defined in a future version of MATLAB
% handles    empty - handles not created until after all CreateFcns
called
```

```
% Hint: edit controls usually have a white background on Windows.
%       See ISPC and COMPUTER.
if ispc && isequal(get(hObject,'BackgroundColor'),
get(0,'defaultUicontrolBackgroundColor'))
    set(hObject,'BackgroundColor','white');
end



function txVerticalStep_Callback(hObject, eventdata, handles)
% hObject    handle to txVerticalStep (see GCBO)
% eventdata  reserved - to be defined in a future version of MATLAB
% handles    structure with handles and user data (see GUIDATA)

% Hints: get(hObject,'String') returns contents of txVerticalStep as
text
%        str2double(get(hObject,'String')) returns contents of
txVerticalStep as a double
    handles = parseInput(handles);
    guidata(hObject , handles);


% --- Executes during object creation, after setting all properties.
function txVerticalStep_CreateFcn(hObject, eventdata, handles)
% hObject    handle to txVerticalStep (see GCBO)
% eventdata  reserved - to be defined in a future version of MATLAB
% handles    empty - handles not created until after all CreateFcns
called

% Hint: edit controls usually have a white background on Windows.
%       See ISPC and COMPUTER.
if ispc && isequal(get(hObject,'BackgroundColor'),
get(0,'defaultUicontrolBackgroundColor'))
    set(hObject,'BackgroundColor','white');
end



function txAcquisitionTime_Callback(hObject, eventdata, handles)
% hObject    handle to txAcquisitionTime (see GCBO)
% eventdata  reserved - to be defined in a future version of MATLAB
% handles    structure with handles and user data (see GUIDATA)

% Hints: get(hObject,'String') returns contents of txAcquisitionTime
as text
%        str2double(get(hObject,'String')) returns contents of
txAcquisitionTime as a double
    handles = parseInput(handles);
    guidata(hObject , handles);



% --- Executes during object creation, after setting all properties.
function txAcquisitionTime_CreateFcn(hObject, eventdata, handles)
% hObject    handle to txAcquisitionTime (see GCBO)
% eventdata  reserved - to be defined in a future version of MATLAB
% handles    empty - handles not created until after all CreateFcns
called

% Hint: edit controls usually have a white background on Windows.
```

```
%       See ISPC and COMPUTER.
if ispc && isequal(get(hObject,'BackgroundColor'),
get(0,'defaultUicontrolBackgroundColor'))
    set(hObject,'BackgroundColor','white');
end



% --- Executes on selection change in comboAcquisitionUnit.
function comboAcquisitionUnit_Callback(hObject, eventdata, handles)
% hObject    handle to comboAcquisitionUnit (see GCBO)
% eventdata  reserved - to be defined in a future version of MATLAB
% handles    structure with handles and user data (see GUIDATA)

% Hints: contents = cellstr(get(hObject,'String')) returns
comboAcquisitionUnit contents as cell array
%        contents{get(hObject,'Value')} returns selected item from
comboAcquisitionUnit

    handles = parseInput(handles);
    guidata(hObject , handles);



% --- Executes during object creation, after setting all properties.
function comboAcquisitionUnit_CreateFcn(hObject, eventdata, handles)
% hObject    handle to comboAcquisitionUnit (see GCBO)
% eventdata  reserved - to be defined in a future version of MATLAB
% handles    empty - handles not created until after all CreateFcns
called

% Hint: popupmenu controls usually have a white background on Windows.
%       See ISPC and COMPUTER.
if ispc && isequal(get(hObject,'BackgroundColor'),
get(0,'defaultUicontrolBackgroundColor'))
    set(hObject,'BackgroundColor','white');
end




function [handles , inputOK]= checkInput(handles)


    if isempty(handles.Corners.TopLeft) ||
isempty(handles.Corners.BottomRight)
        inputOK = 'Please define a ROI';
        return
    end


    inputOK = 1;





function handles = parseInput(handles)



    handles.StepSizeHorizontal  =
str2double(get(handles.txHorizontalStep , 'String'));
```

```
    handles.StepSizeVertical     =
str2double(get(handles.txVerticalStep , 'String'));
    handles.AcquisitionsPerStep =
str2double(get(handles.txAcquisitionsPerStep , 'String'));
    handles.AcquisitionTime      =
str2double(get(handles.txAcquisitionTime , 'String'));

    % Time in seconds
    if get(handles.comboAcquisitionUnit , 'Value') == 2;
        handles.AcquisitionTime = handles.AcquisitionTime * 60;
    end

    [handles , Nscans] = buildPath(handles);

    setTimeRemaining(0 , Nscans , handles.AcquisitionTime,
handles.txEstimatedTime);



function popupErrorMessage(message)

    waitfor(msgbox(message , 'modal'))



function enableGUI(handles , option)

switch option
    case 'running'
        set(handles.btSetCorner1 , 'Enable' , 'off');
        set(handles.btSetCorner2 , 'Enable' , 'off');

        set(handles.txHorizontalStep , 'Enable' , 'off');
        set(handles.txVerticalStep , 'Enable' , 'off');
        set(handles.txAcquisitionTime , 'Enable' , 'off');
        set(handles.txAcquisitionsPerStep , 'Enable' , 'off');
        set(handles.comboAcquisitionUnit , 'Enable' , 'off');

        set(handles.btStart , 'Enable' , 'off');
        set(handles.btGoToStep , 'Enable' , 'off');
        set(handles.btReset , 'Enable' , 'off');
        set(handles.btStop , 'Enable' , 'on');

    case 'paused'
        set(handles.btSetCorner1 , 'Enable' , 'off');
        set(handles.btSetCorner2 , 'Enable' , 'off');

        set(handles.txHorizontalStep , 'Enable' , 'off');
        set(handles.txVerticalStep , 'Enable' , 'off');
        set(handles.txAcquisitionTime , 'Enable' , 'off');
        set(handles.txAcquisitionsPerStep , 'Enable' , 'off');
        set(handles.comboAcquisitionUnit , 'Enable' , 'off');

        set(handles.btStart , 'Enable' , 'on');
        set(handles.btGoToStep , 'Enable' , 'on');
        set(handles.btReset , 'Enable' , 'on');
        set(handles.btStop , 'Enable' , 'off');

    case 'idle'
        set(handles.btSetCorner1 , 'Enable' , 'on');
```

```
        set(handles.btSetCorner2 , 'Enable' , 'on');

        set(handles.txHorizontalStep , 'Enable' , 'on');
        set(handles.txVerticalStep , 'Enable' , 'on');
        set(handles.txAcquisitionTime , 'Enable' , 'on');
        set(handles.txAcquisitionsPerStep , 'Enable' , 'on');
        set(handles.comboAcquisitionUnit , 'Enable' , 'on');

        set(handles.btStart , 'Enable' , 'on');
        set(handles.btGoToStep , 'Enable' , 'on');
        set(handles.btReset , 'Enable' , 'off');
        set(handles.btStop , 'Enable' , 'off');
    case 'finished'

        set(handles.btSetCorner1 , 'Enable' , 'on');
        set(handles.btSetCorner2 , 'Enable' , 'on');

        set(handles.txHorizontalStep , 'Enable' , 'on');
        set(handles.txVerticalStep , 'Enable' , 'on');
        set(handles.txAcquisitionTime , 'Enable' , 'on');
        set(handles.txAcquisitionsPerStep , 'Enable' , 'on');
        set(handles.comboAcquisitionUnit , 'Enable' , 'on');

        set(handles.btStart , 'Enable' , 'on');
        set(handles.btGoToStep , 'Enable' , 'on');
        set(handles.btReset , 'Enable' , 'on');
        set(handles.btStop , 'Enable' , 'off');
end




% --- Executes on button press in btStart.
function btStart_Callback(hObject, eventdata, handles)
% hObject    handle to btStart (see GCBO)
% eventdata  reserved - to be defined in a future version of MATLAB
% handles    structure with handles and user data (see GUIDATA)


    [handles , inputOK] = checkInput(handles);

    % If some input is not valid, quit now
    if ischar(inputOK);    popupErrorMessage(inputOK);     return;
end

    % The path of the motors have already been buildt. Retrieve the
array
    % to keep track of how many scans have been done
    ScansDone = getappdata(handles.GUI_Motor_and_camera ,
'ScansDone');
    N = length(ScansDone);

    % DETERMINE NEXT POSITION TO SCAN
    nextPosition = find(ScansDone , 1 , 'last') + 1;
    if isempty(nextPosition);
        nextPosition = 1 ;
    elseif nextPosition >= N
        enableGUI(handles , 'paused');
        popupErrorMessage('The job was completed; please press Reset
before starting a new one');
```

```
        return
    end

    enableGUI(handles , 'running');
    % Move to next (first?) position and scan
    result = moveAndScan(handles , nextPosition);
    if result ~= 0;
        enableGUI(handles , 'idle');
        return;
    end   % Quit if something went wrong

    ScansDone(nextPosition) = 1;
    setappdata(handles.GUI_Motor_and_camera , 'ScansDone' ,
ScansDone);

    % Timer object
    out = timerfind('Tag' , 'GUI_Motor_and_camera');
    handles.hScanTimer = timer('ExecutionMode' , 'fixedSpacing' , ...
           'StartDelay' , handles.AcquisitionTime, 'Period' ,
handles.AcquisitionTime , ...
           'TimerFcn' , @scanFinished , 'Tag' ,
'GUI_Motor_and_camera');


    setTimeRemaining(nextPosition , N , handles.hScanTimer.Period,
handles.txEstimatedTime);
    set(handles.hProgressBar , 'Position' , [0 , 0 , nextPosition / N
, 1]);

    guidata(hObject , handles);

    start(handles.hScanTimer);
    updateJobStatus(handles);




function updateJobStatus(handles)

    ScansDone = getappdata(handles.GUI_Motor_and_camera ,
'ScansDone');
    currentPosition = find(ScansDone , 1 , 'last');

    if isempty(currentPosition)
        set(handles.txJobRunning , 'String' , 'Job not running' ,
'ForegroundColor' ,'r');
        set(handles.btStart , 'Enable' , 'on');
    elseif currentPosition < length(ScansDone)
        if ~isempty(handles.hScanTimer) && isvalid(handles.hScanTimer)
&& ...
                strcmpi(handles.hScanTimer.Running , 'on')

            set(handles.txJobRunning , 'String' , 'Job running' ,
'ForegroundColor' , [204,204,0]/255);
            set(handles.btStart , 'Enable' , 'off');
        else
            set(handles.txJobRunning , 'String' , 'Job paused' ,
'ForegroundColor' , 'r');
            set(handles.btStart , 'Enable' , 'on');
        end
```

```
    else
        set(handles.txJobRunning , 'String' , 'Job done!' ,
'ForegroundColor' ,'g');
        set(handles.btStart , 'Enable' , 'on');
    end




function   result = moveAndScan(handles , positionN)

    % Move to step
    result = moveToStepN(handles , positionN);

    if result ~= 0
        popupErrorMessage(['Could not move motors to position N. ' ,
num2str(positionN)])
    end

    result = sendSynch(handles);
     if result ~= 0
        popupErrorMessage('Could not synch scan')
    end




function result = moveToPosition(handles, coordinates)


    if handles.DEBUGMODE;
        result = 0;
        return
    end

    state_UP = ximc_get_status(handles.device_idUP);
    state_LR = ximc_get_status(handles.device_idLR);

    coordinates = mm2step(coordinates);

    if state_UP.CurPosition == coordinates(1) && ...
       state_LR.CurPosition == coordinates(2)

        % Already in position
        result = 0;
        return
    end

    result(1) = calllib('libximc','command_move', handles.device_idUP,
coordinates(1) , 0);
    result(2) = calllib('libximc','command_move', handles.device_idLR,
coordinates(2) , 0);

    result = ~all(result == 0);
    if result ~= 0
        popupErrorMessage('Error when moving motors!');
        return
```

```
    end



    %%%%%%%%%%%%%%%%%%%%%%%%%%%%%%
    %%%%%%%%%%%%%%%%%%%%%%%%%%%%%%
    calllib('libximc','command_wait_for_stop', handles.device_idUP,
300);
    calllib('libximc','command_wait_for_stop', handles.device_idLR,
300);







function result = moveToStepN(handles , nStep)

    MotorPath = getappdata(handles.GUI_Motor_and_camera ,
'MotorPath');
    result    = moveToPosition(handles, MotorPath(nStep , :));









function handles = jobFinished(handles)







function scanFinished(obj, event)
    % One scan has finished

    % Measure time required to move motors and send synch
    tic

    % Retrieve handles
    h = findall(0,'Type','figure' , 'Tag' , 'GUI_Motor_and_camera');
    handles = guidata(h(1));


    ScansDone = getappdata(handles.GUI_Motor_and_camera ,
'ScansDone');


    % Determine NEXT POSITION TO SCAN
    N = length(ScansDone);
    nextPosition = find(ScansDone , 1 , 'last') + 1;
    if isempty(nextPosition);
        nextPosition = 1;
    elseif nextPosition > N
        stop(obj);
```

```
        delete(obj);
        enableGUI(handles , 'finished');

        updateJobStatus(handles);
        setTimeRemaining(nextPosition , N , obj.Period,
handles.txEstimatedTime);
        guidata(h(1) , handles);
        return;
    end

    % Move to next position and scan
    result = moveAndScan(handles , nextPosition);


    if result ~= 0;    obj.stop;  return;    end   % Quit if something
went wrong

    % Output to microscope scanner right after movement
    result = sendSynch(handles);

    if result ~= 0;    obj.stop;  return;    end   % Quit if something
went wrong

    ScansDone(nextPosition) = 1;
    setappdata(handles.GUI_Motor_and_camera , 'ScansDone' ,
ScansDone);

    handles = updateGraph(handles);

    set(handles.hProgressBar , 'Position' , [0 , 0 , min([0.01 ,
nextPosition / N]) , 1]);

    ScanDuration = obj.Period + toc;

    setTimeRemaining(nextPosition , N , ScanDuration,
handles.txEstimatedTime);




function result = sendSynch(handles)

    if handles.DEBUGMODE;
        result = 0;
        return
    end


    % Read settings to automatically get the output structure
sync_settings
    sync_settings = struct('SyncOutFlags', 0, 'SyncOutPulseSteps', 0,
'SyncOutPeriod', 0, 'Accuracy', 0, 'uAccuracy', 0);
    [result, sync_settings] =
calllib('libximc','get_sync_out_settings', handles.device_idUP,
sync_settings);

    % What I want: 00100001 (Enabled + synch when motor stop +
duration in ms)
```

```
    % SYNCOUT_ENABLED   0X01  // 00000001  // Synchronization out pin
follows the synchronization logic, if set.
    % SYNCOUT_STATE     0X02  // 00000010  // When output state is
fixed by negative SYNCOUT_ENABLED flag, the pin state is in accordance
with this flag state.
    % SYNCOUT_INVERT    0X04  // 00000100  // Low level is active, if
set, and high level is active otherwise
    % SYNCOUT_IN_STEPS  0X08  // 00001000  // Use motor steps/encoder
pulses instead of milliseconds for output pulse generation if the flag
is set
    % SYNCOUT_ONSTART   0X10  // 00010000  // Generate synchronization
pulse when movement starts.
    % SYNCOUT_ONSTOP    0X20  // 00100000  // Generate synchronization
pulse when movement stops.
    % SYNCOUT_ONPERIOD  0X40  // 01000000  // Generate synchronization
pulse every SyncOutPeriod encoder pulses
    % hexToBinaryVector('0x20')

    sync_settings.SyncOutFlags  = bin2dec('00101101');  % Synch
enabled, on stop, motor steps/encoder pulses instead of milliseconds
    sync_settings.SyncOutPeriod = 100;  % ms
    sync_settings.Accuracy = 0;  % distance to the target position. As
soon as the distance to
                                 % target on approach is less than or
equal to this distance
                                 % a synchronizing pulse will be
generated if "on stop" option is used.

    result(1) = calllib('libximc','set_sync_out_settings',
handles.device_idUP, sync_settings);
    result(2) = calllib('libximc','set_sync_out_settings',
handles.device_idLR, sync_settings);

    if ~all(result == 0)
        popupErrorMessage('Error writing motor setup');
        return
    end

    % Wait a little
    pause(0.5)

    % Switch it off
    sync_settings.SyncOutFlags  = bin2dec('00000000');  % Synch
disabled


    result(1) = calllib('libximc','set_sync_out_settings',
handles.device_idUP, sync_settings);
    result(2) = calllib('libximc','set_sync_out_settings',
handles.device_idLR, sync_settings);

    result = ~all(result == 0);

    if result
        popupErrorMessage('Error writing motor setup');
        return
    end
```

```
function setTimeRemaining(currentPosition , N , Period , h)

    currentTimeRemaining = (N - currentPosition + 1) * Period;

    if currentTimeRemaining <= 0
        T = 'Job done!';
        set(h , 'String' , T);
        return

    elseif currentTimeRemaining < 60  % Seconds
        currentTimeRemaining = round(currentTimeRemaining , 1);
        T = ['Estimated time: ' num2str(currentTimeRemaining) ' s'];

    elseif currentTimeRemaining < 60*60  % minutes
        currentTimeRemaining = round(currentTimeRemaining / 60 , 1);
        T = ['Estimated time: ' num2str(currentTimeRemaining) ' min'];

    else   % Hours
        currentTimeRemaining = currentTimeRemaining / 60 / 60;

        T = ['Estimated time: ' num2str(floor(currentTimeRemaining))
'h ' ...
            num2str(round(60 * (currentTimeRemaining -
floor(currentTimeRemaining)))) 'min'];
    end

    T = {T ; ['Scanning N. ' num2str(currentPosition) '/'
num2str(N)]};

    set(h , 'String' , T);




% --- Executes on button press in btStop.
function btStop_Callback(hObject, eventdata, handles)
% hObject    handle to btStop (see GCBO)
% eventdata  reserved - to be defined in a future version of MATLAB
% handles    structure with handles and user data (see GUIDATA)

    if ~isempty(handles.hScanTimer)
        stop(handles.hScanTimer);

        delete(handles.hScanTimer);
        handles.hScanTimer = [];
    end

    enableGUI(handles , 'paused');
    updateJobStatus(handles);
    guidata(hObject , handles);



% --- Executes on button press in btReset.
function btReset_Callback(hObject, eventdata, handles)
% hObject    handle to btReset (see GCBO)
% eventdata  reserved - to be defined in a future version of MATLAB
% handles    structure with handles and user data (see GUIDATA)
```

```
    answer = questdlg('Are you sure you want to lose all scans?' ,
'Reset', 'Yes' , 'No' , 'Cancel' , 'Cancel');

    if ~strcmp(answer , 'Yes');    return;   end

    % Reset number of scans done
    ScansDone = getappdata(handles.GUI_Motor_and_camera ,
'ScansDone');
    ScansDone = ScansDone .*0;
    setappdata(handles.GUI_Motor_and_camera , 'ScansDone' ,
ScansDone);

    handles = updateGraph(handles);


    % Stop timer if it was running
    if ~isempty(handles.hScanTimer) && isvalid(handles.hScanTimer)
        stop(handles.hScanTimer)

        delete(handles.hScanTimer)
        handles.hScanTimer = [];
    end

    updateJobStatus(handles);
    enableGUI(handles , 'idle');
    guidata(hObject , handles);




% --- Executes when user attempts to close GUI_Motor_and_camera.
function GUI_Motor_and_camera_CloseRequestFcn(hObject, eventdata,
handles)
% hObject    handle to GUI_Motor_and_camera (see GCBO)
% eventdata  reserved - to be defined in a future version of MATLAB
% handles    structure with handles and user data (see GUIDATA)

% Hint: delete(hObject) closes the figure
% Close devices

    if ~handles.DEBUGMODE
        device_id_ptr = libpointer('int32Ptr', handles.device_idUP);
        calllib('libximc','close_device', device_id_ptr);
        device_id_ptr = libpointer('int32Ptr', handles.device_idLR);
        calllib('libximc','close_device', device_id_ptr);
    end

    delete(hObject);



function out = checkStrNumber(str)


    out = all(ismember(str, '0123456789+-.'));
    out = out && ~isnan(str2double(str));
```

```
% --- Executes on button press in btGoToStep.
function btGoToStep_Callback(hObject, eventdata, handles)
% hObject    handle to btGoToStep (see GCBO)
% eventdata  reserved - to be defined in a future version of MATLAB
% handles    structure with handles and user data (see GUIDATA)


    ScansDone = getappdata(handles.GUI_Motor_and_camera ,
'ScansDone');
    N = length(ScansDone);

    Nstep = inputdlg(['Enter step number [1 - ' num2str(N) ']:'] , 'Go
to step #' , 1);
    if isempty(Nstep);    return;    end

    checkstr = checkStrNumber(Nstep{1});
    Nstep = str2double(Nstep{1});

    if checkstr ~= 1 || Nstep == 0 || Nstep > N || Nstep < 1;
        msgbox(['Please enter a number between 1 and '  num2str(Nstep)
' !']);
        return;
    end


    ScansDone = ScansDone .* 0;
    if Nstep > 1;  ScansDone(1 : Nstep - 1) = 1;   end


    setappdata(handles.GUI_Motor_and_camera , 'ScansDone' ,
ScansDone);

    updateROIstatus(handles);
    handles = updateGraph(handles);
    setTimeRemaining(Nstep , N , handles.AcquisitionTime,
handles.txEstimatedTime);
    set(handles.hProgressBar , 'Position' , [0 , 0 , (Nstep - 1) / N ,
1]);


    enableGUI(handles , 'idle');
    % Move to next (first?) position and scan


% --------------------------------------------------------------------
function uiSave_ClickedCallback(hObject, eventdata, handles)
% hObject    handle to uiSave (see GCBO)
% eventdata  reserved - to be defined in a future version of MATLAB
% handles    structure with handles and user data (see GUIDATA)


    DefaultName = clock;
    DefaultName = [num2str(DefaultName(1)) ' ' num2str(DefaultName(2))
' ' num2str(DefaultName(3))...
               ' - ' num2str(DefaultName(4)) '_'
num2str(DefaultName(5)) '.mat'];


    if ~isempty(handles.lastSavePath) && exist(handles.lastSavePath ,
'file')
```

```
        cd(handles.lastSavePath);
    end


    [FileName,PathName] = uiputfile('*.mat','Save
scan...',DefaultName);

    if FileName == 0;
        return
    end

    handles.lastSavePath = PathName;
    writeConfig(handles)


    ScansDone = getappdata(handles.GUI_Motor_and_camera ,
'ScansDone');
    MotorPath = getappdata(handles.GUI_Motor_and_camera ,
'MotorPath');

    StepSizeHorizontal_mm = handles.StepSizeHorizontal;
    StepSizeVertical_mm   = handles.StepSizeVertical;

    ScanTime_seconds = handles.AcquisitionTime;

    save([PathName FileName] , 'ScansDone' , 'MotorPath' ,...
        'StepSizeHorizontal_mm' , 'StepSizeVertical_mm' ,
'ScanTime_seconds');

    guidata(hObject , handles);



function handles = loadConfig(handles)

    configFile = [fileparts(mfilename('fullpath')) '\config_GUI.mat'];
    if ~exist(configFile, 'file')
        return;
    end

    load(configFile)

    handles.lastSavePath = lastSavePath;




function writeConfig(handles)

    configFile = [fileparts(mfilename('fullpath')) '\config_GUI.mat'];

    lastSavePath = handles.lastSavePath;

    save(configFile , 'lastSavePath');


% --- Executes on button press in pushbutton7.
function pushbutton7_Callback(hObject, eventdata, handles)
```

```
% hObject    handle to pushbutton7 (see GCBO)
% eventdata  reserved - to be defined in a future version of MATLAB
% handles    structure with handles and user data (see GUIDATA)



function txAcquisitionsPerStep_Callback(hObject, eventdata, handles)
% hObject    handle to txAcquisitionsPerStep (see GCBO)
% eventdata  reserved - to be defined in a future version of MATLAB
% handles    structure with handles and user data (see GUIDATA)

% Hints: get(hObject,'String') returns contents of
txAcquisitionsPerStep as text
%        str2double(get(hObject,'String')) returns contents of
txAcquisitionsPerStep as a double


    handles = parseInput(handles);
    guidata(hObject , handles);




% --- Executes during object creation, after setting all properties.
function txAcquisitionsPerStep_CreateFcn(hObject, eventdata, handles)
% hObject    handle to txAcquisitionsPerStep (see GCBO)
% eventdata  reserved - to be defined in a future version of MATLAB
% handles    empty - handles not created until after all CreateFcns
called

% Hint: edit controls usually have a white background on Windows.
%       See ISPC and COMPUTER.
if ispc && isequal(get(hObject,'BackgroundColor'),
get(0,'defaultUicontrolBackgroundColor'))
    set(hObject,'BackgroundColor','white');
end
```

Measure Peak

```
function MeasurePeak_V01
    if exist('\\isad.isadroot.ex.ac.uk\UOE\User\MATLAB' , 'file')
        cd('\\isad.isadroot.ex.ac.uk\UOE\User\MATLAB')
    end
        cd('\\isad.isadroot.ex.ac.uk\UOE\User\MATLAB')


    [FileName,PathName] = uigetfile('*.fig' , 'Open File' ,
'MultiSelect', 'on');
    %FileName = fullfile(PathName, FileName);
    if iscell(FileName)
        if FileName{1} == 0;  return;   end


        for k = 1 : length(FileName)
            openfig([PathName FileName{k}]);
            set(gca,'ButtonDownFcn',@ButtonClicked);
        end
```

```
    else
        if FileName == 0;  return;   end

        FileName = [PathName FileName];

        openfig(FileName);
        set(gca,'ButtonDownFcn',@ButtonClicked);

    end


function ButtonClicked(hObject , eventdata)
    disp('yay')
    cp = get(gca,'CurrentPoint');
    cp = cp(1 , 1:2);


    % Find the line in the figure
    objLine = get(hObject,'Children');
    objLine = findobj(objLine , 'Type' , 'line' ,'-
not','Tag','MeasurePeak');
    XData   = get(objLine,'XData'); %get the x data
    YData   = get(objLine,'YData'); %get the y data


    % Find highest peak near the clicked point
    where = XData > (cp(1) - 30) & XData <( cp(1) + 30);

    % Smooth data to detect points
    YData_smooth = moving_average2(YData,2);

    % Remove points far away from click
    YData_clicked = YData_smooth;
    YData_clicked(~where) = NaN;
    [PeakValue , posMax] = nanmax(YData_clicked);

    % Keep the actual max value, not the smoothed one
    YData_clicked = YData;
    YData_clicked(~where) = NaN;
    PeakValue = nanmax(YData_clicked);

    % Show detected peak
    hold(hObject , 'on');
    plot(hObject , XData(posMax) , PeakValue , 'ro' , 'Tag' ,
'MeasurePeak');


    % Now find a change of derivative sign before the peak...
    plot(XData , YData_smooth , 'g-', 'Tag' , 'MeasurePeak');
    D = diff(YData_smooth);
    posMin1 = find(D(1 : posMax - 1) < 0 , 1 , 'last');

    % ...And after the peak
    posMin2 = find(D(posMax + 1 : end) > 0 , 1 , 'first') + posMax;

    YValueBefore = YData(posMin1);
    YValueAfter  = YData(posMin2);

    % Peak difference from background
    PeakMagnificence = PeakValue - mean([YValueBefore , YValueAfter]);
```

```
    % Plot the baseline just because
    plot(XData([posMin1 , posMin2]) , [YValueBefore , YValueAfter] ,
'r-' , 'Tag', 'MeasurePeak')
    plot(XData([posMin1 , posMin2]), YData([posMin1 , posMin2]) , 'ro'
, 'Tag', 'MeasurePeak')


    % Print the text
    xtext = XData(posMin2);
    ytext = mean([YValueBefore , YValueAfter]) + PeakMagnificence / 2;
    t = {['Height = ' num2str(PeakMagnificence)] ;...
         ['Absolute height = ' num2str(PeakValue)]  ;...
         ['Foot values = ' num2str([YData([posMin1 , posMin2])])]};
    disp(t)
    text(xtext , ytext , t , 'Tag', 'MeasurePeak')
    %text(hObject , xtext , ytext , t , 'Tag', 'MeasurePeak');


    % Store result in workspace
    W = evalin('base','whos');

    if any(ismember('Peak_Height',[W(:).name]))
        Peak_Height = evalin('base' , 'Peak_Height');
    else
        Peak_Height = [];
    end

    Peak_Height = [Peak_Height ; [PeakMagnificence , PeakValue ,
YData([posMin1 , posMin2])]];

    assignin('base' , 'Peak_Height' , Peak_Height);



function [ signal ] = moving_average2( signal , points )
% 2-pass moving average filter

    if points==1;   return;   end;

    b = ones(1,points)/points;
    L=length(signal);


    BORDER=2*points;


    if size(signal,1)~=1
        signal=signal';
        signal=filter(b,1,[zeros(1,BORDER)+signal(1) signal
zeros(1,BORDER)+signal(L)]);
        signal=fliplr(filter(b,1,fliplr(signal)));
        signal=signal(BORDER+1:length(signal)-BORDER);
        signal=signal';
    else
        signal=filter(b,1,[zeros(1,BORDER)+signal(1) signal
zeros(1,BORDER)+signal(L)]);
        signal=fliplr(filter(b,1,fliplr(signal)));
        signal=signal(BORDER+1:length(signal)-BORDER);
```

```
    end
```

Bibliography

1 D. Long, *Quantum Mechanical Theory of Rayleigh and Raman Scattering*, 2002, vol. 8.

2 A. Smekal, *Naturwissenschaften*, 1923, **11**, 873–875.

3 C. V. Raman and K. S. Krishnan, *Nature*, 1928, **121**, 501–502.

4 T. H. Maiman, 1960, 493–494.

5 A. J. McQuillan, *Notes Rec. R. Soc.*, 2009, **63**, 105–109.

6 M. Fleischmann, P. J. Hendra and A. . McQuillan, *Chem. Commun.*, 1973, 80–81.

7 P. Hendra, *Analyst*, 2016, **141**, 4996–4999.

8 M. Fleischmann, P. J. Hendra and A. J. McQuillan, *Chem. Phys. Lett.*, 1974, **26**, 163–166.

9 D. L. Jeanmarie and R. P. Van Duyne, *J. Electroanal. Chem.*, 1977, **84**, 1–20.

10 M. G. Albrecht and J. A. Creighton, *J. Am. Chem. Soc.*, 1977, **99**, 5215–5217.

11 P. Matousek, I. P. Clark, E. R. C. Draper, M. D. Morris, a E. Goodship, N. Everall, M. Towrie, W. F. Finney and a W. Parker, *Appl. Spectrosc.*, 2005, **59**, 393–400.

12 N. Stone, M. Kerssens, G. R. Lloyd, K. Faulds, D. Graham and P. Matousek, *Chem. Sci.*, 2011, **2**, 776.

13 L. H. Oakley, S. A. Dinehart, S. A. Svoboda and K. L. Wustholz, *Anal. Chem.*, 2011, **83**, 3986–3989.

14 C. L. Brosseau, F. Casadio and R. P. Van Duyne, *J. Raman Spectrosc.*, 2011, **42**, 1305–1310.

15 C. Conti, C. Colombo, M. Realini, G. Zerbi and P. Matousek, *Appl. Spectrosc.*, 2014, **68**, 686–691.

16 S. Botti, L. Cantarini and A. Palucci, *J. Raman Spectrosc.*, 2010, **41**, 866–869.

17 E. M. A. Ali, H. G. M. Edwards, M. D. Hargreaves and I. J. Scowen, *J. Raman Spectrosc.*, 2010, **41**, 938–943.

18 C. JW, J. JH, G. X, L. GK, S. GL and Y. RQ, *Chem. Eur. J.*, 2008, **14**, 8374–8382.

19 E. L. Holthoff, D. N. Stratis-Cullum and M. E. Hankus, *Sensors*, 2011, **11**, 2700–2714.

20 C. Eliasson and P. Matousek, *Lasers Sci. Facil. Program.*, 2007, 115–116.

21 P. Matousek, *Appl. Spectrosc.*, 2006, **60**, 1341–1347.

22 C. Ricci, C. Eliasson, N. A. MacLeod, P. N. Newton, P. Matousek and S. G. Kazarian, *Anal. Bioanal. Chem.*, 2007, **389**, 1525–1532.

23 O. for N. S. National Cancer Registry, *Stat. Bull.*, 2016, 1–17.

24 M. Quaresma, M. P. Coleman and B. Rachet, *Lancet*, 2015, **385**, 1206–1218.

25 Office for National Statistics, *Incidence of, and mortality from, malignant neoplasm of breast in*

England, 2004 to 2014, 2015.

26 O. for N. Statistics, *Breast Cancer Statistics*, 2015.

27 S. C. Formenti, A. a Arslan and S. M. Love, *Int. J. Breast Cancer*, 2012, **2012**, 249501.

28 O. for N. Statistics, *Breast Cancer: Incidence , Mortality and Survival , 2010*, 2012.

29 for H. and C. E. National Insitute, *Clinical Guideline Familial breast cancer : Classification and care of people at risk of familial breast*, 2013.

30 N. E. Hynes and C. J. Watson, *Cold Spring Harb. Perspect. Biol.*, 2010, **2**, a003186.

31 D. T. Geddes, *Int. Breastfeed. J.*, 2009, **4**, 4.

32 D. T. Ramsay, J. C. Kent, R. A. Hartmann and P. E. Hartmann, *J. Anat.*, 2005, **206**, 525–34.

33 A. Sir Cooper, *The Anatomy and Diseases of the Breast*, Lea & Blanchard, 1845.

34 V. Kumar, A. K. Abbas, N. Fausto, S. L. Robbins and R. S. Cotran, *Robbins and Cotran Pathologic Basis of Disease*, Elsevier, 9th Editio., 2014.

35 S. M. Love and S. H. Barsky, *Cancer*, 2004, **101**, 1947–1957.

36 W. H. Organisation, *Pathology & genetics: tumours of the breast and female genital organs*, 2003.

37 H. Kobayashi, R. Watanabe and P. L. Choyke, *Theranostics*, 2014, **4**, 81–89.

38 J. Folkman, *Nat. Med.*, 1995, **1**, 27–31.

39 A. K. Iyer, G. Khaled, J. Fang and H. Maeda, *Drug Discov. Today*, 2006, **11**, 812–818.

40 B. Weigelt and H. Horlings, *J. Pathol.*, 2008, 141–150.

41 P. Eroles, A. Bosch, J. A. Pérez-Fidalgo and A. Lluch, *Cancer Treat. Rev.*, 2012, **38**, 698–707.

42 M. Smid, Y. Wang, Y. Zhang, A. M. Sieuwerts, J. Yu, J. G. M. Klijn, J. a Foekens and J. W. M. Martens, *Cancer Res.*, 2008, **68**, 3108–14.

43 C. a Hudis and L. Gianni, *Oncologist*, 2011, **16 Suppl 1**, 1–11.

44 C.-L. Chen, J.-S. Chu, W.-C. Su, S.-C. Huang and W.-Y. Lee, *Virchows Arch.*, 2010, **457**, 53–61.

45 W. H. Organisation, *Breast cancer: Prevention and control*, 2007.

46 R. F. Cox, a Hernandez-Santana, S. Ramdass, G. McMahon, J. H. Harmey and M. P. Morgan, *Br. J. Cancer*, 2012, **106**, 525–37.

47 R. R. Millis, R. Davis and A. J. Stacey, *Br. J. Radiol.*, 1976, **49**, 12–26.

48 L. Frappart, M. Boudeulle, J. Boumendil, H. C. Lin, I. Martinon, C. Palayer, Y. Mallet-Guy, D. Raudrant, a Bremond and Y. Rochet, *Hum. Pathol.*, 1984, **15**, 880–889.

49 M. M. Kerssens, P. Matousek, K. Rogers and N. Stone, *Analyst*, 2010, **135**, 3156–3161.

50 R. Baker, K. D. Rogers, N. Shepherd and N. Stone, *Br. J. Cancer*, 2010, **103**, 1034–9.

51 R. G. G. Russell, N. B. Watts, F. H. Ebetino and M. J. Rogers, *Osteoporos. Int.*, 2008, **19**, 733–759.

52 J. A. Cramer, D. T. Gold, S. L. Silverman and E. M. Lewiecki, *Osteoporos. Int.*, 2007, **18**, 1023–1031.

53 S. L. Ruggiero, B. Mehrotra, T. J. Rosenberg and S. L. Engroff, *J. Oral Maxillofac. Surg.*, 2004, **62**, 527–534.

54 J. E. Dunford, K. Thompson, F. P. Coxon, S. P. Luckman, F. M. Hahn, C. D. Poulter, F. H. Ebetino and M. J. Rogers, *J. Pharmacol. Exp. Ther.*, 2001, **296**, 235–242.

55 S. Boissier, M. Ferreras, O. Peyruchaud, S. Magnetto, F. H. Ebetino, M. Colombel, P. Delmas, J. M. Delaissé and P. Clézardin, *Cancer Res.*, 2000, **60**, 2949–2954.

56 J. R. Green, *Cancer*, 2003, **97**, 840–847.

57 M. A. Merrell, S. Wakchoure, J. M. Ilvesaro, K. Zinn, B. Gehrs, P. P. Lehenkari, K. W. Harris and K. S. Selander, *Eur. J. Pharmacol.*, 2007, **559**, 21–31.

58 R. E. Coleman, *Cancer Treat. Rev.*, 2001, **27**, 165–176.

59 L. E. Cole, T. Vargo-Gogola and R. K. Roeder, *Biomaterials*, 2014, **35**, 2312–2321.

60 W. Hamilton, S. Stapley, C. Campbell, G. Lyratzopoulos, G. Rubin and R. D. Neal, *BMC Cancer*, 2015, **15**, 820.

61 W. H. Organisation, *Guide To Cancer Early Diagnosis*, 2017.

62 S. Walters, C. Maringe, M. P. Coleman, M. D. Peake, J. Butler, N. Young, S. Bergström, L. Hanna, E. Jakobsen, K. Kölbeck, S. Sundstrøm, G. Engholm, A. Gavin, M. L. Gjerstorff, J. Hatcher, T. B. Johannesen, K. M. Linklater, C. E. McGahan, J. Steward, E. Tracey, D. Turner, M. a Richards and B. Rachet, *Br. J. Cancer*, 2013, **108**, 1195–1208.

63 M. Richards, A. Westcombe, S. Love, P. Littlejohns and A. Ramirez, *Lancet*, 1999, **353**, 1119–1126.

64 NICE Guideline, *NICE Guidel.*, 2015, 1–378.

65 W. Hamilton, F. M. Walter, G. Rubin and R. D. Neal, *Nat. Rev. Clin. Oncol.*, 2016, **13**, 740–749.

66 P. D. P. Pharoah, B. Sewell, D. Fitzsimmons, H. S. Bennett and N. Pashayan, *Bmj*, 2013, **346**, f2618–f2618.

67 S. and I. Team, *Breast Screening Programme, England 2014-15*, 2016.

68 I. Nice, 2009, 1–33.

69 Y. Meng, S. Ward, K. Cooper, S. Harnan and L. Wyld, *Eur. J. Surg. Oncol.*, 2011, **37**, 40–46.

70 N. C. C. for Cancer, *Natl. Collab. Cent. Cancer*, 2013.

71 National Insitute for Health and Care Excellence, *Breast Cancer Quality Standard [QS12]*, 2016, vol. V 1.

72 J. P. Kosters and P. C. Gotzsche, *Cochrane Database Syst Rev*, 2003, 0.

73 Okonkwo, G. Draisma, A. Kinderen, M. Brown and H. Koning, *J. Natl. Cancer Inst.*, 2008, **100**, 1290–1300.

74 D. Saslow, J. Hannan, J. Osuch, M. H. Alciati, C. Baines, M. Barton and D. Kopans, *CA. Cancer J. Clin.*, 2004, **54**, 327–344.

75 R. E. Hendrick, *Radiology*, 2010, **257**, 246–253.

76 D. O' Leary, A. Teape, J. Hammond, L. Rainford and T. Grant, *Eur. Congr. Radiol. 2011*, 2011, 1–19.

77 A. Poulos and D. McLean, *Radiography*, 2004, **10**, 131–137.

78 M. Faulk and A. Sickles, *Radiology*, 1992, **185**, 87–90.

79 U. N. L. of Medicine, *MedPix*.

80 M. G. Marmot, D. G. Altman, D. a Cameron, J. a Dewar, S. G. Thompson and M. Wilcox, *Br. J. Cancer*, 2013, **108**, 2205–40.

81 O. for N. Statistics, *Breast Screening Programme, England 2011-12*, 2013.

82 N. C. I. Network, *Screen-Detected Breast Cancer*, 2011.

83 NHS England, 2015, 1–21.

84 P. Whelehan, A. Evans, M. Wells and S. MacGillivray, *Breast*, 2013, **22**, 389–394.

85 M. Robinson and C. J. Kotre, *Br. J. Radiol.*, 2008, **81**, 214–218.

86 P. H. England, *Prevalence of underweight, healthy weight, overweight, obesity, and excess weight among adults at local authority level for England*, 2016.

87 C. E. Mercer, K. Szczepura, J. Kelly, S. R. Millington, E. R. E. Denton, R. Borgen, B. Hilton and P. Hogg, *Radiography*, 2015, **21**, 68–73.

88 P. B. Gordon and S. L. Goldenberg, *Cancer*, 1995, **76**, 626–630.

89 W. A. Berg, Z. Zhang, D. Lehrer, R. A. Jong, E. D. Pisano, R. G. Barr, M. Bohm-Velez, M. C. Mahoney, W. P. Evans 3rd, L. H. Larsen, M. J. Morton, E. B. Mendelson, D. M. Farria, J. B. Cormack, H. S. Marques, A. Adams, N. M. Yeh and G. Gabrielli, *Jama*, 2012, **307**, 1394–1404.

90 J. E. Cantera, I. S. Yarza, P. Slon and L. J. P. Insausti, 2013, 1–24.

91 R. J. Hooley, L. M. Scoutt and L. E. Philpotts, *Radiology*, 2013, **268**, 642–659.

92 M. E. Anderson, M. S. Soo, R. C. Bentley and G. E. Trahey, *J. Acoust. Soc. Am.*, 1997, **101**, 29–39.

93 C. Borrelli, S. Cohen, A. Duncan, R. Given-Wilson, J. Jenkins, O. Kearins, S. Pinder, N. Sharma, M. Sibbering, J. Steel, A. Turnbull and M. G. Wallis, 2016.

94 W. H. Hindle and K. Mokbel, *Glob. Libr. Women's Med.*, 2009.

95 N. P. Ehrhart and S. J. Withrow, 2016.

96 L. Tabár, P. B. Dean, N. Lindhe and M. Ingvarsson, *Int. J. Breast Cancer*, 2012, **2012**, 489345.

97 P. Robbins, S. Pinder, N. de Klerk, H. Dawkins, J. Harvey, G. Sterrett, I. Ellis and C. Elston, *Hum. Pathol.*, 1995, **26**, 873–879.

98 J. G. Elmore, G. M. Longton, P. A. Carney, B. M. Geller, T. Onega, A. N. A. Tosteson, H. D. Nelson, M. S. Pepe, K. H. Allison, S. J. Schnitt, F. P. O'Malley and D. L. Weaver, *Jama*, 2015, **313**, 1122.

99 S. H. Heywang-Köbrunner, P. Viehweg, A. Heinig and C. Küchler, *Eur. J. Radiol.*, 1997, **24**, 94–108.

100 National institue for Health and Care Excellence. UK, 2015.

101 National Insitute for Health and Care Excellence, *Early and locally advanced breast cancer: diagnosis and treatment (Guideline CG80)*, 2005.

102 A. J. Primeau, A. Rendon, D. Hedley, L. Lilge and I. F. Tannock, *Clin. Cancer Res.*, 2005, **11**, 8782–8788.

103 E. Smith and G. Dent, *Modern Raman Spectroscopy - A Practical Approach*, John Wiley & Sons, Ltd, Chichester, UK, 2005.

104 M. J. Baker, S. R. Hussain, L. Lovergne, V. Untereiner, C. Hughes, R. A. Lukaszewski, G. Thiéfin and G. D. Sockalingum, *Chem. Soc. Rev.*, 2016, **45**, 1803–1818.

105 T. Soderberg, *Organic Chemistry with a Biological Emphasis, Volume I*, Chemistry Faculty, 2016.

106 R. L. McCreery, *Raman Spectroscopy for Chemical Analysis*, John Wiley & Sons, Inc., Hoboken, NJ, USA, 2000.

107 M. H. Niemz, *Laser-Tissue Interactions, Fundamentals and Applications*, Springer International Publishing, Third Edit., 2007.

108 E. Smith and G. Dent, *Modern Raman Sectroscopy - A Practical Approach*, John Wiley & Sons, Ltd, 2005.

109 E. Le Ru and P. Etchegoin, *Principles of Surface-Enhanced Raman Spectroscopy: and related plasmonic effects*, Elsevier, 2008, vol. 2008.

110 X. Yang, M. Yang, B. Pang, M. Vara and Y. Xia, *Chem. Rev.*, 2015, **115**, 10410–10488.

111 S. M. Morton, E. Ewusi-Annan and L. Jensen, *Phys. Chem. Chem. Phys.*, 2009, **11**, 7424–7429.

112 J. R. Lombardi and R. L. Birke, *J. Phys. Chem.*, 2008, **112**, 5605− 5617.

113 N. Valley, N. Greeneltch, R. P. Van Duyne and G. C. A. Schatz, *J. Phys. Chem. Lett.*, 2013, **4**, 2599−2604.

114 P. Strobbia, E. Languirand and B. M. Cullum, *Opt. Eng.*, 2015, **54**, 100902.

115 E. C. Le Ru, E. J. Blackie, M. Meyer and P. G. Etchegoin, *J. Phys. Chem. C*, 2007, **111**, 13794–13803.

116 K. Kneipp, Y. Wang, H. Kneipp, I. Itzkan, R. Dasari and M. Feld, *Phys. Rev. Lett.*, 1996, **76**, 2444–2447.

117 S. Nie and S. R. Emory, *Science (80-.).*, 1997, **275**, 1102–1106.

118 S. a Maier, *Fundamentals and Applications Plasmonics : Fundamentals and Applications*, 2004, vol. 677.

119 D. Cialla, A. März, R. Böhme, F. Theil, K. Weber, M. Schmitt and J. Popp, *Anal. Bioanal. Chem.*, 2012, **403**, 27–54.

120 S. Schlucker, Ed., *Surface Enhanced Raman Spectroscopy: Analytical, Biophysical and Life Science Applications*, 2011.

121 C. D'Andrea, A. Irrera, B. Fazio, A. Foti, E. Messina, O. M. Maragò, S. Kessentini, P. Artoni, C. David and P. G. Gucciardi, *J. Opt.*, 2015, **17**, 114016.

122 P. L. Stiles, J. A. Dieringer, N. C. Shah and R. P. Van Duyne, *Annu. Rev. Anal. Chem.*, 2008, **1**, 601–626.

123 N. Berkovitch, P. Ginzburg and M. Orenstein, *J. Phys. Condens. Matter*, 2012, **24**, 73202.

124 M. Tréguer-Delapierre, J. Majimel, S. Mornet, E. Duguet and S. Ravaine, *Gold Bull.*, 2008, **41**, 195–207.

125 K. L. Wustholz, A.-I. Henry, J. M. McMahon, R. G. Freeman, N. Valley, M. E. Piotti, M. J. Natan, G. C. Schatz and R. P. Van Duyne, *J. Am. Chem. Soc.*, 2010, **132**, 10903–10.

126 B. C. Galarreta, E. Harté, N. Marquestaut, P. R. Norton and F. Lagugné-Labarthet, *Phys. Chem. Chem. Phys.*, 2010, **12**, 6810–6.

127 L. E. Hennemann, A. Kolloch, A. Kern, J. Mihaljevic, J. Boneberg, P. Leiderer, A. J. Meixner and D. Zhang, *Beilstein J. Nanotechnol.*, 2012, **3**, 674–683.

128 L. A. Lane, X. Qian and S. Nie, *Chem. Rev.*, 2015, **115**, 10489–10529.

129 C. L. Haynes, A. D. McFarland, L. Zhao, R. P. Van Duyne, G. C. Schatz, L. Gunnarsson, J. Prikulis, B. Kasemo and M. Käll, *J. Phys. Chem. B*, 2003, **107**, 7337–7342.

130 Nanocomposix, .

131 C. Hoskins, Y. Min, M. Gueorguieva, C. McDougall, A. Volovick, P. Prentice, Z. Wang, A. Melzer, A. Cuschieri and L. Wang, *J. Nanobiotechnology*, 2012, **10**, 27.

132 Z. Ban, Y. a. Barnakov, F. Li, V. O. Golub and C. J. O'Connor, *J. Mater. Chem.*, 2005, **15**, 4660.

133 R. K. Ambasta, A. Sharma and P. Kumar, *Vasc. Cell*, 2011, **3**, 26.

134 Y.-N. Wu, P.-C. Wu, L.-X. Yang, K. R. Ratinac, P. Thordarson, K. a Jahn, D.-H. Chen, D.-B. Shieh and F. Braet, *Int. J. Nanomedicine*, 2013, **8**, 3321–31.

135 C.-H. Liang, C.-C. Wang, Y.-C. Lin, C.-H. Chen, C.-H. Wong and C.-Y. Wu, *Anal. Chem.*, 2009, **81**, 7750–6.

136 N. D. Israelsen, C. Hanson and E. Vargis, *Sci. World J.*, 2015, **2015**.

137 S. P. Mulvaney, M. D. Musick, C. D. Keating and M. J. Natan, *Langmuir*, 2003, **19**, 4784–4790.

138 C. L. Zavaleta, B. R. Smith, I. Walton, W. Doering, G. Davis, B. Shojaei, M. J. Natan and S. S. Gambhir, *Proc. Natl. Acad. Sci. U. S. A.*, 2009, **106**, 13511–13516.

139 A. C. Templeton, W. P. Wuelfing and R. W. Murray, *Acc. Chem. Res.*, 2000, **33**, 27–36.

140 D. V Leff, L. Brandt and J. R. Heath, *Langmuir*, 1996, **12**, 4723–4730.

141 D. Jaque, L. Martínez Maestro, B. del Rosal, P. Haro-Gonzalez, A. Benayas, J. L. Plaza, E. Martín Rodríguez and J. García Solé, *Nanoscale*, 2014, **6**, 9494–9530.

142 X. Huang, I. H. El-Sayed, W. Qian and M. a El-Sayed, *J. Am. Chem. Soc.*, 2006, **128**, 2115–20.

143 G. Zhang, X. Sun, J. Jasinski, D. Patel and A. M. Gobin, *J. Nanomater.*, 2012, **2012**, 1–9.

144 Prashant K. Jain, Kyeong Seok Lee, Ivan H. El-Sayed and Mostafa A. El-Sayed, *J. Phys. Chem. B*, 2006, **110**, 7238–7248.

145 L. R. Hirsch, R. J. Stafford, J. A. Bankson, S. R. Sershen, B. Rivera, R. E. Price, J. D. Hazle, N. J. Halas and J. L. West, *Proc. Natl. Acad. Sci. U. S. A.*, 2003, **100**, 13549–54.

146 R. Weissleder, *Nat. Biotechnol.*, 2001, **19**, 316–317.

147 S. L. Jacques, *Phys. Med. Biol.*, 2013, **58**, 5007–5008.

148 P. K. Jain, X. Huang, I. H. El-Sayed and M. a. El-Sayed, *Plasmonics*, 2007, **2**, 107–118.

149 R. Weissleder, *Nat. Biotechnol.*, 2001, **19**, 316–317.

150 D. Boas, D. Brooks, E. Miller, C. Dimarzio, M. Kilmer, R. Gaudette and Q. Zhang, *IEEE Signal Process. Mag.*, 2001, **18**, 57–75.

151 B. C. Wilson and G. Adam, *Med. Phys.*, 1983, 10, 824–830.

152 S. L. Jacques and S. A. Prahl, *Lasers Surg. Med.*, 1987, **6**, 494–503.

153 R. Steiner, in *Laser and IPL Technology in Dermatology and Aesthetic Medicine*, eds. C. Raulin and S. Karsai, Springer-Verlag Berlin Heidelberg, 2011, pp. 23–36.

154 Z. Movasaghi, S. Rehman and I. U. Rehman, *Appl. Spectrosc. Rev.*, 2007, **42**, 493–541.

155 H. J. Butler, L. Ashton, B. Bird, G. Cinque, K. Curtis, J. Dorney, K. Esmonde-white, N. J. Fullwood, B. Gardner, P. L. Martin-Hirsch, M. J. Walsh, M. R. Mcainsh, N. Stone and F. L. Martin, *Nat. Protoc.*, 2016, **11**, 664–687.

156 A. Mahadevan-Jansen, M. F. Mitchell, N. Ramanujam, U. Utzinger and R. Richards-Kortum, *Photochem. Photobiol.*, 1998, **68**, 427–431.

157 Z. Huang, A. McWilliams, H. Lui, D. I. McLean, S. Lam and H. Zeng, *Int. J. cancer*, 2003, **107**, 1047–1052.

158 A. Molckovsky, L. M. W. K. Song, M. G. Shim, N. E. Marcon and B. C. Wilson, *Gastrointest. Endosc.*, 2003, **57**, 396–402.

159 M. Jermyn, K. Mok, J. Mercier, J. Desroches, J. Pichette, K. Saint-Arnaud, L. Bernstein, M.-C. Guiot, K. Petrecca and F. Leblond, *Sci. Transl. Med.*, 2015, **7**, 274ra19-274ra19.

160 L. M. Fullwood, I. E. Iping Petterson, A. P. Dudgeon, G. R. Lloyd, C. Kendall, C. Hall, J. C. C. Day and N. Stone, *Biomed. Vib. Spectrosc.*, 2016, 1–8.

161 K. Kong, C. Kendall, N. Stone and I. Notingher, *Adv. Drug Deliv. Rev.*, 2015, **89**, 121–134.

162 F. Jobsis, *Science (80-.).*, 1977, **198**, 1264–1267.

163 M. Ferrari and V. Quaresima, *Neuroimage*, 2012, **63**, 921–935.

164 S. F. Malin, T. L. Ruchti, T. B. Blank, S. N. Thennadil and S. L. Monfre, *Clin. Chem.*, 1999, **45**, 1651–1658.

165 E. Sadauskas, G. Danscher, M. Stoltenberg, U. Vogel, A. Larsen and H. Wallin, *Nanomedicine Nanotechnology, Biol. Med.*, 2009, **5**, 162–169.

166 S. K. Balasubramanian, J. Jittiwat, J. Manikandan, C. N. Ong, L. E. Yu and W. Y. Ong, *Biomaterials*, 2010, **31**, 2034–2042.

167 Z. Lin, N. A. Monteiro-Riviere, R. Kannan and J. E. Riviere, *Nanomedicine (Lond).*, 2016, **11**, 107–19.

168 A. E. Nel, L. Mädler, D. Velegol, T. Xia, E. M. V Hoek, P. Somasundaran, F. Klaessig, V. Castranova and M. Thompson, *Nat. Mater.*, 2009, **8**, 543–557.

169 A. Bianco, K. Kostarelos and M. Prato, *Curr. Opin. Chem. Biol.*, 2005, **9**, 674–679.

170 C. W. Lam, J. T. James, R. McCluskey and R. L. Hunter, *Toxicol. Sci.*, 2004, **77**, 126–134.

171 J. Muller, F. Huaux, N. Moreau, P. Misson, J. F. Heilier, M. Delos, M. Arras, A. Fonseca, J. B. Nagy and D. Lison, *Toxicol. Appl. Pharmacol.*, 2005, **207**, 221–231.

172 R. Hardman, *Environ. Health Perspect.*, 2006, **114**, 165–172.

173 R. Shukla, V. Bansal, M. Chaudhary, A. Basu, R. R. Bhonde and M. Sastry, *Langmuir*, 2005, **21**, 10644–10654.

174 J. R. Morones and J. L. Elechiguerra, *Nanotechnology*, 2005, **16**, 2346–53.

175 J. S. Kim, E. Kuk, K. N. Yu, J. H. Kim, S. J. Park, H. J. Lee, S. H. Kim, Y. K. Park, Y. H. Park, C. Y. Hwang, Y. K. Kim, Y. S. Lee, D. H. Jeong and M. H. Cho, *Nanomedicine Nanotechnology, Biol. Med.*, 2007, **3**, 95–101.

176 X. D. Zhang, D. Wu, X. Shen, P. X. Liu, N. Yang, B. Zhao, H. Zhang, Y. M. Sun, L. A. Zhang and F. Y. Fan, *Int. J. Nanomedicine*, 2011, **6**, 2071–2081.

177 W. S. Cho, M. Cho, J. Jeong, M. Choi, B. S. Han, H. S. Shin, J. Hong, B. H. Chung, J. Jeong and M. H. Cho, *Toxicol. Appl. Pharmacol.*, 2010, **245**, 116–123.

178 W. S. Cho, M. Cho, J. Jeong, M. Choi, H. Y. Cho, B. S. Han, S. H. Kim, H. O. Kim, Y. T. Lim, B. H. Chung and J. Jeong, *Toxicol. Appl. Pharmacol.*, 2009, **236**, 16–24.

179 J. Kim, J. Kim, H. Choi, S. Lee, B. Jun, K. Yu, E. Kuk, Y. Kim, D. H. Jeong, M. Cho and Y. Lee, 2006, **78**, 6967–6973.

180 A. Kunzmann, B. Andersson, T. Thurnherr, H. Krug, A. Scheynius and B. Fadeel, *Biochim. Biophys. Acta - Gen. Subj.*, 2011, **1810**, 361–373.

181 U. Taylor, C. Rehbock, C. Streich, D. Rath and S. Barcikowski, *Nanomedicine*, 2014, **9**, 1971–1989.

182 T. Mironava, M. Hadjiargyrou, M. Simon, V. Jurukovski and M. H. Rafailovich, *Nanotoxicology*, 2010, **4**, 120–137.

183 P. C. Hiemenz and R. Rajagopalan, *Principles of Colloid and Surface Chemistry*, Marcel Dekker Inc, Third Edit., 1997.

184 D. J. Shaw, *Introduction to Colloid and Surface Chemistry*, Butterworth Heinemann, Fouth Edit., 1992.

185 I. Lynch and K. A. Dawson, *Nano Today*, 2008, **3**, 40–47.

186 J. Jiang, G. Oberdörster and P. Biswas, *J. Nanoparticle Res.*, 2009, **11**, 77–89.

187 R. A. Alvarez-Puebla, E. Arceo, P. J. Goulet, J. J. Garrido and R. F. Aroca, *J Phys Chem B*, 2005, **109**, 3787–3792.

188 Silver-Colloids.com, 2015.

189 A. Verma and F. Stellacci, *Small*, 2010, **6**, 12–21.

190 T. Niidome, M. Yamagata, Y. Okamoto, Y. Akiyama, H. Takahashi, T. Kawano, Y. Katayama and Y. Niidome, *J. Control. Release*, 2006, **114**, 343–347.

191 R. Xu, G. Zhang, J. Mai, X. Deng, V. Segura-Ibarra, S. Wu, J. Shen, H. Liu, Z. Hu, L. Chen, Y. Y. Y. Y. Huang, E. Koay, Y. Y. Y. Y. Huang, J. Liu, J. E. Ensor, E. Blanco, X. Liu, M. Ferrari and H. Shen, *Nat. Biotechnol.*, 2016, **34**, 1–7.

192 M. A. Dobrovolskaia, A. K. Patri, J. Zheng, J. D. Clogston, N. Ayub, P. Aggarwal, B. W. Neun, J. B. Hall and S. E. McNeil, *Nanomedicine Nanotechnology, Biol. Med.*, 2009, **5**, 106–117.

193 C. D. Walkey and W. C. W. Chan, *Chem. Soc. Rev.*, 2012, **41**, 2780–99.

194 M. P. Monopoli, C. Åberg, A. Salvati and K. A. Dawson, *Nat. Nanotechnol.*, 2012, **7**, 779–786.

195 M. Rahman, S. Laurent, N. Tawil, L. Yahia and M. Mahmoudi, in *Protein-Nanoparticle Interactions The Bio-Nano Interface*, Springer International Publishing, 2013, vol. 15, pp. 21–45.

196 M. Lundqvist, J. Stigler, G. Elia, I. Lynch, T. Cedervall and K. A. Dawson, *Proc. Natl. Acad. Sci. U. S. A.*, 2008, **105**, 14265–70.

197 P. Roach, D. Farrar and C. C. Perry, *J. Am. Chem. Soc.*, 2006, **128**, 3939–3945.

198 R. Weissleder, M. Nahrendorf and M. J. Pittet, *Nat. Mater.*, 2014, **13**, 125–38.

199 D. Simberg, T. Duza, J. H. Park, M. Essler, J. Pilch, L. Zhang, A. M. Derfus, M. Yang, R. M. Hoffman, S. Bhatia, M. J. Sailor and E. Ruoslahti, *Proc. Natl. Acad. Sci. U. S. A.*, 2007, **104**, 932–936.

200 C. J. Hu, R. H. Fang, K. Wang, B. T. Luk, S. Thamphiwatana, D. Dehaini, P. Nguyen, P. Angsantikul, C. H. Wen, A. V Kroll, C. Carpenter, M. Ramesh, V. Qu, S. H. Patel, J. Zhu, W. Shi, F. M. Hofman, T. C. Chen, W. Gao, K. Zhang, S. Chien and L. Zhang, *Nature*, 2015, **526**, 118–21.

201 J. V Jokerst, T. Lobovkina, R. N. Zare and S. S. Gambhir, *Nanomedicine (Lond).*, 2011, **6**, 715–728.

202 F. Alexis, E. Pridgen, L. K. Molnar and O. C. Farokhzad, *Mol. Pharm.*, 2008, **5**, 505–515.

203 E. C. Dreaden, S. C. Mwakwari, Q. H. Sodji, A. K. Oyelere and M. A. El-Sayed, *Bioconjug. Chem.*, 2009, **20**, 2247–2253.

204 T. Stuchinskaya, M. Moreno, M. J. Cook, D. R. Edwards and D. a Russell, *Photochem. Photobiol. Sci.*, 2011, **10**, 822–831.

205 S. Takae, Y. Akiyama, H. Otsuka, T. Nakamura, Y. Nagasaki and K. Kataoka, *Biomacromolecules*, 2005, **6**, 818–824.

206 X. Qian, X.-H. Peng, D. O. Ansari, Q. Yin-Goen, G. Z. Chen, D. M. Shin, L. Yang, A. N. Young, M. D. Wang and S. Nie, *Nat. Biotechnol.*, 2008, **26**, 83–90.

207 S. D. Perrault, C. Walkey, T. Jennings, H. C. Fischer and W. C. W. Chan, *Nano Lett.*, 2009, **9**, 1909–1915.

208 Q. Yang, S. W. Jones, C. L. Parker, W. C. Zamboni, J. E. Bear and S. K. Lai, *Mol. Pharm.*, 2014, **11**, 1250–1258.

209 H. Maeda, J. Wu, T. Sawa, Y. Matsumura and K. Hori, *J. Control. Release*, 2000, **65**, 271–284.

210 H. Maeda, H. Nakamura and J. Fang, *Adv. Drug Deliv. Rev.*, 2013, **65**, 71–79.

211 G. F. Paciotti, L. Myer, D. Weinreich, D. Goia, N. Pavel, R. E. McLaughlin and L. Tamarkin, *Drug Deliv.*, 2004, **11**, 169–183.

212 P. Mukherjee, R. Bhattacharya, P. Wang, L. Wang, S. Basu, J. A. Nagy, D. Mukhopadhyay and S. Soker, 2005, **11**, 3530–3535.

213 C. Parolo, A. De La Escosura-Muñiz, E. Polo, V. Grazú, J. M. De La Fuente and A. Merkoçi, *ACS Appl. Mater. Interfaces*, 2013, **5**, 10753–10759.

214 A. Salvati, A. S. Pitek, M. P. Monopoli, K. Prapainop, F. B. Bombelli, D. R. Hristov, P. M. Kelly, C. Åberg, E. Mahon and K. a Dawson, *Nat. Nanotechnol.*, 2013, **8**, 137–43.

215 A. I. Henry, B. Sharma, M. F. Cardinal, D. Kurouski and R. P. Van Duyne, *Anal. Chem.*, 2016, **88**, 6638–6647.

216 K. K. Maiti, U. S. Dinish, C. Y. Fu, J. J. Lee, K. S. Soh, S. W. Yun, R. Bhuvaneswari, M. Olivo and Y. T. Chang, *Biosens. Bioelectron.*, 2010, 26, 398–403.

217 G. Zhang, Z. Yang, W. Lu, R. Zhang, Q. Huang, M. Tian, L. Li, D. Liang and C. Li, *Biomaterials*, 2009, **30**, 1928–1936.

218 X. D. Zhang, H. Y. Wu, D. Wu, Y. Y. Wang, J. H. Chang, Z. Bin Zhai, A. M. Meng, P. X. Liu, L. A. Zhang and F. Y. Fan, *Int. J. Nanomedicine*, 2010, **5**, 771–781.

219 H. Chen, Z. Zhen, T. Todd, P. K. Chu and J. Xie, *Mater. Sci. Eng. R. Rep.*, 2013, **74**, 35–69.

220 Y. S. Chen, Y. C. Hung, I. Liau and G. S. Huang, *Nanoscale Res. Lett.*, 2009, **4**, 858–864.

221 U. S. Dinish, G. Balasundaram, Y.-T. Chang and M. Olivo, *Sci. Rep.*, 2014, **4**, 4075.

222 A. Samanta, K. K. Maiti, K. S. Soh, X. Liao, M. Vendrell, U. S. Dinish, S. W. Yun, R. Bhuvaneswari, H. Kim, S. Rautela, J. Chung, M. Olivo and Y. T. Chang, *Angew. Chemie - Int. Ed.*, 2011, **50**, 6089–6092.

223 J. Turkevich, *Disscussions Faraday Soc.*, 1951, **11**, 55–75.

224 S. Kumar, K. S. Gandhi and R. Kumar, *Ind. Eng. Chem. Res.*, 2007, **46**, 3128–3136.

225 A. Scientific, .

226 G. Zhang, J. B. Jasinski, J. L. Howell, D. Patel, D. P. Stephens and A. M. Gobin, *Nanoscale Res. Lett.*, 2012, **7**, 337.

227 Q. Control and L. Science, .

228 R. A. Alvarez-Puebla, D. S. Dos Santos Júnior and R. F. Aroca, *Analyst*, 2004, **129**, 1251–1256.

229 R. A. Alvarez-Puebla, D. J. Ross, G.-A. Nazri and R. F. Aroca, *Langmuir*, 2005, **21**, 10504–10508.

230 A. Michota and J. Bukowska, *J. Raman Spectrosc.*, 2003, **34**, 21–25.

231 L. E. Cole, T. Vargo-gogola, R. K. Roeder and C. E. T. Al, *Am. Chem. Soc. Nano*, 2015, **9**, 8923–8932.

232 L. E. Cole, T. Vargo-Gogola and R. K. Roeder, *Adv. Drug Deliv. Rev.*, 2016, **99**, 12–27.

233 L. A. Lane, X. Qian, A. M. Smith and S. Nie, *Annu. Rev. Phys. Chem.*, 2015, **66**, 521–547.

234 C. Tassa, J. L. Duffner, T. A. Lewis, R. Weissleder, S. L. Schreiber, A. N. Koehler and S. Y. Shaw, *Bioconjug. Chem.*, 2010, **21**, 14–19.

235 L. De Miguel, M. Noiray, G. Surpateanu, B. I. Iorga and G. Ponchel, *Int. J. Pharm.*, 2014, **460**, 73–82.

236 S. Zhang, G. Gangal and H. Uludag, *Chem. Soc. Rev.*, 2007, **36**.

237 T. Liu and B. Thierry, *Langmuir*, 2012, **28**, 15634–15642.

238 B. R. Mbi, 2013.

239 N. Nakajima and Y. Ikada, *Bioconjug. Chem.*, 1995, **6**, 123–130.

240 H. Mojarradi, *Uppsala Univ. Publ.*, 2011, 44.

241 Z. Grabarek and J. Gergely, *Anal. Biochem.*, 1990, **185**, 131–135.

242 D. J. Watmough, *Radiology*, 1983, **147**, 89–92.

243 J. Linford, S. Shalev, J. Bews, R. Brown and H. Schipper, *Med. Phys.*, 1986, **13**, 869–875.

244 R. Cubeddu, C. D'Andrea, A. Pifferi, P. Taroni, A. Torricelli and G. Valentini, *Photochem. Photobiol.*, 2000, **72**, 383.

245 N. Shah, A. Cerussi, C. Eker, J. Espinoza, J. Butler, J. Fishkin, R. Hornung and B. Tromberg, *Pnas*, 2001, **98**, 4420–4425.

246 S. Srinivasan, B. W. W. Pogue, S. Jiang, H. Dehghani, C. Kogel, S. Soho, J. J. J. Gibson, T. D. D. Tosteson, S. P. P. Poplack and K. D. D. Paulsen, *Proc. Natl. Acad. Sci. U. S. A.*, 2003, **100**, 12349–54.

247 X. Intes, *Acad. Radiol.*, 2005, **12**, 934–947.

248 A. E. Cerussi, A. J. Berger, F. Bevilacqua, N. Shah, D. Jakubowski, J. Butler, R. F. Holcombe and B. J. Tromberg, *Acad. Radiol.*, 2001, **8**, 211–218.

249 B. W. Pogue and M. S. Patterson, *J. Biomed. Opt.*, 2006, **11**, 41102-41102–16.

250 G. C. Beck, N. Akgün, A. Rück and R. Steiner, *Lasers Med. Sci.*, 1998, **13**, 160–171.

251 F. P. Bolin, L. E. Preuss, R. C. Taylor and R. J. Ference, *Appl. Opt.*, 1989, **28**, 2297–2303.

252 G. Lamouche, B. F. Kennedy, K. M. Kennedy, C. Bisaillon, A. Curatolo, G. Campbell and D. D. Sampson, *Biomed. Opt. Express*, 2012, **3**, 1381–1398.

253 H. G. Akarçay, S. Preisser, M. Frenz and J. Rička, *Biomed. Opt. Express*, 2012, **3**, 418.

254 A. N. Bashkatov, E. A. Genina, V. I. Kochubey and V. V Tuchin, *J. Phys. D Appl. Phys*, 2005, **38**, 2543–2555.

255 S. Grabtchak, L. G. Montgomery and W. M. Whelan, *Phys. Med. Biol.*, 2014, **59**, 2431–44.

256 E. Zamora-Rojas, B. Aernouts, A. Garrido-Varo, D. Pérez-Marín, J. E. Guerrero-Ginel and W. Saeys, *Innov. Food Sci. Emerg. Technol.*, 2013, **19**, 218–226.

257 R. L. P. van Veen, H. J. C. M. Sterenborg, A. Pifferi, A. Torricelli, E. Chikoidze and R. Cubeddu, *J. Biomed. Opt.*, 2005, **10**, 54004.

258 X. Ma, J. Q. Lu, H. Ding and X.-H. Hu, *Opt. Lett.*, 2005, **30**, 412–414.

259 Q. Li, B. J. Lee, Z. M. Zhang and D. W. Allen, *J. Biomed. Opt.*, 2010, **13**, 54064.

260 D. Cai, A. Neyer, R. Kuckuk and H. M. Heise, *J. Mol. Struct.*, 2010, **976**, 274–281.

261 T. J. Pope, M. Read, T. Medsker, A. Buschi and A. Brenbridge, *J. Can. Assoc. Radiol.*, 1984, **35**, 365–8.

262 D. M. de Bruin, R. H. Bremmer, V. M. Kodach, R. de Kinkelder, J. van Marle, T. G. van Leeuwen and D. J. Faber, *J. Biomed. Opt.*, 2010, **15**, 25001.

263 I. E. Iping Petterson, F. W. L. Esmonde-White, W. de Wilde, M. D. Morris and F. Ariese, *Analyst*, 2015, 2504–2512.

264 G. J. Greening, R. Istfan, L. M. Higgins, K. Balachandran, D. Roblyer, M. C. Pierce and T. J. Muldoon, *J. Biomed. Opt.*, 2014, **19**, 115002.

265 N. Stone and P. Matousek, *Cancer Res.*, 2008, **68**, 4424–30.

266 T. J. Farrell and S. M. Patterson, *Med. Phys.*, 1992, 19, 879.

267 M. S. Patterson, B. Chance and B. C. Wilson, *Appl. Opt.*, 1989, **28**, 2331–2336.

268 S. Fantini, M. A. Franceschini and E. Gratton, *J. Opt. Soc. Am. B*, 1994, 11, 2128.

269 S. Destounis, *Appl. Radiol.*, 2004, **33**.

270 R. B. Saager, C. Kondru, K. Au, K. Sry, F. Ayers and A. J. Durkin, *Proc. SPIE*, 2010, **7567**, 756706-756706–8.

271 D. A. Boas, C. Pitris and N. Ramanujam, *Handbook of Biomedical Optics*, 2001.

272 K. L. Lurie, G. T. Smith, S. a Khan, J. C. Liao and A. K. Ellerbee, *J. Biomed. Opt.*, 2014, **19**, 36009.

273 R. S. A.- Student, I. Member, K. A.-I. Member, R. S. Akki and K. Arunachalam, *Annu. Int. Conf. IEEE Eng. Med. Biol. Soc.*, 2014, **2014**, 1119–1122.

274 European Commision, *European guidelines for quality assurance in breast cancer screening and diagnosis*, 2013.

275 G. Greening, K. Balachandran and T. J. Muldoon, *Biomed. Opt.*, 2014, 5–7.

276 M. J. Pelletier, *Appl. Spectrosc.*, 2013, **67**, 829–840.

277 P. Matousek, *J. Opt. Soc. Am. B*, 2008, **25**, 1223.

278 M. Z. Vardaki, P. Matousek and N. Stone, *Biomed. Opt. Express*, 2016, **7**, 2130.

279 I. L. Wapnir, N. Barnard, D. Wartenberg and R. S. Greco, *Breast J.*, 2001, **7**, 184–188.

280 A. A. Andea, D. Bouwman, T. Wallis and D. W. Visscher, *Cancer*, 2004, **100**, 20–27.

281 R. L. Glaser and C. Dimitrakakis, *Menopause*, 2014, **21**, 673–678.

282 G. M. Clarke, M. Murray, C. M. B. Holloway, K. Liu, J. T. Zubovits and M. J. Yaffe, *Int. J. Breast*

Cancer, 2012, **2012**, 1–9.

283 S. R. Ward and R. L. Lieber, *J. Biomech.*, 2005, **38**, 2317–2320.

284 R. Ross, L. Léger, R. Guardo, J. De Guise and B. G. Pike, *J. Appl. Physiol.*, 1991, **70**, 2164–2172.

285 M. S. Farvid, T. W. K. Ng, D. C. Chan, P. H. R. Barrett and G. F. Watts, *Diabetes. Obes. Metab.*, 2005, **7**, 406–413.

286 F. Severcan and P. I. Haris, Eds., *Vibrational Spectroscopy in Diagnosis and Screening*, IOS Press, Volume 6 o., 2012.

287 J. I.T., *Principal Comonent Analysis*, Springer Series in Statistics, 1986.

288 F. Bonnier and H. J. Byrne, *Analyst*, 2012, **137**, 322–332.

289 M. Z. Vardaki, B. Gardner, N. Stone and P. Matousek, *Analyst*, 2015, 5112–5119.

290 J. Huang, K. H. Kim, N. Choi, H. Chon, S. Lee and J. Choo, *Langmuir*, 2011, **27**, 10228–10233.

291 S. Lee, H. Chon, J. Lee, J. Ko, B. H. Chung, D. W. Lim and J. Choo, *Biosens. Bioelectron.*, 2014, **51**, 238–43.

292 J. P. Gleeson, N. A. Plunkett and F. J. O'Brien, *Eur. Cells Mater.*, 2010, **20**, 218–230.

293 F. G. Lyons, J. P. Gleeson, S. Partap, K. Coghlan and F. J. O'Brien, *Clin. Orthop. Relat. Res.*, 2014, **472**, 1318–1328.

294 A. Haka, K. Shafer-Peltier and M. Fitzmaurice, *Cancer Res.*, 2002, 5375–5380.

295 C. Ayala-Orozco, C. Urban, S. Bishnoi, A. Urban, H. Charron, T. Mitchell, M. Shea, S. Nanda, R. Schiff, N. Halas and A. Joshi, *J. Control. Release*, 2014, **191**, 90–97.

296 C. Ayala-orozco, C. Urban, M. W. Knight, A. S. Urban, O. Neumann, S. W. Bishnoi, S. Mukherjee, A. M. Goodman, H. Charron, T. Mitchell, M. Shea, R. Roy, S. Nanda, R. Schiff, N. J. Halas and A. Joshi, *ACS Nano*, 2014, **8**, 6372–6381.

297 W. S. Cho, S. Kim, B. S. Han, W. C. Son and J. Jeong, *Toxicol. Lett.*, 2009, **191**, 96–102.

298 K. M. Tsoi, S. A. MacParland, X.-Z. Ma, V. N. Spetzler, J. Echeverri, B. Ouyang, S. M. Fadel, E. A. Sykes, N. Goldaracena, J. M. Kaths, J. B. Conneely, B. A. Alman, M. Selzner, M. A. Ostrowski, O. A. Adeyi, A. Zilman, I. D. McGilvray and W. C. W. Chan, *Nat. Mater.*, 2016, **1**, 1–10.

299 M. Longmire, P. L. Choyke and H. Kobayashi, *Nanomedicine (Lond).*, 2008, **3**, 703–17.

300 T. Sun, Y. S. Zhang, B. Pang, D. C. Hyun, M. Yang and Y. Xia, *Angew. Chemie - Int. Ed.*, 2014, **53**, 12320–12364.

301 A. K. R. Lytton-Jean, K. J. Kauffman, J. C. Kaczmarek and R. Langer, in *Nanotechnology-Based Precision Tools for the Detection and Treatment of Cancer*, eds. C. A. Mirkin, T. J. Meade, S. H. Petrosko and A. H. Stegh, Volume 166., 2015, pp. 293–322.

302 G. Oberdörster, E. Oberdörster and J. Oberdörster, *Environ. Health Perspect.*, 2005, **113**, 823–839.

303 B. J. Tromberg, N. Shah, R. Lanning, A. Cerussi, J. Espinoza, T. Pham, L. Svaasand and J. Butler, *Neoplasia*, 2000, **2**, 26–40.

304 S. Thomsen and D. Tatman, *Ann. N. Y. Acad. Sci.*, 1998, **838**, 171–193.